



Searches for invisibly decaying Higgs bosons with the CMS detector

Patrick James Dunne
of Imperial College London

A dissertation submitted to Imperial College London
for the degree of Doctor of Philosophy

The copyright of this thesis rests with the author and is made available under a Creative Commons Attribution Non-Commercial No Derivatives licence. Researchers are free to copy, distribute or transmit the thesis on the condition that they attribute it, that they do not use it for commercial purposes and that they do not alter, transform or build upon it. For any reuse or redistribution, researchers must make clear to others the licence terms of this work

Abstract

Searches for invisibly decaying Higgs bosons using the Compact Muon Solenoid (CMS) detector at the CERN Large Hadron Collider (LHC) and their interpretations are described. These searches are motivated both by a desire to characterise the newly observed Higgs boson, and by the cosmological observation of very weakly interacting matter in the universe, which is called dark matter. In order to provide context for these searches, introductions to the Standard Model (SM) of particle physics and several extensions to the SM which incorporate dark matter are given.

The searches described in this thesis use data recorded in proton-proton collisions in 2012 and focus on the most sensitive mode, Vector Boson Fusion (VBF) production. The first search uses 19.5 fb^{-1} of data promptly reconstructed in 2012 and results in an observed (expected) limit on the invisible branching fraction of the 125 GeV Higgs boson, $\mathcal{B}(H \rightarrow \text{inv})$, of 0.65 (0.49) at the 95% confidence level (CL) [1]. The second search uses 19.2 fb^{-1} of data collected using triggers with looser thresholds and reconstructed later, in 2013. This search resulted in an observed (expected) limit on $\mathcal{B}(H \rightarrow \text{inv})$ of 0.57 (0.40) at the 95% CL [2].

Combinations of these searches with searches in other production channels are also described, the most sensitive of which results in an observed (expected) limit on $\mathcal{B}(H \rightarrow \text{inv})$ of 0.36 (0.30) at 95% CL [3]. Projections of the sensitivity of these analyses in Run 2 and interpretations of their results as limits on various models of dark matter are also given [4].

Declaration

This dissertation is the result of my own work. Where figures and results are taken from other sources this is indicated by an appropriate reference. Some figures referenced as from other sources were created by me, but appear in other public documents.

The description of the analysis described in Chapter 4 follows Ref. [5], which includes elements of my work, and was [made public](#) in Ref. [1]. Specifically, I was responsible for cross-checking the results of all the W+jets background estimations, I contributed to the development of the formula used to carry out the Z+jets background estimation, I calculated and cross-checked several of the systematic uncertainties, I produced plots of the discriminating variables for final publication, and I performed all limit setting and production of limit plots.

I was the main analyser for the analysis described in [Chapter 4.4](#), responsible for all steps of the analysis including trigger efficiency measurement, background estimation, systematic uncertainty studies and limit setting. The QCD background estimation method was developed and implemented collaboratively with other members of the Imperial College high energy physics (HEP) group. This work was [made public](#) in Ref. [2].

I was also solely responsible for the combinations described in Chapter 5. For the interpretations of the VBF invisibly decaying Higgs boson searches as limits on dark mater models described in Chapter 6 I worked collaboratively with theorists at Rutgers University and members of the Imperial College and Bristol University HEP groups. This work was [made public](#) in Ref. [4].

As well as the work described in this thesis I have also carried out preparations for a search for VBF produced invisibly decaying Higgs bosons using Run 2 data from the LHC. These preparations have included measurements of the trigger efficiency for the triggers used in 2015 CMS data taking and

comparisons of the kinematic distributions of signal and background events at the increased 13 TeV centre of mass energy used in Run 2 with those from Run 1, this work is currently under approval. Together with a new PhD student, I have also carried out a combination of the first Run 2 invisibly decaying Higgs boson searches in the VBF and ZH channels with those in Run 1, which is currently being approved for publication.

Patrick James Dunne

Acknowledgements

I would like to thank my wife Stephanie for her love and endless support and also for proofreading the entirety of this document. I'd also like to thank my parents Rebecca and Patrick, without whom I wouldn't have got to the position of being able to apply for a PhD.

The help of my two supervisors Gavin Davies and David Colling has also been invaluable; thank you for always having your doors open when I needed advice. Thanks must also go to my colleagues on CMS and at Imperial, especially Anne-Marie Magnan, Joao Pela, Jim Brooke, Andrew Gilbert and Nick Wardle. I've learned a lot from our long discussions both on physics and on CMS politics. Finally, I would like to thank the Science Technology Facilities Council who funded this work, and Imperial College for all the resources they made available.

Contents

List of figures	x
List of tables	xx
1. Introduction and theory	2
1.1. The standard model of particle physics	2
1.1.1. Fundamental particles in nature	3
1.1.2. Introduction to gauge theories	5
1.1.3. The SM gauge group and fundamental particle representations . .	6
1.1.4. Spontaneous symmetry breaking and the Higgs mechanism . . .	8
1.1.5. Dark matter	10
1.2. Searching for dark matter with Higgs bosons	12
1.2.1. Higgs boson production and decay at the LHC	12
1.2.2. Some extensions of the standard model incorporating dark matter	17
1.3. Simulation	20
1.4. Statistics of exclusion limits	21
2. The LHC and the CMS experiment	24
2.1. The LHC	24
2.2. The CMS experiment	27
2.2.1. Tracker	31
2.2.2. Electromagnetic calorimeter	32
2.2.3. Hadronic calorimeter	34
2.2.4. Muon system	35
2.2.5. Trigger system	37
2.2.6. Data processing	40
3. Physics objects and event reconstruction	41
3.1. Tracks	41

3.2.	Primary vertex	42
3.3.	Particle flow	43
3.4.	Electrons	44
3.5.	Muons	46
3.6.	Jets	47
3.6.1.	Jet clustering	48
3.6.2.	Jet identification	49
3.6.3.	Jet energy corrections	50
3.7.	Missing transverse energy	51
3.8.	Taus	52
3.9.	MC weights	53
4.	Search for invisibly decaying VBF produced Higgs bosons in Run 1 prompt data	55
4.1.	Event selection	55
4.1.1.	Trigger	56
4.1.2.	Offline selection	59
4.2.	Background estimation	60
4.2.1.	$W \rightarrow e\nu + \text{jets}$	60
4.2.2.	$W \rightarrow \mu\nu + \text{jets}$	62
4.2.3.	$W \rightarrow \tau\nu + \text{jets}$	64
4.2.4.	$Z \rightarrow \nu\nu + \text{jets}$	66
4.2.5.	QCD	71
4.2.6.	Minor backgrounds	73
4.3.	Systematic uncertainties	73
4.3.1.	Jet energy scale	73
4.3.2.	Jet energy resolution	75
4.3.3.	Unclustered energy scale	76
4.3.4.	Lepton identification and isolation efficiency	76
4.3.5.	Other uncertainties	77
4.4.	Results	77
4.5.	Trigger	82
4.6.	Event selection	85
4.6.1.	Preselection	86
4.6.2.	Signal region selection	90

4.7.	Background estimation	92
4.7.1.	Top quarks	92
4.7.2.	$W \rightarrow e\nu + \text{jets}$	94
4.7.3.	$W \rightarrow \mu\nu + \text{jets}$	95
4.7.4.	$W \rightarrow \tau\nu + \text{jets}$	97
4.7.5.	Differences between the $W \rightarrow e\nu$, $W \rightarrow \mu\nu$ and $W \rightarrow \tau\nu + \text{jets}$ backgrounds	101
4.7.6.	$Z \rightarrow \nu\nu + \text{jets}$	104
4.7.7.	$V + \text{jets}$ consistency tests	107
4.7.8.	$V + \text{jets}$ scale factor investigations	107
4.7.9.	QCD	110
4.7.10.	Minor backgrounds	115
4.8.	Systematic uncertainties	115
4.9.	Results	116
4.9.1.	Improvement relative to the prompt data analysis	120
4.9.2.	Conclusion	123
5.	Combinations of Run 1 searches for invisibly decaying Higgs bosons	124
5.1.	Searches in other channels	124
5.1.1.	$Z(\ell\ell)H \rightarrow \text{invisible}$ selection	126
5.1.2.	$Z(b\bar{b})H \rightarrow \text{invisible}$ selection	126
5.1.3.	Monojet selection	127
5.2.	Combination with prompt data VBF search	128
5.3.	Combination with the parked data VBF search	129
6.	Dark matter interpretations of Run 1 searches for invisibly decaying Higgs bosons	135
6.1.	Simulation techniques and validation	135
6.2.	Results	139
6.3.	Conclusions	143
7.	Conclusions	145
A.	Parked data trigger efficiencies	147
Bibliography		154
Acronyms		164

List of figures

1.1. Evidence for dark matter (DM): (a) Rotation velocity in the galaxy NGC 6503 as a function of distance from the galactic centre ^[28] . (b) The disk and gas components shown are made of visible matter, while the halo component shows the effect of adding an additional DM halo to the galaxy. A superposition of X-ray (colour-scale) and gravitational lensing (green contours) images of the bullet cluster of galaxies ^[26]	11
1.2. Feynman diagrams for the four standard model (SM) Higgs boson production processes with the highest cross-sections: gluon fusion (ggH) (a), vector boson fusion (VBF) (b), vector boson associated production (VH) (c) and top quark associated production (d).	14
1.3. Cross-sections for Higgs boson production via the most common production processes at $\sqrt{s} = 8$ TeV as a function of Higgs boson mass, m_H ^[29] . The widths of the lines represent the theoretical uncertainties on the cross-section calculation.	15
1.4. Branching ratios for the dominant Higgs boson decays as a function of Higgs boson mass with the line widths representing the uncertainties (a), and the SM Higgs boson total width, Γ_H , as a function of Higgs boson mass (b) ^[29]	16
1.5. Best fit results for the decay signal strengths of the five highest branching ratio Higgs boson decays from a combination of CMS and ATLAS ^[34] Run 1 data (a). The negative log-likelihood as a function of $\mathcal{B}(H \rightarrow \text{inv})$, here denoted BR_{BSM} (b) ^[35]	16
1.6. Feynman diagrams for the dark matter theories considered. (a) VBF production of a scalar, H , or pseudoscalar A mediator. (b) Gluon based production of an H or A mediator. (c) An effective field theory where the mediator has been replaced by a contact interaction between the vector bosons and a hypothetical DM particle.	17

1.7.	A schematic diagram of the factorised components of the simulation of proton-proton collisions. First the hard-scatter of two of the incoming partons (shown in blue) is simulated at the centre of the event. The results of this scatter then undergo parton showering (shown in red), followed by hadronisation (shown in green) when the energy of the quarks and gluons is low enough that bound states can be formed[52].	22
2.1.	The layout of the chain of accelerators feeding into the LHC, showing the position of the four main detectors[59].	25
2.2.	A summary of the luminosity delivered to CMS during Run 1 of the LHC[61].	26
2.3.	Cross-sections for several processes in collisions of protons with protons or anti-protons as a function of centre of mass energy. The energies that the LHC and Tevatron ran at are highlighted[62].	28
2.4.	Distribution of the number of interactions per bunch crossing in CMS during 2012 running of the LHC[61].	29
2.5.	A diagram of the subsystems making up the CMS detector, illustrating the hermeticity and layered structure of the experiment[63].	30
2.6.	A schematic cross-section of the CMS experiment showing the path taken by several types of particles[64].	31
2.7.	A cross-section of the CMS tracker, indicating the subsystems that comprise it. Each line indicates a detector module[30] and the labels for each subsection are the names given by CMS to the various subsections of the tracker.	32
2.8.	A schematic of the CMS electromagnetic calorimeter (ECAL), indicating the subsystems that comprise it. The ECAL is 7.8m long by 3.5m wide[30].	33
2.9.	A schematic of a quadrant of the CMS hadron calorimeter (HCAL) in the $r - z$ plane, indicating the subsystems that comprise it[30].	36
2.10.	A schematic of a quadrant of the CMS muon system in the $r - z$ plane, indicating the subsystems that comprise it[69].	38
2.11.	A schematic of the Level-1 (L1) trigger system. The arrows indicate the flow of data, the information transferred between systems is also indicated [30].	39
3.1.	Total jet-energy-correction factor as a function of jet η for jets with $p_T = 50\text{ GeV}$ (left) and $p_T = 200\text{ GeV}$ (right), for several types of jet reconstruction used at CMS. The bands indicate the corresponding uncertainty[88].	51

3.2. Distributions of the uncorrected \cancel{E}_T in $Z \rightarrow \mu\mu$ events (left) and $\gamma + \text{jets}$ events (right) in $\sqrt{s} = 8 \text{ TeV}$ data and simulation. The shaded band corresponds to the systematic uncertainty[89].	52
4.1. The efficiency of the high-level trigger (HLT) requirements used in the prompt (blue) and parked (purple and red) data analyses as a function of the values of several offline variables, measured in a sample of events recorded on a single-muon trigger. (a) Efficiency as a function of offline $\Delta\eta_{jj}$, (b) efficiency as a function of sub-leading jet p_T , (c) efficiency as a function of offline $\cancel{E}_T^{\text{no-}\mu}$, (d) efficiency as a function of M_{jj}	57
4.2. The combined efficiency of the HLT and L1 trigger requirements used in the prompt (blue) and parked (purple and red) data analyses as a function of the values of several offline variables, measured in a sample of events recorded on a single-muon trigger. (a) Efficiency as a function of offline $\Delta\eta_{jj}$, (b) efficiency as a function of sub-leading jet p_T , (c) efficiency as a function of offline $\cancel{E}_T^{\text{no-}\mu}$, (d) efficiency as a function of M_{jj}	58
4.3. Distributions of (a) M_{jj} , (b) $\Delta\eta_{jj}$, (c) $\Delta\phi_{jj}$ and (d) leading central jet p_T in background and signal Monte Carlo (MC) events. The events shown are required to have two jets in opposite forward/backward halves of the detector with $p_T > 50 \text{ GeV}$, $M_{jj} > 150 \text{ GeV}$ and $\cancel{E}_T^{\text{no-}\mu} > 130 \text{ GeV}$. EWK refers to the V+jets and minor backgrounds described in Section 4.2 and Quantum Chromodynamics (QCD) refers to the QCD multijet background. The dashed lines indicate the offline selection criteria applied to these variables, which are motivated in the text[1].	61
4.4. Distributions of the visible W boson p_T (i.e. the electron p_T) (a) and $\cancel{E}_T^{\text{no-}\mu}$ (b) in the single electron control region. WNJets+EWK indicates the W+jets contribution to this region, SingleT+TTBar indicates the contribution from top quark related processes, DYJets+EWK indicates the Z+jets contribution, QCD indicates the QCD multijet contribution and DiBoson indicates the two vector boson contribution. All of these contributions are estimated from MC. The hatched region illustrates the systematic uncertainty[5]. Whilst the overall rate of data and MC is very different, the shape can be seen to agree well.	63

4.5. Distributions of the visible W boson p_T (i.e. the muon p_T) (a) and $\cancel{E}_T^{\text{no-}\mu}$ (b) in the single muon control region. WNJets+EWK indicates the W+jets contribution to this region, SingleT+TTBar indicates the contribution from top quark related processes, DYJets+EWK indicates the Z+jets contribution, QCD indicates the QCD multijet contribution and DiBoson indicates the two vector boson contribution. All of these contributions are estimated from MC. The hatched region illustrates the systematic uncertainty[5]. Whilst the overall rate of data and MC is very different, the shape can be seen to agree well.	65
4.6. Distributions of the the tau p_T (a) and $\Delta\phi_{jj}$ (b) in the single tau control region. WNJets+EWK indicates the W+jets contribution to this region, ZJets indicates the contribution from Z+jets, SingleT+TTBar indicates the contribution from top quark related processes, QCD indicates the QCD multijet contribution and DiBoson indicates the two vector boson contribution. All of these contributions are estimated from MC. The hatched region illustrates the systematic uncertainty[5].	67
4.7. Distributions of the $\cancel{E}_T^{\text{no-}\mu}$ (a) and M_{jj} (b) in a relaxed Z control region, with no requirement on $\Delta\phi_{jj}$, the central jet veto (CJV) removed, and the requirements on M_{jj} and $\Delta\eta_{jj}$ relaxed to 1000 GeV and 3.5 respectively. DY(ll)+jets indicates the contribution from Z+jets processes and $t\bar{t}$, tW , VV indicates the contribution from minor backgrounds. The hatched region illustrates the systematic uncertainty[1].	70
4.8. A diagram of the regions used in the QCD ABCD background estimation method. Region D is the signal region and regions A, B and C are mutually exclusive control regions.	71
4.9. Distribution of the $\cancel{E}_T^{\text{no-}\mu}$ for events passing and failing the CJV. The largest difference seen in any bin is 40%. This difference is used to assign as a systematic uncertainty on the QCD background estimation.	72
4.10. The distribution of the sub-leading jet's p_T in W+Jets MC events with the nominal jet energy scale (JES) and for JESUP and JESDOWN.	74

4.11. Distributions of the $\cancel{E}_T^{\text{no-}\mu}$ (a) and M_{jj} (b) of events observed in data and expected from the background estimation methods described in Section 4.2 in the signal region. tt+DY+VV indicates the contribution from minor backgrounds. The hatched region illustrates the systematic uncertainty. The QCD background is not shown due to the very low number of events in the MC samples. The cumulative effect of a signal from a Higgs boson with mass of 125 GeV, decaying 100% to invisible final states is also shown[1].	79
4.12. Expected and observed 95% confidence level (CL) upper limits on the VBF $\sigma \times \mathcal{B}$ in pb (a) and normalised to the SM VBF Higgs boson production cross-section (b)[1]. The green and yellow bands indicate the 68% and 95% confidence intervals on the expected limit respectively.	81
4.13. The efficiency for the trigger (color-scale) used in eras B and C (a) and era D (b), as a function of M_{jj} and sub-leading jet p_T for events with $\cancel{E}_T^{\text{no-}\mu}$ between 60 and 120 GeV. The efficiency was measured using a single muon dataset collected with an orthogonal trigger.	84
4.14. The results of performing a fit of the function in Equation 4.9 to the efficiency of the trigger used in era D, measured in a sample of single muon events collected with an orthogonal trigger. The dashed bands show the uncertainty on the fit due to each of the three parameters of the fit. The two bins of dijet mass (m_{jj}) and sub-leading jet's p_T ($j2pt$) shown are those with the two highest numbers of events from the final signal region described in Section 4.6. The results of the fits in the other bins are shown in Appendix A.	85
4.15. (a) \mathcal{S} after the trigger driven selection described in Equation 4.11. (b) $\min\Delta\phi(j, \cancel{E}_T^{\text{no-}\mu})$ after the trigger driven selection and requiring $\mathcal{S} > 3$. (c) M_{jj} after the trigger driven selection and requiring $\mathcal{S} > 3$ and $\min\Delta\phi(j, \cancel{E}_T^{\text{no-}\mu}) > 1$. All three plots are of the signal-like region with the MC scaled using the background estimation methods described in Section 4.7. The disagreement between data and the predictions from background MC samples is believed to be due to mismeasured QCD multi-jet events which are not well modelled by the available MC samples. The last bin of each distribution contains the events above the range displayed. Signal ($gg \rightarrow H$) refers to an SM VBF (ggH) produced Higgs boson with $\mathcal{B}(H \rightarrow \text{inv}) = 100\%$.	88

4.16. From top to bottom, left to right, distributions of $\Delta\eta_{jj}$, M_{jj} , leading jet p_T , sub-leading jet p_T , $\cancel{E}_T^{\text{no-}\mu}$, \mathcal{S} and $\min\Delta\phi(j, \cancel{E}_T^{\text{no-}\mu})$ for events passing the full preselection. No QCD contribution is shown, which accounts for the difference between the data observation and background prediction. The last bin of each distribution contains the events above the range displayed.	89
4.17. Matrices of correlation coefficients for several variables in signal (a) and V+jets background (b) events passing the signal region selection. The variables are 1) the azimuthal angle difference between the $\cancel{E}_T^{\text{no-}\mu}$ and the unclustered energy in the event, 2) the square root of the hadronic energy in the event, 3) \mathcal{S} , 4) $\cancel{E}_T^{\text{no-}\mu}$, 5) M_{jj} , 6) the number of jets with $p_T > 30$ GeV between the two tag jets in η , 7) the vectorial sum of the tag jets p_T and the $\cancel{E}_T^{\text{no-}\mu}$, 8) the ratio between the magnitude of the vectorial sum of the tag jet's p_T and the $\cancel{E}_T^{\text{no-}\mu}$	91
4.18. The distribution of $\min\Delta\phi(j, \cancel{E}_T^{\text{no-}\mu})$ (a) and M_{jj} (b) in the top control region with one tight electron and one tight muon. The last bin of each distribution contains the events above the range displayed.	93
4.19. The distribution of $\min\Delta\phi(j_{1/2}, \cancel{E}_T^{\text{no-}\mu})$ (a) and M_{jj} (b) in the single top control region. The last bin of each distribution contains the events above the range displayed.	95
4.20. Distributions of variables in data and MC events in the $W \rightarrow e\nu$ control region. MC events from V+jets backgrounds are scaled by their data-driven scale factors. The variables shown are from top to bottom and left to right $\Delta\eta_{jj}$, M_{jj} , the leading and sub-leading jet's p_T , $\cancel{E}_T^{\text{no-}\mu}$, \mathcal{S} and $\min\Delta\phi(j, \cancel{E}_T^{\text{no-}\mu})$. The last bin of each distribution contains the events above the range displayed[2].	96
4.21. Distributions of variables in data and MC events in the $W \rightarrow \mu\nu$ control region. MC events from V+jets backgrounds are scaled by their data-driven scale factors. The variables shown are from top to bottom and left to right $\Delta\eta_{jj}$, M_{jj} , the leading and sub-leading jet's p_T , $\cancel{E}_T^{\text{no-}\mu}$, \mathcal{S} and $\min\Delta\phi(j, \cancel{E}_T^{\text{no-}\mu})$. The last bin of each distribution contains the events above the range displayed[2].	98

4.22. Distributions of variables in data and MC events in the $W \rightarrow e\nu$ control region. MC events from V+jets backgrounds are scaled by their data-driven scale factors. The variables shown are from top to bottom and left to right $\Delta\eta_{jj}$, M_{jj} , the leading and sub-leading jet's p_T , $E_T^{\text{no-}\mu}$, \mathcal{S} , $\min\Delta\phi(j_{1/2}, E_T^{\text{no-}\mu})$ and the tau- E_T system's transverse mass. The last bin of each distribution contains the events above the range displayed[2].	100
4.23. Distributions of the number of jets with $p_T > 15$ GeV (a), $\min\Delta\phi(j, E_T^{\text{no-}\mu})$ (b) and the p_T of the leading generator level electron/muon (c) in $W \rightarrow e/\mu\nu$ events in a region with cuts which are the same as those of the signal region except that the $\min\Delta\phi(j, E_T^{\text{no-}\mu})$ requirement has been loosened to 1 and a generator level lepton outside the detector acceptance for both electrons and muons is required. The last bin of each distribution contains the events above the range displayed.	103
4.24. Distributions of variables in data and MC events in the dimuon control region. MC events from V+jets backgrounds are scaled by their data-driven scale factors. The variables shown are from top to bottom and left to right $\Delta\eta_{jj}$, M_{jj} , the leading and sub-leading jet's p_T , $E_T^{\text{no-}\mu}$, \mathcal{S} , $\min\Delta\phi(j_{1/2}, E_T^{\text{no-}\mu})$ and the invariant mass of the dimuon system. The contributions to this region from electroweak and QCD produced Z+jets events are shown separately. The last bin of each distribution contains the events above the range displayed[2].	105
4.25. The distribution of $E_T^{\text{no-}\mu}$ expected in the single electron (a), single tau (b) and dimuon control regions (c) from MC (red), data minus other background processes (blue) and MC weighted by the data driven scale factor calculated for each bin of the $E_T^{\text{no-}\mu}$ distribution in the single muon control region as described in Section 4.7.7 (green). The lower plot shows the ratio between the data driven scale factor weighted MC and the data minus other background processes. The grey band on the lower plots represents the systematic uncertainty from all sources described in Section 4.8.	108

4.26. The data driven scale factor obtained from a single muon control region, as described in Section 4.7.8, as a function of the cuts on $\min\Delta\phi(j, \cancel{E}_T^{\text{no-}\mu})$ and M_{jj} (a) and $\Delta\phi_{jj}$ and M_{jj} (b). It is important to note that the requirement on $\Delta\phi_{jj}$ is that the event have a value lower than the cut threshold, so the requirement is tighter to the left of the plot. The parked data analysis preselection requirements correspond to the top right bin of (a).	109
4.27. The reconstructed \cancel{E}_T , PFMET, as a function of the generator level \cancel{E}_T , genMET in a MC sample with no generator level cuts on \cancel{E}_T or jet kinematics. For reference, the cut placed on genMET in the dedicated VBF QCD multijet sample is shown in red, and the offline prompt analysis cut on PFMET is shown in blue[104].	111
4.28. A schematic of the regions used in the QCD background estimation.	112
4.29. The distribution of \mathcal{S} in the inverted (a) and 3-jet (b) regions used in the QCD background estimation. In (a) the QCD shape is estimated using the VBF QCD sample, and in (b) the QCD shape is taken from the inverted region as described in the text. Both shapes are normalised to the total number of events seen in the region minus the expected contribution from other background[2].	113
4.30. The QCD scale factor obtained in sideband 1 as a function of the lower bound on $\min\Delta\phi(j, \cancel{E}_T^{\text{no-}\mu})$ (a) and \mathcal{S} (b). Exponential fits which are used to extrapolate to higher values of these requirements are overlaid on both distributions, and the values of these fits at several representative values are displayed.	114
4.31. From top to bottom and left to right $\Delta\eta_{jj}$, M_{jj} , the leading and sub-leading jet's p_T , $\cancel{E}_T^{\text{no-}\mu}$, \mathcal{S} and $\min\Delta\phi(j, \cancel{E}_T^{\text{no-}\mu})$ in the signal region. The hatched band indicates the size of the total uncertainty on the background estimate[2].	119
4.32. The 95% CL limit on the cross-section times $\mathcal{B}(H \rightarrow \text{inv})$ (a) and the 95% CL limit on $\mathcal{B}(H \rightarrow \text{inv})$ of a SM Higgs boson (b) as a function of the Higgs boson mass, assuming SM Higgs boson acceptances. The green and yellow bands indicate the 68% and 95% confidence intervals on the expected limit respectively[2].	121
4.33. Scans of the profile likelihood (i.e. with the nuisance parameters at each point chosen to maximise the likelihood) versus $\mathcal{B}(H \rightarrow \text{inv})$ of a SM Higgs boson with a mass of 125 GeV for the prompt and parked data analyses.	122

-
- 5.1. Expected and observed 95% CL upper limits on the Z boson associated production (ZH) $\sigma \times \mathcal{B}(H \rightarrow \text{inv})$ in pb (a) and normalised to the SM VBF Higgs boson production cross-section (b) obtained from the combination of the $Z(\ell\ell)H$ and $Z(b\bar{b})H$ searches. The green and yellow bands indicate the 68% and 95% confidence intervals on the expected limit respectively[1]. 130
- 5.2. Expected and observed 95% CL upper limits on the $\sigma \times \mathcal{B}(H \rightarrow \text{inv}) / \sigma_{SM}$ obtained from the combination of the VBF, $Z(\ell\ell)H$ and $Z(b\bar{b})H$ searches. The green and yellow bands indicate the 68% and 95% confidence intervals on the expected limit respectively[1]. 130
- 5.3. Expected and observed 95% CL upper limits on the $\sigma \times \mathcal{B}(H \rightarrow \text{inv}) / \sigma_{SM}$ obtained from the combination of the VBF and $Z(\ell\ell)H$ searches. The green and yellow bands indicate the 68% and 95% confidence intervals on the expected limit respectively[1]. 131
- 5.4. Log-likelihood versus $\mathcal{B}(H \rightarrow \text{inv})$. The solid curve represents the observation in data and the dashed curves represent the median expected result for no invisible decays of the Higgs boson[3]. 133
- 5.5. Expected and observed 95% CL upper limits on production cross-section times $\mathcal{B}(H \rightarrow \text{inv})$ normalised to the SM production cross-section obtained from the combination of all channels targeting each Higgs boson production mode. The green and yellow bands indicate the 68% and 95% confidence intervals on the expected limit respectively[3]. 134
- 6.1. The \cancel{E}_T distribution for two effective field theory (EFT) signal models (D5a and D6a), and spin-0 simplified models, described in Section 1.2.2, with representative model parameter values. For the 125 GeV Higgs boson model, the dark matter mass, m_χ is assumed to be 56.2 GeV, whereas for the other models m_χ is assumed to be 100 GeV. For the scalar and pseudoscalar models the mass of the mediator is assumed to be 316.2 GeV. It is important to note that the 125 GeV Higgs boson model simulation includes VH production of the Higgs boson as well as VBF[4]. 138
- 6.2. (a) Expected limits on $\mathcal{B}(H \rightarrow \text{inv})$ for a 125 GeV Higgs boson, as a function of integrated luminosity, projections were made both assuming constant systematic uncertainties (red) and assuming the systematic uncertainties improve with the square root of the integrated luminosity (blue).
 (b) Expected limits on the coupling, g_χ , of DM to the 125 GeV Higgs boson as a function of DM mass, m_χ for several integrated luminosities[4]. 141

6.3. Expected exclusions on the coupling of DM to scalar (a) and pseudoscalar (b) mediators as a function of mediator mass, m_H/m_A , and DM mass, m_χ . Note that some contours are not shown because the corresponding value of the coupling is not excluded at that integrated luminosity[4].	142
6.4. Expected 95% CL lower limits on the EFT scale, Λ , for D5 (a), D6 (b) and D7 (c) type EFT operators for several values of the integrated luminosity. The D5a, D7b and D7d operators have very similar exclusions to the D5b, D7a and D7c operators respectively, so are not shown for clarity[4].	144
A.1. The measured efficiency of the trigger used in run A as a function of MET in bins of dijet mass (m_{jj}) and sub-leading jet p_T ($j2pt$). The bin that each plot corresponds to is displayed at the top of the plot.	147
A.2. The measured efficiency of the trigger used in run A as a function of MET in bins of dijet mass (m_{jj}) and sub-leading jet p_T ($j2pt$). The bin that each plot corresponds to is displayed at the top of the plot.	148
A.3. The measured efficiency of the trigger used in runs B and C as a function of MET in bins of dijet mass (m_{jj}) and sub-leading jet p_T ($j2pt$). The bin that each plot corresponds to is displayed at the top of the plot.	149
A.4. The measured efficiency of the trigger used in runs B and C as a function of MET in bins of dijet mass (m_{jj}) and sub-leading jet p_T ($j2pt$). The bin that each plot corresponds to is displayed at the top of the plot.	150
A.5. The measured efficiency of the trigger used in run D as a function of MET in bins of dijet mass (m_{jj}) and sub-leading jet p_T ($j2pt$). The bin that each plot corresponds to is displayed at the top of the plot.	151
A.6. The measured efficiency of the trigger used in run D as a function of MET in bins of dijet mass (m_{jj}) and sub-leading jet p_T ($j2pt$). The bin that each plot corresponds to is displayed at the top of the plot.	152

List of tables

1.1.	The fundamental fermions observed in nature separated into their three generations. Each particle shown also has an antiparticle with opposite charge and identical mass[14]	4
1.2.	The fundamental vector bosons observed in nature separated by the force which they mediate[14].	4
4.1.	The inputs to, and results of, the $W \rightarrow e\nu$ background estimation. $N_{W \rightarrow e\nu}$ is, for the signal region the number of events expected from $W \rightarrow e\nu$ backgrounds, and for the control region the number of events remaining in the region after the subtraction of other backgrounds.	62
4.2.	The inputs to, and results of, the $W \rightarrow \mu\nu$ background estimation. $N_{W \rightarrow \mu\nu}$ is, for the signal region the number of events expected from $W \rightarrow \mu\nu$ backgrounds, and for the control region the number of events remaining in the region after the subtraction of other backgrounds.	64
4.3.	The inputs to, and results of, the $W \rightarrow \tau\nu$ background estimation. $N_{W \rightarrow \tau\nu}$ is, for the signal region the number of events expected from $W \rightarrow \tau\nu$ backgrounds, and in the control region the number of events remaining in the region after the subtraction of other backgrounds.	66
4.4.	The input variables for the calculation of ϵ_{VBF}^S and ϵ_{VBF}^C using Equations 4.4 and 4.5 respectively.	69
4.5.	The inputs to, and results of, the $Z \rightarrow \nu\nu$ background estimation using Equation 4.3. ϵ_{VBF} in the signal (control) region is calculated using Equation 4.4 (4.5). $N_{Z \rightarrow \nu\nu}/N_{Z/\gamma^* \rightarrow \mu\mu}$ is in the signal region the number of events expected from $Z \rightarrow \nu\nu$ backgrounds, and for the control region the number of events remaining in the region after the subtraction of other backgrounds. The systematic uncertainties are calculated as described in Section 4.3.	70
4.6.	Numbers of events from data and MC in each region used in the QCD background estimate and the final estimated number of events.	72

4.7. A summary of the uncertainties in the total expected signal and background yields. All uncertainties are quoted as the percentage change in the yield when each effect is varied up and down according to its uncertainty. The signal yields assume a Higgs boson mass of 125 GeV.	78
4.8. The estimated numbers of background and signal events, together with the observed yield, in the signal region. The signal yield assumes a Higgs boson mass of 125 GeV and $\mathcal{B}(H \rightarrow \text{inv}) = 100\%$	78
4.9. A summary of the requirements of the triggers used for this analysis in each Run 1 era. All triggers require that there is at least one pair of jets in the event satisfying all of the jet requirements listed in this table. All requirements are on HLT variables unless stated otherwise.	82
4.10. The inputs to, and results of, Equation 4.14, when used to estimate the $W \rightarrow e\nu$ estimate in the signal region.	95
4.11. The inputs to, and results of, Equation 4.14, when used to estimate the $W \rightarrow \mu\nu$ estimate in the signal region.	97
4.12. The inputs to, and results of, Equation 4.14, when used to estimate the $W \rightarrow \tau\nu$ estimate in the signal region.	99
4.13. The numbers of events predicted by MC in the two sub-regions of the signal region with a generator level lepton that is inside/outside the detector acceptance for both electrons and muons from $W \rightarrow e\nu$ and $W \rightarrow \mu\nu$ processes. The errors shown are the MC statistical uncertainties.	102
4.14. The inputs to Equations 4.15, 4.16 and 4.17 and the final estimate of the $Z \rightarrow \nu\nu$ background in the signal region for the parked data analysis. Also shown for comparison is the ratio between the MC prediction of the number of $Z/\gamma^* \rightarrow \mu\mu$ events in the control region and the number of data events in the control region. The systematic uncertainties quoted include MC statistical uncertainties and all sources listed in Section 4.8.	106
4.15. A summary of the uncertainties on the total background and signal yields. All uncertainties affect the normalization of the yield, and are quoted as the change in % in the total background or signal estimate, when each systematic effect is varied according to its uncertainties. The signal uncertainties are given for $m_H = 125$ GeV and $\mathcal{B}(H \rightarrow \text{inv}) = 100\%$	117

4.16. The estimated numbers of background and signal events from each process, together with the observed yield, in the signal region. The signal yield assumes a Higgs boson mass of 125 GeV and $\mathcal{B}(H \rightarrow \text{inv}) = 100\%$. Where two errors are quoted they are the statistical and systematic uncertainties respectively, where only one is quoted it is the systematic uncertainty. . .	118
4.17. The 95% CL expected limits on $\mathcal{B}(H \rightarrow \text{inv})$ obtained when applying both the prompt and parked data analysis selections to both the prompt and parked data.	123
5.1. Summary of the analyses included in the combination. The first column is the name of the analysis. The second and third columns give the integrated luminosity of the 7 and 8 TeV data sets used by each analysis. The fourth column contains the names of the categories in each analysis and the fifth column gives the proportion of signal events expected to come from each Higgs boson production mode.	125
5.2. Summary of 95% CL upper limits on $\frac{\sigma}{\sigma_{SM}} \cdot \mathcal{B}(H \rightarrow \text{inv})$ for a 125 GeV Higgs boson obtained from each individual search contributing to the combinations described in this section[1, 3].	126
5.3. Uncertainties correlated between the VBF prompt data, $Z(\ell\ell)H$ and $Z(b\bar{b})H$ searches and the analyses they affect. Also quoted is the relative change in the expected limit on $\mathcal{B}(H \rightarrow \text{inv})$ on removing each uncertainty from the analysis.	129
5.4. Uncertainties correlated between the VBF parked data, $Z(\ell\ell)H$, $Z(b\bar{b})H$ and monojet searches and the analyses they affect.	132
6.1. Event yields obtained, for several sets of event selection requirements, from two samples where the hard-scatter was simulated using MADGRAPH (second column) and POWHEG (third column), both of which were processed using the DELPHES fast detector reconstruction package. For each line the selection stated in the first column is added to the selection present for the line before. The starting point for the selection is described in Equation 6.1.137	137

Chapter 1.

Introduction and theory

In order to describe the search for invisible decays of the Higgs boson (“Higgs to invisible”), it is necessary to describe the theory behind **them** and the statistical techniques used in carrying out the search. This chapter will start with an introduction to the current best theory of particle physics, the **SM**, focusing on the Higgs mechanism, before outlining the motivations behind, and some candidates for, physics beyond the SM (BSM), then concluding with a discussion of the statistics of hypothesis testing. Natural units, where $\hbar = c = 1$, Einstein summation convention and Feynman slash notation are used throughout. **Four vector** indices are labeled using Greek letters, and gauge group generators using Roman letters.

1.1. The standard model of particle physics

The SM describes the interaction of the particles currently thought to be fundamental with the strong, weak and electromagnetic forces [6–9]. Its predictions, which come from specifying the symmetries the theory respects and how they are broken, the particles in the theory, and 18 free parameters, have been tested in many different experiments, in some cases up to one part in a trillion [10]. However, it does face challenges, one example being that it does not describe **DM**.

The SM is a gauge invariant quantum field theory (QFT). To construct a QFT the symmetries that are respected by the theory and the fields it describes must be specified. The symmetries are important because of Noether’s theorem, which states that for every continuously differentiable symmetry of the Lagrangian of a theory there is a corresponding conservation law [11, 12]. An example of this is the conservation of energy,

linear momentum and angular momentum, which result through Noether's theorem from Poincaré invariance, the invariance of the laws of physics under translations and rotations in space and time. In addition to giving rise to conservation laws, some types of symmetry lead to additional fields being required to preserve invariance, this will be discussed further in Section 1.1.2 [13].

Because particles correspond to the quantised excitations of fields, the fields that can be described by the QFT are constrained by the fundamental particles seen in nature. In order to add a new field an explanation for why the corresponding particle has not yet been observed must, therefore, be provided. Specifically, a scalar field corresponds to a spin zero boson, spinor fields correspond to spin half fermions, and vector fields correspond to spin 1 bosons. We will now go through the particles observed in nature and how they are represented in the SM.

1.1.1. Fundamental particles in nature

There are two types of fundamental particles in nature, fermions and bosons. The fermions observed in nature that are currently thought to be fundamental are then divided into those which interact via the strong force (the quarks), and those which don't (the leptons). Both the quarks and leptons exist in two further types: charged and neutral in the case of the leptons, and up type and down type in the case of the fermions. Another interesting feature of the fermions is that they are arranged in three generations. Each generation has one fermion of each type with the same quantum numbers as those in the other generations, except that the mass is different. Table 1.1 shows this structure.

The bosons in nature also exist in two types. The first type are vector bosons, which mediate the three fundamental interactions described by the SM. The vector bosons are summarised in Table 1.2, where it can be seen that their masses are very different, the photon and the eight gluons being massless, while the W^\pm and Z bosons are massive. As we will see in Section 1.1.4, explaining these masses requires the Higgs mechanism [15–20]. The Higgs mechanism also gives rise to the other type of boson seen in nature, the scalar Higgs boson. In order to see how all of the above particles are represented in the SM, an introduction to gauge theories is necessary.

Table 1.1.: The fundamental fermions observed in nature separated into their three generations. Each particle shown also has an antiparticle with opposite charge and identical mass [14]

Generation	Leptons			Hadrons		
	Particle	Mass	Electric Charge	Particle	Mass	Electric Charge
1	e^-	511 keV	-1	u	2.3 MeV	$+\frac{2}{3}$
	ν_e	~ 0	0	d	4.8 MeV	$-\frac{1}{3}$
2	μ^-	105.7 MeV	-1	c	1.275 GeV	$+\frac{2}{3}$
	ν_μ	~ 0	0	s	95 MeV	$-\frac{1}{3}$
3	τ^-	1.777 GeV	-1	t	173.2 GeV	$+\frac{2}{3}$
	ν_τ	~ 0	0	b	4.18 GeV	$-\frac{1}{3}$

Table 1.2.: The fundamental vector bosons observed in nature separated by the force which they mediate [14].

Force	Particle	Mass	Electric Charge
Electromagnetism	γ	0	0
Weak	W^\pm	80.4 GeV	± 1
	Z	91.2 GeV	0
Strong	g	0	0

1.1.2. Introduction to gauge theories

Gauge symmetries are local transformations, i.e. the transformation can be different at different points in space and time. To see the effect of imposing such a symmetry on a theory, consider imposing local invariance under $U(1)$ transformations on the Dirac Lagrangian for a fermion, ψ , with mass, m :

$$\mathcal{L} = i\bar{\psi}\not{\partial}\psi - m\bar{\psi}\psi \quad [21]. \quad (1.1)$$

This Lagrangian is invariant under a global $U(1)$ transformation $\psi \rightarrow e^{iq\theta}\psi$, where q and θ are constant. However, if the $U(1)$ transformation is local i.e. θ is a function of spacetime position the Lagrangian is no longer invariant and transforms as:

$$\mathcal{L} \rightarrow \mathcal{L} - q(\partial_\mu\theta)\bar{\psi}\gamma^\mu\psi. \quad (1.2)$$

In order to restore invariance, a vector field, A_μ , referred to as a gauge field or gauge boson, which transforms as $A_\mu \rightarrow A_\mu + \partial_\mu\theta$ and has an interaction with the fermion field:

$$\mathcal{L}_{int} = q(\bar{\psi}\gamma^\mu\psi)A_\mu, \quad (1.3)$$

can be added to the theory. The interaction term of the new gauge field transforms as:

$$\mathcal{L}_{int} \rightarrow \mathcal{L}_{int} + q(\partial_\mu\theta)\bar{\psi}\gamma^\mu\psi, \quad (1.4)$$

which precisely cancels the non-gauge invariance seen in Equation 1.2. Assuming the new gauge field to be massless the Lagrangian is now:

$$\mathcal{L} = i\bar{\psi}\not{\partial}\psi - m\bar{\psi}\psi + q(\bar{\psi}\gamma^\mu\psi)A_\mu - \frac{1}{4}F_{\mu\nu}F^{\mu\nu}, \quad (1.5)$$

where $F_{\mu\nu}$ is the field strength tensor of the vector field. For a gauge boson from a general gauge group $F_{\mu\nu}$ is written as:

$$F_{\mu\nu}^a = \partial_\mu A_\nu^a - \partial_\nu A_\mu^a + g f_{abc} A_\mu^b A_\nu^c, \quad (1.6)$$

where f^{abc} are the structure constants of the gauge group, which are a representation of the commutation relations between the group's generators. For $U(1)$, which only has one self-commuting generator, the single structure constant is 0. However, for non-Abelian

gauge groups (i.e. those with non-commuting generators) they can be non-zero causing the $F_{\mu\nu}F^{\mu\nu}$ term in the Lagrangian to include self-interaction terms of the vector bosons.

Equation 1.5 can be rewritten as:

$$\mathcal{L} = i\bar{\psi}\gamma^\mu \mathcal{D}_\mu \psi - m\bar{\psi}\psi - \frac{1}{4}F_{\mu\nu}F^{\mu\nu}, \quad (1.7)$$

where $\mathcal{D}_\mu = \partial_\mu + iqA_\mu$ and is referred to as the covariant derivative. Comparing Equation 1.1 and Equation 1.7 it can be seen that to go from a globally invariant Lagrangian to a locally invariant one we have substituted the normal spacetime derivative for the covariant derivative and added the free term of the vector field.

In the case of $U(1)$ transformations, which have one degree of freedom ~~so~~ can be described by one parameter, in the above case θ , in order to make the Lagrangian locally invariant one interacting gauge boson had to be added. This correspondence between the number of degrees of freedom and the number of gauge bosons holds generally. For each degree of freedom of a group's transformations there exists a generator of the group, and for each generator one interacting gauge boson must be added to achieve local invariance.

1.1.3. The SM gauge group and fundamental particle representations

The SM is locally gauge invariant under the group $SU(3)_C \otimes SU(2)_L \otimes U(1)_Y$. $SU(3)_C$ is the group governing the strong force interactions which couple to colour charge, C. $SU(2)_L$, which couples to left handed fermions, L, and $U(1)_Y$, which couples to weak hypercharge, Y are the groups governing the electroweak interactions. The weak hypercharge of any given particle is:

$$Y = 2(Q - T_3), \quad (1.8)$$

where Q is the electric charge, and T_3 is the third component of the weak isospin, which is $\pm \frac{1}{2}$ for left handed fermions, and zero for all other particles.

Fermions in the SM are spin half spinor representations of these symmetry groups. These spinors can be split into chirally left and right handed components using the projection operators $P_L = \frac{1}{2}(1 \mp \gamma^5)$. Chirally left and right handed fermions transform differently under $SU(2)_L$. The right handed spinors are not charged under $SU(2)_L$ and thus are represented as a singlet, while the left handed spinors transform as a doublet.

The first generation of leptons can, therefore, be written as:

$$\psi_1 = e_R, \psi_2 = L = \begin{pmatrix} \nu_e \\ e_L \end{pmatrix}. \quad (1.9)$$

The SM treats neutrinos as massless and has no right handed neutrino. Similarly the first generation of quarks can be written as:

$$\psi_3 = u_R, \psi_4 = d_R, \psi_5 = \begin{pmatrix} u_L \\ d_L \end{pmatrix}. \quad (1.10)$$

As we saw in Section 1.1.2 gauge symmetries in theories with fermions require the addition of an interacting vector boson per symmetry generator to preserve gauge invariance. $SU(3)_C$ has eight generators whose eight vector bosons, $G_{a\mu}$, correspond to the eight physical gluons of QCD, which mediate the strong interaction. $SU(2)_L$ has three generators whose three vector bosons, W_μ^i , mix with the one vector boson from $U(1)_Y$, B_μ unifying the electromagnetic and weak forces into one electroweak force. The physical states that result are:

$$\begin{aligned} W^\pm_\mu &= \frac{1}{\sqrt{2}} (W_\mu^1 \mp i W_\mu^2) \\ Z_\mu &= \cos(\theta_W) W_\mu^3 - \sin(\theta_W) B_\mu \\ A_\mu &= \sin(\theta_W) W_\mu^3 + \cos(\theta_W) B_\mu, \end{aligned} \quad (1.11)$$

where θ_W is the Weinberg (weak) mixing angle and A_μ is the photon field. Also, as described in Section 1.1.2 the interaction between these vector bosons and the fermion fields occurs through their presence in the covariant derivative, and interactions between the vector bosons occur because $SU(3)_C$ and $SU(2)_L$ are non-Abelian.

Now let us try to construct a Lagrangian for these fields. First ignoring the masses we find:

$$\mathcal{L} = i\bar{\psi}_i \not{D} \psi_i - \frac{1}{4} F_{\mu\nu j} F_j^{\mu\nu}, \quad (1.12)$$

where the sum over all ψ also includes the second and third generations, $F_{\mu\nu}F_j^{\mu\nu}$ is a sum of the free terms of all the SM gauge bosons and \mathcal{D} is the SM covariant derivative:

$$\mathcal{D}_\mu = \partial_\mu + ig_1 \frac{Y}{2} B_\mu + ig_2 \frac{\tau_i}{2} W_\mu^i + ig_3 \frac{\lambda_a}{2} G_\mu^a, \quad (1.13)$$

with Y being the constant generator of $U(1)$, τ_i the generators of $SU(2)_L$, λ_a the generators of $SU(3)_C$ and g_i the coupling constants of the fields. It should be noted that $\frac{g_1}{g_2}$ is equal to $\tan(\theta_W)$.

When we try to include mass a problem occurs. We know that some of the fermions have mass, and consequently we should have fermion mass terms of the form:

$$\begin{aligned} \mathcal{L}_{m_f} &= -m_f \bar{f} f \\ &= -m_f \bar{f} \left[\frac{1}{2} (1 - \gamma^5) + \frac{1}{2} (1 + \gamma^5) \right] f \\ &= -m_f (\bar{f}_R f_L + \bar{f}_L f_R), \end{aligned} \quad (1.14)$$

in our Lagrangian. However, as the left and right handed fields do not transform in the same way under $SU(2)_L$, this term breaks the gauge symmetry of the Lagrangian and can't be present.

A similar problem occurs for vector fields. In Section 1.1.2 ~~we didn't consider the mass term of these vector fields~~:

$$\mathcal{L}_{m_V} = \frac{1}{2} m_V^2 A_\mu A^\mu, \quad (1.15)$$

~~which is~~ not gauge invariant, so it is not possible to include the massive vector bosons on their own in gauge invariant theories either. The additional piece of the SM required to allow particles to have mass is the Higgs mechanism.

1.1.4. Spontaneous symmetry breaking and the Higgs mechanism

The Higgs mechanism is a form of spontaneous symmetry breaking [15–20]. A symmetry is said to be spontaneously broken when the Lagrangian remains invariant while the vacuum state, i.e. that with lowest energy, does not [21]. Terms of the Lagrangian which are not gauge invariant can then be incorporated into the theory by adding a field which has a non-zero vacuum expectation value and coupling it to the other fields present in

the desired term. For the Higgs mechanism this field is a complex scalar $SU(2)_L$ doublet, ϕ , called the Higgs field:

$$\phi = \begin{pmatrix} \phi^+ \\ \phi^0 \end{pmatrix}. \quad (1.16)$$

The main part of the Higgs field Lagrangian is:

$$\mathcal{L} = T - V = (\mathcal{D}_\mu \phi)^\dagger (\mathcal{D}^\mu \phi) + \mu^2 \phi^\dagger \phi - \lambda (\phi^\dagger \phi)^2, \quad (1.17)$$

Where the first two terms on the right hand side make up the kinetic part of the Higgs field Lagrangian, T , and the third term is the Higgs field potential, V . For $\mu^2 > 0$, the values of the Higgs field which minimise the Lagrangian are non-zero and form a circle in the phase space of ϕ . All of these minima are equivalent and a particular minimum can be chosen with no physical effect. By convention we choose the following minimum:

$$\langle 0 | \phi | 0 \rangle = \begin{pmatrix} 0 \\ \sqrt{\frac{\mu^2}{2\lambda}} \end{pmatrix} = \frac{1}{\sqrt{2}} \begin{pmatrix} 0 \\ v \end{pmatrix}. \quad (1.18)$$

Next we consider small perturbations around this minimum. Ignoring perturbations that can be set to zero by gauge freedom gives:

$$\phi = \begin{pmatrix} 0 \\ v + H \end{pmatrix}. \quad (1.19)$$

Inserting this into Equation 1.17 and ignoring terms with more than one type of field gives at leading order:

$$\mathcal{L} = \frac{1}{2} \partial_\mu H \partial^\mu H - \frac{1}{2} \mu^2 H^2 + \frac{v^2}{8} [g_2^2 W_\mu^+ W^{+\mu} + g_2^2 W_\mu^- W^{-\mu} + (g_1^2 + g_2^2) Z_\mu Z^\mu]. \quad (1.20)$$

As expected, the weak vector bosons W_μ^\pm and Z_μ acquire masses $\frac{g_2 v}{2}$ and $\frac{v}{2} \sqrt{g_1^2 + g_2^2}$ respectively. We also see an additional massive scalar H , which is the Higgs boson, with mass $\sqrt{2}\mu$. The photon and gluons do not acquire masses, as the particular choice of coupling constants and the structure of the group generators leads to the terms in A_μ and $G_{\mu a}$ being zero.

The final part of the Higgs field Lagrangian is that giving rise to the fermion masses. These are generated by a Yukawa term in the Lagrangian for each fermion as follows:

$$\mathcal{L}_{Yuk} = y_f (\bar{f}_L \phi f_R + \bar{f}_R \phi^\dagger f_L), \quad (1.21)$$

where y_f is the Yukawa coupling. The fermion's mass is then $\frac{y_f v}{\sqrt{2}}$, so heavier fermions couple more strongly to the Higgs boson. The SM provides no prediction of, or relationship between, the Yukawa couplings of the fermions, however they can be determined using the observed masses of the fermions.

A scalar particle with a mass of approximately 125 GeV, consistent with the SM Higgs boson, was discovered in 2012 by both the ATLAS and CMS collaborations [22, 23].

1.1.5. Dark matter

Despite its many successes, there are phenomena in nature which the SM does not explain. It does not predict the non-zero neutrino masses which are necessary to explain neutrino oscillation experiments [24]. It also does not predict sufficient violation of CP symmetry to explain the large matter-anti-matter asymmetry observed in the universe [21]. However, one of the most striking differences between observation and the SM prediction is the existence of DM.

Evidence for DM was first observed in studies of the rotation velocity of galaxy clusters as a function of distance from the centre of the cluster [25]. As shown in Figure 1.1a, these rotation velocities cannot be explained without the addition of significant additional non-luminous matter, or a modification of the laws of gravity. Further evidence for dark matter is provided by gravitational lensing and X-ray images of galaxy clusters such as the bullet cluster, shown in Figure 1.1b [26]. The figure shows two galaxy clusters which have passed through each other. It can be seen that the visible mass of the galaxy, indicated by the colour-scale, is not in the same place as the majority of the gravitational mass, indicated by the green contours. This difference indicates that most of the mass in the clusters continues unimpeded on collision, and is not visible, i.e. it is DM. Cosmological observations suggest that DM makes up $\sim 25\%$ of the energy in the universe [27].

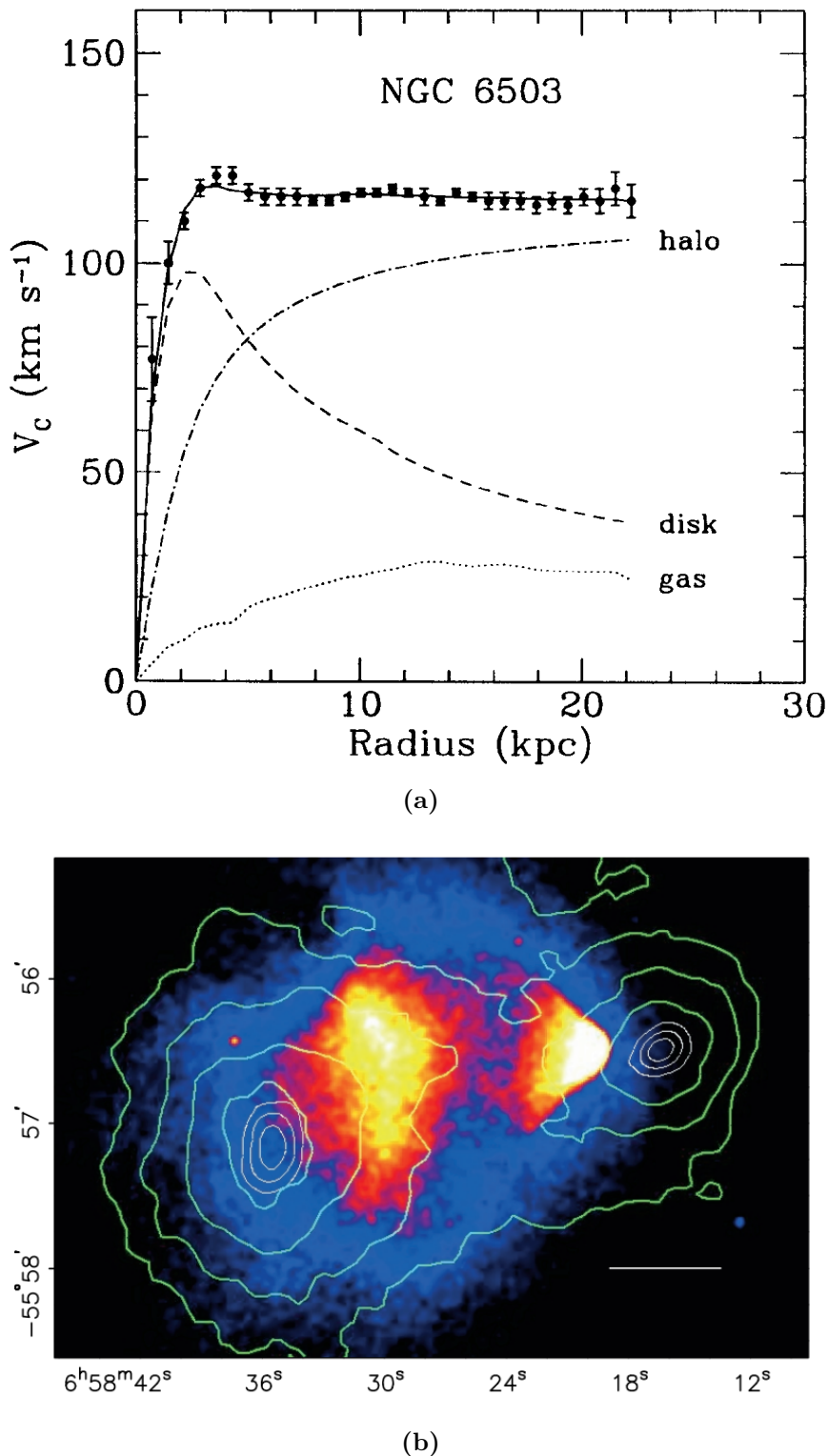


Figure 1.1: Evidence for DM: (a) Rotation velocity in the galaxy NGC 6503 as a function of distance from the galactic centre [28]. (b) The disk and gas components shown are made of visible matter, while the halo component shows the effect of adding an additional DM halo to the galaxy. A superposition of X-ray (colour-scale) and gravitational lensing (green contours) images of the bullet cluster of galaxies [26].

1.2. Searching for dark matter with Higgs bosons

A SM 125 GeV Higgs boson can only decay to invisible final states by first decaying to a pair of Z bosons, which then both decay to neutrinos. The branching fraction for this process is less than 1% [29], so the observation of larger invisible branching ratios of the Higgs boson, $\mathcal{B}(H \rightarrow \text{inv})$, would be strong evidence for new physics and could indicate couplings to DM-like particles. Observing decays of Higgs or Higgs-like bosons to DM presents an experimental problem in that the final state particles are not visible to the particle detectors used at the Large Hadron Collider (LHC), such as the Compact Muon Solenoid, CMS [30], which the data used in this thesis were collected with. Therefore, if a Higgs boson were to be created alone and decay to DM there would be no way to observe these decays. Fortunately, several Higgs boson production mechanisms (as described in Section 1.2.1 below), lead to additional particles being created with the Higgs boson. By conservation of momentum, the vectorial sum of the momenta of these additional particles transverse to the LHC beams will be non-zero due to the unobserved particles. This missing transverse momentum, \cancel{E}_T , can therefore be used to identify the presence of DM particles in the event. This type of search is referred to as a direct search.

Another indication of Higgs boson decays to unseen particles would be a difference between the total decay width of the Higgs boson and the sum of the decay widths of all visible decays. This type of search is referred to as an indirect search. For both direct and indirect searches it is necessary to understand how the Higgs boson is produced and how it decays.

1.2.1. Higgs boson production and decay at the LHC

The LHC (discussed in detail in Section 2.1) collides protons at high energies. The results of these collisions are referred to as “events”. The dominant production mechanisms for Higgs bosons in high energy proton collisions are shown in Figure 1.2, and they have the cross-sections shown in Figure 1.3. It can be seen that ggH production, where two gluons fuse via a quark loop to produce a Higgs boson (as shown in Figure 1.2a), has the highest cross-section across the full Higgs boson mass range shown. Unfortunately, this production mode normally results in no visible particles in the final state and therefore most ggH events cannot be used to search for invisibly decaying Higgs bosons. In some ggH events there is QCD radiation from the initial state particles (initial state radiation (ISR)). Due to asymptotic freedom [31, 32] these radiated quarks and gluons

each result in a collimated “jet” of hadrons in the final state, and thus allow invisibly decaying Higgs boson searches to be performed. However, the visible particles in these events are hard to distinguish from other similar QCD background processes with much larger cross-sections, so ggH is not the most promising channel for invisibly decaying Higgs boson searches.

The next highest production cross-section is that for VBF. As can be seen in Figure 1.2b, this process involves two incoming quarks both radiating vector bosons which fuse, resulting in a Higgs boson. The two initial quarks form jets in the final state, providing visible particles with which to perform an invisibly decaying Higgs boson search. Furthermore, the lack of a strong force connection (referred to as “colour connection”) between the two quarks means that the resulting jets have a distinctive topology, being well separated in their angle to the beamline, and also that there is very little other hadronic activity in VBF events. This distinctive topology and high cross-section make VBF the most sensitive production channel for invisibly decaying Higgs boson searches. For this reason, this thesis will focus on the VBF channel.

After VBF, VH production has the next highest cross-section. VH results in a Higgs boson and a vector boson, which decays resulting in visible particles in the final state allowing invisibly decaying Higgs boson searches to be carried out. In the case of leptonic vector boson decays, these final state particles can be relatively easy to identify, resulting in lower backgrounds than in the case of searches in the VBF and ggH channels. However, the lower cross-section means that the VH channel is not as sensitive as VBF.

Finally, the fourth highest cross-section Higgs boson production channel is top quark associated production, where the final state consists of two top quarks and a Higgs boson. Whilst the top quarks do decay to visible particles which could be identified, the cross-section for this process is too low, and the backgrounds are too high for an invisibly decaying Higgs boson search to be carried out using the Run 1 LHC data.

As mentioned in the introduction to this section, limits can be placed on the Higgs boson’s coupling to invisible particles by comparing the total decay width of the Higgs boson to the sum of the decay widths for all the visible Higgs boson final states. The branching ratio for the dominant Higgs boson decays as a function of the mass of the Higgs boson can be seen in Figure 1.4a. Because a particle’s coupling to the Higgs boson is proportional to its mass, the heavier particles have larger branching ratios, with the caveat that particles above half the mass of the Higgs boson, have reduced couplings due to their being created virtually. The SM total width of the Higgs boson is shown in

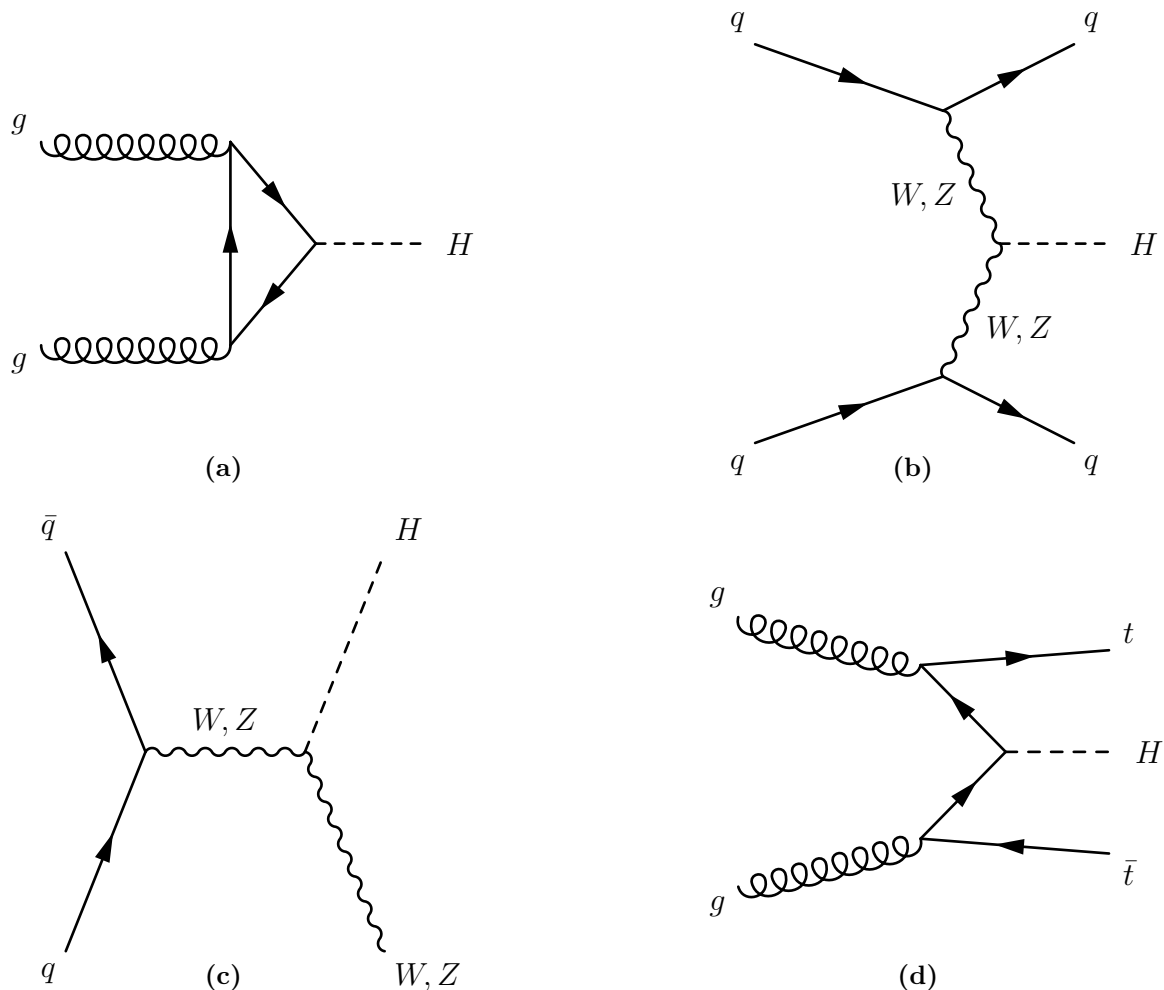


Figure 1.2.: Feynman diagrams for the four SM Higgs boson production processes with the highest cross-sections: ggH (a), VBF (b), VH (c) and top quark associated production (d).

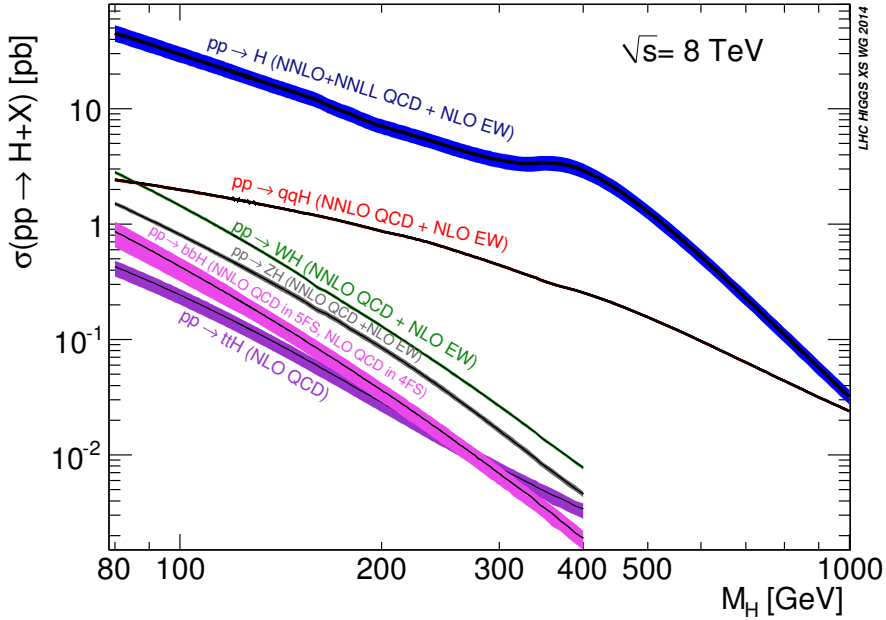


Figure 1.3.: Cross-sections for Higgs boson production via the most common production processes at $\sqrt{s} = 8$ TeV as a function of Higgs boson mass, m_H [29]. The widths of the lines represent the theoretical uncertainties on the cross-section calculation.

Figure 1.4b. For a 125 GeV Higgs boson, the width is only a few MeV, which is below the current resolution with which it can be measured [33]. Therefore, in order to use the total visible decay width to constrain $\mathcal{B}(H \rightarrow \text{inv})$ an assumption about the total decay width must be made.

The current measurements of the branching ratios of the Higgs boson to the 5 most frequent final states can be seen in Figure 1.5a. The log-likelihood as a function of $\mathcal{B}(H \rightarrow \text{inv})$, obtained from these measured branching ratios, assuming the SM total Higgs boson decay width, is shown in Figure 1.5b. It can be seen that whilst the most likely value is approximately zero, values of $\mathcal{B}(H \rightarrow \text{inv})$ up to $\sim 35\%$ are not excluded at the 95% CL. This limit leaves significant parameter space open for BSM Higgs boson decays. As the above limit assumes the SM Higgs boson total width, it is possible that the branching ratio to invisible final states is much larger, making the case for direct measurements even more compelling. Additional Higgs-like bosons that decay to invisible final states are also not excluded.

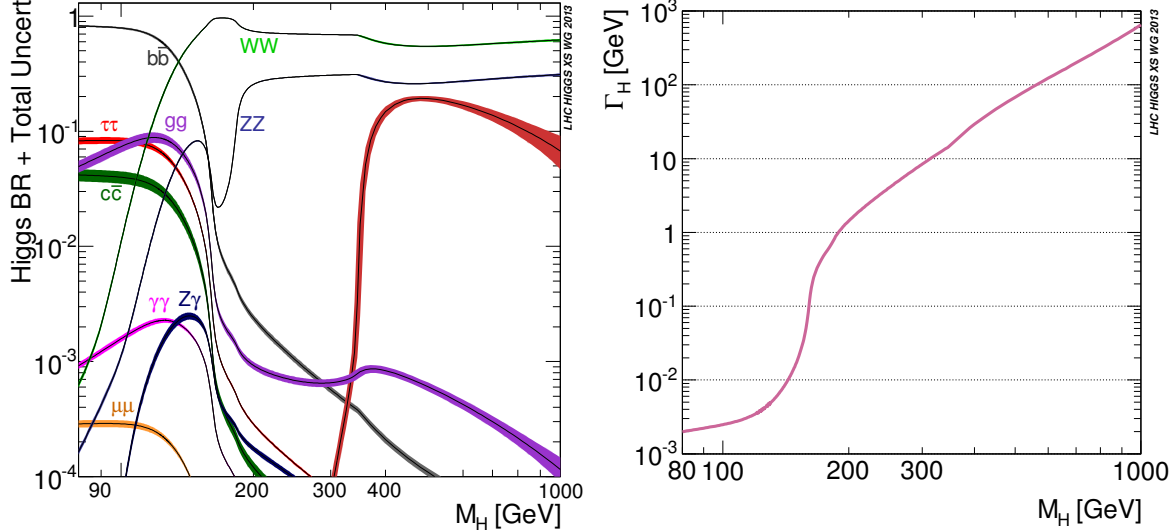


Figure 1.4.: Branching ratios for the dominant Higgs boson decays as a function of Higgs boson mass with the line widths representing the uncertainties (a), and the SM Higgs boson total width, Γ_H , as a function of Higgs boson mass (b) [29].

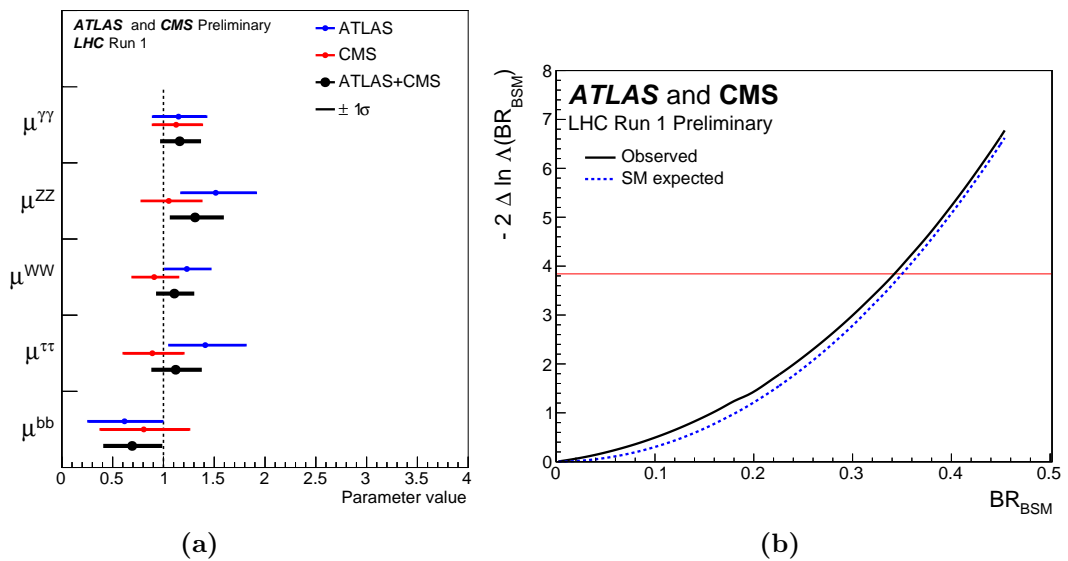


Figure 1.5.: Best fit results for the decay signal strengths of the five highest branching ratio Higgs boson decays from a combination of CMS and ATLAS [34] Run 1 data (a). The negative log-likelihood as a function of $\mathcal{B}(H \rightarrow \text{inv})$, here denoted BR_{BSM} (b) [35].

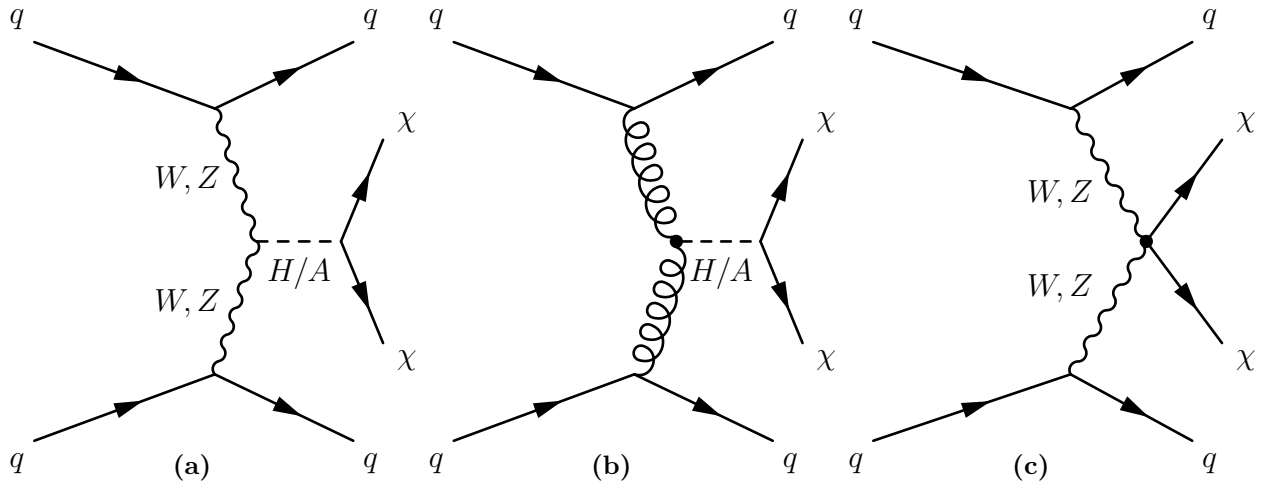


Figure 1.6.: Feynman diagrams for the dark matter theories considered. (a) VBF production of a scalar, H , or pseudoscalar A mediator. (b) Gluon based production of an H or A mediator. (c) An effective field theory where the mediator has been replaced by a contact interaction between the vector bosons and a hypothetical DM particle.

1.2.2. Some extensions of the standard model incorporating dark matter

Whilst current evidence for DM is gravitational, the majority of extensions to the SM which include DM also require other interactions of the proposed DM particles. These interactions then allow the particle the DM interacts with to act as a “mediator” between the SM and DM particles, for example as in Figure 1.6a. As all known particles with mass interact with the Higgs boson, it might be expected that DM’s interactions with the SM are mediated by the Higgs boson or a Higgs-like particle.

In Chapter 6 two classes of these DM interaction models are investigated. The first class is EFT type models. In these models the mediator is assumed to be much heavier than the momentum transferred through it. This high mass allows the behaviour of the mediator to be replaced by a contact interaction between the SM and DM particles as shown in Figure 1.6c. Following the notation in Ref. [36], the particular contact interaction operators considered in this thesis, which each represent a different Lorentz

structure for the contact interaction, are:

$$\mathcal{L}_{D5a} = \frac{1}{\Lambda} [\bar{\chi}\chi] \left[\frac{Z_\mu Z^\mu}{2} + W_\mu^+ W^{-\mu} \right], \quad (1.22)$$

$$\mathcal{L}_{D5b} = \frac{1}{\Lambda} [\bar{\chi}\gamma^5\chi] \left[\frac{Z_\mu Z^\mu}{2} + W_\mu^+ W^{-\mu} \right], \quad (1.23)$$

$$\mathcal{L}_{D5c} = \frac{g_2}{\Lambda} [\bar{\chi}\sigma^{\mu\nu}\chi] \left[\frac{\partial_\mu Z_\nu - \partial_\nu Z_\mu}{\cos\theta_W} - ig_2 (W_\mu^+ W_\nu^- - W_\nu^+ W_\mu^-) \right], \quad (1.24)$$

$$\mathcal{L}_{D5d} = \frac{g_2}{\Lambda} [\bar{\chi}\sigma_{\mu\nu}\chi] \epsilon^{\mu\nu\rho\sigma} \left[\frac{\partial_\sigma Z_\rho - \partial_\rho Z_\sigma}{\cos\theta_W} - ig_2 (W_\sigma^+ W_\rho^- - W_\rho^+ W_\sigma^-) \right], \quad (1.25)$$

$$\mathcal{L}_{D6a} = \frac{g_2}{\Lambda^2} \partial^\nu [\bar{\chi}\gamma^\mu\chi] \left[\frac{\partial_\mu Z_\nu - \partial_\nu Z_\mu}{\cos\theta_W} - ig_2 (W_\mu^+ W_\nu^- - W_\nu^+ W_\mu^-) \right], \quad (1.26)$$

$$\mathcal{L}_{D6b} = \frac{g_2}{\Lambda^2} \partial_\nu [\bar{\chi}\gamma_\mu\chi] \epsilon^{\mu\nu\rho\sigma} \left[\frac{\partial_\sigma Z_\rho - \partial_\rho Z_\sigma}{\cos\theta_W} - ig_2 (W_\sigma^+ W_\rho^- - W_\rho^+ W_\sigma^-) \right], \quad (1.27)$$

$$\mathcal{L}_{D7a} = \frac{1}{\Lambda^3} [\bar{\chi}\chi] W^{i,\mu\nu} W_{\mu\nu}^i, \quad (1.28)$$

$$\mathcal{L}_{D7b} = \frac{1}{\Lambda^3} [\bar{\chi}\gamma^5\chi] W^{i,\mu\nu} W_{\mu\nu}^i, \quad (1.29)$$

$$\mathcal{L}_{D7c} = \frac{1}{\Lambda^3} [\bar{\chi}\chi] \epsilon^{\mu\nu\rho\sigma} W_{\mu\nu}^i W_{\rho\sigma}^i, \quad (1.30)$$

$$\mathcal{L}_{D7d} = \frac{1}{\Lambda^3} [\bar{\chi}\gamma^5\chi] \epsilon^{\mu\nu\rho\sigma} W_{\mu\nu}^i W_{\rho\sigma}^i, \quad (1.31)$$

$$(1.32)$$

where the DM particles, χ , are assumed to be electromagnetically and colour neutral Dirac fermions, and $W^{i,\mu\nu}$ is the field strength tensor for the unbroken $SU(2)_L$ gauge bosons. Λ is the “scale” of the interaction, which is a combination of the mass of the replaced mediator, M , and its couplings to both DM and the SM, g , such that $\Lambda \sim M/g^2$. Whilst the EFT models have the advantage of being simple to interpret, having only one parameter, the validity of the assumption that the momentum transferred through the interaction is much smaller than the mass of the mediator must be checked carefully, especially where the couplings between the mediator and the DM are expected to be small. As well as direct searches for invisibly decaying Higgs bosons, several other experimental techniques, including direct dark matter detection are able to set constraints on these models [4].

The second class of models are so-called simplified models. In these models an explicit choice of mediator is made, removing the need to make an assumption about the transferred momentum. The specific mediators considered are the 125 GeV Higgs boson, and scalar and pseudoscalar mediators with heavier masses.

In the case of the 125 GeV Higgs boson mediator, the following term is added to the Lagrangian:

$$\mathcal{L}_{H\chi\chi} = -g_\chi (\bar{\chi}\chi) H, \quad (1.33)$$

where the DM particles, χ , are again assumed to be Dirac fermions, and g_χ is the Higgs boson coupling to DM. As the mediator is very similar to the SM Higgs boson all the production mechanisms described in Section 1.2.1 are possible, with the most sensitive being VBF. If the dark matter mass is below 62.5 GeV, i.e. it can be created via a real mediator, this interaction leads to an increased invisible decay width of the Higgs boson:

$$\Gamma(H \rightarrow \bar{\chi}\chi) = \frac{g_\chi^2 m_H}{8\pi} \left(1 - \frac{4m_\chi^2}{m_H^2}\right), \quad (1.34)$$

where m_H and m_χ are the masses of the Higgs boson and the dark matter particle respectively [4]. For heavier DM masses, off-shell production, i.e. through a virtual mediator, is still possible, however there is no invisible branching fraction of the Higgs boson.

For the heavier scalar and pseudoscalar mediators, as well as the free term for the mediator, the terms added to the Lagrangian for the scalar, H , and the pseudoscalar, A , are:

$$\mathcal{L}_H = -g_\chi H \bar{\chi}\chi - \sum_f \frac{g_V y_f}{\sqrt{2}} H \bar{f} f \quad (1.35)$$

$$\mathcal{L}_A = -ig_\chi A \bar{\chi}\gamma^5\chi - \sum_f \frac{ig_V y_f}{\sqrt{2}} A \bar{f} \gamma^5 f, \quad (1.36)$$

$$(1.37)$$

respectively, where g_V is the coupling of the mediator to visible particles, f are the SM fermions, and y_f are the SM fermion Yukawa couplings [37]. The couplings to the SM fermions are chosen to be proportional to the SM Yukawa couplings so as to avoid constraints from measurements of flavour physics observables [38]. Due to the measured couplings of the vector bosons to the 125 GeV Higgs boson being compatible with the SM, the new mediators do not interact with vector bosons [35]. This lack of vector boson couplings makes VBF production, as in Figure 1.6a, not possible, and leads to the most common production channel for dark matter in association with two jets being the fusion of two gluons as shown in Figure 1.6b. This gluon fusion occurs, like that seen in the

production of the SM Higgs boson, through a fermion loop, which is dominated by the top quark due to it having the largest Yukawa coupling.

Again, when the dark matter is less than half the mass of the mediator the mediator will have a non-zero invisible branching ratio. The dark matter production rate will be given by this branching ratio multiplied by the production rate of the mediator. For mediator masses below twice the top quark’s mass, and dark matter masses much higher than the b quark’s mass, this branching ratio is approximately 100%. The dark matter production rate is therefore, under the assumption that $g_V = g_\chi$, proportional to g_χ^2 . For mediator masses larger than twice the top quark’s mass, assuming $g_V = g_\chi$, the branching ratio becomes approximately 40% [4] and the production rate remains proportional to g_χ^2 . For dark matter produced through an off-shell mediator the dark matter production rate becomes proportional to $g_v^2 g_\chi^2$, which simplifies to g_χ^4 under the assumption of equal DM and visible couplings.

1.3. Simulation

The simulation of LHC proton-proton collisions can be factorised into several distinct stages, as shown in Figure 1.7. The first stage is the hard-scattering of two incoming elements of the proton, called “partons”. The momentum of each of these partons is sampled from a parton distribution function (PDF). These PDFs give the probability for each incoming parton type to have a certain fraction of the proton’s energy at the given hard-scatter energy scale, sometimes referred to as the QCD scale. Due to the high energy nature of the hard-scatter, perturbation theory at fixed order can be used for both QCD and electroweak interactions at this stage of the simulation. Quantities calculated using the particles which result from the hard-scattering are referred to as “parton level”.

After the hard-scatter the resulting particles undergo “parton showering”, which is an iterative process of repeated QCD radiation until the particles reach an energy where perturbation theory is no longer valid. After parton showering, particles undergo hadronisation, where colourless hadrons are formed, and allowed to decay. The results of this hadronisation and decay process are four-momentum vectors for each particle which are referred to as the “generator level” particles. In most cases the generator level particles are then processed by a GEANT [39] 4 based simulation of the CMS detector. For the work described in Chapter 6 a DELPHES [40] based simulation of the CMS detector,

which is only approximate, but greatly decreases the computational power needed to process the same number of events.

Several MC generators are used to carry out the perturbative hard-scattering calculations. Some, such as PYTHIA [41], are also able to provide the hard-scatter calculation for a wide range of processes as well as perform other stages of the factorisation. Others like MADGRAPH [42] and POWHEG [43–45] only calculate the hard-scattering component. However, these other generators produce more accurate results for certain processes they have been tuned to, or allow for a larger range of processes to be simulated than the multipurpose generators such as PYTHIA. In all of the MC samples used in this thesis, the results of the hard-scatter are then passed on to PYTHIA for parton showering and hadronisation.

Finally, some generators, such as MCFM [46], VBFNLO [47–49], TOP++ [50] and FEWZ [51] are used only to calculate cross-sections very accurately at next-to-leading order (NLO) or next-to-next-to-leading order (NNLO). These calculations are much more computationally intensive than the lower order calculations above, which renders them unsuitable for generating full MC samples with a four vector for each final state particle.

1.4. Statistics of exclusion limits

Limits on the parameters of theoretical models are presented throughout this thesis. These limits are set by performing a hypothesis test to discriminate between a null, **background only** model, hypothesis, b and a test hypothesis, the signal process, s , plus background model. The particular procedure used is based on the CL_S statistic and was developed by the LHC Higgs Combination Group [53]. This procedure is used by both the ATLAS [34] and CMS experiments.

The procedure starts by defining a likelihood function, \mathcal{L} , which quantifies how likely a certain observation is given the expectation under a given hypothesis. \mathcal{L} takes the form:

$$\mathcal{L} = \prod_i \text{Poisson}(n_i | \nu_i(\mu, \theta)) \cdot \prod_j \text{Constraint}(\theta_j, \bar{\theta}), \quad (1.38)$$

where the first term is the contribution from the Poisson probability to observe n_i events in each analysis category, i , given a predicted number of events from the hypothesis, ν_i . ν_i is a function of a signal strength parameter, μ , which in the case of the signal

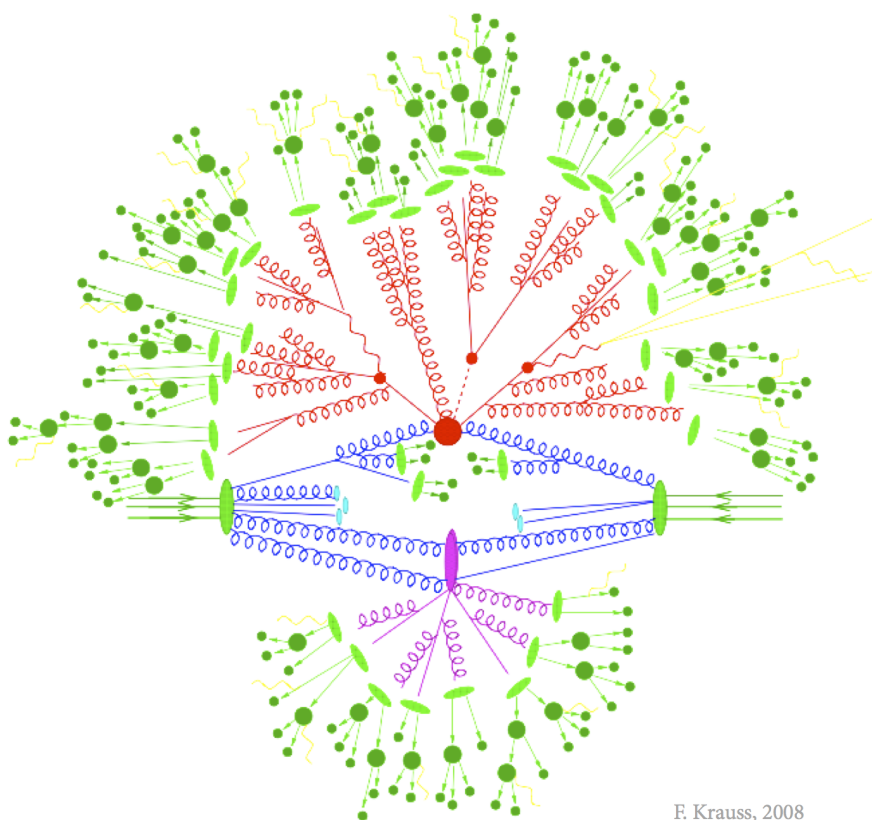


Figure 1.7.: A schematic diagram of the factorised components of the simulation of proton-proton collisions. First the hard-scatter of two of the incoming partons (shown in blue) is simulated at the centre of the event. The results of this scatter then undergo parton showering (shown in red), followed by hadronisation (shown in green) when the energy of the quarks and gluons is low enough that bound states can be formed [52].

hypothesis being an SM Higgs boson is 1 for the SM and 0 for the background only case, and the “nuisance parameters,” θ , which account for the uncertainties on parameters of the signal and background models and any correlations between them. The second term in Equation 1.38 represents the constraints on the allowed values of these nuisance parameters, with $\bar{\theta}$ being the best estimate of θ obtained from external measurements. The shape of the constraint function varies depending on the nuisance parameter it represents. For example, uncertainties on the event yield in a category are usually modelled with log-normal constraints, which exclude negative values of the event yield.

Profile likelihood ratios, q_μ , are then calculated, which are defined as:

$$q_\mu = -2 \ln \frac{\mathcal{L}(obs|\mu \cdot s + b, \hat{\theta}_\mu)}{\mathcal{L}(obs|\hat{\mu} \cdot s + b, \hat{\theta})}, \quad (1.39)$$

where obs is the observation, and $\hat{\mu}$ and $\hat{\theta}$ are the values of μ and θ where the likelihood is maximised given the constraint $0 \geq \hat{\mu} \geq \mu$. $\hat{\theta}_\mu$ are the values of the nuisance parameters that maximise the likelihood for a given μ . The profile likelihood ratio therefore describes how likely it is to observe a signal strength equal to or higher than μ compared to the most likely signal strength.

The CL_s statistic itself is then defined as:

$$CL_s = \frac{P(q_\mu \geq q_\mu^{obs} | \mu \cdot s + b)}{P(q_\mu \geq q_\mu^{obs} | b)}, \quad (1.40)$$

where the probability P of a given q_μ can be calculated using the asymptotic limit approximation [54]. The region in which a signal strength $\mu \cdot s$ is excluded at the $1 - \alpha$ CL is then the region for which CL_s is less than or equal to α , i.e. when the signal hypothesis is α times less probable than the background.

Chapter 2.

The LHC and the CMS experiment

This chapter introduces the CMS experiment and the LHC[55]. In Section 2.1 an overview of the LHC and the chain of accelerators which feed into it is given. This is then followed in Section 2.2 by a description of the CMS experiment focusing on the aspects most relevant to the search for invisibly decaying Higgs bosons.

2.1. The LHC

The LHC is situated **100m** underground in a tunnel formerly built for the LEP accelerator [56] at CERN near Geneva, Switzerland. It is a **27km** storage ring which accelerates both protons and heavy ions and collides them at the highest centre of mass energies of any collider built to date. The work contained in this thesis uses data from proton-proton collisions. These protons are obtained by taking hydrogen gas and stripping its atoms of their electrons with an electric field. The first accelerator in the chain of accelerators feeding into the LHC, Linac 2, accelerates the protons to 50 MeV. The protons are then accelerated to 1.4 GeV by the next accelerator, the Proton Synchrotron Booster (PSB), which is followed by the Proton Synchrotron (PS) where they reach 25 GeV. The beam energy is then increased to 450 GeV in the Super Proton Synchrotron (SPS). Finally, the protons are injected into the LHC where, at time of writing, the maximum energy the beams have been accelerated to is 6.5 TeV, close to the design maximum of 7 TeV.

When fully filled the LHC contains two counter-rotating beams which are formed of up to 2808 bunches spaced ~~either 25 ns or 50 ns~~ apart and each containing $\mathcal{O}(10^{11})$ protons. The two beams are kept travelling in a **circle** by 1232 superconducting dipole magnets and steered to four collision points around the LHC. Detectors are situated at these

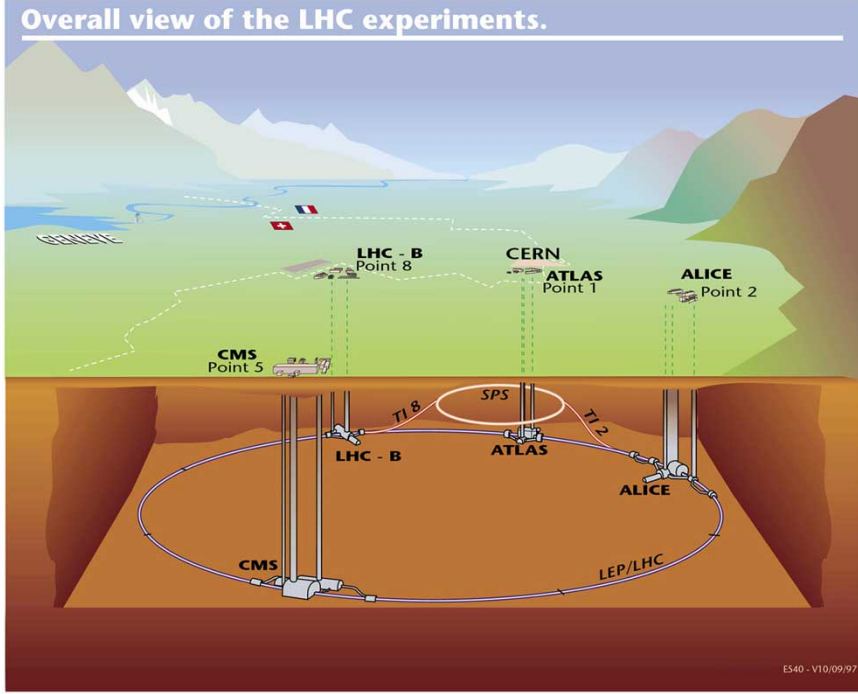


Figure 2.1.: The layout of the chain of accelerators feeding into the LHC, showing the position of the four main detectors [59].

collision points to observe the interactions, the main four being: ALICE [57], ATLAS, CMS and LHCb [58]. A schematic of the chain of accelerators feeding into the LHC and the LHC detectors can be seen in Figure 2.1.

When studying a physical process occurring in particle collisions it is important to know how many times it will occur, this can be expressed as:

$$N = \mathcal{L}\sigma, \quad (2.1)$$

where \mathcal{L} , the integrated luminosity, depends only on the parameters of the collisions, and the cross-section, σ , depends only on the process. In order to observe rare (i.e. low cross-section) processes, such as those studied at the LHC, it is necessary to use very high luminosity datasets. The integrated luminosity is obtained by integrating the instantaneous luminosity over time, so large luminosities can be obtained either by running the accelerator for a long time, or by operating at high instantaneous luminosity. For collisions at the LHC the instantaneous luminosity is given by:

$$\mathcal{L} = \frac{k_b N_b^2 f_{rev} \gamma}{4\pi \epsilon_n \beta} [60], \quad (2.2)$$

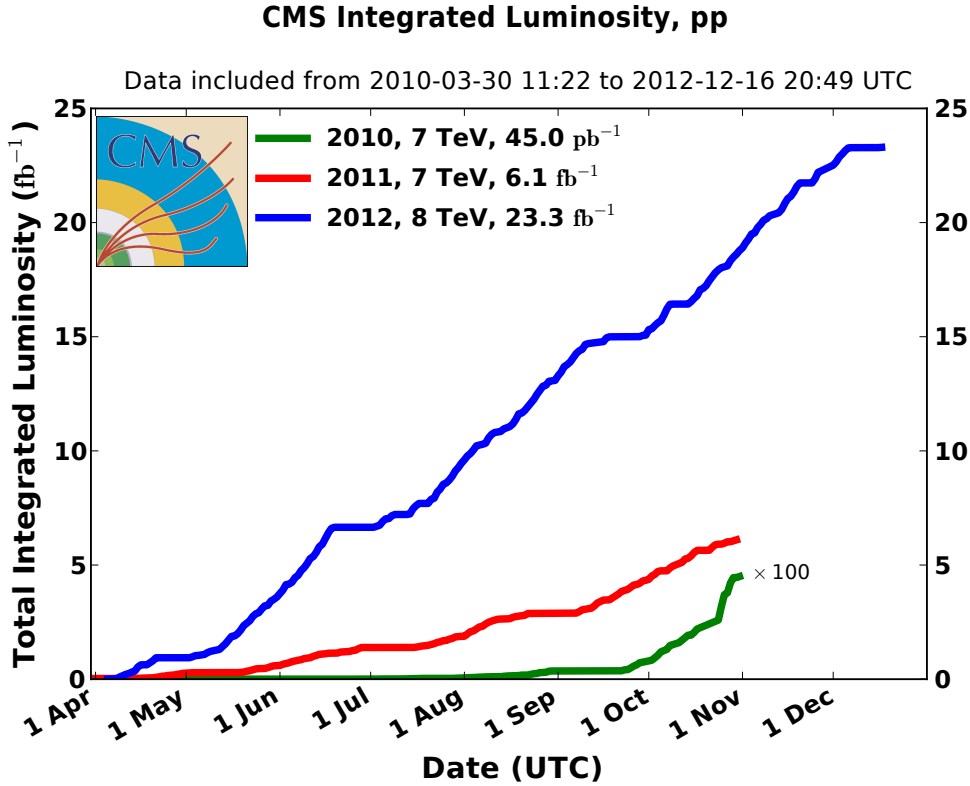


Figure 2.2.: A summary of the luminosity delivered to CMS during Run 1 of the LHC [61].

where k_b is the number of bunches per beam, N_b the number of protons per bunch, f_{rev} the revolution frequency, ϵ_n the normalised transverse beam emittance, β^* the beta-function at the interaction point and γ the Lorentz factor. The design instantaneous luminosity of the LHC is $10^{34} \text{ cm}^{-2}\text{s}^{-1}$ with 25ns bunch spacing. The integrated luminosity is defined as $\mathcal{L}_{int} = \int \mathcal{L} dt$.

The LHC started physics runs in 2010, during which it operated at a centre of mass energy of 7 TeV and delivered an integrated luminosity of 44.2 pb^{-1} to CMS. In 2011 the LHC also operated at 7 TeV and delivered 6.1 fb^{-1} to CMS. The centre of mass energy was increased to 8 TeV in 2012 and 23.3 fb^{-1} of data were delivered to CMS. A summary of the luminosity delivered to CMS during the three periods of Run 1 can be seen in Figure 2.2. In Run 2 the centre of mass energy was further increased to 13 TeV and during 2015 4.09 fb^{-1} of data were delivered to CMS at this energy. In order to be used for physics analysis data must be certified. This certification ensures that the detector was fully operational when the data were recorded. In 2011 5.1 fb^{-1} were certified, in 2012 19.7 fb^{-1} were certified and in 2015 2.2 fb^{-1} were certified.

The cross-sections for several processes are shown in Figure 2.3 and it can be seen that the cross-section for VBF Higgs production is approximately 1.5 pb. Therefore, we expect approximately 30000 VBF produced Higgs bosons in the 2012 dataset. By contrast the vector boson production cross-section is approximately 100 nb and the total cross-section for any process is orders of magnitude higher still. The separation of the relatively small number of signal events from the large background is a major challenge for the search for invisibly decaying Higgs bosons.

The large total cross-section combined with the high instantaneous luminosities that the LHC operates at leads to the probability for multiple proton-proton interactions per bunch crossing being high. The distribution of the number of interactions per bunch crossing, μ , can be seen in Figure 2.4. The additional interactions on top of the process of interest in a bunch crossing are called pile-up (PU).

2.2. The CMS experiment

The CMS detector was designed to search for the SM Higgs and new physics at the TeV energy scale. Both because the nature of new physics is not known and the SM Higgs has a wide range of decays and production mechanisms CMS must be sensitive to many different types of final state particles and topologies. In order to achieve this it has a hermetic design comprising a barrel, endcaps and a forward calorimetry system. It is composed of several layers of subdetectors each sensitive to different particles as shown in Figure 2.5. The hermiticity of the detector is particularly important for the VBF Higgs to invisible search. Further details on the CMS detector beyond those in this section can be found in Ref. [30].

A central design feature of CMS is the superconducting magnet, inside which is generated a 3.8T axial field. This field bends the path of charged particles travelling through it allowing their momentum to be measured. Not all particles are charged however, and the path of several types of particles through the CMS detector is shown in Figure 2.6. The first layer is the tracker which records the paths taken by charged particles, as well as providing a momentum measurement the tracks also allow the vertex from which the particle came to be identified. The next layer is the ECAL where electrons and photons deposit energy through electromagnetic showers. This is followed by the HCAL where hadrons deposit most of their energy. After the calorimetry systems is the superconducting magnet which is not instrumented. Outside the magnet are the muon

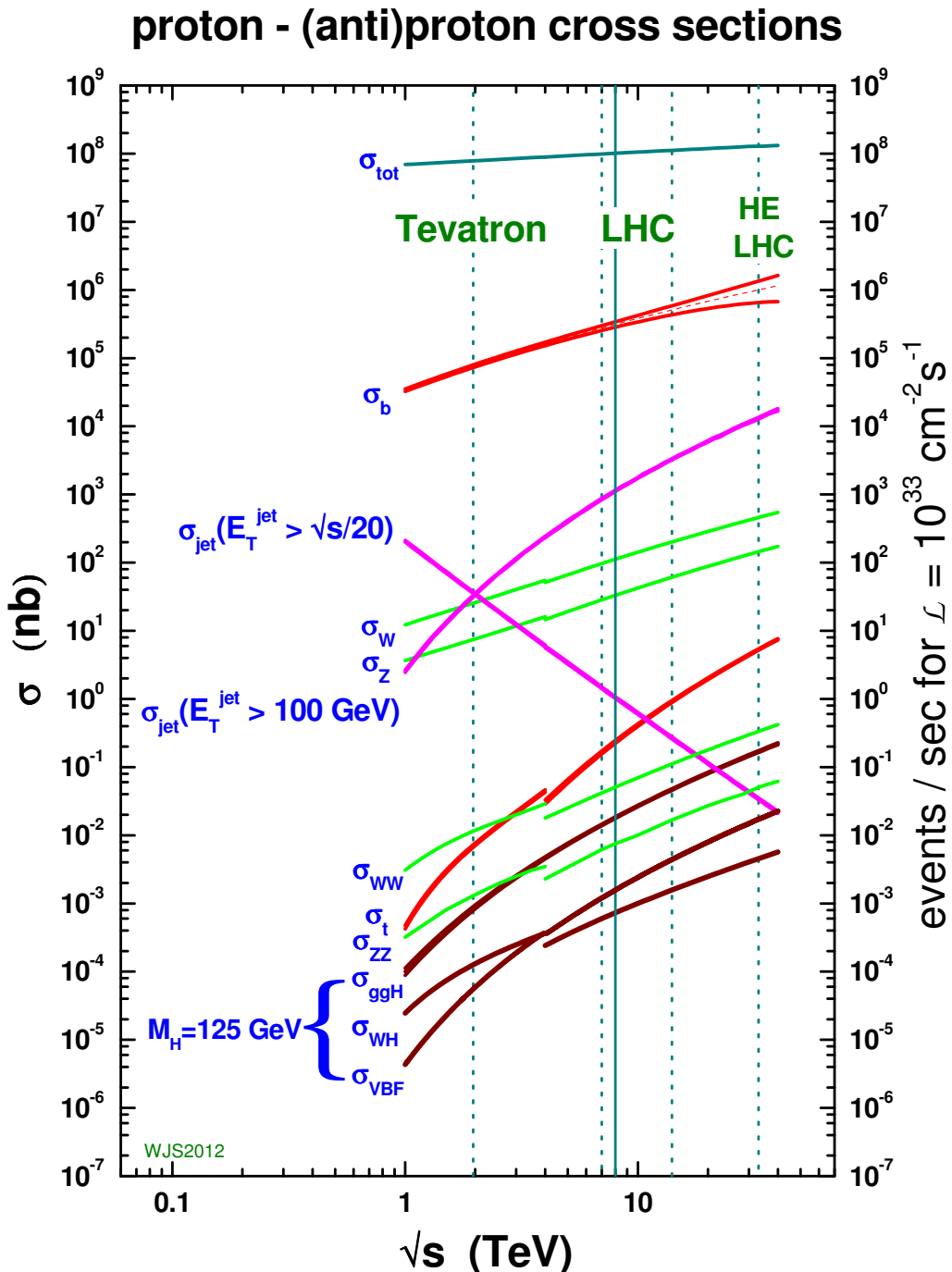


Figure 2.3.: Cross-sections for several processes in collisions of protons with protons or anti-protons as a function of centre of mass energy. The energies that the LHC and Tevatron ran at are highlighted [62].

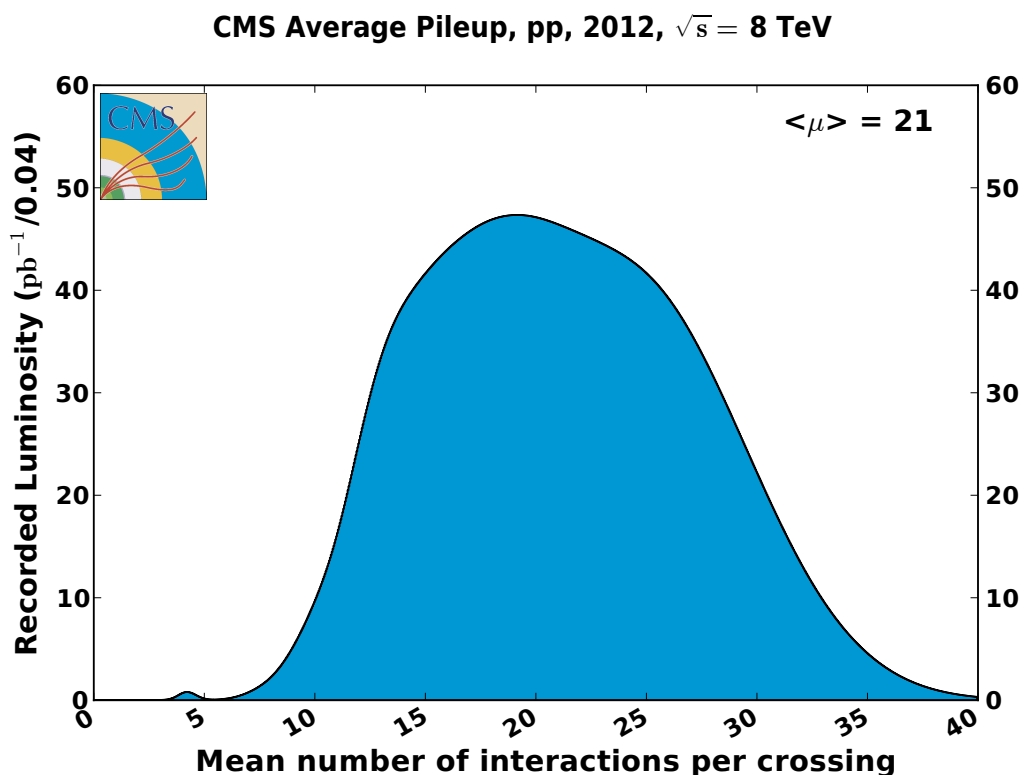


Figure 2.4.: Distribution of the number of interactions per bunch crossing in CMS during 2012 running of the LHC [61].

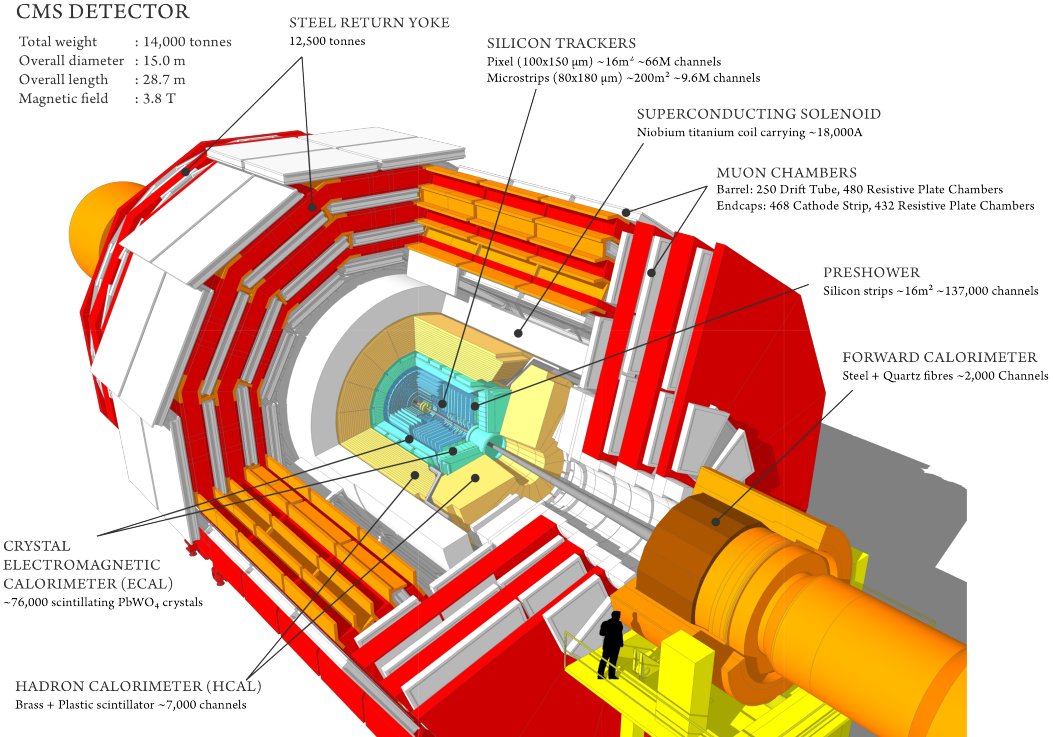


Figure 2.5.: A diagram of the subsystems making up the CMS detector, illustrating the hermeticity and layered structure of the experiment [63].

detection systems, which are interspersed with iron plates which form the return yoke for the magnet. Due to their high mass compared to electrons, muons do not deposit much energy in the detector and often are not stopped, so the muon system is primarily a tracking detector.

The origin of the co-ordinate system used by CMS is at the nominal interaction point. It is a right handed cartesian system with the \hat{x} -axis pointing towards the centre of the LHC ring and the \hat{y} -axis vertically upwards, the \hat{z} axis then points along the beam line. The azimuthal angle ϕ and the polar angle θ are measured in radians from the \hat{x} and \hat{z} axes respectively. It is common to describe the direction of outgoing particles using ϕ and their pseudo-rapidity, η which is defined as:

$$\eta = -\ln[\tan(\theta/2)]. \quad (2.3)$$

Distances in the $\eta - \phi$ plane are given by $\Delta R = \sqrt{\Delta\phi^2 + \Delta\eta^2}$. Two other quantities often used at hadron colliders are the projections of a particle's momentum and energy in the transverse plane, these are denoted as p_T and E_T respectively. The missing transverse energy, defined as the negative vector sum of the momentum in the transverse plane of

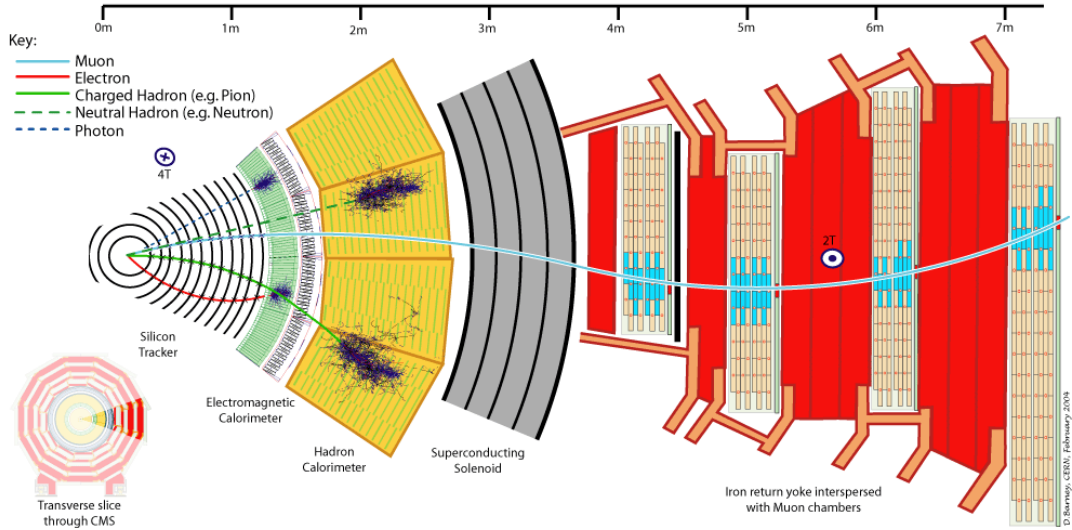


Figure 2.6.: A schematic cross-section of the CMS experiment showing the path taken by several types of particles [64].

all particles in an event, is important in inferring the presence of invisible particles and is denoted \cancel{E}_T . Also, when describing an event the terms **leading** and **sub-leading** refer to the highest and second-highest p_T objects in an event respectively.

2.2.1. Tracker

The tracker is designed to measure the paths of charged particles precisely from LHC collisions which curve in CMS's magnetic field. The design transverse momentum resolution of the full tracking detector is 1-2% at 100 GeV. In order to measure the particles' positions precisely and ensure the occupancy of the tracker is low a high granularity is required. Due to the frequency of collisions at the LHC and the high instantaneous luminosity a radiation hard system with fast response is also necessary. This combination of requirements motivates the use of a **silicon based** system. When traversing silicon charged particles create electron-hole pairs, which are then separated by an applied electric field, causing a current pulse.

The tracker layout can be seen in Figure 2.7. In order to keep the sensor occupancy below 1% at design luminosity, the innermost component is a silicon pixel detector. This detector has three layers in the barrel, at radii of 4.7, 7.3 and 10.2 cm, and two in the endcap. The are 66 million pixels each $100\mu\text{m} \times 150\mu\text{m}$ in size. The resulting resolution of the pixel detector is approximately $10\mu\text{m}$ in the $r - \phi$ plane and $17\mu\text{m}$ in the $r - z$

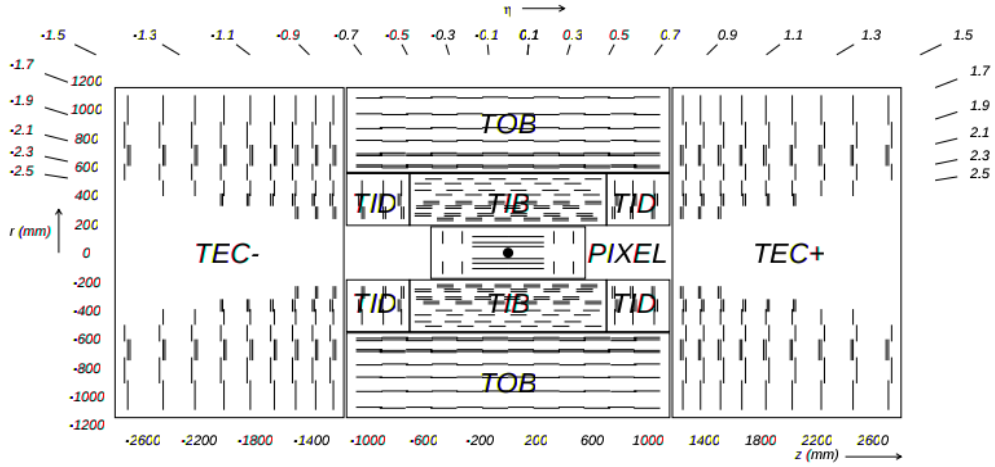


Figure 2.7.: A cross-section of the CMS tracker, indicating the subsystems that comprise it. Each line indicates a detector module [30] and the labels for each subsection are the names given by CMS to the various subsections of the tracker.

plane [65]. During run 1 the proportion of modules in the pixel (strip) tracker known to be defective was 2.4% (2.3%) [66].

Surrounding the pixel detector is a silicon strip detector with 10 layers in the barrel, at radii of 20 to 116 cm, and 12 pairs of disks in the endcap. The strips are typically 10-20 cm long and 80-180 μm wide, with the strip size increasing with radius as the particle flux decreases. The strip detector's single point resolution is 230-530 μm in the $r - z$ plane and 23-52 μm in the $r - \phi$ plane. The better resolution in the $r - \phi$ plane allows p_T to be measured with higher precision, as this is the direction in which a particle's track bends in the CMS magnetic field. The barrel and endcap detectors together have an acceptance of $|\eta| < 2.5$ for both the pixel and strip detectors. Further details on the position resolution of the tracking detector for vertex reconstruction will be given in Section 3.2.

2.2.2. Electromagnetic calorimeter

The ECAL is designed to provide accurate photon and electron reconstruction and precise measurement of the electromagnetic component of hadron jets. It is a homogeneous calorimeter made of lead tungstate (PbWO_4) crystals, separated into a barrel section, with 61200 crystals and two endcaps each with 7234 crystals. These crystals are 25.8 radiation lengths in depth in the barrel and instrumented with photodetectors, avalanche photodiodes being used in the barrel and vacuum phototriodes in the endcap.

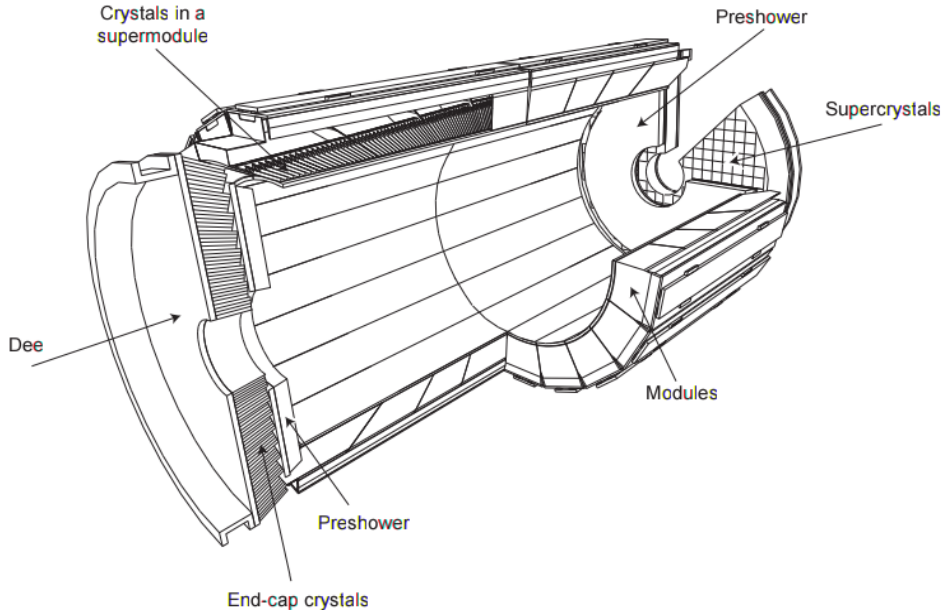


Figure 2.8.: A schematic of the CMS ECAL, indicating the subsystems that comprise it. The ECAL is 7.8m long by 3.5m wide [30].

The layout of the ECAL is shown in Figure 2.8. The ECAL barrel (EB) crystals have a 170 \times 360 arrangement in $\eta - \phi$ space such that the gaps between crystals are offset by 3° from the vector to the detector origin, thus avoiding particles travelling through the gaps. The EB extends to $|\eta| = 1.479$, with higher values of η covered by the ECAL endcaps (EE). The crystals in the EE are arranged in an $x - y$ grid pointing at a focus 1.3m from the nominal interaction point, giving a 2 – 8° separation between the gaps between crystals and the vector to the detector origin. In addition to the main PbWO₄ detector the endcaps also have a preshower detector. This preshower is a lead silicon strip sampling calorimeter, which initiates the electromagnetic showers and provides sufficient position resolution to distinguish single photons from pairs produced in neutral pion decays. The total acceptance of the barrel and endcap detectors is $|\eta| < 3.0$.

On entering the ECAL high energy electrons or photons initiate an electromagnetic shower by undergoing Bremsstrahlung or pair production respectively. The resulting cascade of particles continues to lose energy by successive Bremsstrahlung and pair production until their energy is low enough that the photons no longer undergo pair-production and the electrons lose their energy mainly by ionisation. The excitation of the PbWO₄ crystals leads to the emission of scintillation light, proportional to the amount of energy deposited, which is collected by the photodetectors.

The choice of PbWO₄ is motivated by its high density (8.28 g/cm³), short radiation length (0.89 cm), small Moli  re radius (2.2cm) and radiation hardness. These properties lead to the showers being contained in a small area and allows the calorimeter to be compact and have fine granularity. Another advantage of PbWO₄ is that 80% of the scintillation light is emitted within the LHC's 25ns design bunch crossing time, so particles can be properly associated with the bunch crossing from which they originate.

For particle energies below 500 GeV, where the resulting shower ceases to be contained in the full depth of the ECAL, the ECAL resolution can be parameterised as:

$$\left(\frac{\sigma}{E}\right)^2 = \left(\frac{S}{\sqrt{E}}\right)^2 + \left(\frac{N}{E}\right)^2 + C^2. \quad (2.4)$$

Where S is the stochastic term, N the noise term and C the constant term. The stochastic term is comprised of fluctuations in the lateral containment of showers and also in the amount of scintillation light. The noise term is made up of electronic and digital noise, and signals from other bunch crossings which do not fully dissipate in time. The constant term comes from non-uniformity of light collection along the crystals, errors in the calibration of crystals against each other and leakage of energy from the back of the calorimeter. The energy resolution was measured without an applied magnetic field in an electron beam using particles with momenta between 20 and 250 GeV. The stochastic, noise and constant terms were found to be 0.028 GeV^{1/2}, 0.12 GeV and 0.003 respectively.

As the ECAL is exposed to radiation the PbWO₄ crystals darken and as a result fewer photons are collected per unit energy deposited. The loss of response due to this darkening at the end of Run I varies from 6% for crystals in the most central region of the ECAL to 30% in the endcaps [67].

2.2.3. Hadronic calorimeter

The HCAL is designed to measure the energy of strongly interacting particles. This measurement is particularly important for neutral hadrons which do not leave tracks in the tracking system and deposit most of their energy in the HCAL, and for the determination of \cancel{E}_T . The main part of the HCAL consists of a brass and scintillator plus wavelength shifting fibre sampling calorimeter split into hadron barrel (HB) and hadron endcaps (HE) sections. The primary design consideration for the HCAL is that it must fit between the outer edge of the ECAL ($r = 1.77$ m) and the inner edge of

the magnet ($r = 2.95$ m). In order to satisfy this requirement and achieve satisfactory containment of hadronic showers the magnet coil is also used as an absorber, and there is a further layer of scintillator outside the magnet coil (hadron outer (HO)). The barrel and endcap detectors extend to $|\eta| < 3$.

Brass is chosen as the main HCAL absorber because it is not magnetic and has a relatively short nuclear interaction length of 16.42 cm. Once showers have been initiated in the absorber layers they then pass through the plastic scintillator tiles, where they create pulses of light. These pulses are transferred via wavelength shifting fibres to hybrid photodiodes. The segmentation of the scintillator is such that the $\eta - \phi$ resolution in the HB (HE) is 0.087×0.087 (between 0.087×0.087 and 0.17×0.17 depending on η).

In addition to the barrel and endcap sections of the HCAL there is also a steel and quartz fibre Cherenkov forward calorimeter (hadron forward (HF)), which extends the calorimetry coverage of CMS to $|\eta| < 5.2$. The choice of this technology is driven by its ability to withstand the very high particle fluxes present so close to the beamline. Showers are initiated by the steel absorber and signals are generated in the quartz fibres by particles above the Cherenkov threshold generating Cherenkov light, which is collected by photomultiplier tubes. Due to the Cherenkov energy threshold increasing with particle mass the HF is primarily sensitive to the electromagnetic component of showers.

A diagram of the HCAL layout can be seen in Figure 2.9. In total the HCAL corresponds to 10-15 interaction lengths, depending on η . The resolution of the barrel and endcap sections of the HCAL as a function of the incident particle energy was measured in a pion beam and has been found to be well parameterised by:

$$\left(\frac{\sigma}{E}\right)^2 = \left(\frac{94.3\%}{\sqrt{E}}\right)^2 + (8.4\%)^2 \quad [68]. \quad (2.5)$$

2.2.4. Muon system

As described above muons are highly penetrating, and thus are only rarely contained by the inner detector. Very few other charged particles are able to leave the calorimeters, so the presence of tracks in the muon system is sufficient to identify muons. The muon tracking system uses three types of gaseous particle detectors, located throughout the iron magnet return yoke. In all three types of detector when a charged particle travels through the gaseous detector it ionises the gas, the resulting free electrons then drift

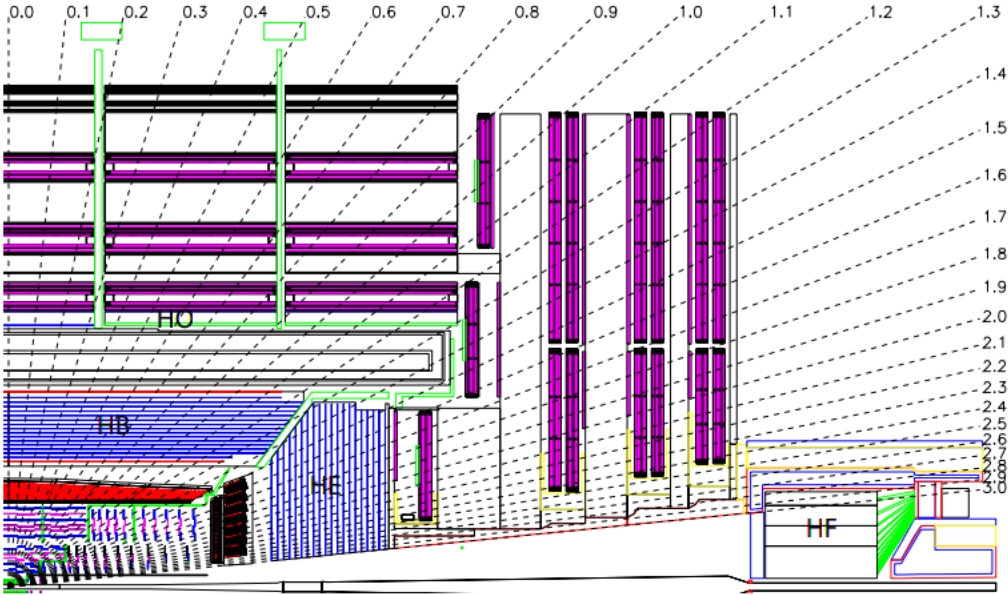


Figure 2.9.: A schematic of a quadrant of the CMS HCAL in the $r - z$ plane, indicating the subsystems that comprise it [30].

towards the detector's anode resulting in an electrical signal. The two primary types of detectors used are the drift tube (DT), which is used in the barrel section of the detector ($|\eta| < 1.2$), and the cathode strip chamber (CSC), which is used in the endcap ($0.9 < |\eta| < 2.4$). The DT and CSC systems identify muons and provide measurements of their momentum. These measurements can be combined with those from the tracker to improve the muon momentum resolution. This combined reconstruction and momentum measurement along with its resolution is described in Section 3.5. Additionally there is a resistive plate chamber (RPC) system in both the barrel and endcap regions ($|\eta| < 1.6$), the primary purpose of which is to provide trigger and **bunch crossing** identification information. A diagram of the CMS muon system can be found in Figure 2.10.

Each system has its own particular advantages and disadvantages which make it best suited for use in the various parts of the muon system. DTs are inexpensive and reliable, but they are not usable in regions with high muon and neutron background rates, making them well suited to the barrel portion of the detector, where large areas must be instrumented and rates are low. Each DT is a 2.4m long wire in a $13 \times 42\text{mm}^2$ tube. The length is limited by the segmentation of the iron return yoke, and the cross-section by the requirement that the occupancy and drift time are low enough to prevent multiple muon hits being read out at the same time. The DTs are organised in 4 stations, interspersed with return yoke iron plates. The first three stations have 8 chambers each, 4 to measure

the muon’s position in the $r - \phi$ plane and 4 to measure the z co-ordinate. The final outermost layer does not have the z -measuring chambers. These chambers consist of 8-12 stacked DTs, with each layer offset from the previous one by half the width of a tube to avoid gaps.

Due to their fast response time, fine segmentation and radiation resistance CSCs are ideal for the endcap region where the muon and background rates are higher. Each CSC is a multiwire proportional chamber with 7 planes of cathode strips running radially outwards with 6 planes of anode wires, which run azimuthally, interleaved between them. Both the anode and cathode wires are read out to provide η and $r - \phi$ co-ordinate measurements respectively. Similarly to the DT system the design number of CSC stations in each endcap is 4 interspersed with iron return yoke plates. During Run I only three of the CSC stations were present, the fourth station in each endcap was added during the long shutdown and is present for Run 2. The position resolution in the $r - \phi$ plane of the CSCs varies from 75-80 μm .

The RPCs are gas gaps surrounded by anode and cathode plates with read out strips between them. The advantage of RPCs is that their response is good at high rates, and they have very good time resolution, making them ideal for use in the trigger and assignment of muons to a bunch crossing. However, they have much poorer position resolution than the DTs or CSCs. There are 6 layers of RPCs in the barrel and 3 in the endcap.

2.2.5. Trigger system

The design bunch crossing rate of the LHC is 40 MHz, and for the data used in this thesis it varied from 20-40 MHz. Since each event consists of approximately 1 MB of data, writing every event to tape would correspond to a data rate of 20-40 TB/s which is not feasible. It is also not feasible for the detector electronics to read out the detector at this frequency. It is therefore necessary to use a trigger system to perform an “online” reconstruction and reduce the event rate by selecting only the most interesting events.

The trigger is separated into two stages, the L1 trigger and the HLT. First the L1 trigger, which is built of custom-designed electronics, reduces the rate to a maximum of 100 kHz. The decision to accept an event in the L1 trigger or not starts with local information on the energy deposits in the calorimeters and hits in the muon systems, which is stored for all events for 128 bunch crossings. A decision must therefore be made within 128 bunch

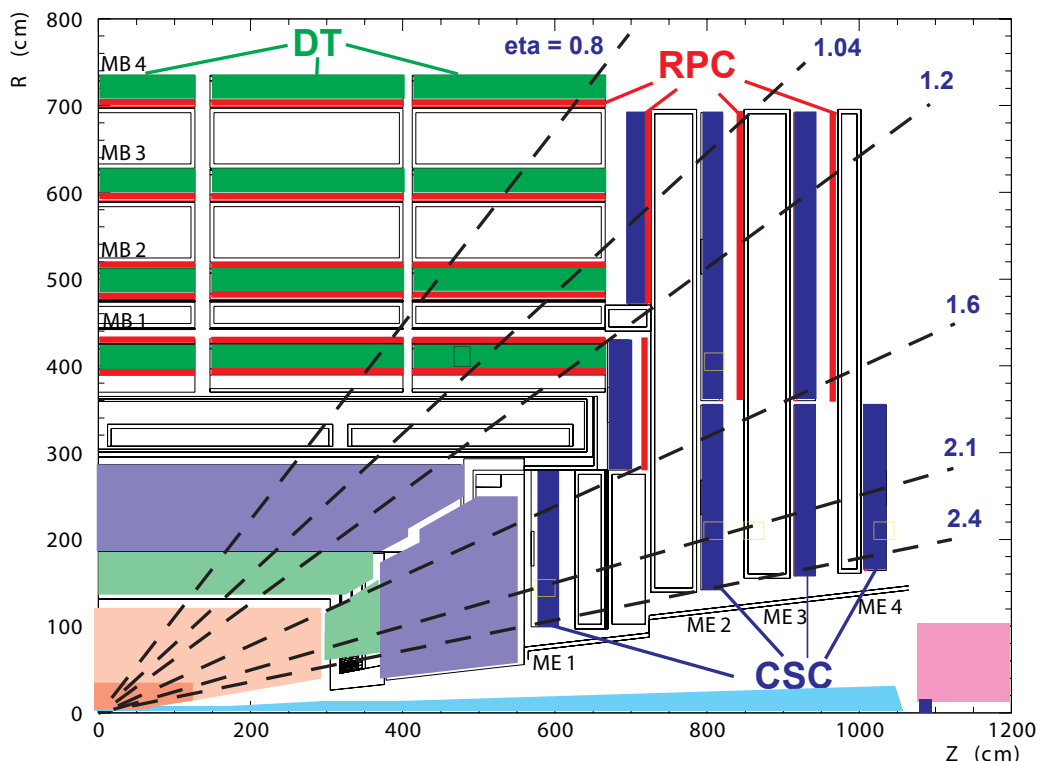


Figure 2.10.: A schematic of a quadrant of the CMS muon system in the $r - z$ plane, indicating the subsystems that comprise it [69].

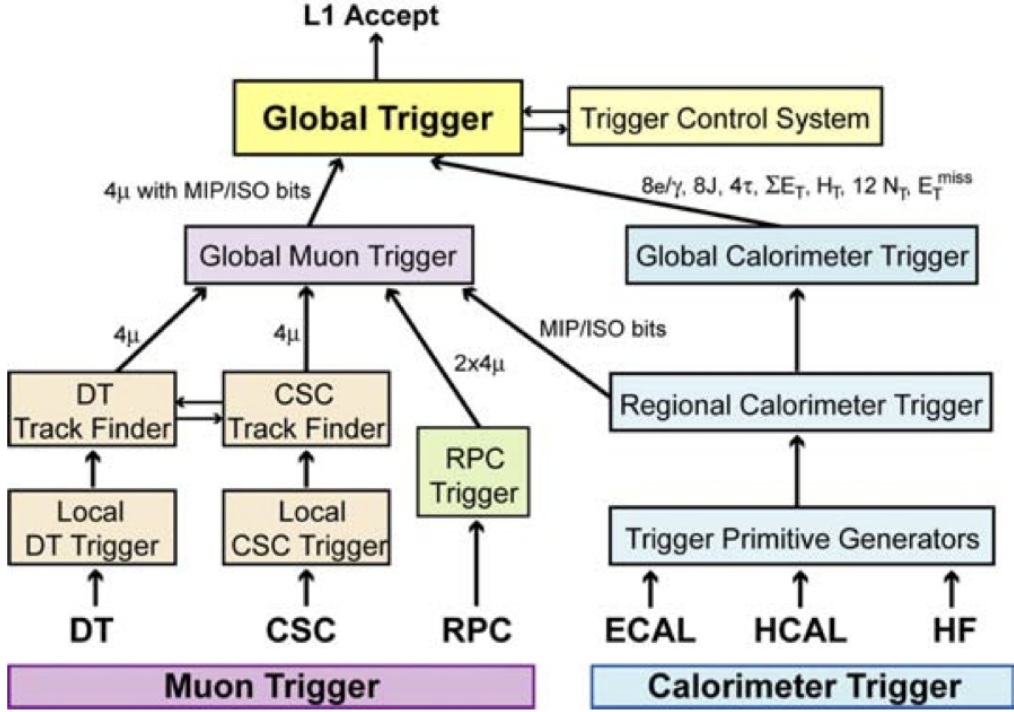


Figure 2.11.: A schematic of the L1 trigger system. The arrows indicate the flow of data, the information transferred between systems is also indicated [30].

crossings or the event is discarded. Due to the limited time available and the limited available bandwidth of the data acquisition system, this information is generally not available at the detector's full resolution. After it is collected from the detector the local information is then passed to the regional trigger systems, which generate lists of trigger candidates, such as electrons or jets, ranked by energy and quality. These ranked lists from each region are then passed to the global muon and calorimeter system triggers, which select the highest ranked candidates across the whole detector and give them to the global trigger, which makes a final decision. This process is shown in Figure 2.11.

If an event is accepted by the L1 trigger the full detector information is read out to the HLT farm on the surface, which reduces the rate further still to approximately 1 kHz. The HLT consists of several thousand commercially available CPUs. Despite having the full detector information, the time available does not allow for the full offline reconstruction to be performed. ~~Never the less,~~ the algorithms available at the HLT are much closer to those used offline than those available at L1, allowing the trigger to better select events that would also pass requirements on the offline quantities. If they are accepted

by the HLT, events are sent to be reconstructed using the Worldwide LHC Computing Grid (WLCG).

2.2.6. Data processing

The WLCG consists of several tiers. Data is first fully reconstructed at the Tier 0 centres. During Run I there was only one of these at CERN, for Run II there will also be a Tier 0 centre in Budapest. It is then sent to at least one Tier 1 centre, so that a full copy of the data is available at multiple sites in different geographic locations. Tier 2 and 3 centres then process this data according to the needs of specific analyses.

During 2012 running it was realised that it was possible for data to be written to tape from the CMS detector at a higher rate than it could be reconstructed by the Tier 0. 30% of the output of CMS was therefore immediately sent for “prompt” reconstruction, while the remainder was “parked” to tape to be reconstructed during LHC shutdown periods when there is spare computing capacity available [70]. The extra events that could be stored through this parking allowed significantly lower trigger selection thresholds to be used for some of the analyses described in this thesis.

Chapter 3.

Physics objects and event reconstruction

The invisible Higgs analysis uses a wide range of objects from the jets and \cancel{E}_T that are present in the signal process, to charged leptons that are present in background processes. This range of objects means that information from all the CMS subdetectors must be used. The reconstruction of each physics object used from data collected by the CMS detector is described in this chapter, along with the overarching “particle flow” approach to data reconstruction used by CMS.

3.1. Tracks

The tracks reconstructed in the inner tracking detector of CMS are a key part of the reconstruction of most other objects used for physics analyses. For example the jet reconstruction algorithm combines information from the tracks and calorimeter energy deposits. The algorithm used by CMS is the Kalman filter based combinatorial track finder (CTF), which is described in Ref. [71].

The CTF starts with seeds generated from either two or three hits in the pixel tracker. Seeds with two hits use the nominal crossing point of the beams to constrain the initial momentum of the track. The layers of the tracker are then iterated through, from inside to outside. The most compatible hit in each layer is added to the track and the track is refitted before moving to the next layer. Once the outside of the detector is reached the algorithm checks for tracks which share more than 19% of their hits and discards the track with the fewest hits. In the case of the two tracks having an equal number of

hits the track with the best fit, i.e. that having the lowest χ^2 , is kept. This process of reconstructing tracks starting from seeds is repeated up to six times, with hits associated to a successfully reconstructed track removed for the next iteration.

After the full set of iterations is complete the tracks are refitted again using another Kalman filter, initialised with the innermost hit on the track and proceeding to iteratively add the hits on the track from inside to outside. This refitting aims to reduce biases from the track’s seed including those introduced for **two hit** seeds that include constraints from the beamspot. The refitted tracks are then smoothed by another Kalman filter, which is initialised with the current **best fit** track hypothesis and iterates from the outside of the detector inwards.

The smoothed tracks then have quality criteria, such as a requirement on the maximum number of layers the track traverses without leaving a hit, imposed to reject fake tracks. The efficiency of the CTF is estimated in data using tracks from muons from Z decays, and is found to be greater than 99% for muons with $1 < p_T < 100$ GeV. For muons with $p_T = 100$ GeV the p_T resolution of the CTF is found to be approximately 2.8% [71].

3.2. Primary vertex

The very high instantaneous luminosities present at the LHC lead to a large probability of multiple proton-proton interactions occurring in each bunch crossing. It is therefore essential to identify the Primary vertex (PV), which relates to the highest energy interaction or “hard scatter”. It is also useful to identify the PV to distinguish “prompt” particles directly from the hard scatter from those resulting from processes which occur later such as heavy flavour hadron decay or photon conversion.

The CMS PV reconstruction algorithm has three steps, track selection, clustering of tracks into vertices and finally fitting the position of these vertices and is described in more detail in Ref. [71]. In the first step, track selection, the subset of tracks with non-significant transverse impact parameters is chosen. This selection removes tracks not coming from the primary interaction region.

The next step of clustering tracks into prototype vertices uses a “deterministic annealing” (DA) algorithm [72]. These prototype vertices then have their position determined by an adaptive vertex fitter [73]. This fitter starts by performing a fit to the position of the vertex, then assigning weights, w_i to each track according to the probability that it

belongs to the vertex, before repeating the process iteratively. Both of these algorithms also use the concept of “cooling,” where the algorithm is performed repeatedly as a temperature parameter, which controls the size of fluctuations around the current state of the system, is gradually reduced, to increase the chance of finding the global best fit solution.

The number of degrees of freedom of the resulting vertex is defined as:

$$n_{dof} = 2 \sum_{i=1}^{\# \text{tracks}} w_i - 3. \quad (3.1)$$

This variable is highly correlated with the number of tracks compatible with the vertex and can therefore be used to select vertices coming from true proton-proton interactions.

The PV is defined to be the vertex with the highest sum of the squared p_T of all the tracks contributing to it. If there is no reconstructed vertex the nominal beam crossing point is used. In the analyses described in this thesis events are required to have a real vertex, which has $n_{dof} > 4$ and a maximum displacement in the z -direction (xy -plane) direction from the centre of the detector of 24 cm (2 cm).

The performance of the vertex reconstruction algorithm has been measured using events with at least one jet with $p_T > 20$ GeV [71]. The efficiency to reconstruct at least one primary vertex in these events is found to be greater than 99% for vertices with at least three tracks. The position resolution is found to vary as a function of the number of tracks associated to the vertex, being approximately $100\mu\text{m}$ for vertices with 5 tracks and approaching $10\mu\text{m}$ for vertices with greater than 50 tracks.

3.3. Particle flow

Particle flow (PF) is an algorithm used by CMS to combine information from different sub-detectors into individual particles [74–76]. This approach is particularly beneficial for CMS as it allows the accurate momentum measurements of the inner tracker, and the excellent energy measurements and granularity of the ECAL to be combined and used to improve the energy measurement of objects seen in the HCAL. The PF approach also allows calibrations specific to charged and neutral hadrons to be applied. The PF algorithm classifies particles as charged hadrons, neutral hadrons, photons, muons and electrons. This set of particles, referred to as PF candidates, can then further be used

to calculate the \cancel{E}_T , as input to the jet reconstruction, for reconstructing taus and to calculate the isolation of leptons.

The PF algorithm starts with tracks, reconstructed as described in Section 3.1, and calorimeter clusters, which are reconstructed separately in each sub-detector of the calorimeter system. Clustering starts with seeds, which are the calorimeter cells which have the local maximum energy which is also more than twice the expected calorimeter noise, which is 80 (300) MeV in the EB (EE) and 800 MeV in the HCAL. Cells adjacent to the cluster are added if they also have energy more than twice the expected calorimeter noise. Cluster-track pairs whose cluster position and track trajectory are compatible are then linked together to identify charged particles. Linking between tracks from the inner tracker and the muon system is also performed to identify muons. The information from tracks with associated ECAL clusters, i.e. those compatible with electrons, is further used to search for clusters compatible with having come from Bremsstrahlung photons from the electron, this is described further in Section 3.4.

Once electrons, muons and charged hadrons have been identified, further calorimeter clusters are identified as neutral hadrons or photons if they are in the HCAL or ECAL respectively. Excess energy in a calorimeter cluster compared to that expected from the associated tracks also allows the presence of neutral particles that would otherwise not have been identified to be determined.

3.4. Electrons

As described in Section 3.3, electrons are reconstructed by matching ECAL deposits with tracks from the inner tracker. This process is complicated by the fact that electrons can lose significant amounts of energy, in the form of Bremsstrahlung photons, as they traverse the inner tracker. Approximately 35% of electrons lose at least 70% of their initial energy in this way [77]. The Bremsstrahlung photons often convert to electron-positron pairs which are then further spread in the ϕ direction by CMS’s solenoidal magnetic field. The electron reconstruction, which is described in detail in Ref. [78], employs so-called “supercluster” algorithms to combine ECAL deposits from both the initial electron and the Bremsstrahlung photons.

Due to their different geometries, different supercluster algorithms are used in the barrel and endcaps. In the barrel the “hybrid” clustering algorithm is used, this begins with a seed crystal which is the crystal with local maximum energy greater than 1 GeV. Arrays

of 5×1 crystals in $\eta \times \phi$ are then added around the seed crystal if they are within 17 crystals of it in either direction in ϕ and have energy greater than 0.1 GeV. Contiguous arrays are grouped into clusters. The final supercluster consists of all clusters from a seed with cluster energy greater than 0.35 GeV.

In the endcap the “multi- 5×5 ” algorithm is used. This algorithm also starts with seed crystals, in this case those with energy higher than their four direct neighbours and also greater than 0.18 GeV. Clusters are then made up of the 5×5 square of crystals centered on the seed. Individual clusters whose seeds are within 0.07 in η and 0.3 in ϕ of each other are grouped and kept as a supercluster if their total energy is greater than 1 GeV. A reference position for the supercluster is taken to be the energy-weighted average position of all the clusters belonging to it, and the maximum difference in ϕ between any cluster and the reference position is taken to be the size of the cluster in ϕ . The individual clusters in a supercluster are then extrapolated to the preshower detector. Any preshower deposits within the supercluster’s ϕ size plus 0.15 in ϕ and within 0.15 in η of a cluster in the supercluster are added to it.

The energy-weighted average position and energy of the final supercluster are then used to extrapolate the electron’s track back to the innermost layers of the tracker for both electron charge hypotheses. This extrapolation is then matched to hits within a $\phi - z$ window of it, whose size is determined by the uncertainties on the ϕ position of the supercluster and the z position of the beamspot. This size was typically 5 cm in 2012. This matched hit is used to update the estimated electron trajectory so that a hit in the second layer of the inner tracker can be searched for in a much narrower window. Hits in both the first and second layers compatible with a supercluster are then used as seeds for dedicated electron track reconstruction, performed using a Gaussian sum filter (GSF) algorithm [79], which performs better than a Kalman Filter for tracks with significant energy loss.

Electron identification criteria are applied to reject fake electrons caused by other particles such as pions. The variables used include:

- $\Delta\eta_{in}$ and $\Delta\phi_{in}$, which are the η and ϕ distances between the electron track position extrapolated to the ECAL and the supercluster position.
- $\sigma_{in\eta}$, the energy-weighted η width of the cluster.
- H/E , the ratio between the energy deposited in the HCAL and in the ECAL in the region of the electron’s seed cluster.

All of these variables are generally lower for real prompt electrons.

~~We also require the~~ electrons to be isolated, i.e. have a low amount of other activity present around them in the detector. The variable used for this requirement is the effective area corrected PF isolation, I_{PF} . In Run 1 it was defined as the sum of the p_T of the PF candidates within a cone of $\Delta R < 0.4$ around the direction of the electron, minus the expected contribution from PU across the area of the electron.

In the VBF invisible Higgs boson decay searches described later in this thesis two sets of requirements on the above variables are used to identify electrons, both of which require that $|\eta| < 2.4$. The “veto” set of identification criteria is looser and is used to veto events containing electrons. The other “tight” set of criteria is stricter and is used ~~when we want~~ to study events containing electrons. Tight electrons are required to be separated by more than 0.3 in ΔR from any veto muons to remove fake electrons from muons. The veto (tight) criteria have an efficiency of 93% (85%) for reconstructing central electrons with $p_T > 50$ GeV [80]. The veto (tight) electrons used in the analyses described in this thesis are required to have $p_T > 10(20)$ GeV unless stated otherwise.

3.5. Muons

Due to their relatively high mass and lack of strong force interactions, most muons deposit very little energy in the CMS calorimeters and thus leave the detector after passing through the muon system. As described in Section 3.3, this means that muons can be reconstructed by searching for compatible tracks from the inner tracker and the muon system. The approach of requiring both inner tracker and muon system tracks greatly improves the discrimination between muons and hadronic activity and is referred to as “global” muon reconstruction.

The CMS global muon reconstruction algorithm starts with each track in the muon system and searches for compatible tracks in the inner tracker [81]. If a compatible inner tracker track is found, a track fit, similar to that described in section Section 3.1, is performed using the hits in both the inner tracker and muon system. The fit accounts for energy losses as the muon traverses the detector. It is found that for muons with $p_T > 200$ GeV the global-muon fit is better than that from the tracker only [81]. However, due to the increased hadron discrimination described above all muons used for analyses in this thesis are required to have both inner tracker and muon system tracks. As with electrons it is also required that muons are isolated. The same isolation variable, I_{PF} ,

as described in Section 3.4 is used for muon isolation. Global muon reconstruction is sufficient for use in vetoing events containing muons, and muons passing the above reconstruction are referred to as “veto” muons.

Where we want to study events containing muons, further identification criteria are used. This is because whilst global muon reconstruction removes most hadrons, some so-called “punch through” hadrons, which are energetic enough to travel all the way through the CMS calorimeters, can still be reconstructed as muons. Furthermore, it is desirable to separate real but non-prompt muons from hadron decay, from prompt muons from the hard scatter or tau decay. The identification consists of requiring a high quality global muon track fit, that the muon’s track passes through at least ~~at least~~ 5 inner tracker layers, with at least one being a pixel layer, that the muon’s track includes at least two hits in the muon system, and that there is at least one muon system track segment present. Muons passing these additional requirements are referred to as “tight” muons. In addition to the above requirements both veto and tight muons are required to have $|\eta| < 2.1$.

The efficiency of veto (tight) muon reconstruction has been found to be 98-99% (96-98%) depending on the η of the muon, for muons with $p_T > 10 \text{ GeV}$ [81]. This efficiency measurement was performed using events with J/ψ or Z boson decays to muon pairs. The veto (tight) muons used in the analyses described in this thesis are required to have $p_T > 10(20) \text{ GeV}$ unless stated otherwise.

3.6. Jets

As it is a hadron collider, quarks and gluons are very common at the LHC. Furthermore, the presence of two final state quarks is one of the primary signatures of VBF Higgs production, which is one of the main focuses of this thesis. Ascertaining the momentum of these strongly interacting particles is therefore very important. As discussed in Section 1.2.1, the hadronisation of strongly interacting particles results in highly collimated jets of particles. The momentum of the original parton which gave rise to the jet can be reconstructed by combining all of the particles in the resulting jet.

3.6.1. Jet clustering

Jet clustering algorithms take the many different types of particles that are expected to be present in the particle showers from hadronisation, and combine them into jets [82]. It is important that jet clustering algorithms do not produce different reconstructed jets if a jet undergoes soft gluon radiation (called infrared unsafety) or if a gluon in it splits in two (called colinear unsafety). The algorithm used by CMS is a so-called sequential recombination algorithm. This class of algorithms requires a metric for calculating the distance between particles in the event, d_{ij} , and a metric for calculating the distance to a nominal beamline particle, d_{iB} to be defined. The algorithms then proceed as follows:

- 1 Calculate the distance between all pairs of particles in the event including the nominal beamline.
- 2 If the smallest distance is a d_{ij} combine i and j together into a single new [particle](#) and return to step 1.
- 3 If the smallest distance is a d_{iB} , consider i to be a final state jet and remove it from the list of particles. Return to step 1.
- 4 Stop when no particles remain.

The particular algorithm used by CMS is the infrared and colinear safe anti- k_T algorithm [83], its distances are defined as:



$$d_{ij} = \min(p_{Ti}^{-2}, p_{Tj}^{-2}) \frac{\Delta R_{ij}^2}{R^2}, \quad (3.2)$$

$$d_{iB} = p_{Ti}^{-2}, \quad (3.3)$$

where ΔR_{ij} is the distance in the $\eta - \phi$ plane between particles i and j and R is a parameter of the algorithm analogous to the maximum radius of the jet. This algorithm starts by clustering around the hardest particle in a region and therefore usually produces circular [jets](#), with easy to calculate areas.

The anti- k_T algorithm is implemented using the FASTJET package [84] with the PF candidates, described in Section 3.3, used as input, the output jets are referred to as PF jets. For analyses using data from LHC Run 1 R of 0.5 is used. In addition to these jets reconstructed from PF candidates, in MC events “generator” jets are also reconstructed by applying the anti- k_T algorithm, with the same radius as that used for the PF jets, to

the final state particles produced by the generator before they are passed through the detector simulation.

3.6.2. Jet identification

In order to reject jets that are badly reconstructed or just due to detector noise, identification criteria are imposed on the jets reconstructed by the above algorithm. These requirements are that:

- The jet contains at least two PF candidates.
- The total jet energy contribution from neutral hadrons must be less than 99%.
- The total jet energy contribution from photons must be less than 99%.
- The jet has contributions from both the ECAL and HCAL.
- Jets with η such that tracking information is available must have at least one charged object which contributes to the jet's energy and less than 99% of their energy^{blue} from electrons.

Real jets from quarks or gluons pass these requirements with over 99% efficiency [85].

In addition to jets from detector noise, it is also possible for the jet reconstruction to include particles that are not from the PV, but instead come from PU vertices. This can lead either to an overestimation of the energy of a real jet from the PV, or to fake jets made up of energy from several vertices. The CMS pileup jet identification procedure [86] combines several variables sensitive to the pileup contribution in a jet, such as information on how the p_T of the jet is shared between its constituents and the constituents' tracking information, into a boosted decision tree (BDT) [87]. Simulated real jets from quarks pass this identification with 88-99% efficiency depending on how central they are, while jets from pile-up are rejected with 40-87% efficiency [86].

Jets are also required to have $\eta < 4.7$ so that they are fully contained within the CMS detector. Finally, jets which are within 0.5 in the $\eta - \phi$ plane of any veto electron, defined in Section 3.4, or veto muon, defined in Section 3.5, are vetoed, to avoid using jets which are due to misreconstructed leptons.

3.6.3. Jet energy corrections

The energy of the jets clustered and identified by the CMS jet reconstruction often does not match the energy of the particle that initiated the jet. This can have many causes such as additional energy from PU, miscalibration of the energy response of the calorimeters or energy deposited in uninstrumented areas of the detector. To account for these mismatches a correction to the jet energy is applied that has the following functional form and is described in detail in Ref. [88]:

$$p_\mu^{\text{cor}} = C_{\text{offset}}(p_T^{\text{raw}}) \cdot C_{\text{rel}}(\eta) \cdot C_{\text{abs}}(p'_T) \cdot C_{\text{res}}(p''_T, \eta) \cdot p_\mu^{\text{raw}}. \quad (3.4)$$

Each C in the equation represents a correction, p_μ^{cor} is the corrected jet four-momentum, p_μ^{raw} is the jet four-momentum before correction, p'_T is the p_T after the offset and relative correction, C_{offset} , and p''_T is the p_T after all but the residual correction, C_{abs} .

The purpose of C_{offset} is to remove energy from the jet which is not due to activity from the PV such as detector noise and PU. The correction is calculated on a jet-by-jet basis by multiplying the median p_T density of the event in which the jet is by the jet's area.

The relative correction, C_{rel} , serves to make the jet energy response uniform in η . MC truth information and the dijet p_T balance method, where the p_T of a well measured jet in the central region of the detector is compared to a second jet at a different η in Z/γ events with only two jets, ~~in data~~ are used to calculate C_{rel} .

The absolute correction C_{abs} , makes the jet energy response uniform in p_T . As well as being calculated using MC truth information, the correction is also calculated by using $\text{Z}/\gamma + \text{jets}$ events, where the transverse momentum of the jets should balance the Z/γ . Both Z bosons that decay leptonically and photons have very good energy resolution, so any imbalances can be assumed to be due to jet mismeasurement.

Finally C_{res} , which is applied only to data and not MC, corrects for residual differences seen in both p_T and η response between data and MC. The total uncertainty on the overall jet energy correction is taken to be the sum in quadrature of the uncertainties on the individual corrections. The correction and its uncertainty are shown in Figure 3.1, the other two types of jets in the figure are not used in analyses described in this thesis and so are not discussed.

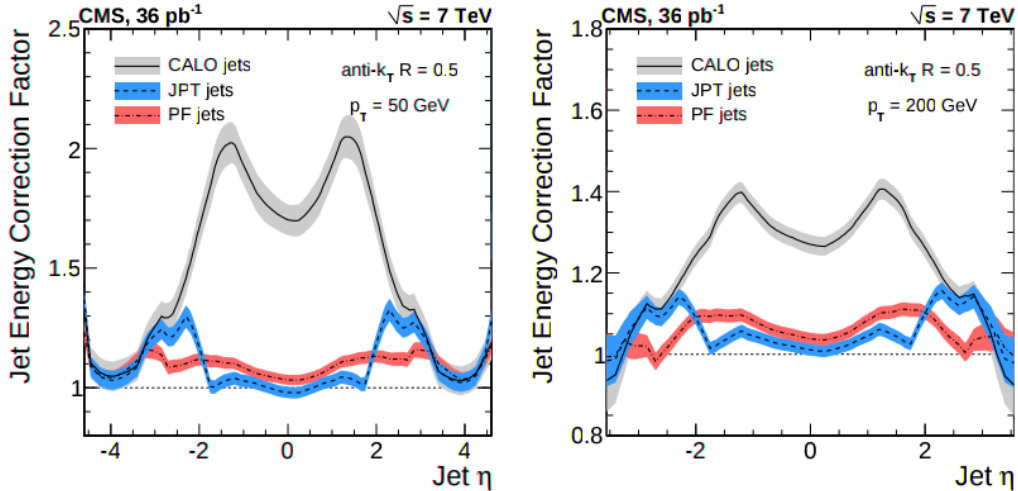


Figure 3.1.: Total jet-energy-correction factor as a function of jet η for jets with $p_T = 50 \text{ GeV}$ (left) and $p_T = 200 \text{ GeV}$ (right), for several types of jet reconstruction used at CMS. The bands indicate the corresponding uncertainty [88].

3.7. Missing transverse energy

Particles which interact only weakly with normal matter such as neutrinos and hypothetical DM particles will pass through the CMS detector without interacting. The only signature that they leave is a momentum imbalance between the visible particles in an event. The high hermeticity of the CMS detector allows this imbalance, the \cancel{E}_T , first described in Section 1.2.1, to be measured accurately. As the analyses described in this thesis are searches for invisibly decaying Higgs bosons, the measurement of \cancel{E}_T is crucial.

The CMS \cancel{E}_T reconstruction algorithm defines the \cancel{E}_T as the negative vectorial sum of the p_T of all PF candidates [89]. For processes such as Z boson decays to muon pairs or $\gamma + \text{jets}$ there should be no \cancel{E}_T as all the decay products are visible. However, as can be seen from Figure 3.2, these events often still appear to have \cancel{E}_T due to the resolution of the p_T measurements of the various objects making up the PF candidates, primarily the jets which are numerous and do not have as good resolution as other objects.

The jet energy corrections, described in Section 3.6.3, alter the energy of jets, and in doing so alter the total energy present in the event. These changes are propagated to the \cancel{E}_T . Furthermore, as charged particle flow candidates can be determined to be from the PV or a PU vertex it is also possible to correct the \cancel{E}_T for PU contributions. This correction uses the ratio of the energy response of CMS for charged and neutral particles to estimate the neutral PU contribution from the charged PU contribution.

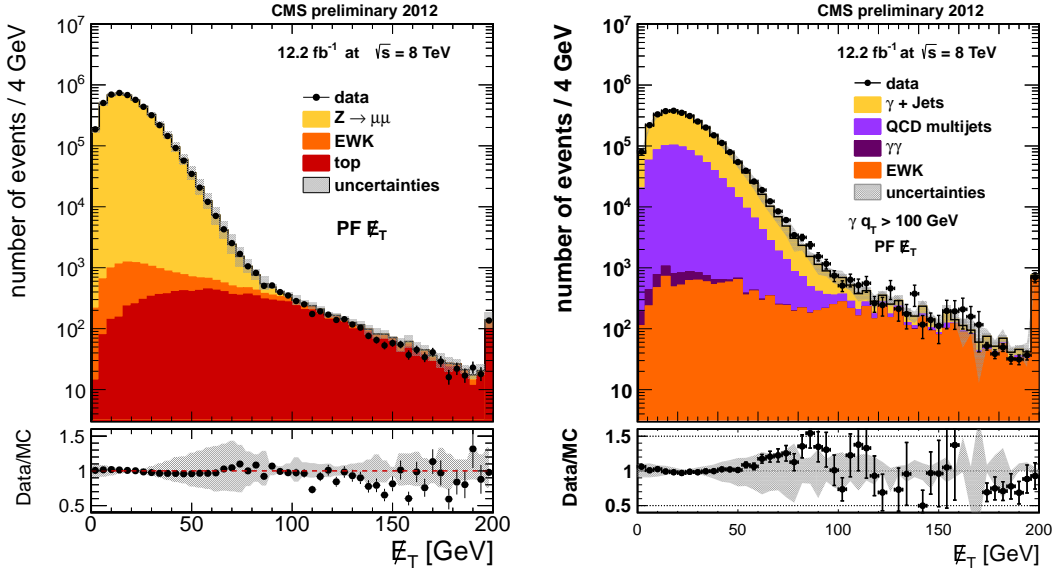


Figure 3.2.: Distributions of the uncorrected \cancel{E}_T in $Z \rightarrow \mu\mu$ events (left) and $\gamma + \text{jets}$ events (right) in $\sqrt{s} = 8$ TeV data and simulation. The shaded band corresponds to the systematic uncertainty [89].

In addition to the above corrections, filters are applied to reject events where detector or beam effects lead to a high probability of spurious \cancel{E}_T . Examples of the effects which are removed with these filters include particles directly hitting the photodetectors in the ECAL or significant energy deposits from the halo of particles surrounding the LHC beam.

In the VBF invisible Higgs boson decay searches described below events with W or Z boson decays to muons are used to estimate the rate of some background processes. As part of this estimation the muons from the W or Z boson decays are ignored when calculating the \cancel{E}_T . The variable $\cancel{E}_T^{\text{no-}\mu}$, which is the \cancel{E}_T calculated ignoring all tight muons, is used for this estimation.

3.8. Taus

Approximately 35% of taus decay to lighter charged leptons and neutrinos [90]. In this case, due to the short lifetime of the tau, the resulting charged leptons are reconstructed as prompt electrons or muons and the neutrinos cause \cancel{E}_T , therefore no specific tau reconstruction is necessary. However, the other $\sim 65\%$ of tau decays are so-called hadronic tau decays, where the decay products are hadrons and a tau neutrino. This section will describe the reconstruction of these tau decays.

CMS uses a **hadron plus strips** (HPS) algorithm for reconstructing hadronic tau decays, described in detail in Ref. [91]. Almost all hadronic tau decay modes consist of one or three charged hadrons and up to two neutral pions [90]. The HPS algorithm aims to reconstruct both the charged hadrons and the photons which result from the neutral pion decays.

The HPS algorithm is seeded by a PF jet, described in Section 3.6, and starts by creating a **strip** with the four-momentum of the most energetic electromagnetic (EM) PF candidate, i.e. photon or electron, in the jet. Other EM candidates are then searched for within a window of 0.05 (0.2) in η (ϕ) of the strip’s centre. The most energetic particle that is found is added to the strip and the four-momentum is updated. This process is repeated until no more particles are found, and if the strip has $p_T > 1 \text{ GeV}$ at this point it is kept. Combinations of charged hadrons and strips consistent with tau decay modes are then searched for, and if one is found the resulting combination is taken to be a hadronic tau.

Taus are required to be isolated. The isolation is calculated as the sum of all hadronic and photon PF candidates from the PV within a cone of size $\Delta R = 0.5$ of the tau. PF candidates not compatible with the PV within 0.8 in R of the tau are used to estimate and correct for the contribution to the isolation from PU.

Electrons which emit Bremsstrahlung photons can look very much like one charged hadron plus a neutral pion. A BDT is trained, using similar variables to those used for the electron identification in Section 3.4, to remove these particles. Taus that are consistent with being from a muon are also rejected. This rejection is performed by requiring that the tau is not reconstructed as a track compatible with hits in the muon system. The final efficiency of the CMS hadronic tau reconstruction for taus with $p_T > 20 \text{ GeV}$ is found to be 55%, with a fake rate of 2 (3)% for non-hadronic tau objects to be reconstructed as hadronic taus in the barrel (endcap) region of the detector.

3.9. MC weights

As discussed in Section 1.3 proton-proton collisions at the LHC are simulated using MC generators. In some cases the results of these simulations need to be modified to better match the observed data, by “weighting” the MC events. One example of this is cross-section weighting, where a weight is applied to account for the difference between the number of events generated and that expected to be observed in data for a given integrated luminosity. Further weights are applied to correct the generated distribution

of the number of primary vertices to match that in data (called pileup reweighting), to account for differences between the simulated lepton identification efficiency and that observed in data, and to correct the generated p_T spectrum of top quarks to better match that observed in data.

Chapter 4.

Search for invisibly decaying VBF produced Higgs bosons in Run 1 prompt data

As described in Chapter 1, searches for invisible Higgs boson decays are well motivated by their sensitivity to new physics, such as DM. Because $\mathcal{B}(H \rightarrow \text{inv})$ of an SM 125 GeV Higgs boson is very small, any evidence for invisible Higgs boson decays at the LHC would be evidence for physics beyond the SM. This chapter describes the search for invisible Higgs boson decays using data taken by CMS in 2012 which was promptly reconstructed. A dedicated trigger was developed specifically for this analysis. The total integrated luminosity collected with this trigger that was certified for use in physics analyses was 19.5 fb^{-1} [92]. The analysis was published in Ref. [1].

4.1. Event selection

Signal events are expected to have two jets with a characteristic VBF topology and a large amount of \cancel{E}_T . Several background processes, with significantly higher cross-sections than the signal process, can also produce events containing these objects. It is therefore necessary to design selection criteria, known as “cuts”, to remove as many of these background events from the analysis as possible, whilst retaining the maximum number of signal events.

The most significant of these background processes is the production of a vector boson in association with jets, “V+jets”. Leptonic decays of W bosons and Z boson decays to

neutrinos both produce \cancel{E}_T and, due to the approximately 1000 times higher cross-section for vector boson production than Higgs boson production, in many events the associated jets have a VBF-like topology [93]. V+jets backgrounds with a W (Z) are referred to as “W (Z)+jets”. A further background process that can produce significant numbers of VBF-like jets due to its very large cross-section is QCD production of multiple jets (“QCD multijets” or simply “QCD”). Whilst these multijet events have very little \cancel{E}_T from real invisible particles, it is possible for significant “fake” \cancel{E}_T to be caused by mismeasurement of the jets. The production of two vector bosons or top quarks can also lead to two jets and real \cancel{E}_T , although they have much lower cross-sections than the other background processes and their contribution is not as significant.

4.1.1. Trigger

The trigger requirements can be viewed as the first stage of the event selection. Their primary role is to reduce the rate of events that must be recorded by the detector, whilst retaining the maximum number of signal events. As described in Section 2.2.5, the decision whether to keep an event must be made very rapidly and, as a result, the object reconstruction algorithms used are less sophisticated, and the granularity of the information available from the CMS subdetectors is worse than those offline. The trigger criteria have therefore been chosen to be as loose as possible whilst achieving the required rate reduction.

As it is the key variable which indicates the presence of invisible particles, all events passing the trigger are required to have significant \cancel{E}_T . To pass the L1 trigger selection events are required to have $\cancel{E}_T > 40$ GeV. The HLT selection also requires that events have $\cancel{E}_T^{\text{no-}\mu} > 65$ GeV. The use of $\cancel{E}_T^{\text{no-}\mu}$ at trigger level ensures that events that are needed for the control regions used in the background estimation techniques described in Section 4.2 are not rejected. In addition to this $\cancel{E}_T^{\text{no-}\mu}$ requirement events must have at least one pair of jets ~~in the event~~ which is VBF-like to pass the HLT selection. The VBF-like requirements on the jets consist of requiring their η separation, $\Delta\eta_{jj}$, be greater than 3.5, that they are in opposite forward/backward halves of the detector and that they have high invariant mass, $M_{jj} > 800$ GeV. All of these jet requirements are motivated by the lack of colour connection between VBF events leading to large angular separations between the two jets, as described in Section 1.2.1. Not requiring that the VBF-like pair of jets also be the two highest p_T jets reduces inefficiencies caused by different p_T orderings in jets reconstructed by the trigger and by the offline reconstruction.

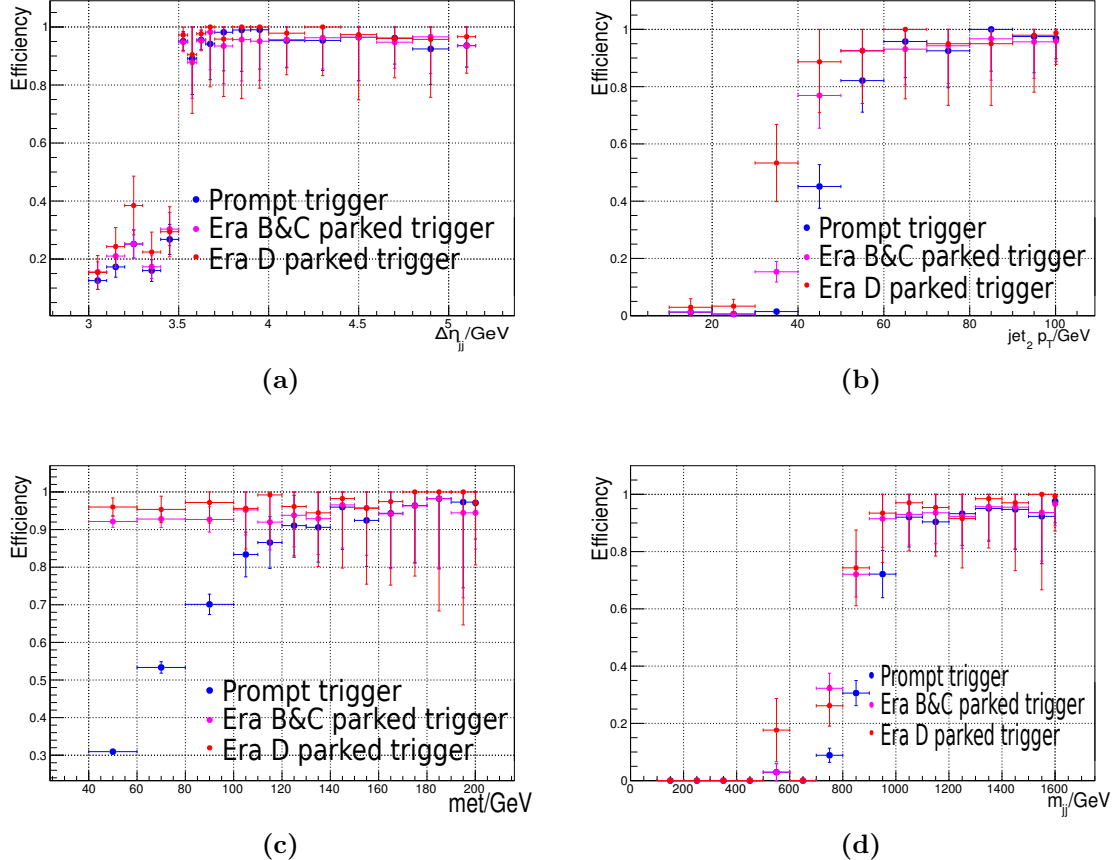


Figure 4.1.: The efficiency of the HLT requirements used in the prompt (blue) and parked (purple and red) data analyses as a function of the values of several offline variables, measured in a sample of events recorded on a single-muon trigger. (a) Efficiency as a function of offline $\Delta\eta_{jj}$, (b) efficiency as a function of sub-leading jet p_T , (c) efficiency as a function of offline $\cancel{E}_T^{\text{no-}\mu}$, (d) efficiency as a function of M_{jj} .

The efficiency for events passing both the prompt analysis trigger and the two triggers used for the parked data analysis, described in Chapter 4.4 as a function of their values of several offline variables, measured in single muon data collected using an uncorrelated trigger, is shown in Figs. 4.1 and 4.2. The events used in the trigger efficiency measurement are required to pass the following cuts:

$$M_{jj} > 1100 \text{ GeV}, \cancel{E}_T^{\text{no-}\mu} > 130 \text{ GeV}, \text{leading 2 jets' } p_T > 50 \text{ GeV}, \Delta\eta_{jj} > 4.2, \eta_{j1} \cdot \eta_{j2} < 0. \quad (4.1)$$

In each measurement the cut on the variable being studied is removed. The measured trigger efficiency is applied as an event-by-event weight to all MC samples.

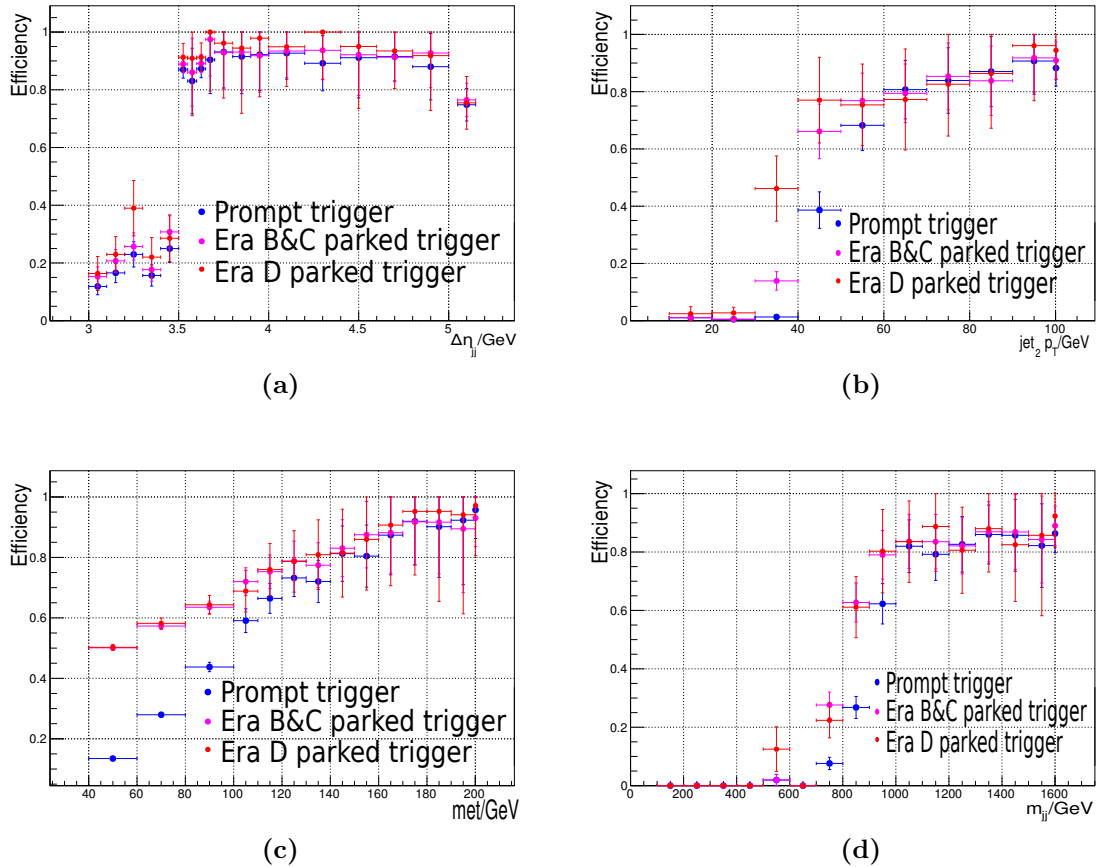


Figure 4.2.: The combined efficiency of the HLT and L1 trigger requirements used in the prompt (blue) and parked (purple and red) data analyses as a function of the values of several offline variables, measured in a sample of events recorded on a single-muon trigger. (a) Efficiency as a function of offline $\Delta\eta_{jj}$, (b) efficiency as a function of sub-leading jet p_T , (c) efficiency as a function of offline $\cancel{E}_T^{\text{no-}\mu}$, (d) efficiency as a function of M_{jj} .

4.1.2. Offline selection

The offline selection is chosen for three reasons. Firstly, the reconstruction algorithms for some objects are only well validated for certain values of p_T and η . This consideration decides the p_T thresholds for jets and leptons to be used. Secondly, as can be seen from Figure 4.1, the values of the offline variables where the trigger becomes fully efficient are in some cases much higher than the online cut. Because the variables used in the trigger are highly correlated, and the measurements of trigger efficiency made do not take this into account, the offline cuts on all variables used in the trigger were chosen such that the trigger efficiency for the variable at that point is greater than 95%. Finally, some of the cuts imposed aim to reduce the contribution from background processes, which improves the signal to background ratio in the resulting region, and thus the expected limit on $\mathcal{B}(H \rightarrow \text{inv})$.

The specific set of offline selection cuts chosen begins by requiring that events have no veto muons or electrons, as defined in sections 3.4 and 3.5. Signal events are not expected to contain leptons, while background events are, so this lepton veto reduces the background from W and Z boson decays and also from top quarks without removing signal events. The two highest p_T jets in the event are then identified as the VBF tag pair, and tighter versions of the trigger selection, motivated by the trigger efficiency considerations described above, are then applied. Specifically, the tag jets are required to be in opposite forward/backward halves of the detector, to both have $p_T > 50$ GeV to have $M_{jj} > 1100$ GeV and $\Delta\eta_{jj} > 4.2$. Again due to trigger efficiency considerations, $\cancel{E}_T^{\text{no-}\mu}$ is required to be greater than 130 GeV. Because events with veto muons have been removed by the lepton veto, $\cancel{E}_T^{\text{no-}\mu}$ in this region is identical to \cancel{E}_T . However, it is important for background estimation methods that $\cancel{E}_T^{\text{no-}\mu}$ and not \cancel{E}_T is used.

As well as the trigger based selection, further cuts are made to reduce the QCD background to a level much lower than the V+jets backgrounds. The two tag jets are required to have an azimuthal separation, $\Delta\phi_{jj} < 1.0$, since multijet events with \cancel{E}_T due to mismeasurement are most likely to have their jets back-to-back in the detector, i.e. with $\Delta\phi_{jj} = \pi$. Events where there are any jets with $p_T > 30$ GeV between the two tag jets in η are also vetoed. This CJV is motivated by the lack of colour connection, described in Section 1.2.1, between the quarks in VBF production that makes the presence of such jets unlikely in genuine signal events. The region of phase space remaining after all these cuts have been applied is called the signal region.

Finally, the values of the cuts are optimised to provide the best expected limit on $\mathcal{B}(H \rightarrow \text{inv})$ for a 125 GeV Higgs boson, which is calculated using the method described in Section 1.4 using the same background estimation and systematic uncertainties as the final analysis as described in Sections 4.2 and 4.3 respectively. For the tag jet p_T and $\cancel{E}_T^{\text{no-}\mu}$, no improvement in the expected limit is seen by tightening the cut, so the requirement is set at the 95% efficiency point of the trigger. The distributions and cut values for several of the other variables used are shown in Figure 4.3. The full selection gives an efficiency of $(6.8 \pm 0.3) \times 10^{-3}$ for selecting events from invisible decays of a VBF produced 125 GeV Higgs boson, measured using MC.

4.2. Background estimation

As discussed in Section 4.1 there are several background processes which are capable of producing VBF-like jets in association with \cancel{E}_T . The event selection removes most of these events, however a significant number still remain and it is important to estimate this number precisely. Data-driven methods, where data “control regions”, which are similar to the signal region, are used to estimate the most significant backgrounds. This data-driven approach is particularly important as the very stringent kinematic requirements placed on the tag jets lead to large uncertainties on estimates taken from MC alone. The particular method used to estimate each of the backgrounds will be described in this section.

4.2.1. $W \rightarrow e\nu + \text{jets}$

The $W + \text{jets}$ background where the W boson decays to an electron and an electron neutrino, $W \rightarrow e\nu$, is estimated using single electron events. All aspects of the event selection are the same as those used in the signal region, except for the electron veto, which is replaced with the requirement that there is exactly one tight electron in the event and no other veto electrons. These requirements give a single electron control region composed of events with jets that have the same kinematics as those in the signal region, but which is dominated by $W \rightarrow e\nu$ events.

The number of $W \rightarrow e\nu$ events in the signal region is then estimated by using the ratio between the expected number of events in the signal and control regions from MC to extrapolate from the number of events seen in data in the single electron control region

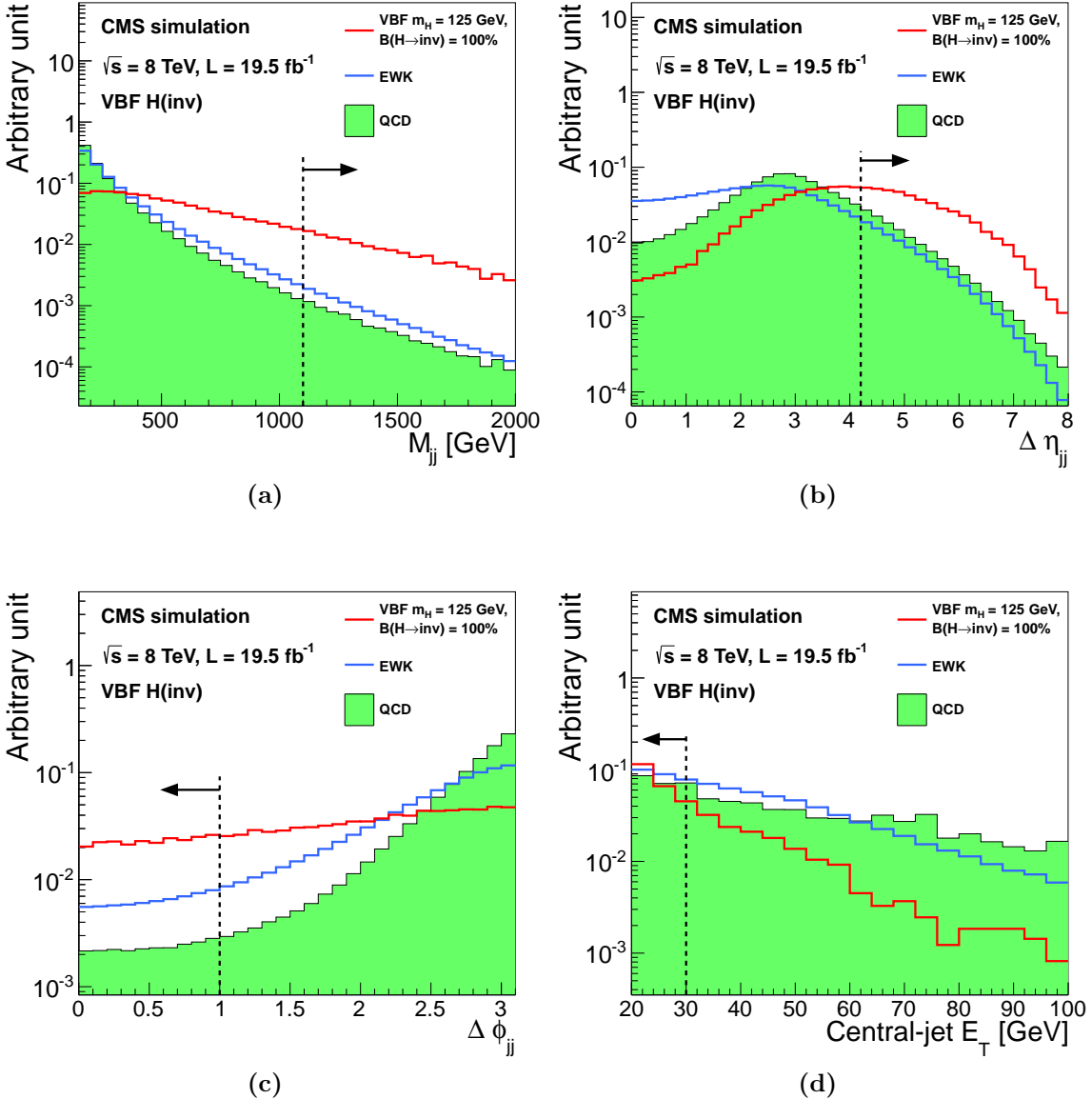


Figure 4.3.: Distributions of (a) M_{jj} , (b) $\Delta\eta_{jj}$, (c) $\Delta\phi_{jj}$ and (d) leading central jet p_T in background and signal MC events. The events shown are required to have two jets in opposite forward/backward halves of the detector with $p_T > 50$ GeV, $M_{jj} > 150$ GeV and $\cancel{E}_T^{\text{no-}\mu} > 130$ GeV. EWK refers to the V+jets and minor backgrounds described in Section 4.2 and QCD refers to the QCD multijet background. The dashed lines indicate the offline selection criteria applied to these variables, which are motivated in the text [1].

Table 4.1.: The inputs to, and results of, the $W \rightarrow e\nu$ background estimation. $N_{W \rightarrow e\nu}$ is, for the signal region the number of events expected from $W \rightarrow e\nu$ backgrounds, and for the control region the number of events remaining in the region after the subtraction of other backgrounds.

	Signal region	Control region
N_{Data}	N/A	64
N_{Bkg}	N/A	7.42 ± 2.78 (MC stat.)
N_{MC}	105 ± 10 (MC stat.)	86.6 ± 7.1 (MC stat.)
$N_{W \rightarrow e\nu}$	68.7 ± 10.3 (stat) ± 8.8(MC stat.)	56.6 ± 8.5 (stat)

using the following formula:

$$N_{Exp}^S = (N_{Data}^C - N_{Bkg}^C) \cdot \frac{N_{MC}^S}{N_{MC}^C}, \quad (4.2)$$

where N_{Exp}^S is the number of expected events in the signal region from this background process, N_{Data}^C is the number of events seen in the control region in data, N_{Bkg}^C is the number of events from other backgrounds in the control region estimated using MC, which is expected to be small, and N_{MC}^S and N_{MC}^C are the numbers of events predicted by MC to be in the signal and control regions respectively. The fact that estimations from MC are only used in ratios, or where they are expected to be small, significantly reduces the dependence of the final background estimation on the overall rate of the process predicted by MC and instead allows the observed rate in data to be used. It is important that the shape of the variables which differ between the control and signal regions are well modelled by the MC. The modelling of the shape of two key variables, the $E_T^{no-\mu}$ and the electron p_T , are shown in Figure 4.4. It can be seen that whilst the overall rate is significantly different between data and MC, the shape of the distribution is modelled well. The inputs to, and results of, the background estimation are shown in Table 4.1.

4.2.2. $W \rightarrow \mu\nu + \text{jets}$

The method used to estimate the background from $W+\text{jets}$ where the W boson decays to a muon and a muon neutrino, $W \rightarrow \mu\nu$, is very similar to that used for $W \rightarrow e\nu$. A single muon control region is used which replaces the muon veto of the signal region with a requirement that there is exactly one tight muon and no other veto muons. All

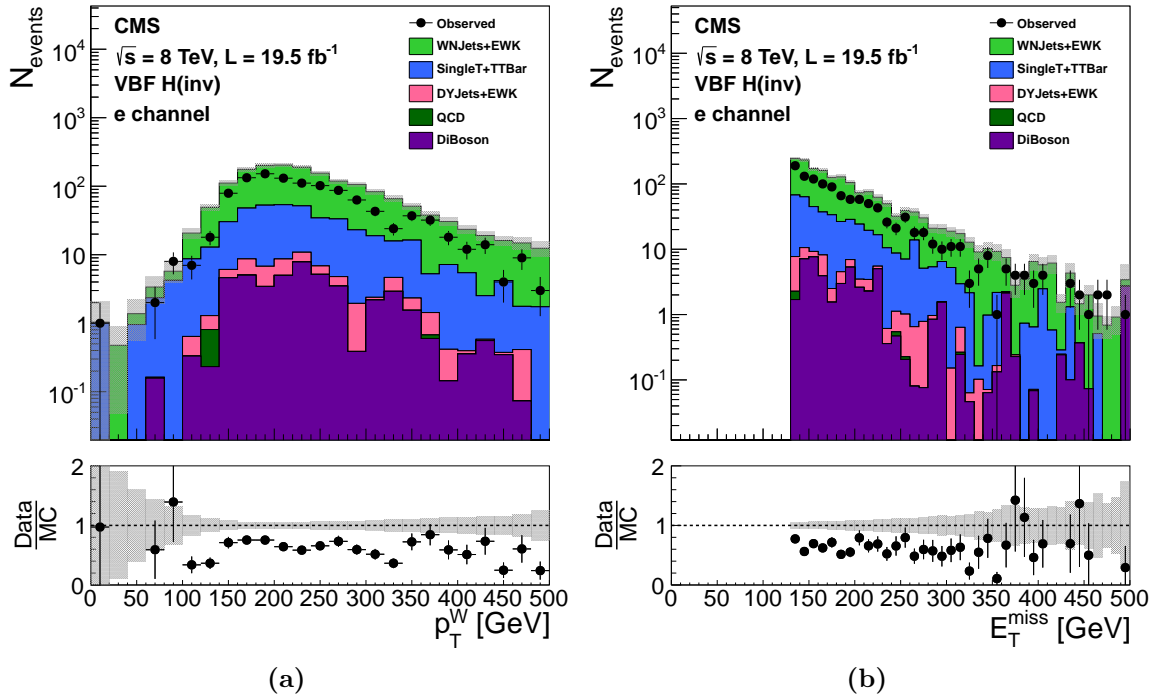


Figure 4.4.: Distributions of the visible W boson p_T (i.e. the electron p_T) (a) and E_T^{miss} (b) in the single electron control region. WNJets+EWK indicates the W+jets contribution to this region, SingleT+TTBar indicates the contribution from top quark related processes, DYJets+EWK indicates the Z+jets contribution, QCD indicates the QCD multijet contribution and DiBoson indicates the two vector boson contribution. All of these contributions are estimated from MC. The hatched region illustrates the systematic uncertainty [5]. Whilst the overall rate of data and MC is very different, the shape can be seen to agree well.

Table 4.2.: The inputs to, and results of, the $W \rightarrow \mu\nu$ background estimation. $N_{W \rightarrow \mu\nu}$ is, for the signal region the number of events expected from $W \rightarrow \mu\nu$ backgrounds, and for the control region the number of events remaining in the region after the subtraction of other backgrounds.

	Signal region	Control region
N_{Data}	N/A	216
N_{Bkg}	N/A	30.1 ± 4.5 (MC stat.)
N_{MC}	108 ± 10 (MC stat.)	306 ± 15 (MC stat.)
$N_{W \rightarrow \mu\nu}$	65.8 ± 5.4 (stat) ± 6.7 (MC stat.)	186 ± 15 (stat)

other signal region cuts remain unchanged. Equation 4.2 is then used, with the control region now being the single muon control region, to estimate the number of events from $W \rightarrow \mu\nu$ expected in the signal region. The inputs to, and results of, the background estimation are shown in Table 4.2, and distributions of the muon p_T and the $\cancel{E}_T^{\text{no-}\mu}$ in the single muon control region are shown in Figure 4.5.

4.2.3. $W \rightarrow \tau\nu + \text{jets}$

The background from $W+\text{jets}$ where the W boson decays to a tau and a tau neutrino, $W \rightarrow \tau\nu$, is estimated using a single tau control region data-driven method. However, in this case the control region used has more differences from the signal region than those used above. The reason for these increased differences is that the reconstruction efficiency for tau leptons is significantly lower than that for electrons or muons, and they are also more likely to be misreconstructed as jets, causing the event to be vetoed by the CJV. There are therefore only 3.76 ± 1.27 (stat) $W \rightarrow \tau\nu$ events with identified taus with $p_T > 20$ GeV expected in the signal region from MC.

To increase the number of events in the single tau control region, the CJV has been removed. The resulting control region has 29.2 ± 3.61 (stat) $W+\text{jets}$ events expected and thus a much lower statistical uncertainty. As there is no veto of tau leptons in the signal region the tau control region and the signal region are not mutually exclusive. However, as stated above the number of events in the signal region with identified taus is expected to be small, so the overlap is considered negligible.

In addition to the tau identification algorithm described in Section 3.8, alternative algorithms were studied to check for better performance in terms of identification

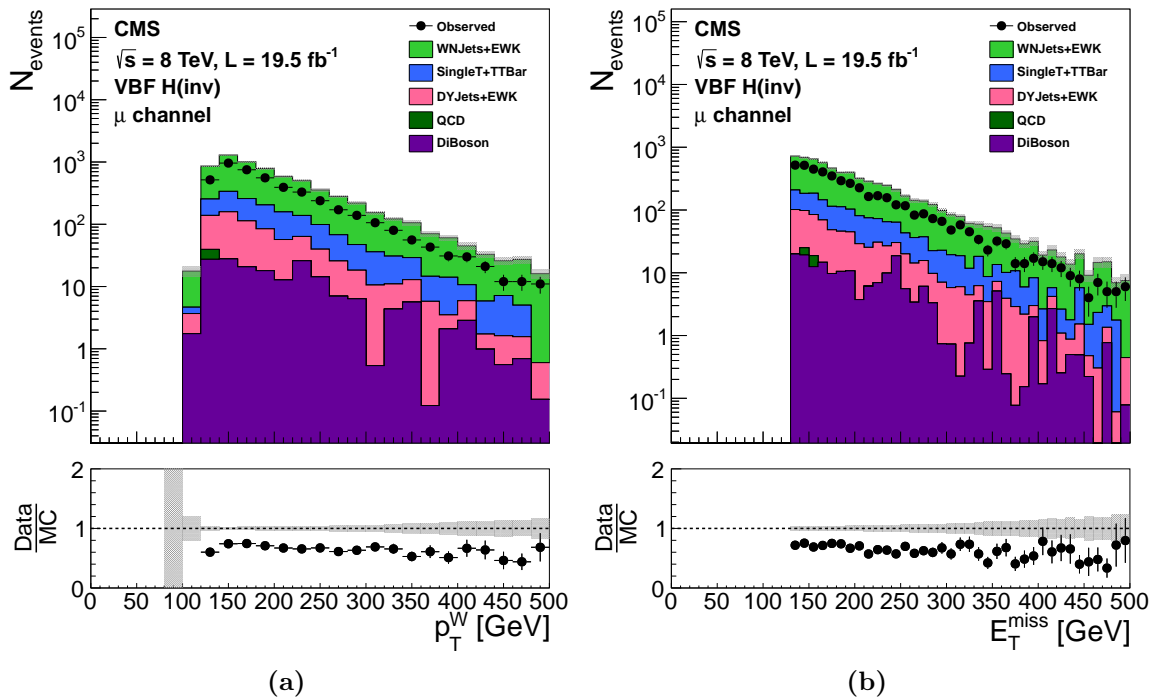


Figure 4.5.: Distributions of the visible W boson p_T (i.e. the muon p_T) (a) and E_T^{miss} (b) in the single muon control region. WNJets+EWK indicates the $W+jets$ contribution to this region, SingleT+TTBar indicates the contribution from top quark related processes, DYJets+EWK indicates the $Z+jets$ contribution, QCD indicates the QCD multijet contribution and DiBoson indicates the two vector boson contribution. All of these contributions are estimated from MC. The hatched region illustrates the systematic uncertainty [5]. Whilst the overall rate of data and MC is very different, the shape can be seen to agree well.

Table 4.3.: The inputs to, and results of, the $W \rightarrow \tau\nu$ background estimation. $N_{W \rightarrow \tau\nu}$ is, for the signal region the number of events expected from $W \rightarrow \tau\nu$ backgrounds, and in the control region the number of events remaining in the region after the subtraction of other backgrounds.

	Signal region	Control region
N_{Data}	N/A	32
N_{Bkg}	N/A	14.7 ± 3.4 (MC stat.)
N_{MC}	95.6 ± 8.5 (MC stat.)	29.2 ± 3.6 (MC stat.)
$N_{W \rightarrow \tau\nu}$	56.5 ± 21.5(stat) ± 8.6(MC stat.)	17.3 ± 3.9 (stat)

efficiency and fake rate. Specifically an alternative isolation algorithm was investigated which used a multi-variate analysis (MVA) approach to estimate the isolation sum, as well as different working points for the anti-electron and anti-muon discriminators [91]. The tau identification efficiency was found to be higher for both the alternative isolation algorithm and different working points for the anti-lepton discriminators, being twice as large if both were used compared to the standard tau identification. However, the rate of $W \rightarrow e\nu$ events being identified as $W \rightarrow \tau\nu$ was also significantly increased, going from 2% for the standard identification to 15% when the alternative isolation and anti-lepton discriminators were used. It was therefore decided to use the tau identification described in Section 3.8.

The final estimation of the background from $W \rightarrow \tau\nu$ is carried out using Equation 4.2, with the single tau control region with no CJV being used as the control region. The inputs to, and results of, the background estimation are shown in Table 4.3. Distributions of the tau p_T and $\Delta\phi_{jj}$ in the single tau control region are shown in Figure 4.6, it can be seen that the shape of the two distributions in data and MC agree well with the exception of the high $\Delta\phi_{jj}$ region which is not part of either the signal or tau control regions.

4.2.4. $Z \rightarrow \nu\nu + \text{jets}$

The background from $Z+\text{jets}$ where the Z decays to neutrinos, $Z \rightarrow \nu\nu$, is different from the $W+\text{jets}$ backgrounds described above, in that nothing is required to be misidentified in order for these events to contribute to the signal region. The method used to estimate the $Z \rightarrow \nu\nu$ background therefore differs slightly from that used above. The method

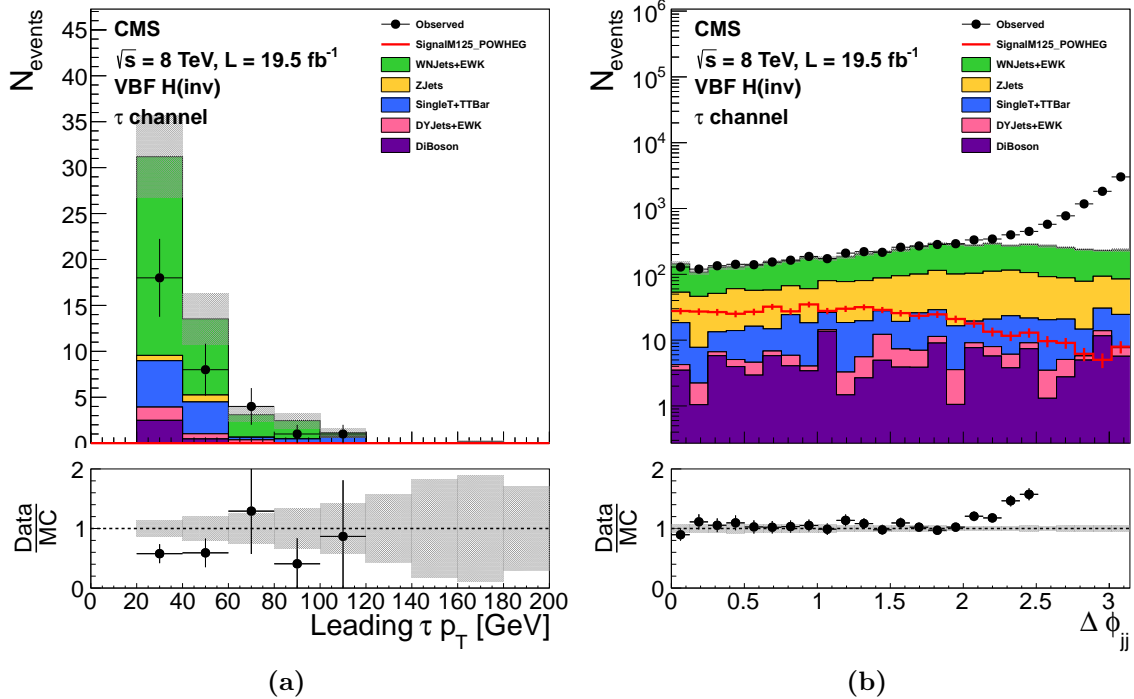


Figure 4.6.: Distributions of the the tau p_T (a) and $\Delta\phi_{jj}$ (b) in the single tau control region. WNJets+EWK indicates the W+jets contribution to this region, ZJets indicates the contribution from Z+jets, SingleT+TTBar indicates the contribution from top quark related processes, QCD indicates the QCD multijet contribution and DiBoson indicates the two vector boson contribution. All of these contributions are estimated from MC. The hatched region illustrates the systematic uncertainty [5].

uses a dimuon control region which is populated by events from the process $Z/\gamma^* \rightarrow \mu\mu$. As this process can be mediated by a photon, the kinematics of the jets in $Z/\gamma^* \rightarrow \mu\mu$ events can be different to those from $Z \rightarrow \nu\nu$. The dimuon control region that is defined therefore has a requirement that the invariant mass of the dimuons be between 60 and 120 GeV. The control region is otherwise identical to the signal region, except that the muon veto is replaced with a requirement that there are exactly two tight muons and no other veto muons.

As well as the possibility of different kinematics, $Z/\gamma^* \rightarrow \mu\mu$ and $Z \rightarrow \nu\nu$ also have different cross-sections. The formula used to estimate the $Z \rightarrow \nu\nu$ background takes this into account as follows:

$$N_{Exp}^S = (N_{Data}^C - N_{Bkg}^C) \cdot \frac{\sigma(Z \rightarrow \nu\nu)}{\sigma(Z/\gamma^* \rightarrow \mu\mu)} \cdot \frac{\epsilon_{VBF}^S}{\epsilon_{VBF}^C}, \quad (4.3)$$

where $\sigma(Z \rightarrow \nu\nu)$ is the cross-section for $Z \rightarrow \nu\nu$ and $\sigma(Z/\gamma^* \rightarrow \mu\mu)$ is the cross-section for $Z/\gamma^* \rightarrow \mu\mu$. ϵ_{VBF}^S and ϵ_{VBF}^C are the efficiencies for $Z \rightarrow \nu\nu$ events to pass the signal region selection and $Z/\gamma^* \rightarrow \mu\mu$ events to pass the control region selection respectively. As Z bosons can be created via either QCD or electroweak processes, which ~~both~~ have different cross-sections and efficiencies, ϵ_{VBF}^S and ϵ_{VBF}^C , are a cross-section weighted average of the efficiency for both types of production, calculated as:

$$\epsilon_{VBF}^S = \frac{\sigma(Z \rightarrow \nu\nu, EWK) \frac{N_{MC}^S(EWK)}{N_{gen}(Zmass,EWK)} + \sigma(Z \rightarrow \nu\nu, QCD) \frac{N_{MC}^S(QCD)}{N_{gen}(Zmass,QCD)}}{\sigma(Z \rightarrow \nu\nu, EWK) + \sigma(Z \rightarrow \nu\nu, QCD)}, \quad (4.4)$$

$$\epsilon_{VBF}^C = \frac{\sigma(Z/\gamma^* \rightarrow \mu\mu, EWK) \frac{N_{MC}^C(EWK)}{N_{gen}(EWK)} + \sigma(Z/\gamma^* \rightarrow \mu\mu, QCD) \frac{N_{MC}^C(QCD)}{N_{gen}(QCD)}}{\sigma(Z/\gamma^* \rightarrow \mu\mu, EWK) + \sigma(Z/\gamma^* \rightarrow \mu\mu, QCD)}, \quad (4.5)$$

where EWK and QCD denote where cross-sections or numbers of events are for electroweak or QCD production of a Z boson. N_{gen} is the number of events in the $Z+jets$ MC sample at generator level. Due to the limited size of the available $Z \rightarrow \nu\nu$ MC samples, the same $Z/\gamma^* \rightarrow \mu\mu$ samples used for the MC estimate of the number of events in the control region are used to obtain an estimate from MC of the number of events from the $Z \rightarrow \nu\nu$ process in the signal region. For this estimate the leptons in the $Z/\gamma^* \rightarrow \mu\mu$ samples are ignored, the production cross-section is scaled to the appropriate $Z \rightarrow \nu\nu$ value and it is required that there is a **generator level** dimuon in the event with invariant mass between 80 and 100 GeV. The generated dimuon mass for this sample was required to be greater than 50 GeV, so the cross-sections used in Equations 4.3, 4.4 and 4.5 are also calculated with this constraint. For the control region N_{gen} is calculated

Table 4.4.: The input variables for the calculation of ϵ_{VBF}^S and ϵ_{VBF}^C using Equations 4.4 and 4.5 respectively.

Variable	Value
$\sigma(Z \rightarrow \nu\nu, EWK)$	1.380 pb
$\sigma(Z \rightarrow \nu\nu, QCD)$	6600 pb
$\sigma(Z/\gamma^* \rightarrow \mu\mu, EWK)$	0.303 pb
$\sigma(Z/\gamma^* \rightarrow \mu\mu, QCD)$	1168 pb
$\frac{N_{MC}^S(EWK)}{N_{gen}(Zmass,EWK)}$	$(1.3 \pm 0.1) \cdot 10^{-3}$
$\frac{N_{MC}^S(QCD)}{N_{gen}(Zmass,QCD)}$	$(1.4 \pm 0.2) \cdot 10^{-6}$
$\frac{N_{MC}^C(EWK)}{N_{gen}^S(EWK)}$	$(7.5 \pm 0.3) \cdot 10^{-4}$
$\frac{N_{MC}^C(QCD)}{N_{gen}^S(QCD)}$	$(9.2 \pm 1.2) \cdot 10^{-7}$

after requiring that the mass of the generator level dimuon is between 60 and 120 GeV, denoted by the label $Zmass$ in Equations 4.4 and 4.5.

The inputs to [equations](#) 4.4 and 4.5 are given in Table 4.4. The cross-sections for electroweak Z boson production were calculated at NLO using VBFNLO which specialises in vector boson production. The cross-section for QCD production of $Z/\gamma^* \rightarrow \mu\mu$ is calculated using FEWZ inclusively for all leptons and then divided by three to obtain the figure for muons only. This cross-section is then multiplied by the ratio between the cross-section for $Z \rightarrow \nu\nu$ and $Z/\gamma^* \rightarrow \mu\mu$, which was calculated to be 5.651 at NLO using MCFM, to obtain the QCD production cross-section for $Z \rightarrow \nu\nu$. The inputs to Equation 4.3 are given in Table 4.5, with the exception of the ratio between the total production cross-sections for $Z \rightarrow \nu\nu$ and $Z/\gamma^* \rightarrow \mu\mu$ which is taken to be the same 5.651 that ~~it is found to be~~ for QCD production. This approximation is used because the electroweak contribution to the ratio is smaller than that from QCD by more than a factor of one thousand and is therefore negligible. The distributions of $E_T^{\text{no-}\mu}$ and M_{jj} for a Z control region with relaxed selection, to ensure sufficient numbers of events, are shown in Figure 4.7, demonstrating that the MC samples model the data distribution well.

Table 4.5.: The inputs to, and results of, the $Z \rightarrow \nu\nu$ background estimation using Equation 4.3. ϵ_{VBF} in the signal (control) region is calculated using Equation 4.4 (4.5). $N_{Z \rightarrow \nu\nu}/N_{Z/\gamma^* \rightarrow \mu\mu}$ is in the signal region the number of events expected from $Z \rightarrow \nu\nu$ backgrounds, and for the control region the number of events remaining in the region after the subtraction of other backgrounds. The systematic uncertainties are calculated as described in Section 4.3.

	Signal region	Control region
N_{Data}	N/A	12
N_{Bkg}	N/A	0.3 ± 0.1 (MC stat.)
ϵ_{VBF}	$(1.65 \pm 0.15 \text{ (stat)} \pm 0.22 \text{ (syst)}) \cdot 10^{-6}$	$(1.11 \pm 0.12 \text{ (stat)} \pm 0.12 \text{ (syst)}) \cdot 10^{-6}$
$N_{Z \rightarrow \nu\nu}/N_{Z/\gamma^* \rightarrow \mu\mu}$	$99 \pm 29 \text{ (stat)} \pm 25 \text{ (syst)}$	11.7 ± 0.1 (MC stat.)

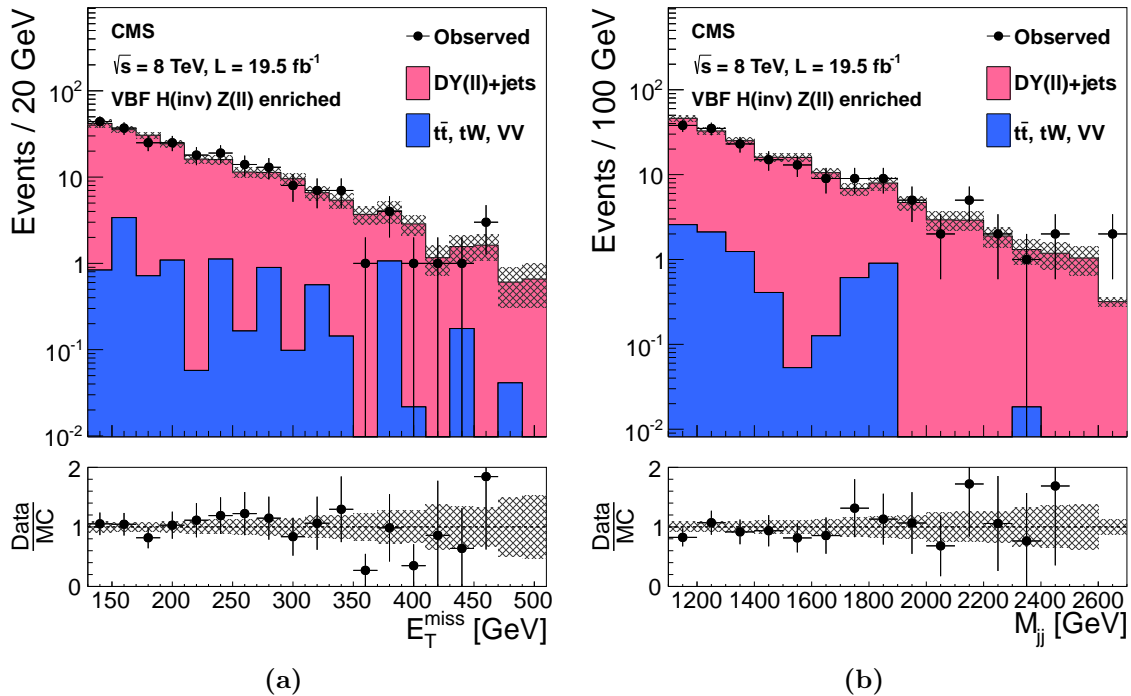


Figure 4.7.: Distributions of the $\cancel{E}_T^{\text{no-}\mu}$ (a) and M_{jj} (b) in a relaxed Z control region, with no requirement on $\Delta\phi_{jj}$, the CJV removed, and the requirements on M_{jj} and $\Delta\eta_{jj}$ relaxed to 1000 GeV and 3.5 respectively. DY(II)+jets indicates the contribution from $Z+jets$ processes and $t\bar{t}$, tW , VV indicates the contribution from minor backgrounds. The hatched region illustrates the systematic uncertainty [1].

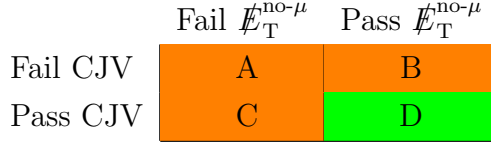


Figure 4.8.: A diagram of the regions used in the QCD ABCD background estimation method. Region D is the signal region and regions A, B and C are mutually exclusive control regions.

4.2.5. QCD

The QCD background remaining after the full event selection is mostly from events where jets are mismeasured. The size of the MC samples available for studying this process is not sufficient for them to be relied upon for extrapolation from a control region to the signal region. The remaining QCD background is therefore estimated using a so-called “ABCD” method. In this method four regions, A, B, C and D, are defined according to whether events pass or fail the $\cancel{E}_T^{\text{no-}\mu}$ and CJV cuts as shown in Figure 4.8. Region D is the signal region and regions A, B and C are three mutually exclusive control regions.

The efficiency to pass the $\cancel{E}_T^{\text{no-}\mu}$ and CJV cuts can be determined from the ratios between regions A and B, and A and C respectively. The number of events expected in the signal region is then:

$$N_D = N_A \cdot \frac{N_B}{N_A} \cdot \frac{N_C}{N_A} = \frac{N_B \cdot N_C}{N_A}, \quad (4.6)$$

where $N_{A,B,C}$ is the number of events observed in region A, B, C in data minus the number expected from V+jets or other minor backgrounds, i.e. the number of events in the region believed to be from QCD. This method relies on the probability of an event passing the CJV being uncorrelated with the $\cancel{E}_T^{\text{no-}\mu}$ of the event. This has been checked by comparing the $\cancel{E}_T^{\text{no-}\mu}$ distribution, below the 130 GeV signal region requirement, for events which pass and fail the CJV. The maximum fractional difference observed between bins of these two distributions is 40%, so this is added as a systematic to the QCD background yield. The method was also tested in a region orthogonal to the signal region with all requirements the same as those of the signal region except $\Delta\phi_{jj}$ which was required to be greater than 2.6. In this test region, which is expected to be QCD dominated, the prediction agreed with the expectation within 15%, which is within the

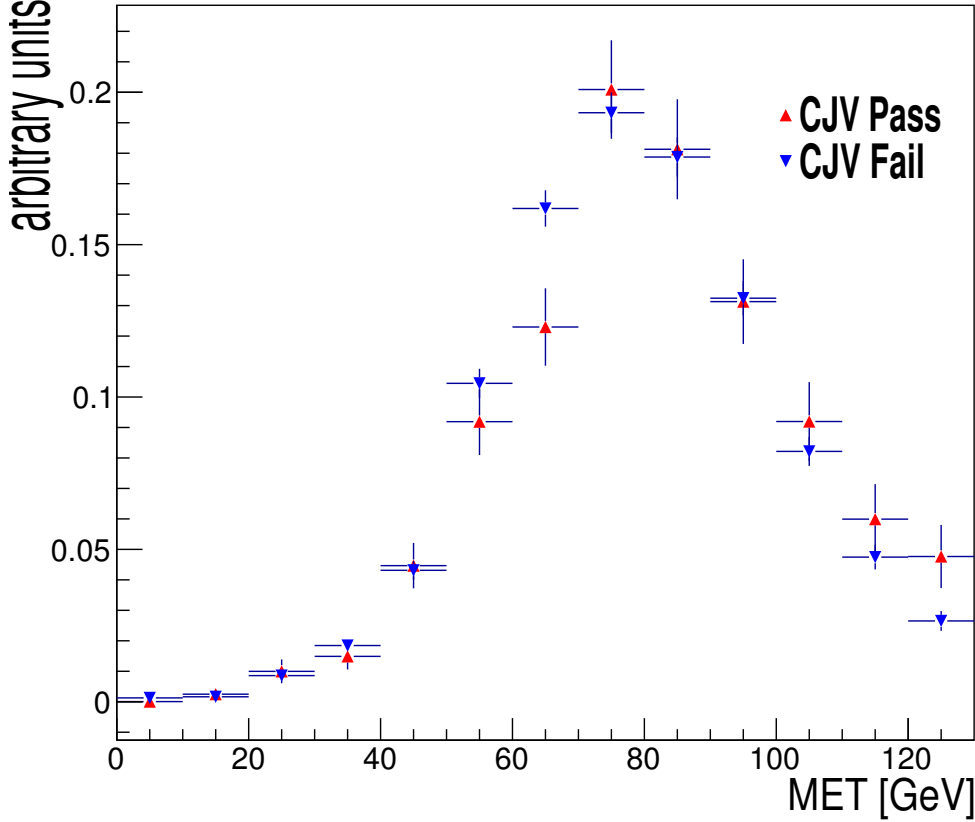


Figure 4.9.: Distribution of the $E_T^{\text{no-}\mu}$ for events passing and failing the CJV. The largest difference seen in any bin is 40%. This difference is used to assign as a systematic uncertainty on the QCD background estimation.

Table 4.6.: Numbers of events from data and MC in each region used in the QCD background estimate and the final estimated number of events.

Region	Data	Background	Data-Background
N_A	5118	222 ± 14	4896 ± 73
N_B	773	586 ± 17	184 ± 33
N_C	896	76.9 ± 8.3	819 ± 31
N_D	-	-	30.9 ± 1.6

systematic uncertainty assigned to the method. The results of using this method to estimate the number of QCD events in the signal region are shown in Table 4.6.

4.2.6. Minor backgrounds

In addition to the V+jets and QCD backgrounds which account for 94% of the expected events in the signal region, there is also a small number of events expected from other minor backgrounds including single top quark production, top quark pair production, diboson production and $Z/\gamma^* \rightarrow \mu\mu$. Due to their small contributions these numbers of events are taken directly from MC. The diboson backgrounds are simulated using PYTHIA 6, the single top quark background using POWHEG and the top quark pair production and $Z/\gamma^* \rightarrow \ell\ell$ backgrounds using MADGRAPH. The cross-sections used to normalise these MC samples were taken from the most up to date CMS published results at the time of the analysis [94–98]. The final estimate of the number of events from minor backgrounds in the signal region is 20 ± 8.2 (MC stat), with 70% of these expected to be from diboson production.

4.3. Systematic uncertainties

The dominant uncertainties in the analysis are the statistical uncertainties on the V+jets backgrounds due to the number of data events observed in the control regions. In addition, as well as those mentioned in Section 4.2, there are several further systematic uncertainties on the expected numbers of signal and background events. These uncertainties are described individually below and the fractional uncertainty on the total expected number of signal and background events from all sources of uncertainty are summarised in Table 4.7.

4.3.1. Jet energy scale

The reconstructed energy of a jet reconstructed by CMS is not necessarily the same as the true energy of all the particles that make it up. As described in Section 3.6.3, jet corrections are applied to remedy this. The correction for the ratio between reconstructed and true jet energy is referred to as the JES. Uncertainties on the JES come from several sources. The JES obtained from the dijet p_T balance method for instance has an uncertainty from the jet resolution bias [88]. This bias arises because the jet p_T spectrum sharply falls with increasing p_T . Such a spectrum leads to the well measured jet being used as the base for the balance method to be more likely to have fluctuated up in p_T than down. The main uncertainties in the photon/Z balance methods come from the

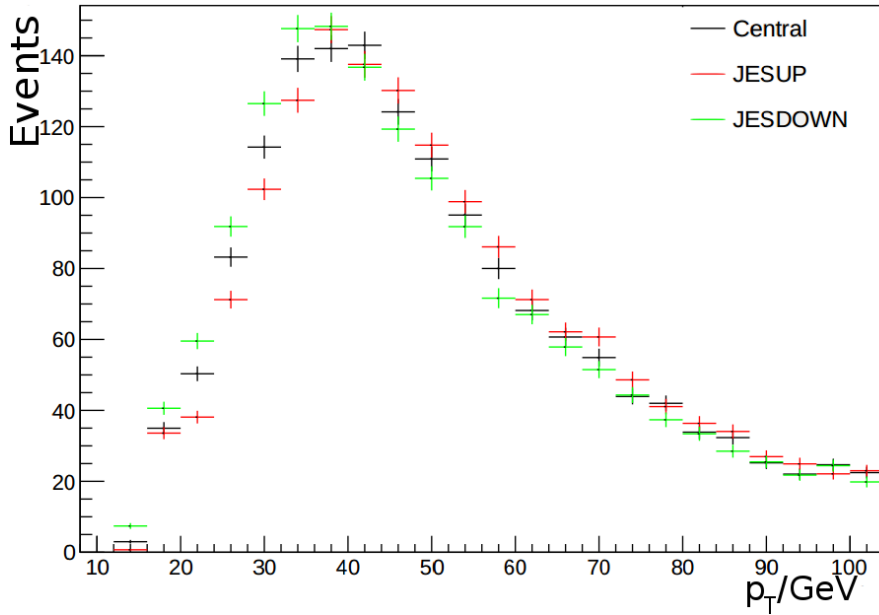


Figure 4.10.: The distribution of the sub-leading jet’s p_T in W+Jets MC events with the nominal JES and for JESUP and JESDOWN.

limited number of events in the samples used. The JES obtained in MC is also different when measured with different MC generators, which leads to an uncertainty.

These uncertainties on the JES give rise to an uncertainty on the energy of all jets in CMS events. The impact of this uncertainty on the expected and observed event yields in this analysis was estimated by altering the JES correction up by one standard deviation, “JESUP”, and down by one standard deviation “JESDOWN”, and recalculating the energy and momentum of all jets in each event. The \cancel{E}_T is recalculated taking into account the updated jet energies. Furthermore, as the jet energy scale uncertainty varies with p_T and η , it is possible for the p_T ordering of the jets to change when the JES is changed. The VBF tag pair is therefore ~~rechosen~~ to be the new highest p_T pair of jets.

After modifying the JES, the analysis is ~~reperformed~~ and the resulting change in the expected signal and background yields is taken to be the uncertainty due to the JES. The sub-leading jet’s p_T in a W+jets MC sample is shown for the nominal JES, JESUP and JESDOWN in Figure 4.10. It can be seen that altering the JES results in a smooth change in the jet p_T , indicating that the difference in the number of events passing the analysis cuts is not due to individual events with large weights migrating in and out of the signal region.

4.3.2. Jet energy resolution

The width of the jet energy distribution, the jet energy resolution (JER), differs between MC and data. This is partly due to MC samples being generated before and during data taking, and thus before a measurement of the exact resolution in data can be performed. Measuring the JER in data is done in a very similar way to the measurement of the JES using dijet and photon/Z-jet balance techniques and by comparing the reconstructed energy to that generated in MC, and thus has the same sources of uncertainty.

To correct the MC resolution to match that in the data, the p_T of all jets in MC is “smeared”. The smearing is carried out using two methods. The first method is used for jets in MC that are within 0.5 in the $\eta - \phi$ plane of a generator jet. In this method the difference between the reconstructed and generator jet p_T is scaled by a correction factor, c , chosen to be the ratio between the resolution of the data and MC and calculated as a function of the jet’s p_T and η . The resulting jet p_T is given by:

$$p'_T = \max [0, p_{T\text{gen}} + \textcolor{yellow}{c}(p_T - p_{T\text{gen}})], \quad (4.7)$$

where p_T is the initial transverse momentum, p'_T is the transverse momentum after smearing and $p_{T\text{gen}}$ is the matched generator jet’s p_T . This procedure has the advantage that the smearing is not reliant on random factors and is therefore reproducible, making synchronisation between analysis implementations easier.

The second method is used when a jet has no matching generator jet. In this case a random correction is necessary. The technique used is to add a fluctuation to the jet’s p_T with a size obtained by sampling a gaussian with width:

$$\sqrt{(c^2 - 1) \sigma_{MC}}, \quad (4.8)$$

where c is the same correction factor from the method above and σ_{MC} is the initial MC resolution as a function of p_T and η . σ_{MC} was measured by performing a gaussian fit to the distribution of the ratio between the generator level and offline jet p_T observed in W+jets MC. As well as being random and thus difficult to reproduce, this method has the disadvantage that it can only be used to worsen the resolution.

The analysis is performed three times with three different smearings, one where the MC resolution is smeared to match the nominal data resolution, which is used for the main signal and background estimations, and two where the MC resolution is made to match the improvement, “JERBETTER” and worsening, “JERWORSE” of the jet energy

resolution by one standard deviation. For the nominal and JERWORSE smearings the limitation that the unmatched jet smearing method can only worsen the resolution is not a problem, as the initial MC resolution is better than that in data for all values of jet p_T and η . However, for the JERBETTER smearing it is necessary to improve the resolution for some jets. Fortunately, the differences between the generated resolution and the JERBETTER resolutions where improved resolution is required are small, so in these cases no smearing is applied. For all smearings the resulting changes in jet p_T are propagated through to the \cancel{E}_T . The differences between the signal and background yields obtained with the nominal JER, JERBETTER and JERWORSE are used to assign an uncertainty due to the JER.

4.3.3. Unclustered energy scale

In addition to the uncertainties on the \cancel{E}_T from the propagation of JES and JER uncertainties there are also uncertainties from the other elements contributing to the \cancel{E}_T . Electrons and muons contribute to the \cancel{E}_T , but have very good resolution and small scale uncertainties compared to jets so their contribution to the \cancel{E}_T uncertainty is considered negligible [89]. Unclustered energy, which is made up of all of the energy deposits in the calorimeters not identified as part of an object, such as a jet or lepton, still contributes to the \cancel{E}_T , and has a non-negligible scale uncertainty [89].

The unclustered energy scale (UES) is measured using photon and Z events with jets present in them, where it can be assumed that the \cancel{E}_T should be zero [89]. After jet energy corrections, the distribution of the remaining difference between the photon or Z momentum and the jets is therefore centered around zero, and its width can be taken as the uncertainty on the UES. The UES in all events is modified up and down by this uncertainty and the \cancel{E}_T recalculated. The differences in the obtained signal and background event yields obtained through this process are used as the uncertainty from this source.

4.3.4. Lepton identification and isolation efficiency

As described in Section 3.9 MC events are reweighted using scale factors to account for differences in the electron and muon identification and isolation efficiency. The weights due to these efficiencies are varied up and down by the uncertainties from the tag and

probe method used to measure them, and the difference in the resulting signal and background yield used as the uncertainty from this source.

An uncertainty of 8% is added to the estimate of the $W \rightarrow \tau\nu$ background to account for the uncertainty in the tau identification efficiency, which is measured using $Z \rightarrow \tau\tau$ events where one tau decays to a muon and the other hadronically [99]. 5% of events in the $W \rightarrow \tau\nu$ control region also appear to be due to $W \rightarrow e\nu$ events where the electron or a jet has been misreconstructed as a tau, so a further 5% systematic is assigned to the $W \rightarrow \tau\nu$ estimate.

4.3.5. Other uncertainties

Additional uncertainties arise from several sources. For instance, the $Z \rightarrow \nu\nu$ background estimate is reliant on the ratio of the cross-sections for the $Z \rightarrow \nu\nu$ and $Z/\gamma^* \rightarrow \mu\mu$ processes in the phase space of this analysis. A 20% uncertainty on this ratio was applied to cover the difference between the values of the ratio calculated using MADGRAPH and using MCFM [5]. Further uncertainties come from the measurement of the distribution of the number of primary vertices used in the pileup weights, described in Section 3.9, the PDFs and QCD scale used in the signal cross-section measurements [100, 101], differences in the ggH $\Delta\phi_{jj}$ spectrum depending on the MC generator used [5], the cross-sections used to normalise the minor backgrounds, described in Section 4.2.6, and the measurement of the total integrated luminosity [92].

4.4. Results

The final results of all the background estimation methods and systematic uncertainty studies are summarised in Table 4.8. The total number of events expected from background processes in the signal region is 332 ± 46 (stat) ± 45 (syst). The presence of a Higgs boson with a mass of 125 GeV, SM production and $\mathcal{B}(H \rightarrow \text{inv}) = 100\%$ would be expected to yield 224 ± 31 signal events would be expected, with 6% of these from ggH and the remainder from VBF production. 390 events are observed, which is within one standard deviation of the **background only** prediction. Figure 4.11 shows the $\cancel{E}_T^{\text{no-}\mu}$ and M_{jj} of the background and signal events expected, and the data observed, in the signal region.

Table 4.7.: A summary of the uncertainties in the total expected signal and background yields. All uncertainties are quoted as the percentage change in the yield when each effect is varied up and down according to its uncertainty. The signal yields assume a Higgs boson mass of 125 GeV.

Uncertainty source	Total background	Signal
Control region statistics	11%	—
MC statistics and $Z \rightarrow \nu\nu$ cross-section ratio	11%	4%
JES, JER and UES	7%	13%
QCD background estimation	4%	—
Lepton efficiency	2%	—
Luminosity	0.2%	2.6%
Cross-sections	0.5–1%	—
PDFs	—	5%
QCD scale	—	4%
ggH $\Delta\phi_{jj}$ spectrum	—	4%
Total	18%	14%

Table 4.8.: The estimated numbers of background and signal events, together with the observed yield, in the signal region. The signal yield assumes a Higgs boson mass of 125 GeV and $\mathcal{B}(H \rightarrow \text{inv.}) = 100\%$.

Process	Event yield
$Z \rightarrow \nu\nu$	$99 \pm 29 \text{ (stat)} \pm 25 \text{ (syst)}$
$W \rightarrow e\nu$	$67 \pm 5 \text{ (stat)} \pm 16 \text{ (syst)}$
$W \rightarrow \mu\nu$	$63 \pm 9 \text{ (stat)} \pm 18 \text{ (syst)}$
$W \rightarrow \tau\nu$	$53 \pm 18 \text{ (stat)} \pm 18 \text{ (syst)}$
QCD multijet	$31 \pm 5 \text{ (stat)} \pm 23 \text{ (syst)}$
Minor backgrounds	$20 \pm 8 \text{ (syst)}$
Total background	$332 \pm 36 \text{ (stat)} \pm 45 \text{ (syst)}$
VBF H(inv.)	$210 \pm 29 \text{ (syst)}$
ggH(inv.)	$14 \pm 10 \text{ (syst)}$
Observed data	390

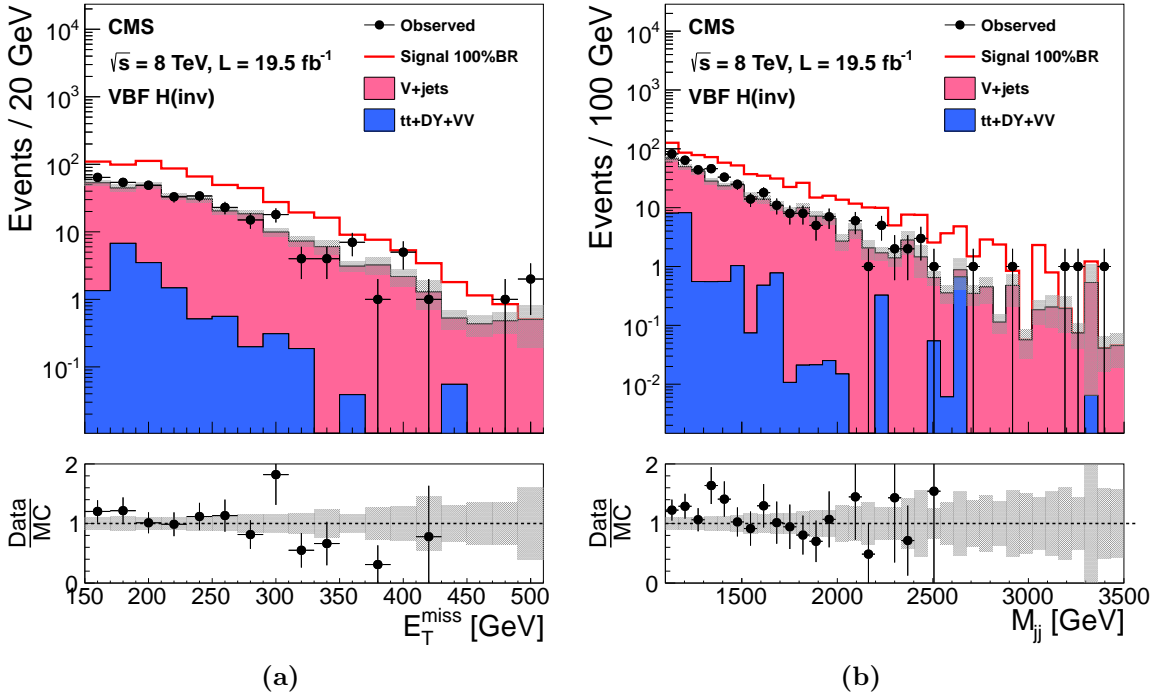


Figure 4.11.: Distributions of the $\cancel{E}_T^{\text{no-}\mu}$ (a) and M_{jj} (b) of events observed in data and expected from the background estimation methods described in Section 4.2 in the signal region. tt+DY+VV indicates the contribution from minor backgrounds. The hatched region illustrates the systematic uncertainty. The QCD background is not shown due to the very low number of events in the MC samples. The cumulative effect of a signal from a Higgs boson with mass of 125 GeV, decaying 100% to invisible final states is also shown [1].

As no excess is observed, the asymptotic CL_S technique, described in Section 1.4, is used to place an upper limit on the production cross-section times branching fraction, $\sigma \times \mathcal{B}$, at 95% CL. Under the assumption of SM production this limit can be interpreted as a limit on $\mathcal{B}(H \rightarrow \text{inv})$. All systematic uncertainties are modelled as log-normally distributed nuisance parameters, with the exception of the statistical uncertainty on the $Z \rightarrow \nu\nu$ background, which is modelled as a gamma-normally distributed nuisance due to the low number of events in the dimuon control region. A gamma-normal distribution is used in the case of control regions with low numbers of events because in this case the central limit theorem does not apply so the Poisson probability of observing a certain number of events is very asymmetric; this asymmetry is well modelled by a gamma-normal distribution [102].

The resulting upper limits are shown as a function of Higgs boson mass in Figure 4.12, with the 95% CL observed (expected) limit on $\mathcal{B}(H \rightarrow \text{inv})$ for a 125 GeV Higgs boson being 65% (49%). The green and yellow bands shown in Figure 4.12 denote the one and two sigma uncertainty bands respectively of the expected limit, also calculated using the asymptotic technique. The one (two) sigma band represents the region that the observation is expected to lie in 68% (95%) of the time if the **background only** hypothesis is true.

This was the first published search for invisibly decaying Higgs bosons in the VBF channel. It can be seen that for all values of Higgs boson mass investigated the observed limit is approximately one sigma above the expected limit. If the measurements of the limit at each Higgs boson mass were not correlated, this could be seen as evidence for an excess. However, as this analysis has only a single bin, and no information on the shape of the event variable distributions is used, the measurements for the different Higgs boson masses are 100% correlated with each other. The analysis therefore sees no significant evidence of non-SM behaviour.

The parked data, described in Section 2.2.5, used for this analysis was collected using a range of triggers with similar but looser requirements than those used for the prompt data (“prompt”) analysis described in the previous chapter. These looser requirements allow areas of phase space which were previously removed by the prompt trigger to be used. However, these areas also have very large QCD backgrounds, and require the analysis selection and some background estimation methods to be redesigned compared to the prompt analysis. As it was reconstructed later the parked data also uses different, better, detector calibrations (such as the jet energy calibrations), calculated with the full Run 1 LHC dataset. The parked data analysis was also carried out using a new code

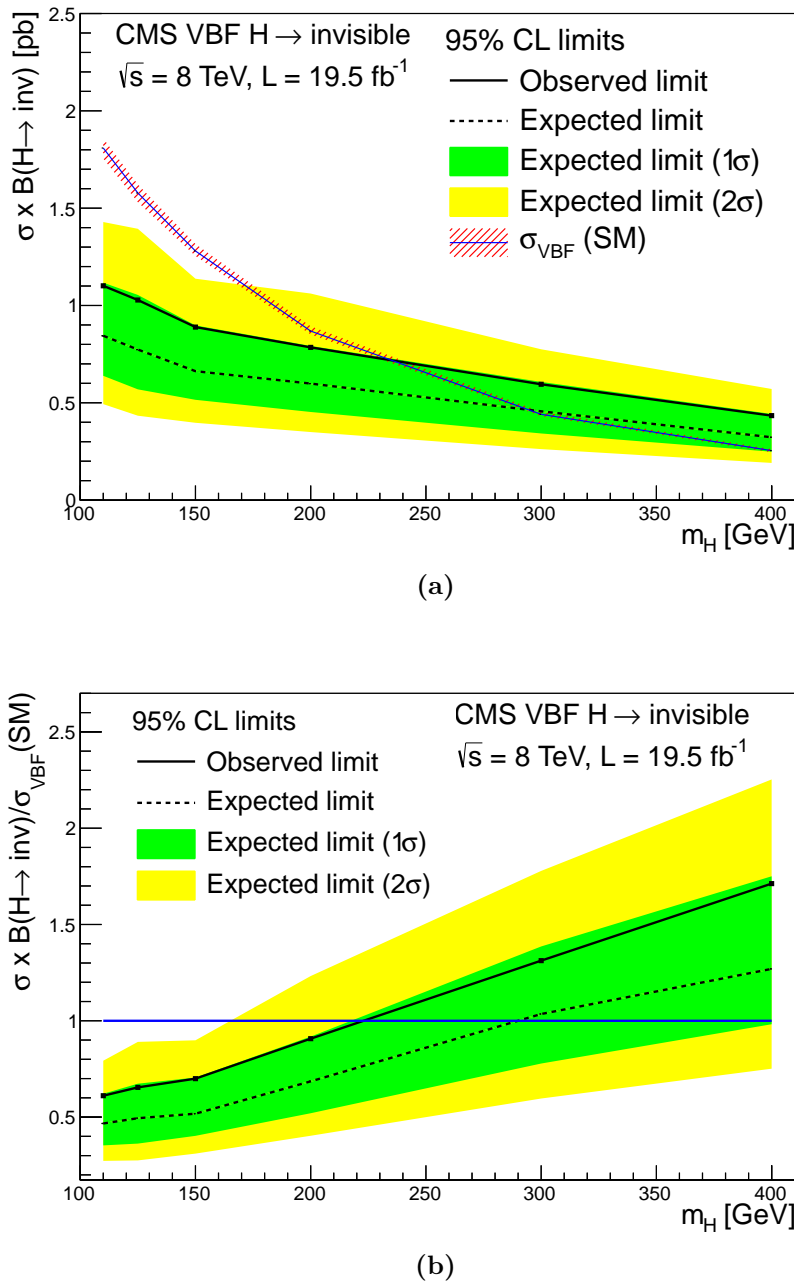


Figure 4.12.: Expected and observed 95% CL upper limits on the VBF $\sigma \times \mathcal{B}$ in pb (a) and normalised to the SM VBF Higgs boson production cross-section (b) [1]. The green and yellow bands indicate the 68% and 95% confidence intervals on the expected limit respectively.

Table 4.9.: A summary of the requirements of the triggers used for this analysis in each Run 1 era. All triggers require that there is at least one pair of jets in the event satisfying all of the jet requirements listed in this table. All requirements are on HLT variables unless stated otherwise.

Variable	Cut in era				
	A	B & C	D		
L1 \cancel{E}_T	> 40 GeV				
$\cancel{E}_T^{\text{no-}\mu}$	> 65 GeV	No requirement			
jet p_T of both jets	> 40 GeV	> 35 GeV	> 30 GeV		
M_{jj}	> 800 GeV	> 700 GeV			
$\Delta\eta_{jj}$	> 3.5				
$\eta_{j1} \cdot \eta_{j2}$	> 0				

framework, which was fully validated against that used in the prompt analysis. This analysis was [made public](#) in Ref. [2].

4.5. Trigger

The triggers used to collect the parked data varied throughout Run 1, due both to the available trigger bandwidth changing, and to the rate of the triggers used varying as the LHC instantaneous luminosity increased during the run. Run 1 was split into 4 “eras”: A, B, C and D, with 0.9, 3.9, 7.2 and 7.3 fb^{-1} of integrated luminosity collected in each respectively. During era A data were not parked, so the prompt data are used. The two other triggers used, one for eras B and C, and one for era D, differed from the prompt trigger in that there was no requirement on the \cancel{E}_T present at the HLT level and the jet p_T and M_{jj} requirements were looser. The exact values of the trigger selection cuts are summarised in Table 4.9. These looser requirements allow the [trigger driven](#) selection applied in the prompt analysis to be relaxed, and [more optimal](#) signal and background control regions to be used. As the region accessible with the parked data includes the prompt data signal region as a subset, no improvement would be possible from applying the analysis designed for the prompt data to the parked data without modification. Measuring the trigger efficiency is essential for any analysis. However, it is particularly

important in this analysis, where several elements of the selection are chosen to avoid regions which are expected to contain significant numbers of signal events but the trigger

is not fully efficient. Therefore, the more accurate the trigger efficiency measurement is, the looser this selection can be and the more signal events can be retained.

As three different triggers are used the measurement of trigger efficiency must be performed separately for each one. Furthermore, as the LHC running conditions were different in each era, it is important to measure each trigger's efficiency using the data from the era that it ran in. Also, the variables used in the trigger are highly correlated with each other. These correlations mean it is important to either only use regions of phase space where the trigger is fully efficient, as was done in the prompt analysis, or to measure the trigger efficiency in a way that accurately models the effect of these correlations. The cuts required to ensure that each trigger is fully efficient throughout the region selected can be ascertained from Figure 4.1, which shows the efficiencies of all three triggers as a function of $\cancel{E}_T^{\text{no-}\mu}$, jet p_T and M_{jj} .

As the trigger used in era A was the same as that used for the prompt analysis, no relaxation would be possible if full trigger efficiency is required and the data from era A is to be used. Era A only accounts for 5% of the total data, so one possibility is not to use the era A data and to relax the selection to the point of full efficiency of the next tightest trigger. However, it would still be necessary to discard data in the trigger turn on regions of the remaining two triggers which are expected to contain signal events. For these reasons several approaches to measuring the trigger efficiency as a function of the values of all variables used in the trigger were investigated.

First, the trigger efficiency was measured three dimensionally as a function of $\cancel{E}_T^{\text{no-}\mu}$, M_{jj} and the sub-leading jet's p_T . An example of one of the results of these measurements in one of the bins in $\cancel{E}_T^{\text{no-}\mu}$ for the era B and C, and the era D triggers can be seen in Figure 4.13. The three variables used were chosen because the trigger becomes fully efficient very quickly as a function of the η related variables, so no parameterisation of this efficiency is necessary. The number and size of the bins was chosen to ensure that sufficient events are present in each bin to prevent the statistical error on the efficiency measurement being larger than the differences between bins. As can be seen from the figure, this leads to very large differences in efficiency between bins, which cause discontinuities in the $\cancel{E}_T^{\text{no-}\mu}$, M_{jj} and sub-leading jet p_T distributions when the measured efficiency is applied to MC events as a weight. This method was therefore not suitable for use in the final analysis.

In order to achieve a smoother parameterisation of the trigger efficiency, coarse bins in M_{jj} and sub-leading jet p_T were chosen, and a fit to the $\cancel{E}_T^{\text{no-}\mu}$ efficiency distribution in

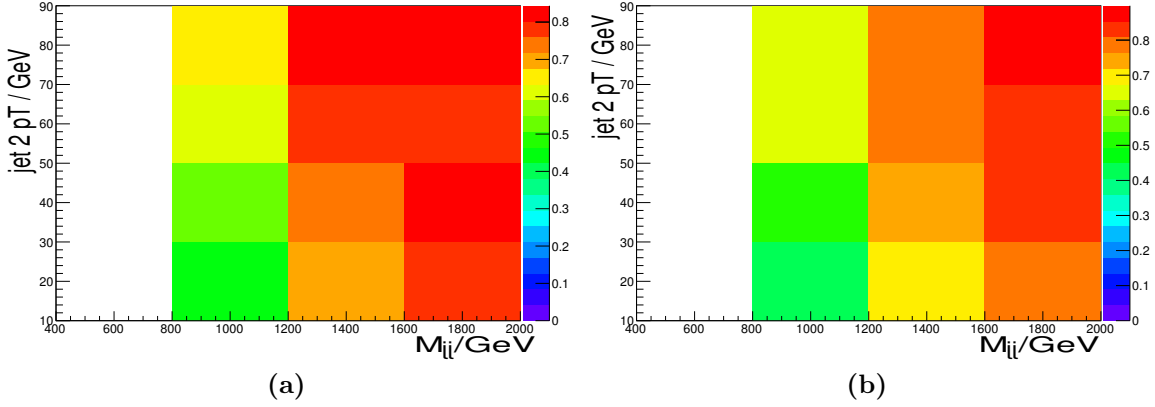


Figure 4.13.: The efficiency for the trigger (color-scale) used in eras B and C (a) and era D (b), as a function of M_{jj} and sub-leading jet p_T for events with $\cancel{E}_T^{\text{no-}\mu}$ between 60 and 120 GeV. The efficiency was measured using a single muon dataset collected with an orthogonal trigger.

each bin was performed, using the following function:

$$f(x) = \frac{A}{2} \cdot \left(1 + \frac{2}{\sqrt{\pi}} \int_0^{\frac{x-B}{\sqrt{C}}} e^{-t^2} dt \right), \quad (4.9)$$

which has a maximum value of A, and is derived from the error function with centre B and width C. The width, maximum and centre of the function are all allowed to float in the fit. The events used in this study were required to have leading jet $p_T > 50$ GeV, $\eta_{j1} \cdot \eta_{j2} < 0$ and $\Delta\eta_{jj} > 3.6$ to ensure that there are no inefficiencies due to these variables. The results of these fits for the two M_{jj} and sub-leading jet p_T bins containing the most events entering the final analysis selection are shown in Figure 4.14. The fit can be seen to describe the data well and the uncertainties are small. The results for the remaining bins are shown in Appendix A. Most bins have good agreement between the fit and the data, however, some of the plots in the appendix indicate that the parameters of the fit have taken extreme values, or have very large uncertainties. These extreme values and poor fits are mostly due to low numbers of events in the bin. The analysis selection described in Section 4.6, ensures that no events in these bins are used in the analysis.

Each MC event was weighted by the average of the efficiency found for each of the three triggers weighted by the amount of integrated luminosity recorded using each trigger as

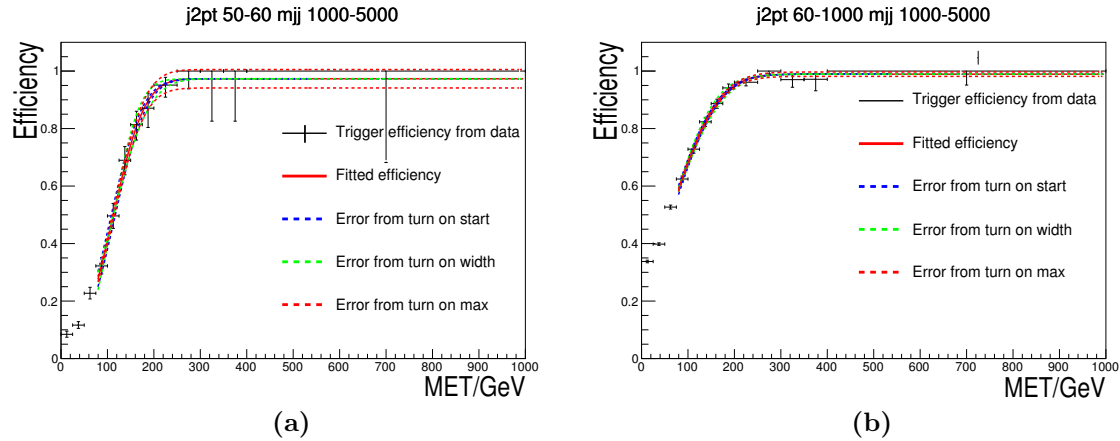


Figure 4.14.: The results of performing a fit of the function in Equation 4.9 to the efficiency of the trigger used in era D, measured in a sample of single muon events collected with an orthogonal trigger. The dashed bands show the uncertainty on the fit due to each of the three parameters of the fit. The two bins of dijet mass (m_{jj}) and sub-leading jet's p_T ($j2pt$) shown are those with the two highest numbers of events from the final signal region described in Section 4.6. The results of the fits in the other bins are shown in Appendix A.

shown in the following equation:

$$w(p_{Tj2}, M_{jj}, \not{E}_T^{\text{no-}\mu}) = \frac{\sum_i \mathcal{L}_i \epsilon_i(p_{Tj2}, M_{jj}, \not{E}_T^{\text{no-}\mu})}{\sum_i \mathcal{L}_i}, \quad (4.10)$$

where i are the three triggers, $\epsilon_i(p_{\mathrm{T}j2}, M_{jj}, \cancel{E}_{\mathrm{T}}^{\mathrm{no-}\mu})$ is the measured efficiency for trigger i as a function of the event's sub-leading jet p_{T} , M_{jj} and $\cancel{E}_{\mathrm{T}}^{\mathrm{no-}\mu}$, and \mathcal{L}_i is the integrated luminosity collected using trigger i . The resulting trigger efficiency varies smoothly and leads to no unphysical discontinuities in the distributions of event variables as can be seen from the figures in the remainder of this chapter.

4.6. Event selection

As mentioned above, a significant challenge in the analysis of the parked data is that the additional areas of phase space collected by these triggers, but not collected by the prompt data triggers, have very large contributions from QCD backgrounds. The QCD contribution to VBF analyses is very hard to model because whilst the cross-sections for these processes are very high, the probability of any individual event being VBF-like is very low. The number of MC events that must be generated to make a representative

sample is therefore prohibitively large. As a result of these difficulties, the parked data selection is separated into two stages. The first “preselection” stage selects a region of phase space which is not expected to be dominated by QCD processes. After this preselection has been made the background processes expected to contribute are the same as in the prompt analysis, and studies were undertaken into which background estimation methods and final signal region selection leads to the best expected limit.

4.6.1. Preselection

The first element of the preselection was motivated by the trigger. The following selection was applied to ensure that the values of all event variables are above the trigger thresholds of all triggers used, and that the $\cancel{E}_T^{\text{no-}\mu}$ was above the lowest value of the turn on centre, B, as defined in Equation 4.9, obtained from the fits described in Section 4.5:

$$\begin{aligned} \eta_{j1} \cdot \eta_{j2} < 0, \text{ leading jet } p_T > 50 \text{ GeV}, \Delta\eta_{jj} > 3.6, \\ \text{sub-leading jet } p_T > 40 \text{ GeV}, M_{jj} > 800 \text{ GeV}, \cancel{E}_T^{\text{no-}\mu} > 90 \text{ GeV}. \end{aligned} \quad (4.11)$$

Where $j1$ and $j2$ are the leading and sub-leading p_T jets in the event and are chosen as the VBF tag jets. We also require that for the “signal-like” selection there are no veto electrons or muons in the event. The W+jets and Z+jets control regions used in the background estimates described in Section 4.7 impose different lepton requirements. QCD multijet processes still dominate the region defined by this selection, as can be seen in Figure 4.15a, where there are a lot more data events than expected from the background MC prediction. This difference is due to mismeasured QCD events not being adequately modelled by the available MC samples, which are described in further detail in Section 4.7.9.

Additional selection requirements were applied to reduce the observed differences from the mismeasured QCD multijet background. The first variable that was used to achieve this reduction is the \cancel{E}_T significance, \mathcal{S} , which is defined as the ratio between $\cancel{E}_T^{\text{no-}\mu}$ and the square root of the sum of the transverse energy of all particles in the event, which is an estimate of the statistical error on the \cancel{E}_T . The intention of the \mathcal{S} cut is to remove events which have a large amount of \cancel{E}_T , but also have an even larger amount of visible energy, meaning that the \cancel{E}_T is likely to be from mismeasurement of the visible particles. The preselection requires that \mathcal{S} be greater than 3. The value of this cut was chosen by looking at Figure 4.15a and removing the region with the most disagreement between

data and MC. The resulting region shown in Figure 4.15b still does not display good data-MC agreement, however the disagreement is smaller.

After the cut on \mathcal{S} , a requirement that the $\cancel{E}_T^{\text{no-}\mu}$ is not too close to any jets in ϕ was made. This requirement was motivated by the fact that if the \cancel{E}_T is due only to the mismeasurement of a jet, the \cancel{E}_T will be aligned with that jet. Two variables were investigated, the first was the minimum azimuthal angle difference between either of the two tag jets and the $\cancel{E}_T^{\text{no-}\mu}$, $\min\Delta\phi(j_{1/2}, \cancel{E}_T^{\text{no-}\mu})$, and the second was the minimum azimuthal angle difference between any jet with p_T greater than 30 GeV and the $\cancel{E}_T^{\text{no-}\mu}$, $\min\Delta\phi(j, \cancel{E}_T^{\text{no-}\mu})$. At a similar signal efficiency the difference between the observed number of events and the MC background prediction, which is an indication of the remaining QCD multijet background, was found to be 80% smaller for a cut on $\min\Delta\phi(j, \cancel{E}_T^{\text{no-}\mu})$ than a cut on $\min\Delta\phi(j_{1/2}, \cancel{E}_T^{\text{no-}\mu})$. The same cut on $\min\Delta\phi(j, \cancel{E}_T^{\text{no-}\mu})$ was also found to reduce top quark related backgrounds by a factor of two compared to a cut on $\min\Delta\phi(j_{1/2}, \cancel{E}_T^{\text{no-}\mu})$. We therefore require that $\min\Delta\phi(j, \cancel{E}_T^{\text{no-}\mu}) > 1.0$ for events to pass the preselection. $\min\Delta\phi(j, \cancel{E}_T^{\text{no-}\mu})$ was found to give significantly better signal efficiency than the $\Delta\phi_{jj}$ variable used in the prompt analysis for the same background rejection, so no cut was made on $\Delta\phi_{jj}$.

The M_{jj} distribution after the $\min\Delta\phi(j, \cancel{E}_T^{\text{no-}\mu})$ cut is shown in Figure 4.15c. Whilst the agreement for large M_{jj} is good, it can be seen that the first bin of the distribution, where mismeasured QCD multijet events would be expected, due to their not recoiling against another object, shows a significant disagreement. The final cut of the preselection is therefore to require $M_{jj} > 1000$ GeV. This cut also ensures that none of the bins used to describe the trigger efficiency which have too few events to be reliable are used. In summary the full preselection is as follows:

$$\begin{aligned} \eta_{j1} \cdot \eta_{j2} &< 0, \text{ leading jet } p_T > 50 \text{ GeV}, \Delta\eta_{jj} > 3.6, \\ \text{sub-leading jet } p_T &> 40 \text{ GeV}, M_{jj} > 1000 \text{ GeV}, \cancel{E}_T^{\text{no-}\mu} > 90 \text{ GeV}, \\ \min\Delta\phi(j, \cancel{E}_T^{\text{no-}\mu}) &> 1.0, \mathcal{S} > 3.0. \end{aligned} \quad (4.12)$$

Distributions of several variables after the full preselection are shown in Figure 4.16. No estimate of the QCD contribution is given in these distributions, and it can be seen that there is still disagreement between data and MC in the areas where QCD would be expected to contribute. Further selection is, therefore, necessary.

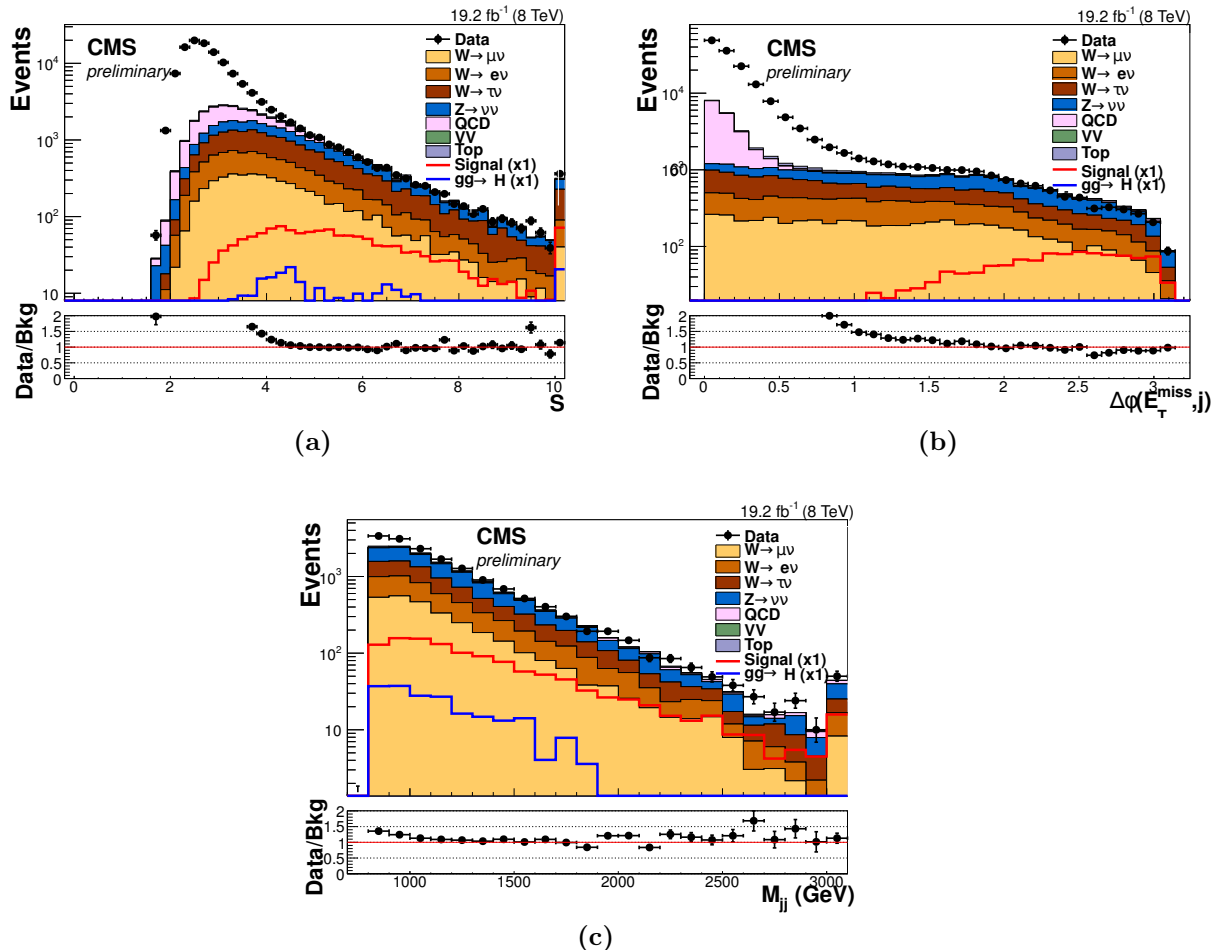


Figure 4.15.: (a) \mathcal{S} after the trigger driven selection described in Equation 4.11. (b) $\min\Delta\phi(j, \not{E}_T^{\text{no-}\mu})$ after the trigger driven selection and requiring $\mathcal{S} > 3$. (c) M_{jj} after the trigger driven selection and requiring $\mathcal{S} > 3$ and $\min\Delta\phi(j, \not{E}_T^{\text{no-}\mu}) > 1$. All three plots are of the signal-like region with the MC scaled using the background estimation methods described in Section 4.7. The disagreement between data and the predictions from background MC samples is believed to be due to mismeasured QCD multijet events which are not well modelled by the available MC samples. The last bin of each distribution contains the events above the range displayed. Signal ($gg \rightarrow H$) refers to an SM VBF (ggH) produced Higgs boson with $\mathcal{B}(H \rightarrow \text{inv}) = 100\%$.

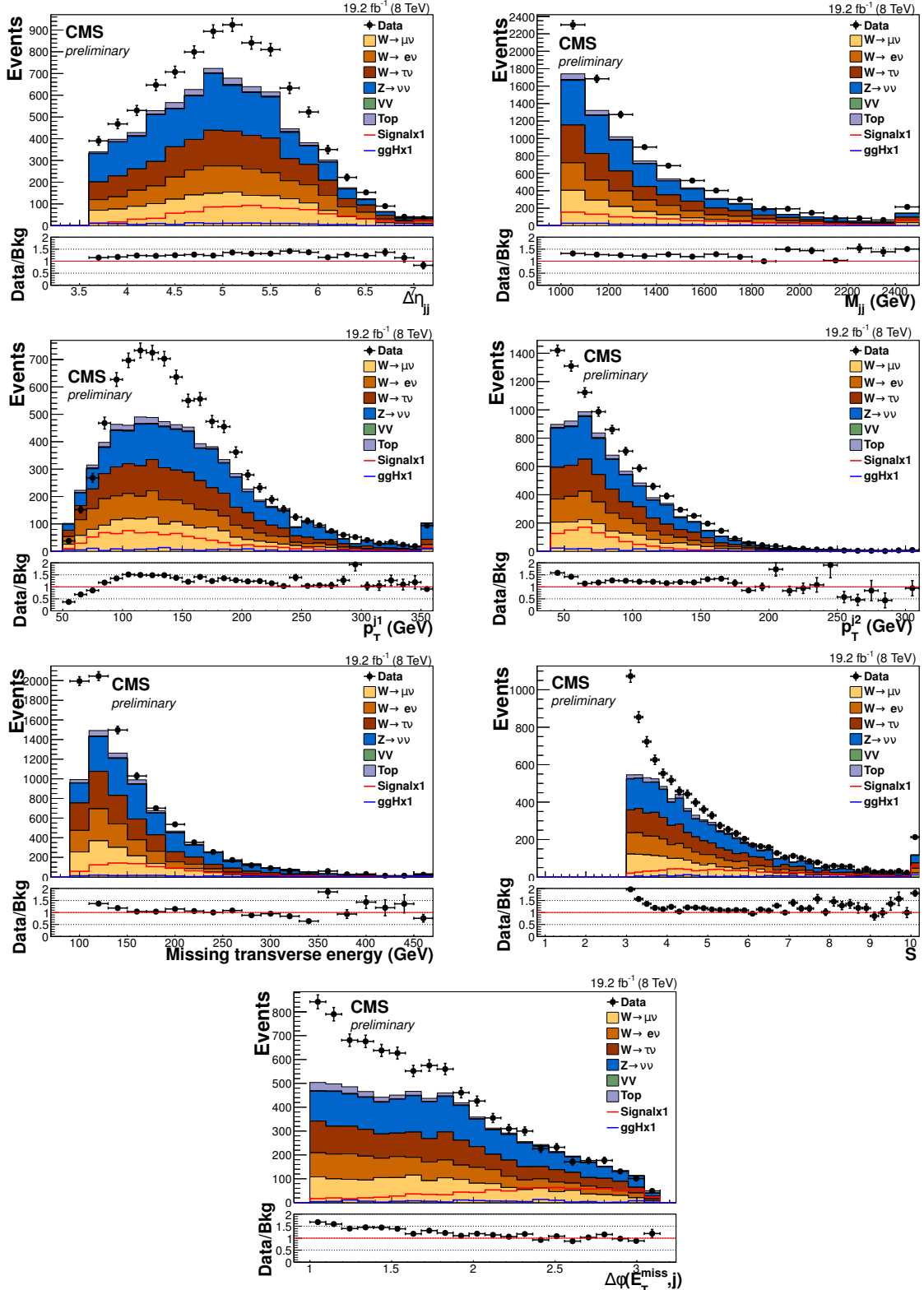


Figure 4.16.: From top to bottom, left to right, distributions of $\Delta\eta_{jj}$, M_{jj} , leading jet p_T , sub-leading jet p_T , E_T^{miss} , S and $\min\Delta\phi(j, E_T^{miss})$ for events passing the full preselection. No QCD contribution is shown, which accounts for the difference between the data observation and background prediction. The last bin of each distribution contains the events above the range displayed.

4.6.2. Signal region selection

As can be seen from Figure 4.16, there is still a significant difference between the data and the MC background prediction. It is also evident that the main areas where disagreement occurs are where contributions from QCD backgrounds (which are not included in the figure) would be expected to contribute, at low \mathcal{S} and low $\min\Delta\phi(j, \cancel{E}_T^{\text{no-}\mu})$, i.e. with jets close to the $\cancel{E}_T^{\text{no-}\mu}$. Outside these QCD-like regions good agreement between data and MC is seen, indicating very low numbers of QCD events remaining. The approach taken was to place tight requirements on these two variables to reduce the QCD background to be much smaller than the other backgrounds considered. The large uncertainty on any estimate of the number of events from QCD multijet processes therefore also became negligible. A requirement that events have $\min\Delta\phi(j, \cancel{E}_T^{\text{no-}\mu}) > 2$ and $\mathcal{S} > 4$, was therefore imposed. The resulting relatively QCD-free “optimisation” region was blinded (i.e. the data were not looked at) to use for studies to determine the final signal region selection. All of the studies described in this chapter from this point until the results section were performed blind unless stated otherwise.

Two methods to select the signal region were investigated. The first method was a **cut based** selection. Starting from the optimisation region the cuts on \mathcal{S} , $\min\Delta\phi(j, \cancel{E}_T^{\text{no-}\mu})$, $\Delta\eta_{jj}$, sub-leading jet p_T and M_{jj} were varied one at a time and the expected limit for each combination of cuts was calculated. The method described in Section 1.4 was used, with the background estimation techniques and systematic uncertainties described in Sections 4.7 and 4.8 respectively, to calculate the expected limit. In the case of the QCD background, which has only a very small contribution to the signal region, the background estimation was performed once for the optimisation selection and used for all cut values. The estimations for all other background processes were repeated for each set of cuts. After each variable was varied the selection was updated to use the cut value that gave the best expected limit. After all the variables had been varied the process was repeated until no improvement in the expected limit was seen so as to avoid ignoring other better sets of cuts. The cut values that gave the best expected limit define the signal region and are as follows:

$$\begin{aligned} \eta_{j1} \cdot \eta_{j2} < 0, \Delta\eta_{jj} > 3.6, \text{ leading jet } p_T > 50 \text{ GeV}, \\ \text{sub-leading jet } p_T > 45 \text{ GeV}, M_{jj} > 1200 \text{ GeV}, \\ \cancel{E}_T^{\text{no-}\mu} > 90 \text{ GeV}, \mathcal{S} > 4.0, \min\Delta\phi(j, \cancel{E}_T^{\text{no-}\mu}) > 2.3. \end{aligned} \quad (4.13)$$

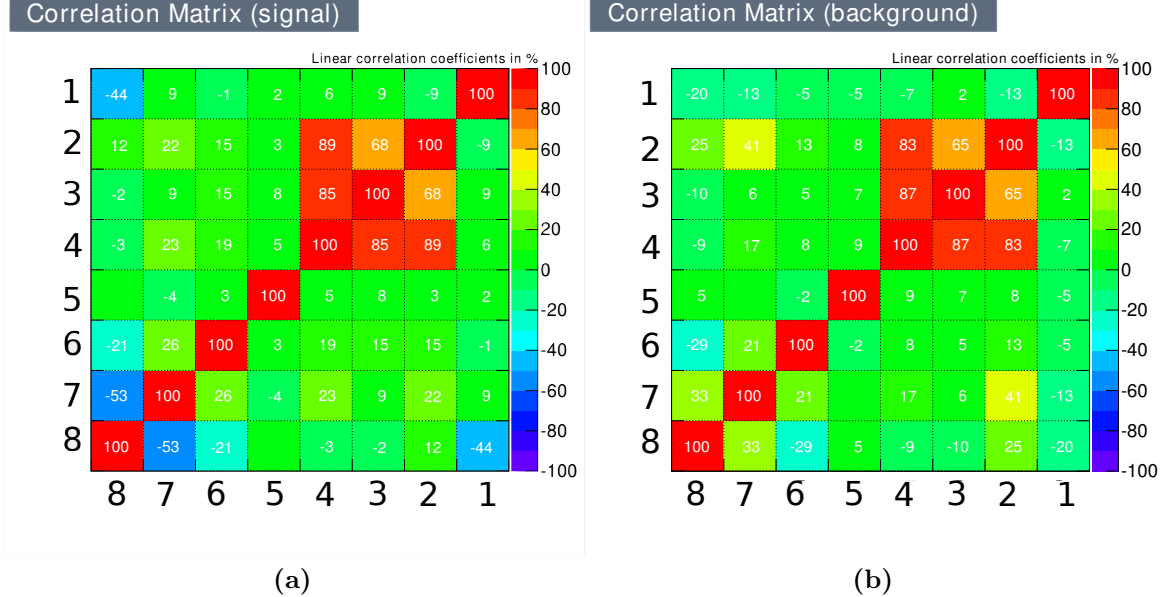


Figure 4.17.: Matrices of correlation coefficients for several variables in signal (a) and V+jets background (b) events passing the signal region selection. The variables are 1) the azimuthal angle difference between the $\vec{E}_T^{\text{no-}\mu}$ and the unclustered energy in the event, 2) the square root of the hadronic energy in the event, 3) \mathcal{S} , 4) $\vec{E}_T^{\text{no-}\mu}$, 5) M_{jj} , 6) the number of jets with $p_T > 30$ GeV between the two tag jets in η , 7) the vectorial sum of the tag jets p_T and the $\vec{E}_T^{\text{no-}\mu}$, 8) the ratio between the magnitude of the vectorial sum of the tag jet's p_T and the $\vec{E}_T^{\text{no-}\mu}$.

After this selection was defined a second MVA based method of optimising the selection was investigated to see if we could improve on the cut based selection. BDT and Fisher discriminants were trained using signal and background events passing the signal region selection [87]. The signal region selection was used as the basis for this training so as to ensure that the number of events from the QCD background in the studied region was small. The optimisation procedure defined above was then repeated with the value of the discriminant considered as an additional variable. One advantage of MVA based selection over simple rectangular cut based selection is that information about the correlation between variables is taken into account. The correlation coefficients between the variables used as inputs to the MVA are shown for signal and V+jets background events in Figure 4.17. These variables were chosen as they showed the most difference between signal and background distributions and correlations out of a wide range of variables investigated. Without the addition of any additional systematic uncertainties associated with the understanding of the variables input to the MVA, the largest improvement in the expected limit was less than 1%. It was therefore decided to use the cut based selection as the final event selection.

4.7. Background estimation

After the full event selection the V+jets backgrounds, as in the prompt analysis, dominate. Also, as in the prompt analysis, contributions are expected from top quark and diboson related processes. Finally, whilst it is reduced significantly by the selection described above, it is also necessary to estimate the expected contribution from the very small number of remaining QCD multijet events.

The methods used to estimate the V+jets backgrounds are based on those used in the prompt analysis. Equation 4.2 is used in several of these methods in this section, and it is repeated here:

$$N_{Exp}^S = (N_{Data}^C - N_{Bkg}^C) \cdot \frac{N_{MC}^S}{N_{MC}^C}. \quad (4.14)$$

The terms on the right hand side of this equation which multiply the estimation from MC of the number of events due to a particular background process are often collectively referred to as the **data driven** scale factor. The changes in event selection for this analysis necessitated several changes from the methods for the prompt analysis. The use of this **data driven** method to investigate the top quark related background was also investigated. Furthermore, among other improvements, the systematic uncertainty on the $Z \rightarrow \nu\nu$ background was re-evaluated. All of these changes and improvements are described in this section.

4.7.1. Top quarks

Almost all top quarks decay to a W boson and a b quark. Top quarks are either created in pairs, or via “single top” production where only one top quark is created in association with other quarks or a W boson. Top pair production results in two W bosons and two b quarks. Single top production results in some combination of W bosons and quarks. Either single or pair production of top quarks can result in the appearance of \cancel{E}_T and jets with no leptons, if at least one of the W bosons decays leptonically and the lepton is misreconstructed. The resulting jets can coincidentally have VBF-like topology. Whilst the contribution from these processes is expected to be small in the signal region, making up around 1% of events there, the presence of W bosons and jets makes these processes very likely to contribute to the control regions used to estimate the W+jets background contribution. In the $W \rightarrow \tau\nu$ control region approximately 15% of events are estimated

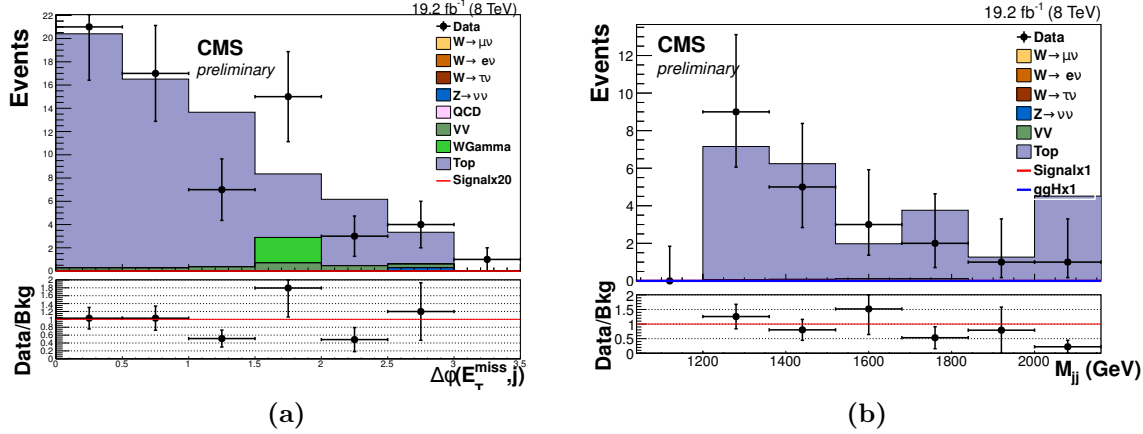


Figure 4.18.: The distribution of $\min\Delta\phi(j, \cancel{E}_T^{\text{no-}\mu})$ (a) and M_{jj} (b) in the top control region with one tight electron and one tight muon. The last bin of each distribution contains the events above the range displayed.

to come from top quark processes. **Data driven** methods for estimating the top quark background and its uncertainties were therefore investigated.

Initially, a dilepton control region was investigated. This had the same cuts on the jet and \cancel{E}_T related variables as the signal region, but the lepton veto was replaced with a requirement that there is exactly one tight electron and one tight muon. This final state would be expected in the case of top quark pair production or single top production with a W boson, where both the resulting W bosons decay leptonically to different flavour leptons. This region had only single figure numbers of events expected, so the cut on $\min\Delta\phi(j, \cancel{E}_T^{\text{no-}\mu})$ was loosened to 0. It can be seen from Figure 4.18 that the ratio between data and MC in this region does not depend significantly on $\min\Delta\phi(j, \cancel{E}_T^{\text{no-}\mu})$. The **data driven** scale factor obtained from this dilepton region was, within the statistics available, consistent with 1 and a good agreement between data and MC was seen in all variables studied. A modification of this control region where events with either two tight electrons or two tight muons, and no other leptons were selected was also studied. This final state would also be expected where two W bosons from top quark production decayed leptonically, except this time to the same flavour of lepton. In order to avoid Z boson contributions the leptons' invariant mass was required to be incompatible with that of a Z boson, i.e. outside of the range from 60 to 120 GeV. This control region also yielded good data-MC agreement and a scale factor compatible with 1.

An issue with both of these control regions is that the ratio of pair production to single top quark production is very different from both the signal region and the $W \rightarrow \tau\nu$ control region. MC estimations indicate that these top control regions have a negligible

single top contribution, while the top background in the signal region has almost no top quark pair contribution. The $W \rightarrow \tau\nu$ region is expected to be a mixture, its top quark background being 30% from single top events and 70% for top quark pairs, again estimated from MC. A single top control region was therefore also investigated.

The single top region differed from the signal region in that the $\min\Delta\phi(j, \cancel{E}_T^{\text{no-}\mu})$ cut was removed, exactly one tight electron or muon was required, further leptons were vetoed and one of the tag jets was required to be compatible with being a b-jet. The restriction to a single lepton significantly reduces the top quark pair production contribution where both resulting W bosons decay leptonically, and the requirement of one b-jet reduces the W+jets contribution.

Identification of the b-jet was done using the combined secondary vertex (CSV) discriminant [103]. B quarks are both heavier and longer lived than many other particles created at the LHC, meaning that their secondary decay vertex can be distinguished from the PV. CSV is an MVA based discriminant which uses information on secondary vertices and the lifetime of the particle to discriminate between jets from b quarks and those from light quarks. The medium working point used for this control region has an efficiency of approximately 85% for b-quarks and mis-identifies light quark jets as b jets approximately 1% of the time.

MC estimates indicate the single top region is 17% single top. This region again showed good data-MC agreement (as can be seen in Figure 4.19) and a scale factor compatible with 1 within uncertainties. Because good agreement between data and MC and scale factors compatible with 1 are seen in all investigated control regions, it was decided to use the MC prediction for the top background in all regions with no additional scale factor. A 20% systematic uncertainty was applied to this prediction which covered the largest deviation from 1 seen in the scale factors from the various control regions.

4.7.2. $W \rightarrow e\nu + \text{jets}$

The $W \rightarrow e\nu$ background in the parked data analysis is estimated using the same method as that used for the prompt analysis ~~based on~~ Equation 4.14. The control region used has the same requirements as the signal region, except that the electron veto is replaced with a requirement that there is one tight electron and no other electrons present in the event. The requirement of an electron removes signal events and enriches the region in $W \rightarrow e\nu$ events. The distributions of several variables in data and MC (which has been

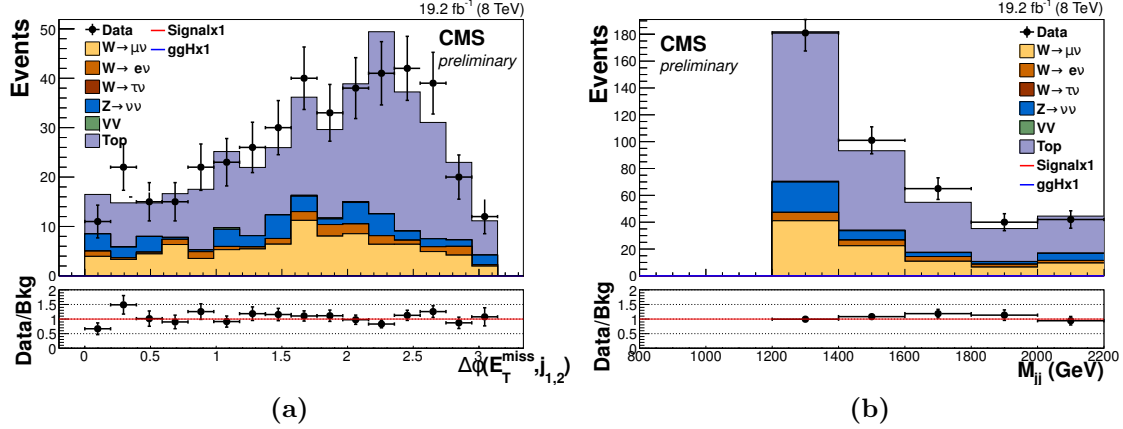


Figure 4.19.: The distribution of $\min\Delta\phi(j_{1/2}, \cancel{E}_T^{\text{no-}\mu})$ (a) and M_{jj} (b) in the single top control region. The last bin of each distribution contains the events above the range displayed.

Table 4.10.: The inputs to, and results of, Equation 4.14, when used to estimate the $W \rightarrow e\nu$ estimate in the signal region.

	Signal region	Control region
N_{Data}	N/A	68 ± 8.2 (stat)
N_{Bkg}	N/A	3.5 ± 1.2 (MC stat)
N_{MC}	114.9 ± 8.9 (MC stat)	128.0 ± 8.0 (MC stat)
$\frac{N_{Data} - N_{Bkg}}{N_C^{WMC}}$	0.50 ± 0.06 (stat) ± 0.03 (MC stat)	
$N_{W \rightarrow e\nu}$	57.9 ± 7.4 (stat) ± 7.7 (syst)	N/A

scaled by the **data driven** scale factor extracted from this control region) are shown in Figure 4.20, where good agreement can be seen. A table of the inputs to, and results of, Equation 4.14 can be seen in Table 4.10. The table also shows that the expected contribution to this region from other background processes is small, being approximately 5%. The scale factor obtained for this background is 0.5, which is significantly different from 1, this difference is further investigated in Section 4.7.8.

4.7.3. $W \rightarrow \mu\nu + \text{jets}$

As for the $W \rightarrow e\nu$ background the $W \rightarrow \mu\nu$ background is estimated using Equation 4.14 with a control region enriched in $W \rightarrow \mu\nu$ events through a change in lepton requirements. The control region used has the same requirements as the signal region, but with the

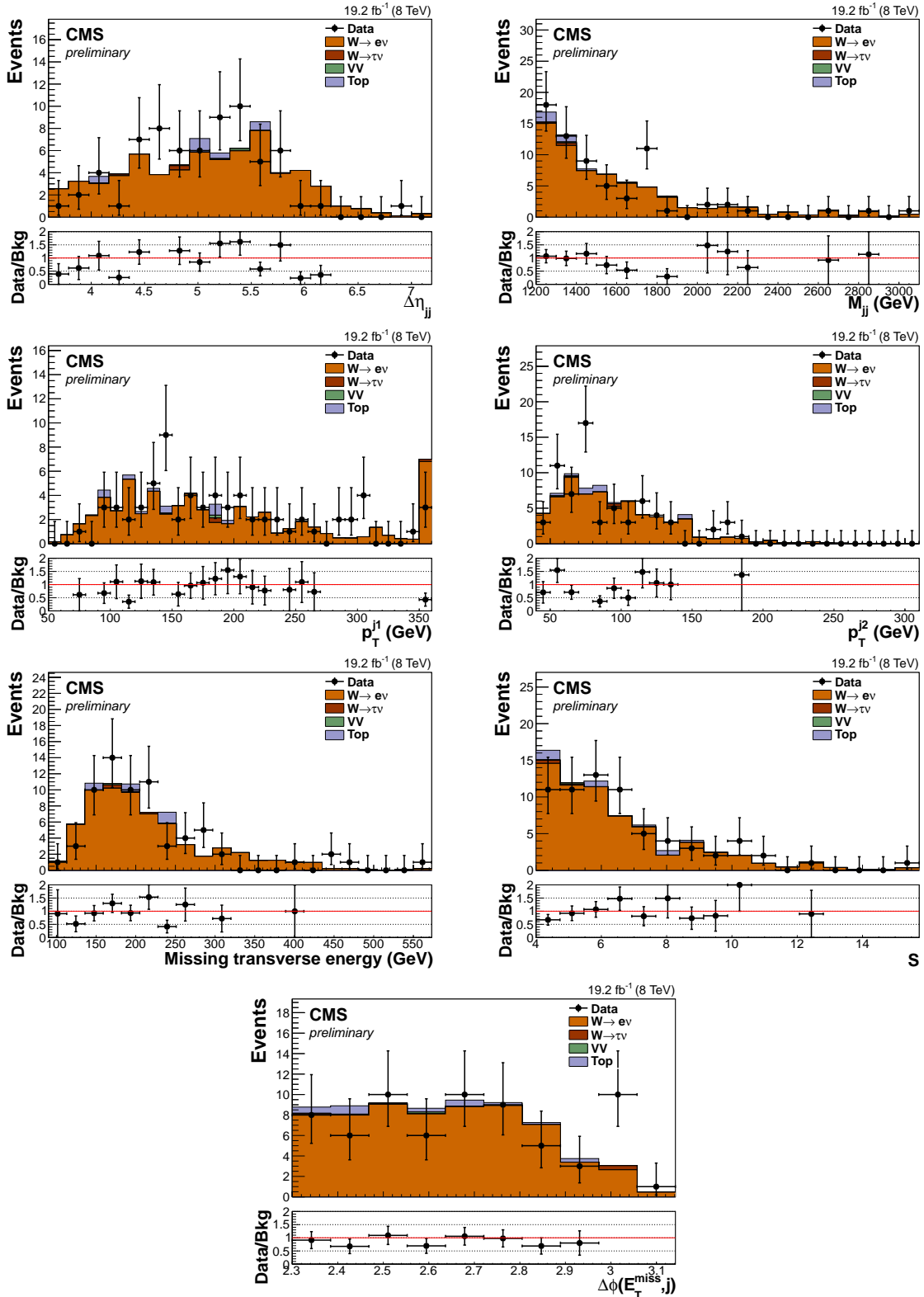


Figure 4.20.: Distributions of variables in data and MC events in the $W \rightarrow e\nu$ control region. MC events from V+jets backgrounds are scaled by their data-driven scale factors. The variables shown are from top to bottom and left to right $\Delta\eta_{jj}$, M_{jj} , the leading and sub-leading jet's p_T , E_T^{miss} , S and $\min\Delta\phi(j, E_T^{\text{miss}})$. The last bin of each distribution contains the events above the range displayed [2].

muon veto replaced with a requirement that there is one tight muon and no other muons present in the event. The distributions of several variables in data and MC (which has been scaled by the **data driven** scale factor extracted from this control region) are shown in Figure 4.21, where good agreement can be seen. A table of the inputs to, and results of, Equation 4.14 can be seen in Table 4.11. The contribution from other backgrounds in the $W \rightarrow \mu\nu$ control region is approximately 5%. Again the scale factor obtained for this background is significantly different from 1, being 0.71, and further investigation of this is detailed in Section 4.7.8. Furthermore, the estimated contribution from this background is very different to that expected from $W \rightarrow e\nu$, an investigation of this difference is described in Section 4.7.5.

Table 4.11.: The inputs to, and results of, Equation 4.14, when used to estimate the $W \rightarrow \mu\nu$ estimate in the signal region.

	Signal region	Control region
N_{Data}	N/A	300 ± 17.3 (stat)
N_{Bkg}	N/A	14.8 ± 2.5 (MC stat)
N_{MC}	143.7 ± 10.2 (MC stat)	399.9 ± 14.9 (MC stat)
$\frac{N_{Data} - N_{Bkg}}{N_C^{MC}}$	0.71 ± 0.04 (stat) ± 0.03 (MC stat)	
$N_{W \rightarrow \mu\nu}$	102.5 ± 6.2 (stat) ± 11.7 (syst)	N/A

4.7.4. $W \rightarrow \tau\nu + \text{jets}$

The signal region requirements do not include a veto of hadronic taus, due to the low identification efficiency and relatively high probability for a jet to be identified as a fake tau. Requiring that there is an identified hadronic tau in addition to the signal region selection results in **a region containing** only 2 data events. In order to increase the number of events in the tau control region the $\min\Delta\phi(j, \cancel{E}_T^{\text{no-}\mu})$ cut was removed. The requirement that there is an identified tau reduces the QCD multijet contribution in the low $\min\Delta\phi(j, \cancel{E}_T^{\text{no-}\mu})$ region significantly compared to what was seen during the choice of the preselection. However, poor data-MC agreement was still observed in the $\min\Delta\phi(j, \cancel{E}_T^{\text{no-}\mu}) < 1$ region, which is evidence that some events from multijet processes are still present. To remove these QCD multijet events, whilst keeping a reasonable number of events in the resulting control region, a requirement that $\min\Delta\phi(j_{1/2}, \cancel{E}_T^{\text{no-}\mu})$ is greater than 1 and that the transverse mass of the hadronic tau and \cancel{E}_T system is

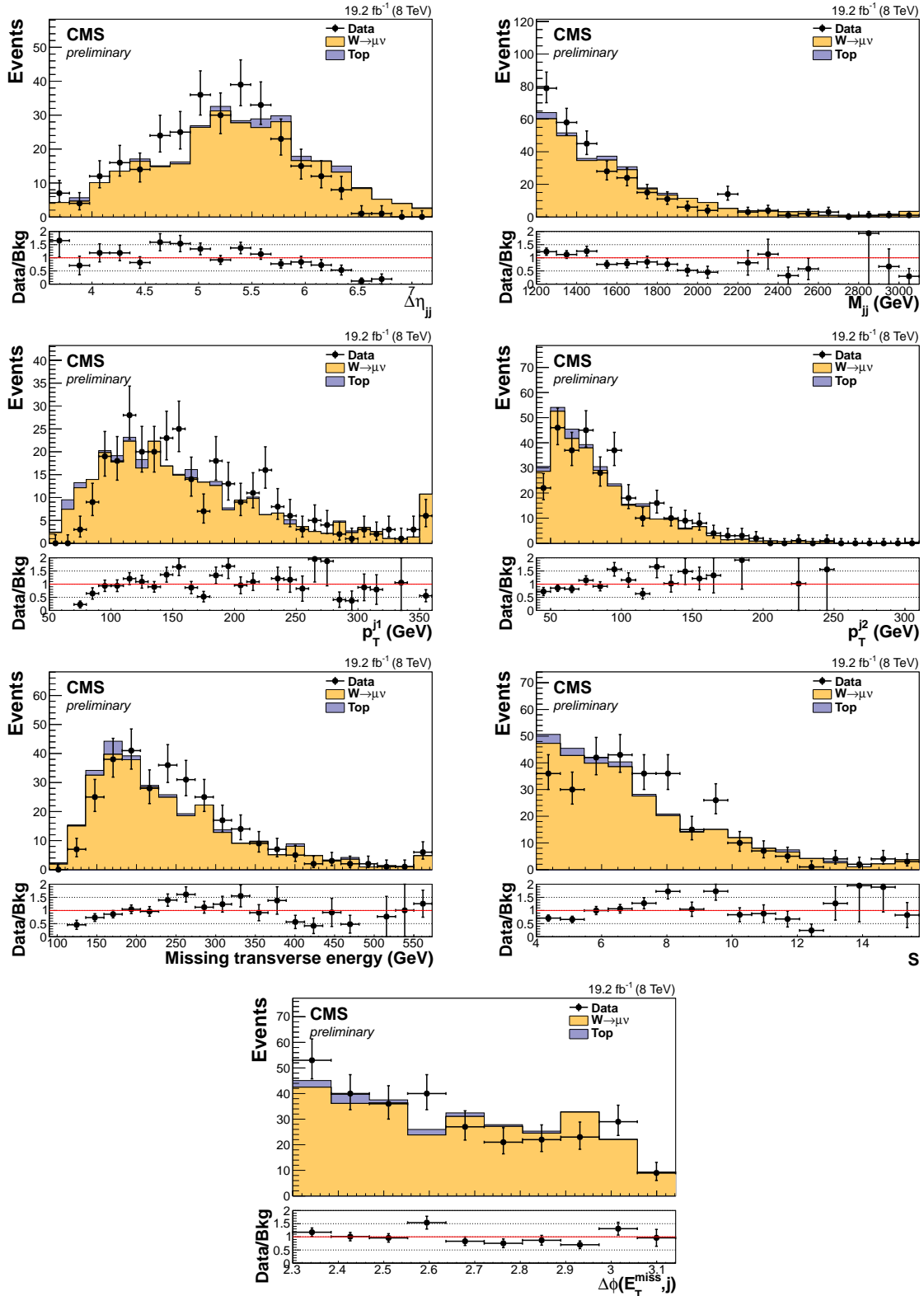


Figure 4.21.: Distributions of variables in data and MC events in the $W \rightarrow \mu\nu$ control region. MC events from V+jets backgrounds are scaled by their data-driven scale factors. The variables shown are from top to bottom and left to right $\Delta\eta_{jj}$, M_{jj} , the leading and sub-leading jet's p_T , E_T^{miss} , S and $\min\Delta\phi(j, E_T^{\text{miss},j})$. The last bin of each distribution contains the events above the range displayed [2].

greater than 20 GeV is applied. The $\min\Delta\phi(j_{1/2}, \cancel{E}_T^{\text{no-}\mu})$ requirement reduces QCD backgrounds for the same reason that $\min\Delta\phi(j, \cancel{E}_T^{\text{no-}\mu})$ does, but it is a slightly looser requirement as it only considers the two leading jets. The transverse mass of the tau- \cancel{E}_T system is a good variable to reject QCD where a lepton is present as in real W boson events the tau and \cancel{E}_T are expected to originate from the same object and therefore have significant invariant mass, which is not the case for QCD multijet events.

After the anti-QCD cuts the agreement between data and MC is good as can be seen in Figure 4.22. To account for the different $\min\Delta\phi(j, \cancel{E}_T^{\text{no-}\mu})$ selection in this region and the signal region, the **data driven** scale factor was calculated both in the $W \rightarrow \mu\nu$ control region, which has the signal region $\min\Delta\phi(j, \cancel{E}_T^{\text{no-}\mu})$ selection, and in a modified single muon control region with the $W \rightarrow \tau\nu$ control region $\min\Delta\phi(j, \cancel{E}_T^{\text{no-}\mu})$ selection. The difference between these two scale factors was found to be 20%, so a 20% systematic uncertainty was added to the estimate of the $W \rightarrow \tau\nu$ background.

The single tau control region with a $\min\Delta\phi(j_{1/2}, \cancel{E}_T^{\text{no-}\mu})$ cut and no $\min\Delta\phi(j, \cancel{E}_T^{\text{no-}\mu})$ cut was used with Equation 4.14 to estimate the number of $W \rightarrow \tau\nu$ events in the signal region. A table of the inputs to, and results of, Equation 4.14 can be seen in Table 4.12. The contribution from other backgrounds in the $W \rightarrow \tau\nu$ control region is approximately 15%, with most of these other background events being due to top quark related processes. The scale factor obtained for this background is 0.78, which is closer to 1 than those seen in the other W+jets backgrounds, however it also has the largest uncertainty. Further investigation of the V+jets scale factors is detailed in Section 4.7.8.

Table 4.12.: The inputs to, and results of, Equation 4.14, when used to estimate the $W \rightarrow \tau\nu$ estimate in the signal region.

	Signal region	Control region
N_{Data}	N/A	76 ± 8.7 (stat)
N_{Bkg}	N/A	13.3 ± 2.8 (MC stat)
N_{MC}	121.9 ± 8.7 (MC stat)	80.8 ± 6.4 (MC stat)
$\frac{N_{Data} - N_{Bkg}}{N_C^{MC}}$	0.78 ± 0.11 (stat) ± 0.07 (MC stat)	
$N_{W \rightarrow \mu\nu}$	94.6 ± 13.1 (stat) ± 23.8 (syst)	N/A

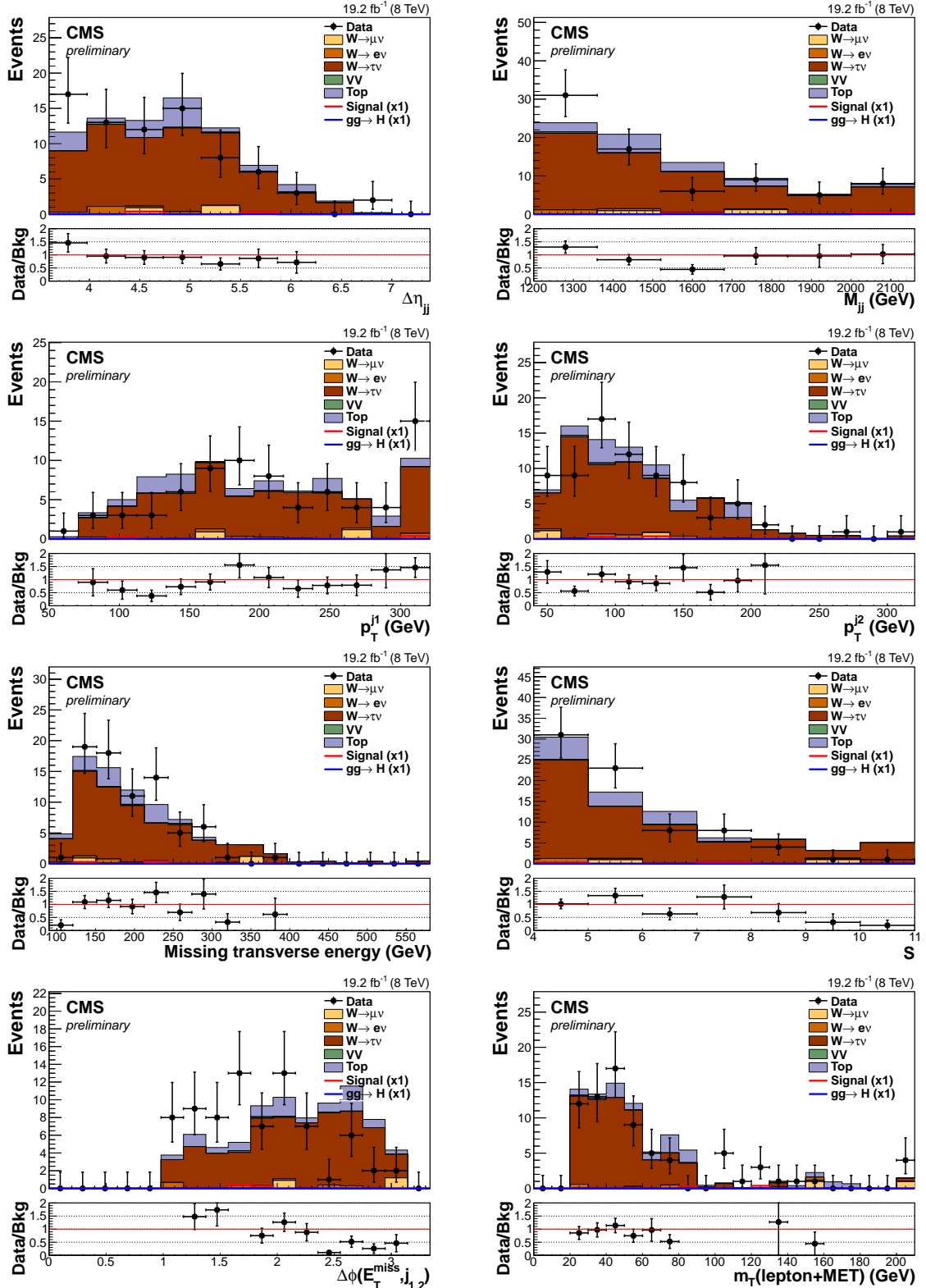


Figure 4.22.: Distributions of variables in data and MC events in the $W \rightarrow e\nu$ control region. MC events from $V+jets$ backgrounds are scaled by their data-driven scale factors. The variables shown are from top to bottom and left to right $\Delta\eta_{jj}$, M_{jj} , the leading and sub-leading jet's p_T , $E_T^{\text{no-}\mu}$, S , $\min\Delta\phi(j_{1/2}, E_T^{\text{no-}\mu})$ and the tau- E_T system's transverse mass. The last bin of each distribution contains the events above the range displayed [2].

4.7.5. Differences between the $W \rightarrow e\nu$, $W \rightarrow \mu\nu$ and $W \rightarrow \tau\nu + \text{jets}$ backgrounds

The number of $W + \text{jets}$ events decaying to a particular flavour of lepton with VBF-like jet kinematics should be the same for all three flavours of lepton through lepton universality. Differences between the numbers of background events from $W \rightarrow e\nu$, $W \rightarrow \mu\nu$ and $W \rightarrow \tau\nu$ must therefore be due to differences in the identification of the leptons. Hadronic taus have much lower identification efficiencies than the other two flavours of leptons, so might naively be expected to give rise to a much larger number of background events. However, due to the similarities between hadronic taus and jets, unidentified taus often lead to additional jets in the event and therefore increase the probability that an event will fail the $\min\Delta\phi(j, \cancel{E}_T^{\text{no-}\mu})$ cut [91]. These two competing effects mean that the number of background events from $W \rightarrow \tau\nu$ passing the signal region selection is not necessarily expected to be the same as that from $W \rightarrow e\nu$ and $W \rightarrow \mu\nu$.

By contrast, electrons and muons have much more similar identification efficiencies (see Sections 3.4 and 3.5). The 45% difference seen in the number of expected background events from these two processes was therefore unexpected. This difference was also not seen in the prompt analysis, as can be seen from Table 4.8. The prediction of the $W \rightarrow e/\mu\nu$ backgrounds is made up of a **data driven** scale factor and an estimate from MC of the number of events from the process expected in the signal region, N_{MC}^S . Both these elements were studied to try to understand the observed differences.

Firstly, the **data driven** scale factors for the electron and muon backgrounds differ by 30%, which is not sufficient to explain the full difference between the electron and muon background estimates. Furthermore, when systematic errors are taken into account this difference is only approximately one standard deviation. On the other hand, N_{MC}^S does show a significant difference.

To study the difference in N_{MC}^S two sub-regions of the signal region were studied, that with a generator level lepton inside the detector acceptance for both electrons and muons ($|\eta| < 2.1$), and that with a generator lepton outside the detector acceptance for both electrons and muons ($|\eta| > 2.4$). The number of events in these two sub-regions from both $W \rightarrow e\nu$ and $W \rightarrow \mu\nu$ MC can be seen in Table 4.13. The numbers of events with a generator level lepton inside acceptance are approximately one standard deviation higher for electrons. This small difference is expected due to the lower identification efficiency for veto leptons making them less likely to cause an event to fail the lepton

Table 4.13.: The numbers of events predicted by MC in the two sub-regions of the signal region with a generator level lepton that is inside/outside the detector acceptance for both electrons and muons from $W \rightarrow e\nu$ and $W \rightarrow \mu\nu$ processes. The errors shown are the MC statistical uncertainties.

Process	Inside acceptance	Outside acceptance
$W \rightarrow e\nu$	73.7 ± 6.8	30.2 ± 4.9
$W \rightarrow \mu\nu$	61.5 ± 6.8	74.4 ± 7.3

veto. Distributions of several variables were also studied for events inside the acceptance and found to be very similar for both $W \rightarrow e\nu$ and $W \rightarrow \mu\nu$ events.

Outside the acceptance there are a lot more muon events than electron events. In this region neither flavour of lepton can be reconstructed and therefore cannot lead to an event failing the lepton veto, which implies that any difference is due to one or both flavours of lepton being reconstructed as a different object and affecting the jet or \cancel{E}_T related variables in the signal region selection. To study this effect further, the $\min\Delta\phi(j, \cancel{E}_T^{\text{no-}\mu})$ requirement was relaxed to 1 and the distributions of several variables plotted for electron and muon events outside the acceptance. Three of these distributions are shown in Figure 4.23. It can be seen from Figure 4.23a that electron events generally have more jets than muon events. Figure 4.23b indicates that the electron events also have much lower values of $\min\Delta\phi(j, \cancel{E}_T^{\text{no-}\mu})$. Finally, Figure 4.23c shows that there are very few events passing this region’s selection requirements which have a generator level electron with $p_T > 30$ GeV, the threshold for jets to be included in the $\min\Delta\phi(j, \cancel{E}_T^{\text{no-}\mu})$ cut. These three pieces of information suggest that electrons are being reconstructed as jets when outside acceptance significantly more often than muons are. These misreconstructed jets then cause the electron events to fail the $\min\Delta\phi(j, \cancel{E}_T^{\text{no-}\mu})$ requirement.

It is to be expected that electrons outside of the detector acceptance will be reconstructed as jets, as these electrons will only be seen as deposits in the forward HCAL and therefore be indistinguishable from jets. By contrast, muons deposit very little energy in the calorimeter systems, so will simply not be identified if they are outside the acceptance of the muon system. In the prompt analysis, no requirements were made on jets which were further forward in η than the tag jets, explaining why the difference in the numbers of $W \rightarrow e\nu$ and $W \rightarrow \mu\nu$ events was not seen there.

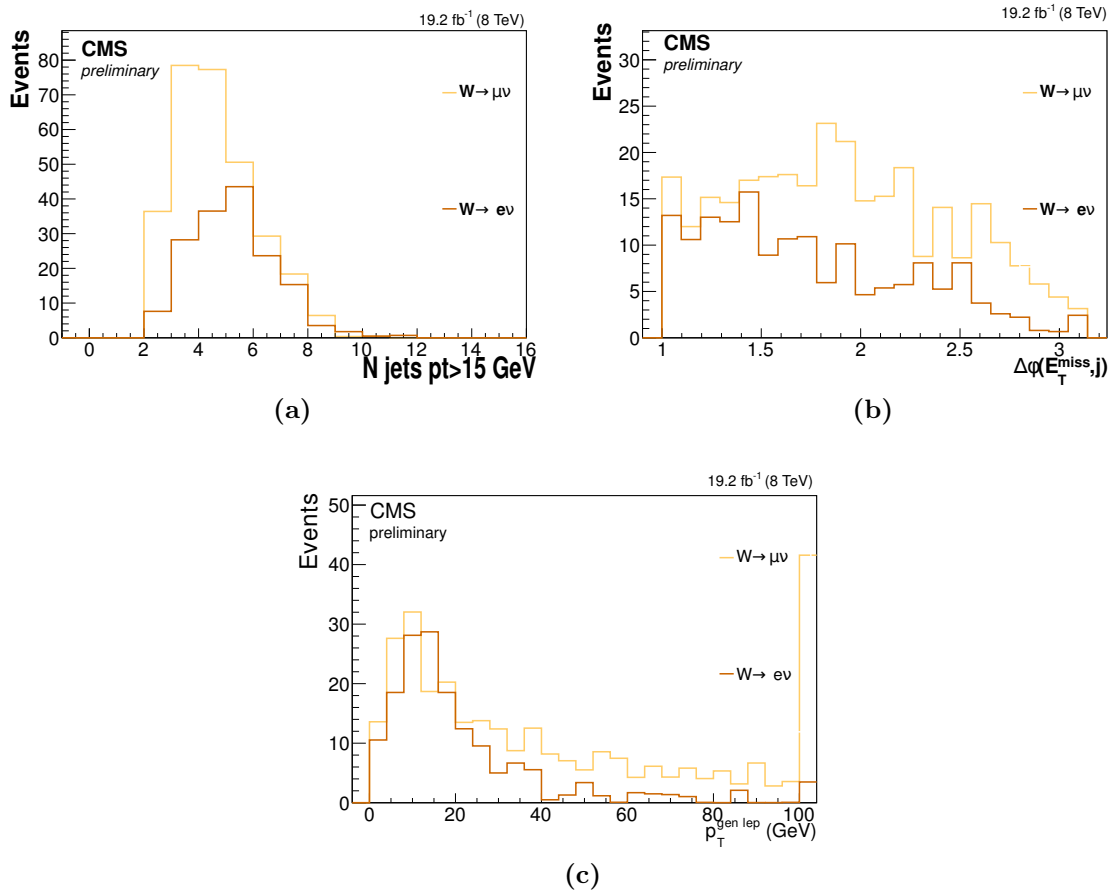


Figure 4.23.: Distributions of the number of jets with $p_{\text{T}} > 15 \text{ GeV}$ (a), $\min\Delta\phi(j, E_{\text{T}}^{\text{no-}\mu})$ (b) and the p_{T} of the leading generator level electron/muon (c) in $W \rightarrow e/\mu\nu$ events in a region with cuts which are the same as those of the signal region except that the $\min\Delta\phi(j, E_{\text{T}}^{\text{no-}\mu})$ requirement has been loosened to 1 and a generator level lepton outside the detector acceptance for both electrons and muons is required. The last bin of each distribution contains the events above the range displayed.

4.7.6. $Z \rightarrow \nu\nu + \text{jets}$

The irreducible $Z \rightarrow \nu\nu$ background is estimated using a very similar method to that used in the prompt analysis (Section 4.2.4). A reminder of the method highlighting the differences from the prompt analysis is given here.

The method starts by defining a dimuon control region by taking the signal region requirements and replacing the muon veto with the requirement that there are two tight muons with invariant mass compatible with a Z boson, i.e. between 60 and 120 GeV, and no other muons in the event. The number of events in this dimuon control region is then extrapolated to the signal region using efficiencies and cross-section ratios calculated using MC events. As in the prompt analysis a $Z/\gamma^* \rightarrow \mu\mu$ MC sample with the reconstructed leptons ignored and a requirement that there is a generator level dimuon system with invariant mass between 80 and 100 GeV (i.e. compatible with a Z boson) is used to estimate the contribution in the signal region from $Z \rightarrow \nu\nu$ processes. The mass window used here is tighter than that used to define the dimuon control region because the generator level lepton p_T resolution is better than that of reconstructed leptons. $Z \rightarrow \nu\nu$ MC events are not used for this estimation due to the limited size of the available $Z \rightarrow \nu\nu$ MC samples. Whilst the number of events in the dimuon control region is small the agreement between data and MC is good as can be seen from Figure 4.24.

The formulae used to carry out the extrapolation from the control region to the signal region are given in Equation 4.3 which is repeated here for reference:

$$N_{Exp}^S = (N_{Data}^C - N_{Bkg}^C) \cdot \frac{\sigma(Z \rightarrow \nu\nu)}{\sigma(Z/\gamma^* \rightarrow \mu\mu)} \cdot \frac{\epsilon_{VBF}^S}{\epsilon_{VBF}^C}, \quad (4.15)$$

where ϵ^S and ϵ^C are calculated as in Equations 4.4 and 4.5 repeated here:

$$\epsilon_{VBF}^S = \frac{\sigma(Z \rightarrow \nu\nu, EWK) \frac{N_{MC}^S(EWK)}{N_{gen}(Z\text{mass},EWK)} + \sigma(Z \rightarrow \nu\nu, QCD) \frac{N_{MC}^S(QCD)}{N_{gen}(Z\text{mass},QCD)}}{\sigma(Z \rightarrow \nu\nu, EWK) + \sigma(Z \rightarrow \nu\nu, QCD)}, \quad (4.16)$$

$$\epsilon_{VBF}^C = \frac{\sigma(Z/\gamma^* \rightarrow \mu\mu, EWK) \frac{N_{MC}^C(EWK)}{N_{gen}(EWK)} + \sigma(Z/\gamma^* \rightarrow \mu\mu, QCD) \frac{N_{MC}^C(QCD)}{N_{gen}(QCD)}}{\sigma(Z/\gamma^* \rightarrow \mu\mu, EWK) + \sigma(Z/\gamma^* \rightarrow \mu\mu, QCD)}. \quad (4.17)$$

As the $Z/\gamma^* \rightarrow \mu\mu$ and $Z \rightarrow \nu\nu$ cross-sections are calculated before the analysis selection cuts and do not depend on detector calibration, the same values are used as in the prompt analysis shown in Table 4.4. The other inputs to the above equations and the results of the estimation are shown in Table 4.14.

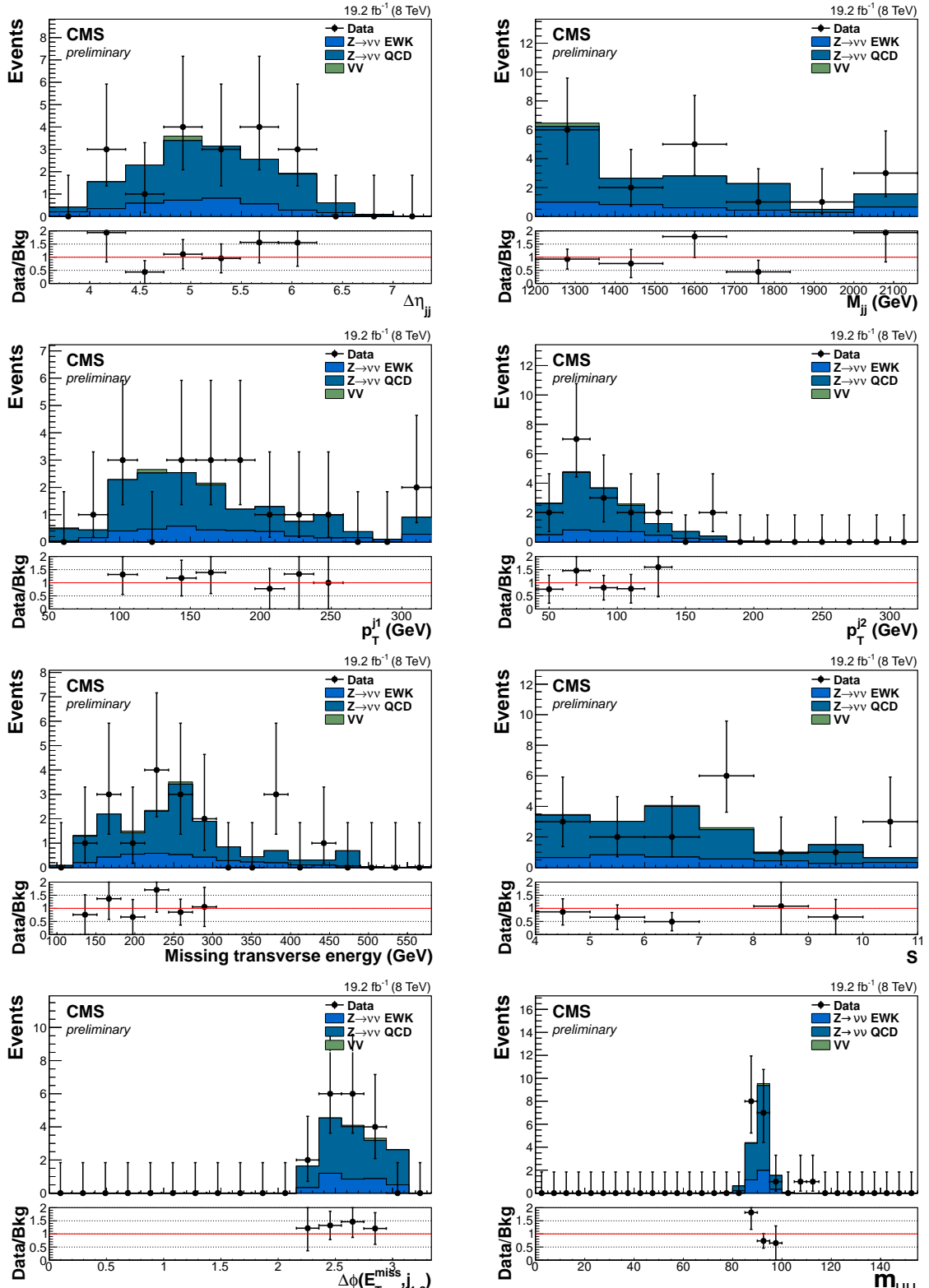


Figure 4.24.: Distributions of variables in data and MC events in the dimuon control region. MC events from V+jets backgrounds are scaled by their data-driven scale factors. The variables shown are from top to bottom and left to right $\Delta\eta_{jj}$, M_{jj} , the leading and sub-leading jet's p_T , $E_T^{\text{no-}\mu}$, S , $\min\Delta\phi(j_{1/2}, E_T^{\text{no-}\mu})$ and the invariant mass of the dimuon system. The contributions to this region from electroweak and QCD produced Z+jets events are shown separately. The last bin of each distribution contains the events above the range displayed [2].

Table 4.14.: The inputs to Equations 4.15, 4.16 and 4.17 and the final estimate of the $Z \rightarrow \nu\nu$ background in the signal region for the parked data analysis. Also shown for comparison is the ratio between the MC prediction of the number of $Z/\gamma^* \rightarrow \mu\mu$ events in the control region and the number of data events in the control region. The systematic uncertainties quoted include MC statistical uncertainties and all sources listed in Section 4.8.

$N_{gen} (EWK)$	5781.9	
$N_{gen} (\text{Zmass}, EWK)$	4226.5	
$N_{gen} (QCD)$	22789000	
$N_{gen} (\text{Zmass}, QCD)$	20334000	
<hr/>		
	Signal region	Control region
N_{Data}	N/A	$18 \pm 4.2 \text{ (stat)}$
N_{Bkg}	N/A	$0.2 \pm 0.1 \text{ (MC stat)}$
$N_{MC} (EWK)$	$7.9 \pm 0.2 \text{ (MC stat)}$	$6.0 \pm 0.2 \text{ (MC stat)}$
$N_{MC} (QCD)$	$29.5 \pm 3.0 \text{ (MC stat)}$	$20.5 \pm 2.5 \text{ (MC stat)}$
$\frac{N_{Data}^C - N_{Bkg}^C}{N_{MC}^C (EWK) + N_{MC}^C (QCD)}$	$0.67 \pm 0.16 \text{ (stat)} \pm 0.06 \text{ (MC stat)}$	
$N_{Z \rightarrow \nu\nu / Z \rightarrow \gamma^* \rightarrow \mu\mu}$	$158.1 \pm 37.8 \text{ (stat)} \pm 21.2 \text{ (syst)}$	$17.8 \pm 4.2 \text{ (stat)} \pm 0.1 \text{ (MC stat)}$

Although it is not used in the $Z \rightarrow \nu\nu$ background estimation method, the ratio between the number of MC dimuon events, both from electroweak and QCD events, and the number of data events minus expected backgrounds from other processes is shown for comparison with the **data driven** scale factors used in the W+jets background estimate. The ratio is, like those in the W+jets background estimation found to be significantly different from 1.

In the prompt analysis one of the largest uncertainties, being 44% of the size of the total systematic uncertainty on the total background estimate, was the uncertainty on the ratio between the $Z/\gamma^* \rightarrow \mu\mu$ and $Z \rightarrow \nu\nu$ cross-sections in the VBF phase space. To reduce this uncertainty in this analysis the cross-section ratio was calculated both with **MADGRAPH** and **AMCNLO_MG5**. The **AMCNLO_MG5** calculation was carried out by generating both $Z/\gamma^* \rightarrow \mu\mu$ and $Z \rightarrow \nu\nu$ events and calculating the ratio of the efficiencies of events in each sample to pass the analysis selection. The selection was applied to generator level objects, with jets being constructed using the algorithm described in Section 3.6 from the generator level quarks and gluons, and the \cancel{E}_T being taken to be the Z boson's p_T . For the **MADGRAPH** calculation, the same

generator level selection was applied to the $Z/\gamma^* \rightarrow \mu\mu$ samples that are used in the background estimation method and the small available $Z \rightarrow \nu\nu$ sample and the same efficiency ratio was calculated. Within statistical errors (4% for MADGRAPH and 15% for AMCNLO_MG5) the ratios from the two generators were found to be compatible. As there was no evidence for a non-statistical discrepancy between the two, the statistical uncertainty from the MADGRAPH calculations was used as the uncertainty on this ratio. As the samples used for the MADGRAPH calculation are the same as those used in the background estimation method this error is already accounted for by the MC statistical uncertainty on the numbers of events in the $Z/\gamma^* \rightarrow \mu\mu$ sample predicted to be in the signal and control regions and no additional error is necessary.

4.7.7. V+jets consistency tests

To check the consistency of the scale factors obtained from the different V+jets background estimation methods, a study was undertaken to use the single muon control region scale factor to predict the data yield in the other control regions. Rather than calculate a single scale factor for the control region, as was done in the background estimation methods, scale factors were calculated for each bin of the distribution of several variables. These scale factors were then applied to the MC estimate in the corresponding bin of the other control regions, allowing the behaviour of the scale factor as a function of the variable to be seen. The resulting estimate was compared to the data yield minus the background expected from other processes from MC.

The scale factor weighted MC was found to agree better with data than the unweighted MC, with the differences seen between the weighted MC and the data being less than systematic uncertainty in the majority of bins, which gives confidence that the **data driven** methods improve the background estimations. The results of these studies in the $E_T^{\text{no-}\mu}$ distribution can be seen in Figure 4.25.

4.7.8. V+jets scale factor investigations

The **data driven** scale factors seen in the V+jets background estimation methods are consistently significantly different from 1. To investigate the reason for this difference the variation of the scale factors as a function of the analysis selection criteria was studied. Due to the high thresholds of the triggers with which the parked data were collected, it was necessary to use a different trigger for this study. The particular trigger chosen was

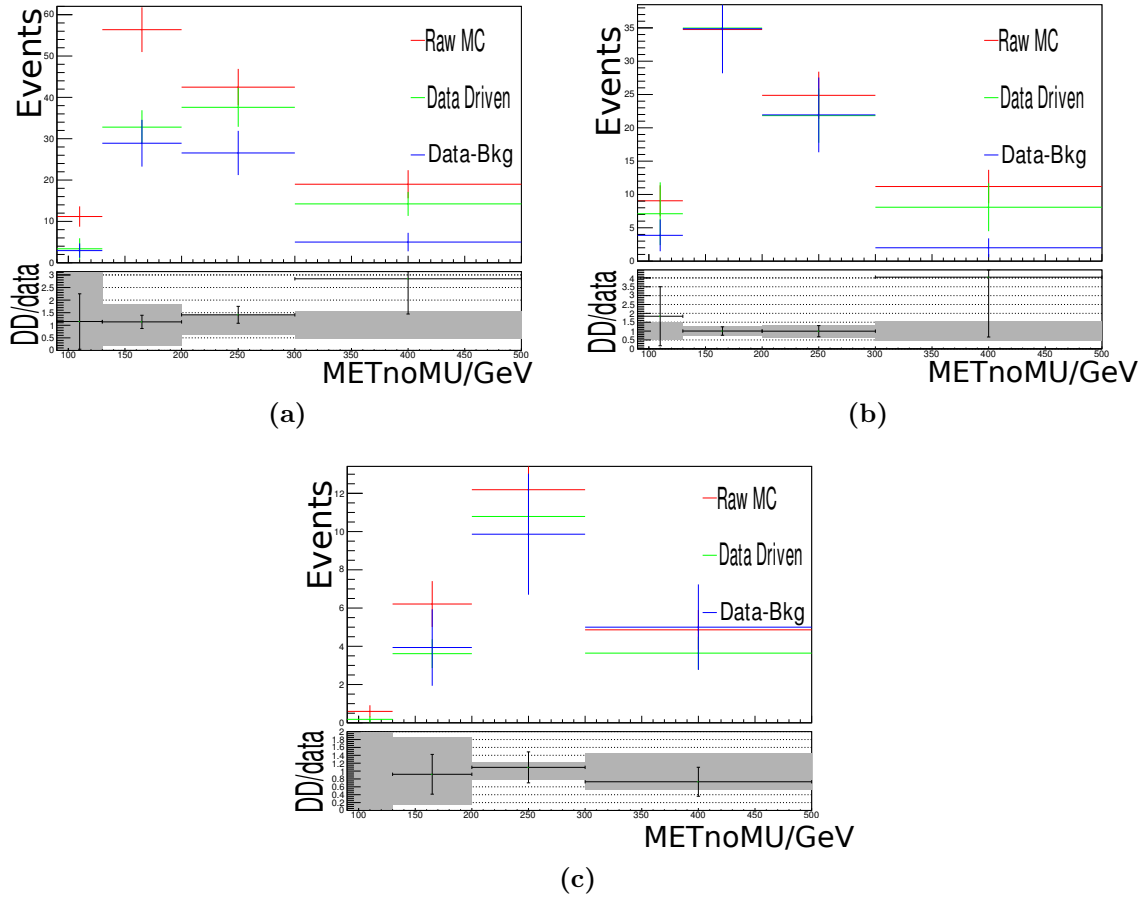


Figure 4.25.: The distribution of $\cancel{E}_T^{\text{no-}\mu}$ expected in the single electron (a), single tau (b) and dimuon control regions (c) from MC (red), data minus other background processes (blue) and MC weighted by the **data driven** scale factor calculated for each bin of the $\cancel{E}_T^{\text{no-}\mu}$ distribution in the single muon control region as described in Section 4.7.7 (green). The lower plot shows the ratio between the **data driven** scale factor weighted MC and the data minus other background processes. The grey band on the lower plots represents the systematic uncertainty from all sources described in Section 4.8.

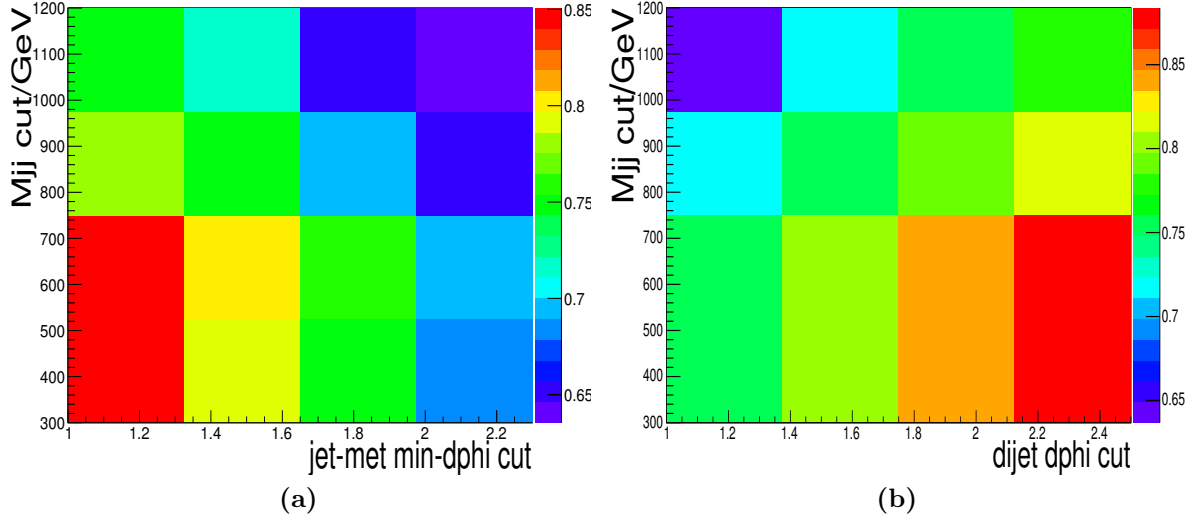


Figure 4.26.: The **data driven** scale factor obtained from a single muon control region, as described in Section 4.7.8, as a function of the cuts on $\min\Delta\phi(j, \cancel{E}_T^{\text{no-}\mu})$ and M_{jj} (a) and $\Delta\phi_{jj}$ and M_{jj} (b). It is important to note that the requirement on $\Delta\phi_{jj}$ is that the event have a value lower than the cut threshold, so the requirement is tighter to the left of the plot. The parked data analysis preselection requirements correspond to the top right bin of (a).

the same single muon trigger used for the trigger efficiency measurements described in Section 4.5. The study was therefore restricted to the single muon control region as it has muons present and contains significantly more events than the dimuon control region. To ensure that the trigger was fully efficient the muon p_T cut was tightened to 25 GeV.

The requirements on the leading and sub-leading jet's p_T , M_{jj} , $\min\Delta\phi(j, \cancel{E}_T^{\text{no-}\mu})$, $\cancel{E}_T^{\text{no-}\mu}$ and \mathcal{S} were then varied to ascertain which requirements caused the largest variations in the scale factor. The $\cancel{E}_T^{\text{no-}\mu}$ and leading jet p_T requirements were found to have no discernible effect on the scale factor. The effects from the sub-leading jet p_T and \mathcal{S} requirements were found to be less than 5%. By contrast, the $\min\Delta\phi(j, \cancel{E}_T^{\text{no-}\mu})$ and M_{jj} requirements were found to significantly alter the scale factor obtained. As can be seen in Figure 4.26a, when these two requirements are loosened the scale factor increases significantly.

To determine whether the scale factor depends more strongly on the jet or $\cancel{E}_T^{\text{no-}\mu}$ azimuthal angle the requirement on $\min\Delta\phi(j, \cancel{E}_T^{\text{no-}\mu})$ was replaced with a requirement on the difference in azimuthal angle between the two tag jets, $\Delta\phi_{jj}$, which doesn't depend on the $\cancel{E}_T^{\text{no-}\mu}$ and the study was repeated. As can be seen in Figure 4.26b, the scale factor was still found to vary in the same range with $\Delta\phi_{jj}$, indicating that the use of the $\cancel{E}_T^{\text{no-}\mu}$

azimuthal angle does not cause a further deviation from 1 than that present already due to jet related effects.

The looser the requirements on the jet kinematics are the closer the scale factor is to 1. It therefore seems that the deviation in the scale factor from 1 is caused by mismodelling of the jet related variables in V+jets MC. The distributions of variables for events in the various control regions shown in Figures 4.20-4.24 show good shape agreement between data and MC, indicating that the shape in these regions is not significantly mismodelled. Also, the data driven methods used to estimate the V+jets background correct for the overall normalisation difference from mismodelling in areas of phase space outside the analysis control and signal regions. For these two reasons this mismodelling is not expected to cause problems for the analysis.

4.7.9. QCD

As mentioned in Section 4.6 events from QCD multijet processes are very difficult to model using MC, as their high production cross-section and low probability to pass the selection cuts makes the number of events which must be generated prohibitively large. In an attempt to circumvent this problem a dedicated sample of QCD multijet events with VBF-like cuts imposed at generator level was produced. Specifically, the \cancel{E}_T was required to be greater than 40 GeV, at least 2 jets with $p_T > 20$ within the detector acceptance had to be present, and at least one pair of those jets was then required to have $M_{jj} > 700$ GeV and $\Delta\eta_{jj} > 3.2$. As can be seen from Figure 4.15 this sample does not adequately describe the events passing the trigger selection.

To investigate where this mismodelling comes from the reconstructed \cancel{E}_T was plotted as a function of the generator level \cancel{E}_T in the QCD multijet MC sample centrally produced by CMS as shown in Figure 4.27. This sample does not have any generator level cuts on the \cancel{E}_T or jet kinematics. Most events fall in the bottom left of this plot, having low \cancel{E}_T at both generator level and offline. These events would therefore not enter the analysis signal region and would also be rejected by the generator level cut as intended. There is then another class of events distributed around the diagonal of the plot due to the \cancel{E}_T resolution, with higher values of both generator level and offline \cancel{E}_T . These on-diagonal events would be expected to be well modelled by the VBF QCD sample as most of them which fall into the analysis signal region, which requires $\cancel{E}_T > 90$ GeV, would be expected to pass the generator level cut. Finally, there is a third type of events, which have low values of generator level \cancel{E}_T , but high values of offline \cancel{E}_T due to

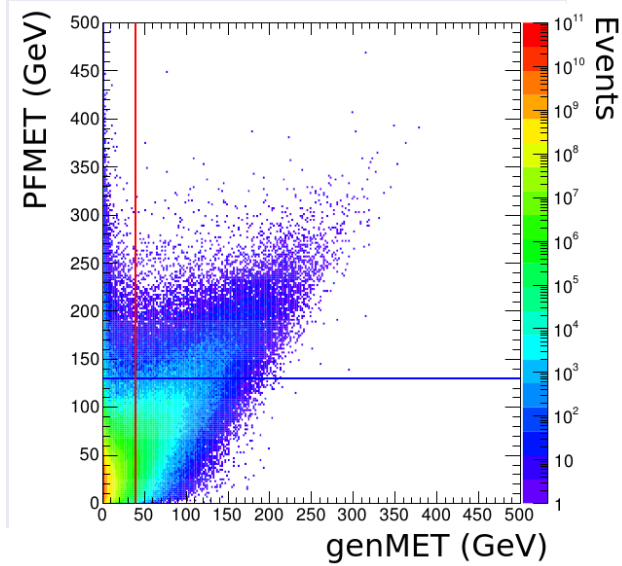


Figure 4.27.: The reconstructed \cancel{E}_T , PFMET, as a function of the generator level \cancel{E}_T , genMET in a MC sample with no generator level cuts on \cancel{E}_T or jet kinematics. For reference, the cut placed on genMET in the dedicated VBF QCD multijet sample is shown in red, and the offline prompt analysis cut on PFMET is shown in blue [104].

mismeasurement. These so-called “fake” \cancel{E}_T events are believed to be the cause of the VBF QCD sample not adequately modelling the QCD background in this analysis, as they will be removed by the generator level cut, but will be present in the analysis signal region.

It can be seen from the location of the gaps between the data and MC predictions in Figure 4.15 that the fake \cancel{E}_T events, like the well modelled on-diagonal events, have at least one jet close in ϕ to the \cancel{E}_T , and have low values of \mathcal{S} . They are therefore expected to be almost entirely removed by the analysis selection. Nevertheless it is important to provide an estimate of the small remaining number of QCD background events of both types. Due to the difficulties with MC estimates outlined above this estimation must be data driven.

The ABCD method used in the prompt analysis cannot be used for this analysis because the regions where only one of the two main anti-QCD cuts is inverted are expected to have non-negligible signal contributions (approximately 10% of the total number of data events assuming a 125 GeV Higgs boson decaying entirely to invisible final states). An alternative method using events with “non-isolated” \cancel{E}_T , i.e. that with a jet close to it in ϕ , is therefore used. This non-isolated method involves three regions: (i) the “inverted” region where the shape of the distributions of key variables for the QCD background

is determined, (ii) the “3-jet” region where this shape is validated, and (iii) a set of “sideband” regions where a normalisation for the QCD shape is extracted. A schematic of these regions is shown in Figure 4.28

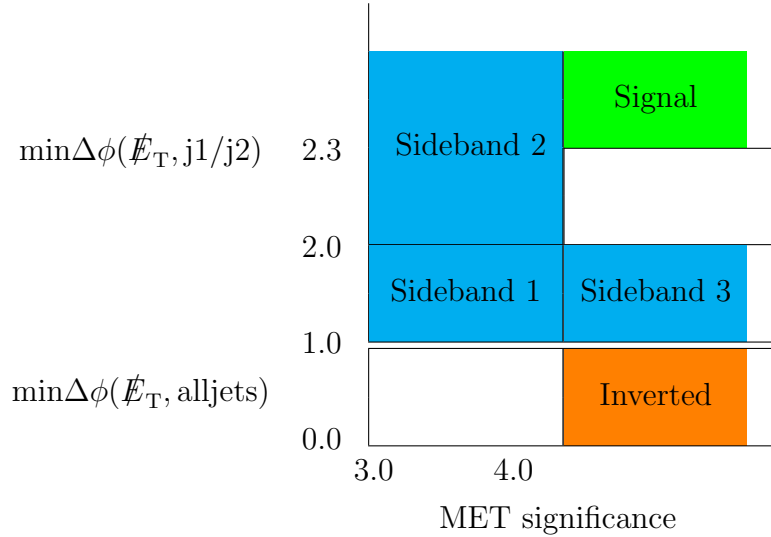


Figure 4.28.: A schematic of the regions used in the QCD background estimation.

The contribution from V+jets backgrounds in these regions is estimated using MC normalised with the **data driven** method described by Equation 4.14. The control regions used for each background in each region are defined by making the same modifications to the region that were made to the signal region to define the V+jets control regions used in Sections 4.7.2-4.7.6.

The inverted region is defined starting from the signal region, by swapping the $\min\Delta\phi(j, \not{E}_T^{\text{no-}\mu}) > 2.3$ requirement for a requirement that only $\min\Delta\phi(j_{1/2}, \not{E}_T^{\text{no-}\mu})$ is greater than 2.3, and then requiring that $\min\Delta\phi(j, \not{E}_T^{\text{no-}\mu})$ is less than 1. The resulting region consists of events with two signal-like jets, well separated from the \not{E}_T , but also an additional jet close to the \not{E}_T making it non-isolated. As can be seen from Figure 4.29a the inverted region is dominated by QCD events with only 20% of the events expected to come from V+jets and other background processes. The QCD shape is taken to be the shape of the data after subtracting the estimated contribution from all other background processes.

To ensure the QCD shape derived from non-isolated \not{E}_T is adequate to describe the QCD background with isolated \not{E}_T in the signal region the 3-jet region is used. This region is defined starting from the signal region by relaxing the $\min\Delta\phi(j, \not{E}_T^{\text{no-}\mu})$ and S requirements from greater than 2.3 to greater than 1 and from greater than 4 to greater than 3 respectively, then requiring that there are at least three jets with $p_T > 30$ GeV in

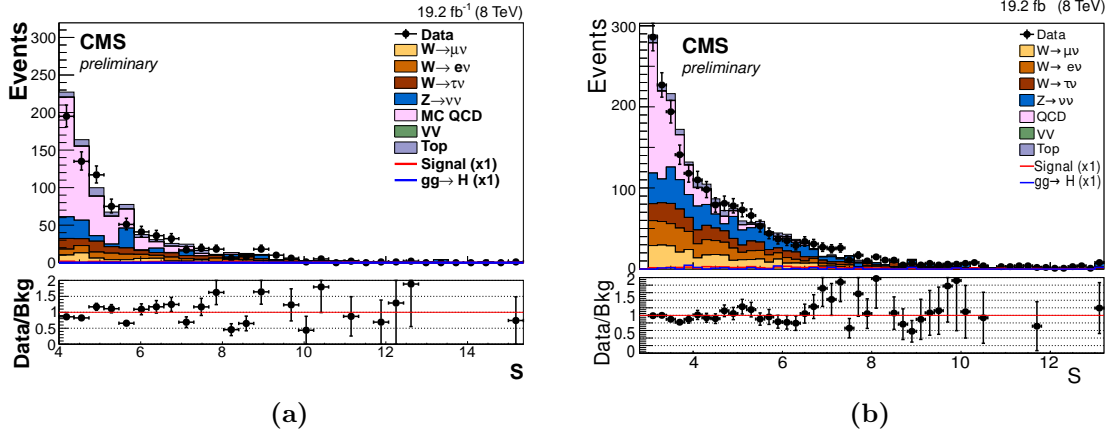


Figure 4.29.: The distribution of \mathcal{S} in the inverted (a) and 3-jet (b) regions used in the QCD background estimation. In (a) the QCD shape is estimated using the VBF QCD sample, and in (b) the QCD shape is taken from the inverted region as described in the text. Both shapes are normalised to the total number of events seen in the region minus the expected contribution from other backgrounds [2].

the event. The QCD shape obtained from the inverted region is then normalised to the data yield minus the expected contribution from other backgrounds in this 3-jet region and plotted as a function of several variables. Good agreement between data and MC is seen and the distribution of \mathcal{S} is shown in Figure 4.29b.

To obtain the QCD normalisation in the signal region several sideband regions were investigated. As has been described above the regions obtained by inverting the requirement on one of the two main anti-QCD discriminant variables, $\min\Delta\phi(j, \cancel{E}_T^{\text{no-}\mu})$ and \mathcal{S} , have non-negligible signal contributions. However by inverting the requirements on both variables a QCD dominated sideband can be obtained. This region is called “sideband 1” and the specific differences from the signal region are that we require $3 < \mathcal{S} < 4$ and $1 < \min\Delta\phi(j_{1/2}, \cancel{E}_T^{\text{no-}\mu}) < 2$.

Whilst the regions obtained from inverting only one of the $\min\Delta\phi(j, \cancel{E}_T^{\text{no-}\mu})$ or \mathcal{S} requirements have signal contributions of approximately 10% for a SM produced 125 GeV Higgs boson with $\mathcal{B}(H \rightarrow \text{inv}) = 100\%$, an invisible branching fraction of 100% has already been ruled out so the actual signal contribution in these regions is expected to be smaller. Therefore, two further sideband regions which are not used in the final estimate, but which are used to validate the method are defined. Sideband 2 is the same as sideband 1, except that we require $\min\Delta\phi(j_{1/2}, \cancel{E}_T^{\text{no-}\mu}) > 2$. Sideband 3 is the same as sideband 1, except that we require $\mathcal{S} > 4$.

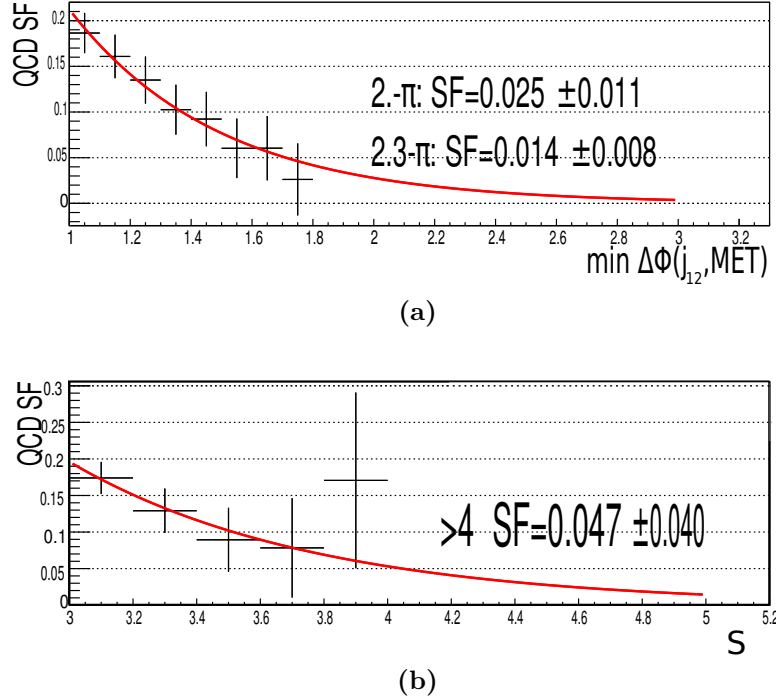


Figure 4.30.: The QCD scale factor obtained in sideband 1 as a function of the lower bound on $\min\Delta\phi(j, \cancel{E}_T^{\text{no-}\mu})$ (a) and S (b). Exponential fits which are used to extrapolate to higher values of these requirements are overlaid on both distributions, and the values of these fits at several representative values are displayed.

Scale factors were then obtained in each of the sideband regions by evaluating the following formula:

$$SF = \frac{N_{Data} - N_{Bkg}}{N_{QCD}}, \quad (4.18)$$

where N_{Data} and N_{Bkg} (N_{QCD}) are (is) evaluated using events passing the cuts of the particular sideband region being studied and also having $\min\Delta\phi(j, \cancel{E}_T^{\text{no-}\mu}) > 1$ ($\min\Delta\phi(j, \cancel{E}_T^{\text{no-}\mu}) < 1$). The scale factor was found to be much lower in sidebands 2 and 3 than in sideband 1. Signal events being present in sideband 2 or 3 would be expected to give larger and not smaller values of the scale factor, so signal contamination is not thought to be a concern. Therefore, the scale factor was studied as a function of the requirements on $\min\Delta\phi(j_{1/2}, \cancel{E}_T^{\text{no-}\mu})$ and S by gradually tightening the requirement on each variable in sideband 1 separately and recalculating the scale factor. The value of the scale factor as a function of the requirement placed on both $\min\Delta\phi(j_{1/2}, \cancel{E}_T^{\text{no-}\mu})$ and S can be seen in Figure 4.30.

The behaviour of the scale factor with each variable is compatible with both an exponential or linear decrease. So as to not underestimate the number of events from QCD an exponential function, which yields slightly larger scale factors than a linear function, was fit to the distributions shown in Figure 4.30. Both these exponentials were then extrapolated to the signal region requirements. The average of these two extrapolations was used as the central prediction of the scale factor, and the envelope of their uncertainties was used to assign a systematic uncertainty. The final value of the scale factor is 0.048 ± 0.040 . The inverted region contains 363 ± 36 events, so the total number of events expected from QCD in the signal region is 17 ± 14 .

It should be noted that the $\min\Delta\phi(j_{1/2}, \cancel{E}_T^{\text{no-}\mu})$ variable is not exactly the same as the $\min\Delta\phi(j, \cancel{E}_T^{\text{no-}\mu})$ used for the signal region selection. This alternate variable was used as cutting on $\min\Delta\phi(j, \cancel{E}_T^{\text{no-}\mu})$ left no QCD events for the higher values of the requirement studied in Figure 4.30a. However, because the $\min\Delta\phi(j, \cancel{E}_T^{\text{no-}\mu})$ variable is more discriminating against QCD than $\min\Delta\phi(j_{1/2}, \cancel{E}_T^{\text{no-}\mu})$ the estimate presented above acts as an upper bound, which is acceptable given the low number of events (< 5% of the total expected background) and its large relative uncertainty. Furthermore, the expected limit for the analysis is found to vary by less than 1% on doubling or halving both the central value of the QCD estimate and its uncertainty.

4.7.10. Minor backgrounds

As in the prompt analysis, due to it being very small, the contribution to the signal and control regions from diboson and $Z/\gamma^* \rightarrow \mu\mu$ background processes was estimated from MC. PYTHIA 6 was used to generate diboson events, while $Z/\gamma^* \rightarrow \mu\mu$ events were generated with MADGRAPH. The MC estimate of the diboson backgrounds was normalised using the most accurate CMS measurement at the time of this analysis [105]. The expected number of events in the signal region from minor background processes is 3.9 ± 0.7 .

4.8. Systematic uncertainties

Most systematic uncertainties are calculated using the same methods as in the prompt analysis (see Section 4.3). The changes to the calculation of systematic errors on the

top, $W \rightarrow \tau\nu$, $Z \rightarrow \nu\nu$ and QCD multijet backgrounds have already been discussed in Sections 4.7.1, 4.7.4, 4.7.6 and 4.7.9 respectively.

Despite the methods used being similar, in several cases the inputs to the methods have been updated to take into account improved measurements of various parameters using the full Run 1 dataset which were not available at the time of the prompt analysis. For example, the impacts of the JES, JER and UES uncertainties are still estimated by recalculating the p_T of all jets and the \cancel{E}_T after varying each parameter up and down by one standard deviation and reperforming the analysis. However, the total uncertainty from these is smaller, being 6% of the total expected background yield for this analysis where it was 7% in the prompt analysis.

In addition to these changes a study was undertaken to estimate the impact of the trigger efficiency measurement uncertainties on the expected limit. As described in Section 4.5, all MC events are reweighted by the measured trigger efficiency as a function of the events sub-leading jet p_T , $\cancel{E}_T^{\text{no-}\mu}$ and M_{jj} . The uncertainty due to the reweighting process cancels in all **data driven** background estimates, as a ratio of MC event yields is taken. To estimate the size of the uncertainty that should be applied to processes not estimated with **data driven** methods, the bin with the largest uncertainties on its fit for each era was chosen. It was then assumed that all bins had this worst-case uncertainty. This assumption resulted in a 2.3% uncertainty on these non-data driven processes. Given that this error is smaller than many of the other errors considered, and that the uncertainty on the efficiency in most of the fit bins is significantly lower than this worst case, this uncertainty was considered negligible.

The fractional uncertainties on the total signal and background estimates from each source of uncertainty considered are shown in Table 4.15 in decreasing order of the size of the uncertainty on the total background yield. It can be seen that the dominant uncertainties are statistical, with these being dominated by the low number of data events in the double muon control region (see Table 4.14).

4.9. Results

The final predicted yields for each background process are shown, along with their uncertainties in Table 4.16. The total predicted event yield from background processes is $439.4 \pm 40.7 \text{ (stat)} \pm 43.5 \text{ (syst)}$. Assuming an SM produced Higgs boson which decays

Table 4.15.: A summary of the uncertainties on the total background and signal yields. All uncertainties affect the normalization of the yield, and are quoted as the change in % in the total background or signal estimate, when each systematic effect is varied according to its uncertainties. The signal uncertainties are given for $m_H = 125$ GeV and $\mathcal{B}(H \rightarrow \text{inv}) = 100\%$.

Source	Total background	Signal
Control region statistics	9.3	-
MC statistics	5.4	3.8
JES	4.6	11
$W \rightarrow \tau\nu$ control region extrapolation	4.3	-
QCD background estimation	3.2	-
JER	3.0	1.8
Lepton ID efficiency	2.4	-
UES	1.9	1.6
Pileup weight	1.1	1.5
Top MC scale factor unc.	0.25	-
Luminosity	0.02	2.6
QCD scale, PDF and cross-section uncertainties	0.01	5.2
Total	13.6	13.3

Table 4.16.: The estimated numbers of background and signal events from each process, together with the observed yield, in the signal region. The signal yield assumes a Higgs boson mass of 125 GeV and $\mathcal{B}(H \rightarrow \text{inv}) = 100\%$. Where two errors are quoted they are the statistical and systematic uncertainties respectively, where only one is quoted it is the systematic uncertainty.

Process	Event yields
$Z \rightarrow \nu\nu$	$158.1 \pm 37.3 \pm 21.2$
$W \rightarrow e\nu$	$57.9 \pm 7.4 \pm 7.7$
$W \rightarrow \mu\nu$	$102.5 \pm 6.2 \pm 11.7$
$W \rightarrow \tau\nu$	$94.6 \pm 13.1 \pm 23.8$
top	5.5 ± 1.8
Minor backgrounds	3.9 ± 0.7
QCD multijet	17 ± 14
Total background	$439.4 \pm 40.7 \pm 43.5$
Signal(VBF)	273.1 ± 31.2
Signal(ggH)	23.1 ± 15.9
Observed data	508

100% of the time to invisible final states, 296.2 ± 39.4 (syst) events from signal processes are expected. 508 events are observed, which is slightly more than one standard deviation above the **background only** prediction. The distributions of the variables in the signal region used in the analysis selection are shown in Figure 4.31. The shapes of these distributions for data and the predicted backgrounds agree well, giving further evidence that the excess of events is not significant.

As no significant excess is observed the upper limits that can be placed on $\sigma \times \mathcal{B}$ at 95% CL are calculated assuming SM Higgs boson acceptances using the asymptotic CL_S technique described in Section 1.4. The resulting observed limits and expected limits with their 68% and 95% confidence intervals are shown in Figure 4.32a. As in the prompt analysis all systematic uncertainties and all the statistical uncertainties on the control regions except the double muon region are modelled as log-normally distributed nuisance parameters. The statistical uncertainty in the double muon control region is again modelled as gamma-normally distributed due to the low number of events in this region. Assuming SM Higgs production the resulting limits can be interpreted as limits on the invisible branching fraction of the Higgs boson, the results of this interpretation are shown in Figure 4.32b. For a Higgs boson with a mass of 125 GeV the resulting

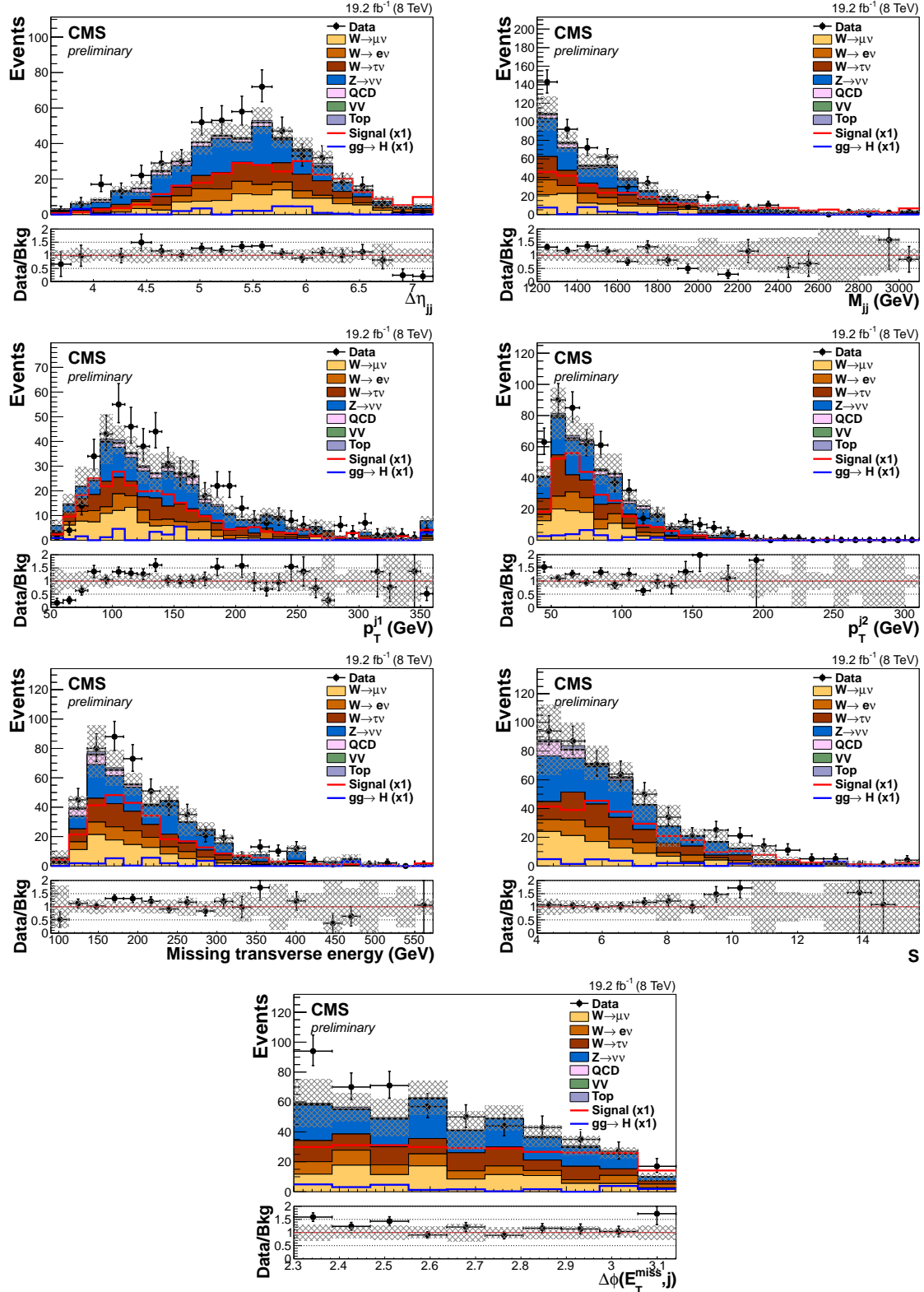


Figure 4.31.: From top to bottom and left to right $\Delta\eta_{jj}$, M_{jj} , the leading and sub-leading jet's p_T , $E_T^{\text{no-}\mu}$, S and $\min\Delta\phi(j, E_T^{\text{no-}\mu})$ in the signal region. The hatched band indicates the size of the total uncertainty on the background estimate [2].

observed (expected) upper limit is $\mathcal{B}(H \rightarrow \text{inv}) = 0.57(0.40)$. Since the analysis has only one bin, and no shape information is used, the measurements for the different Higgs boson masses are 100% correlated, so the fact that all the points show an approximately one sigma excess is not significant evidence of non-SM behaviour.

An interesting feature of the LHC Higgs Combination Group’s interpretation of the CL_S technique is that the expected limit quoted above is dependent on the number of events observed in data in the signal region [53]. This dependence occurs because the values of the nuisance parameters that maximise the likelihood for the observed data are used in Equation 1.39. Therefore, if an excess of events is seen values of the nuisance parameters which lead to a larger expected background yield will be chosen. For this reason the expected limit quoted above is also referred to as the post-fit expected limit. It is also possible to calculate a “pre-fit” expected limit by using the values of the nuisance parameters which maximise the likelihood assuming that the observed number of events is equal to the expected number of background events. The pre-fit expected limit on $\mathcal{B}(H \rightarrow \text{inv})$ is 0.35 at 95% CL for this analysis.

For a 125 GeV Higgs boson the profile likelihood was also calculated as a function of $\mathcal{B}(H \rightarrow \text{inv})$ for both the prompt and parked data analyses as shown in Figure 4.33. It can be seen that the most likely value of $\mathcal{B}(H \rightarrow \text{inv})$ is non-zero, being approximately 0.25 for both analyses. However, as seen above this non-zero value corresponds to only an approximately one standard deviation excess in both cases.

4.9.1. Improvement relative to the prompt data analysis

As an improved limit is seen in this analysis compared to the prompt analysis, it is important to ascertain whether this improvement is due only to the improved analysis selection, or the improved analysis selection and the additional phase space made available by the triggers used to collect the parked data. As discussed above, the additional phase space alone cannot lead to an improved limit as the prompt analysis selection was restricted to the region where the trigger with which the prompt data were collected was fully efficient. To this end both the parked analysis selection (“parked selection”) and the prompt analysis selection (“prompt selection”) were applied to both the prompt data and parked data and new expected limits were calculated under each scenario as shown in Table 4.17. To allow a fair comparison, the prompt analysis was updated to take into account the improved knowledge of the extrapolation uncertainty on the $Z \rightarrow \nu\nu$ background and resulting reduced systematic uncertainty (see Section 4.7.6).

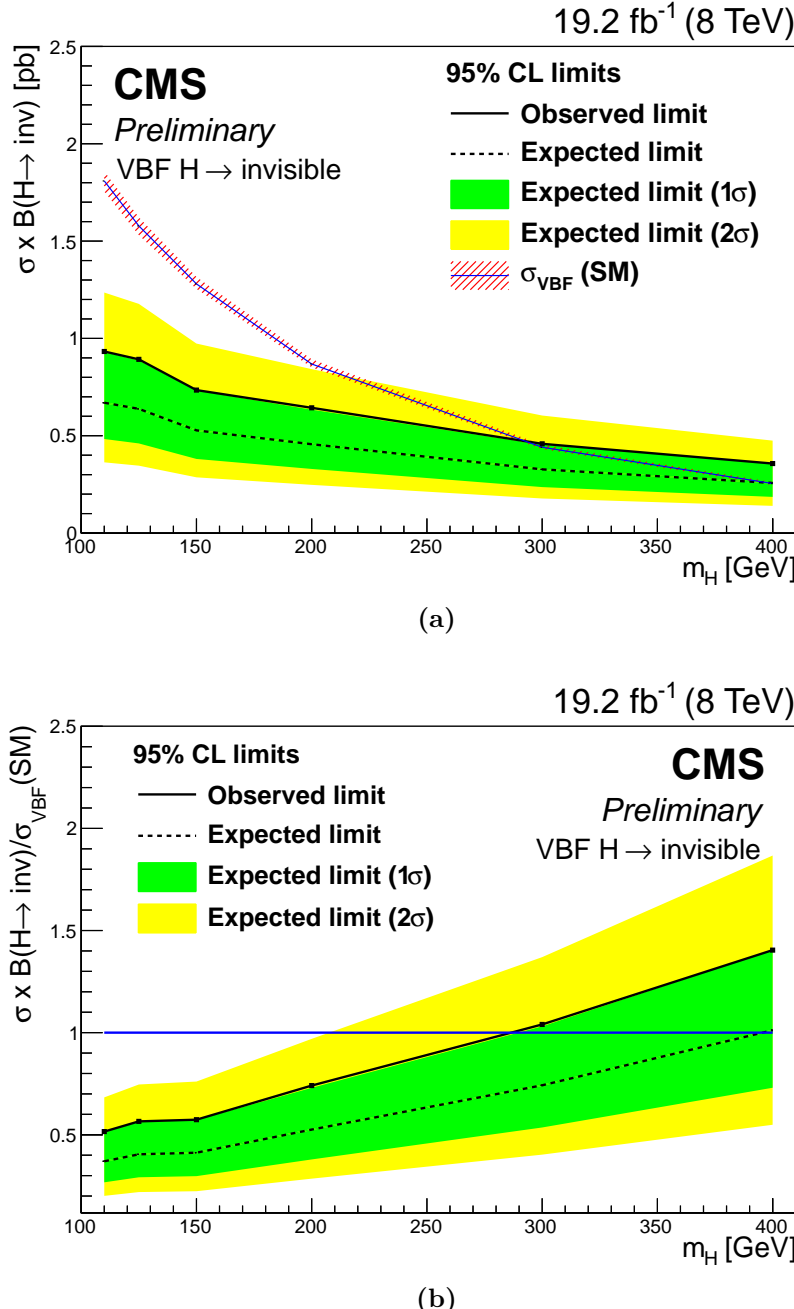


Figure 4.32.: The 95% CL limit on the cross-section times $\mathcal{B}(H \rightarrow \text{inv})$ (a) and the 95% CL limit on $\mathcal{B}(H \rightarrow \text{inv})$ of a SM Higgs boson (b) as a function of the Higgs boson mass, assuming SM Higgs boson acceptances. The green and yellow bands indicate the 68% and 95% confidence intervals on the expected limit respectively [2].

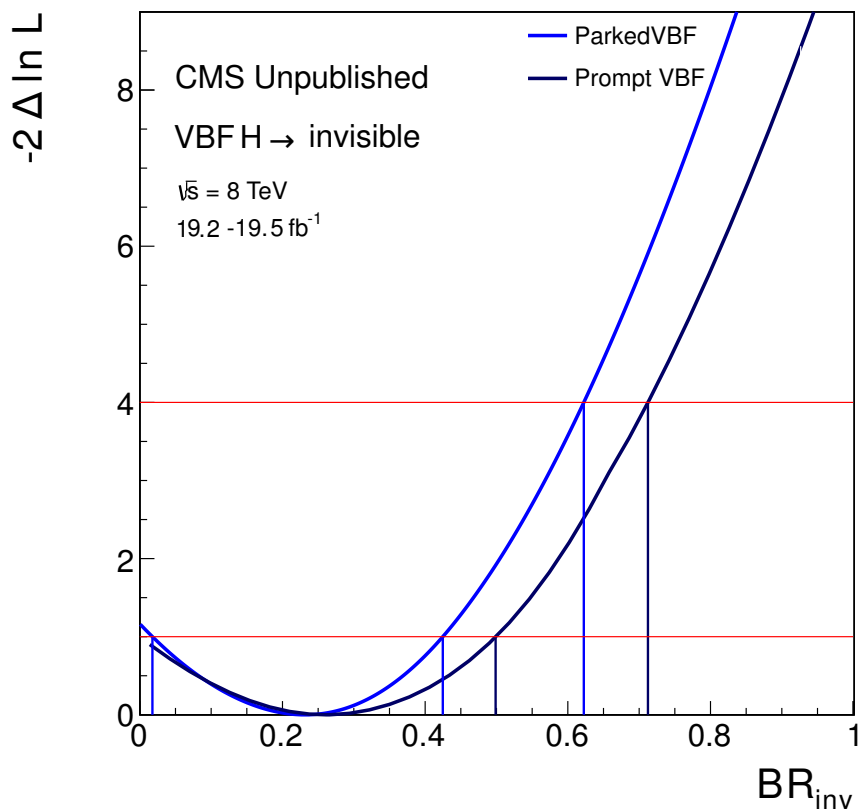


Figure 4.33.: Scans of the profile likelihood (i.e. with the nuisance parameters at each point chosen to maximise the likelihood) versus $\mathcal{B}(H \rightarrow \text{inv})$ of a SM Higgs boson with a mass of 125 GeV for the prompt and parked data analyses.

Table 4.17.: The 95% CL expected limits on $\mathcal{B}(H \rightarrow \text{inv})$ obtained when applying both the prompt and parked data analysis selections to both the prompt and parked data.

	Prompt data	Parked data
Prompt selection	45%	46%
Parked selection	47%	40%

The absolute values of the expected limits in Table 4.17 can therefore not be compared to those shown in Section 4.4.

Applying the parked selection to the prompt data produces a worse limit than applying the prompt selection to the prompt data. Also, applying the prompt selection to the parked data produces a worse limit than applying the prompt selection to the prompt data. The only improvement seen is from applying the parked selection to the parked data, confirming that the improved analysis selection also requires the additional phase space made available by the trigger in order to result in an improved limit.

4.9.2. Conclusion

The sensitivity of the parked data analysis is significantly increased compared to that of the prompt data analysis by the use of parked data recorded with triggers with looser selection. These triggers allow the analysis selection requirements to be less driven by the trigger requirements and to focus on identifying significant \cancel{E}_T coming from genuine invisible particles, which is isolated from jet activity. The observed (expected) limit at 95% CL on $\mathcal{B}(H \rightarrow \text{inv})$ for a 125 GeV Higgs boson is 0.57 (0.40).

Chapter 5.

Combinations of Run 1 searches for invisibly decaying Higgs bosons

Whilst the VBF production mode offers the best sensitivity to invisibly decaying Higgs bosons, the limit on $\mathcal{B}(H \rightarrow \text{inv})$ can be improved by taking into account searches performed using other production channels. According to the CL_S method described in Section 1.4 multiple searches can be combined by constructing a likelihood, according to Equation 1.38. Combinations of the VBF analyses with the other channels are described in sections 5.1 to 5.3.

5.1. Searches in other channels

As described in Section 1.2.1, after VBF the next most sensitive production modes to invisible Higgs boson decays are ggH and VH. VH has a much lower production rate than VBF (approximately 4 times less for a 125 GeV Higgs boson). Compensating for this low cross-section, several of the final states in VH production, particularly ZH, give very clean signatures which are easy to identify. Gluon fusion has a much higher rate than VBF, but in most cases the resulting Higgs boson is created alone so there are no visible particles in the final state. However, one or more jets can result from ISR allowing this channel to also be used.

In addition to the VBF analyses, three invisibly decaying Higgs boson searches were carried out by CMS during Run 1. Two of these searches specifically targeted the ZH production mode, one searching for events where the Z boson decayed to two leptons (the $Z(\ell\ell)H$ search) and another where it decayed to two b quarks (the $Z(b\bar{b})H$ search). The

Table 5.1.: Summary of the analyses included in the combination. The first column is the name of the analysis. The second and third columns give the integrated luminosity of the 7 and 8 TeV data sets used by each analysis. The fourth column contains the names of the categories in each analysis and the fifth column gives the proportion of signal events expected to come from each Higgs boson production mode.

Analysis	Luminosity (fb^{-1})		Category	Expected signal composition
	8 TeV	7 TeV (8 TeV)		
VBF prompt data	19.5		2-jet VBF	94% VBF, 6% ggH
VBF parked data	19.2		2-jet VBF	92% VBF, 8% ggH
Monojet	19.7		Monojet	70% ggH, 20% VBF, 6% WH, 3% ZH
			unresolved	47% WH, 25% ggH, 23% ZH, 5% VBF
			resolved	39% ggH, 32% WH, 18% ZH, 11% VBF
Z($\ell\ell$)H	19.7 (4.9)		$e^+ e^-$ 0-jet	100% ZH
			$e^+ e^-$ 1-jet	100% ZH
			$\mu^+ \mu^-$ 0-jet	100% ZH
			$\mu^+ \mu^-$ 1-jet	100% ZH
Z($b\bar{b}$)H	18.9		2-b-jet - low \cancel{E}_T	100% ZH
			2-b-jet - medium \cancel{E}_T	100% ZH
			2-b-jet - high \cancel{E}_T	100% ZH

third ‘‘monojet’’ search targeted events with one or more jets that are not VBF-like and included categories targeting ggH with ISR, and VH production where the vector boson decays hadronically. The fraction of the signal expected to come from each production mode in each category of each search along with the integrated luminosity used is given in Table 5.1. The limits from each search alone on $\mathcal{B}(H \rightarrow \text{inv})$ for a 125 GeV Higgs boson are given in Table 5.2.

When combining limits from separate analyses it is important that the event selections are mutually exclusive. A brief description of the event selection used in each of the non-VBF invisibly decaying Higgs searches is therefore given in the following subsections. It is also important when constructing the overall likelihood function to understand which uncertainties are correlated between analyses and which are not. The correlated uncertainties are discussed in Sections 5.2 and 5.3.

Table 5.2.: Summary of 95% CL upper limits on $\frac{\sigma}{\sigma_{SM}} \cdot \mathcal{B}(\text{H} \rightarrow \text{inv})$ for a 125 GeV Higgs boson obtained from each individual search contributing to the combinations described in this section [1, 3].

Channel	Observed (expected) upper limits on $\frac{\sigma}{\sigma_{SM}} \cdot \mathcal{B}(\text{H} \rightarrow \text{inv}) (\%)$
VBF prompt data	65 (49)
VBF parked data	57 (40)
$Z(\ell\ell)\text{H}$	84 (87)
$Z(b\bar{b})\text{H}$	192 (198)
Monojet	54 (62)

5.1.1. $Z(\ell\ell)\text{H} \rightarrow \text{invisible}$ selection

The $Z(\ell\ell)\text{H}$ search is described in Ref. [106]. The analysis selection required two tight, oppositely charged, same flavour leptons (either electrons or muons) both with $p_T > 20$ GeV, with invariant mass compatible with the Z boson, no further leptons and large \cancel{E}_T . Events containing two or more jets with $p_T > 30$ GeV are rejected to reduce the Z+jets background.

To reduce backgrounds, in events with a single jet, that jet was required not to be identified using the CSV algorithm (described in Section 4.7.1) as a b-jet. Also, requirements were made on the azimuthal angular separation and p_T balance between the \cancel{E}_T and the dilepton system. In addition to this signal region, control regions, which differ from the signal region in that the lepton system is not compatible with a Z boson decay, were used for background estimation. As events with two or more jets were always vetoed there is no overlap with the events selected in the VBF and $Z(b\bar{b})\text{H}$ analyses (where two jets with $p_T > 30$ GeV are required).

5.1.2. $Z(b\bar{b})\text{H} \rightarrow \text{invisible}$ selection

The $Z(b\bar{b})\text{H}$ search is described in Ref. [107]. The analysis selection required two jets tagged by the CSV algorithm as originating from b-quarks, large \cancel{E}_T , and no reconstructed electrons or muons. The di-b-jet system was required to have high p_T , but low invariant mass (less than 250 GeV). The dijet mass cut ensured there was no overlap with either of the VBF analyses. The main background to the analysis was from QCD multijet processes as in the VBF analysis. Similarly to the selection in the VBF parked data

analysis this background was reduced using requirements on $\min\Delta\phi(j, \cancel{E}_T^{\text{no-}\mu})$ and \mathcal{S} . The neutral component of the \cancel{E}_T was also required to be aligned with the charged component in ϕ . The signal region was separated into three categories with low, medium and high \cancel{E}_T and control regions where the signal region selections are relaxed or inverted are used to estimate the remaining backgrounds.

5.1.3. Monojet selection

The “monojet” search, is described in Ref. [108]. This analysis selected events with large \cancel{E}_T , one or more high- p_T jets, and no reconstructed electrons or muons. To separate events due to ggH production with ISR from those due to VH production where the vector boson decays hadronically, events were classified into three signal categories. The categorisation was sequential, i.e. if an event passed the requirements for the first category it was not considered for the second etc.

The first category targeted “unresolved” vector bosons where the high p_T of the vector boson caused its decay products to be very close together. These unresolved vector bosons were identified by searching for so-called “fat” jets with substructure with $p_T > 200$ GeV, (described in detail in Ref. [108]). One additional normal jet was allowed in this category as long as it was within 2° in ϕ of the fat jet.

The second category was the resolved category where the vector boson had lower p_T and its decay products could be identified as two separate normal jets. These jets were required to have an invariant mass between 60 and 110 GeV. This range overlaps with the range used in the $Z(b\bar{b})H$ analysis regions, leading to a non-negligible number of events passing the selection for both analyses. The resolved category was therefore not used in any combinations.

The third category was the “monojet” category. Events in this category were required to have one jet with $p_T > 150$ GeV. One additional jet within 2° in ϕ of the first jet was allowed to be present, with further jets causing the event to be vetoed. Control regions, which differ from the above categories by the presence of one or more leptons or photons, were used to estimate the background.

The category definitions above are not orthogonal to the VBF analysis. To remedy this any events passing the VBF parked data analysis selection were vetoed. This veto removed less than 4% of the expected signal events in the monojet category and none of the signal events expected in the resolved category. As the monojet analysis was

performed in 2015, after the parked data VBF analysis had been performed, the monojet analysis was not combined with the prompt analysis, so no overlap veto between these two analyses was necessary.

The lepton veto present in all three signal categories means there is no overlap of any of the three categories with the $Z(\ell\ell)H$ analysis. Some of the control regions do overlap slightly with categories in the $Z(\ell\ell)H$ search. However, these overlaps are very small due to the very high jet p_T cut present in the monojet search. In addition to the $Z(b\bar{b})H$ search overlapping with the resolved category, there are also overlaps between the $Z(b\bar{b})H$ search and the unresolved and monojet categories. However, very few events in the $Z(b\bar{b})H$ search have jets with $p_T > 150$ GeV, so these overlaps were considered negligible.

5.2. Combination with prompt data VBF search

The first combination that was performed was between the analyses that were completed in 2013, the two ZH searches and the prompt data VBF search. As has been described above, these analyses do not overlap. However, as the objects used in all three analyses are very similar, several of the systematic uncertainties are correlated. The full list of correlated uncertainties, and the analyses they affect, are given, in decreasing order of the change in the expected limit on $\mathcal{B}(H \rightarrow \text{inv})$ for a 125 GeV Higgs boson as a result of removing the uncertainty, in Table 5.3. The method for determining the jet energy in the $Z(b\bar{b})H$ analysis, involving a regression technique, is very different from that used in the other two analyses [107]. The jet uncertainties are therefore correlated between the $Z(\ell\ell)H$ and VBF searches, but not the $Z(b\bar{b})H$ analysis.

None of the analyses saw any significant excess of events, so limits were set using the asymptotic CL_S procedure described in Section 1.4 for several Higgs boson mass hypotheses. The Higgs boson masses for which the three analyses have generated MC samples are not all the same. Between 115 and 145 GeV the two ZH analyses have samples for the same masses. Limits from the combination of these two analyses were obtained in this range and can be seen in Figure 5.1. Assuming SM Higgs boson production and acceptance the 95% CL observed (expected) limit on $\mathcal{B}(H \rightarrow \text{inv})$ for a 125 GeV Higgs boson is found to be 0.81 (0.83).

The mass points available in the VBF and ZH analyses are quite different. The selection efficiency for VBF and ggH signal events in the VBF analysis was interpolated between the

Table 5.3.: Uncertainties correlated between the VBF prompt data, $Z(\ell\ell)H$ and $Z(b\bar{b})H$ searches and the analyses they affect. Also quoted is the relative change in the expected limit on $\mathcal{B}(H \rightarrow \text{inv})$ on removing each uncertainty from the analysis.

Uncertainty	Analyses affected	$\frac{\Delta((\text{limit}))}{\text{limit}}$ on removal
JES	VBF, $Z(\ell\ell)H$	-0.13
PDFs	VBF, $Z(b\bar{b})$, $Z(\ell\ell)H$	-10
QCD scale	$VBF, Z(b\bar{b})$, $Z(\ell\ell)H$	-0.04
Luminosity	$VBF, Z(b\bar{b})H$, $Z(\ell\ell)H$	-0.02
JER	VBF, $Z(\ell\ell)H$	<0.01
UES	$VBF, Z(b\bar{b})H$, $Z(\ell\ell)H$	<0.01
Lepton efficiency	VBF, $Z(\ell\ell)H$	<0.01

available mass points (these ranged from 110 to 400 GeV). Multiplying the interpolated efficiencies for a mass hypothesis by the corresponding Higgs boson production cross-section gives a signal yield estimate for that mass.

In order to combine limits from multiple production channels it is also necessary to make an assumption about the relative cross-section of these two production mechanisms. Assuming the SM production cross-sections, a combination was performed between all three analyses in the mass range 115 to 145 GeV. The results of this combination can be seen in Figure 5.2. The 95% CL observed (expected) limit on $\mathcal{B}(H \rightarrow \text{inv})$ for a 125 GeV Higgs boson was found to be 0.58 (0.44).

Whilst the $Z(b\bar{b})H$ search has no MC samples available for Higgs boson masses above 145 GeV, the $Z(\ell\ell)H$ search has samples up to 300 GeV. The VBF and $Z(\ell\ell)H$ searches were therefore combined in the mass range 115 to 300 GeV. The results of this combination are shown in Figure 5.3. It can be seen that there is an approximately one sigma excess for all values of the Higgs boson mass. This excess is driven by the VBF channel, which also sees a one sigma excess (as shown in Figure 4.12) which is 100% correlated across all Higgs boson mass hypotheses. The observed excess is therefore not significant.

5.3. Combination with the parked data VBF search

The parked data VBF analysis was combined with both the ZH searches and the monojet search, which was finished in 2015 [3]. The prompt data VBF analysis was not included in this combination due to its large overlap with the parked data analysis. As discussed

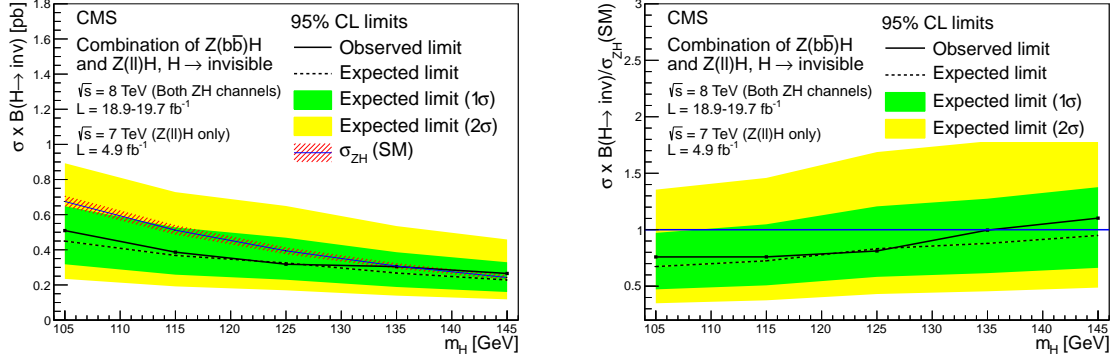


Figure 5.1.: Expected and observed 95% CL upper limits on the ZH $\sigma \times \mathcal{B}(H \rightarrow \text{inv})$ in pb (a) and normalised to the SM VBF Higgs boson production cross-section (b) obtained from the combination of the $Z(\ell\ell)H$ and $Z(b\bar{b})H$ searches. The green and yellow bands indicate the 68% and 95% confidence intervals on the expected limit respectively [1].

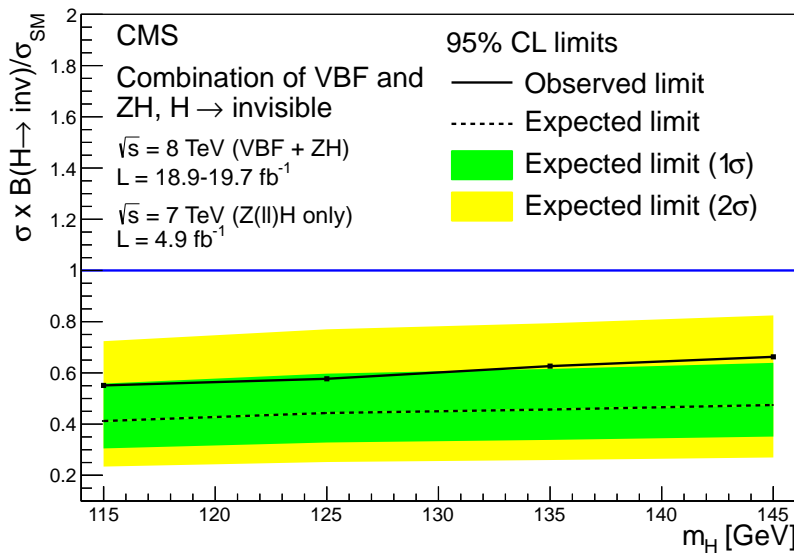


Figure 5.2.: Expected and observed 95% CL upper limits on the $\sigma \times \mathcal{B}(H \rightarrow \text{inv}) / \sigma_{SM}$ obtained from the combination of the VBF, $Z(\ell\ell)H$ and $Z(b\bar{b})H$ searches. The green and yellow bands indicate the 68% and 95% confidence intervals on the expected limit respectively [1].

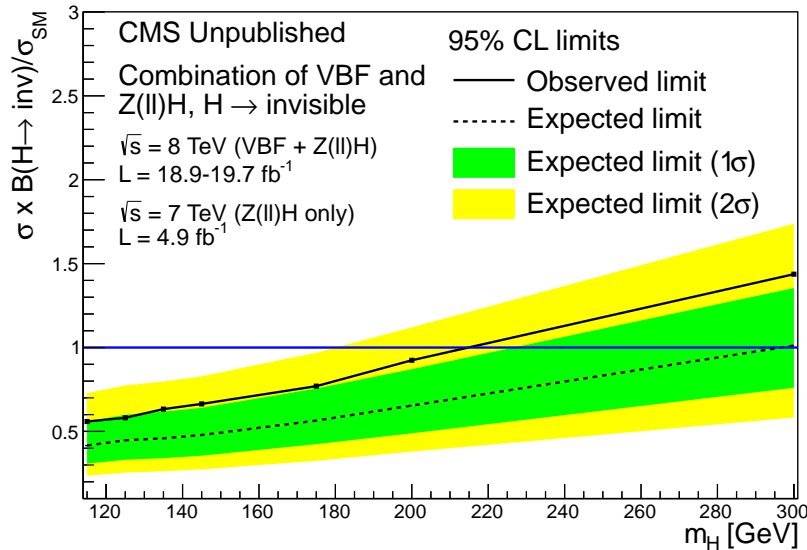


Figure 5.3.: Expected and observed 95% CL upper limits on the $\sigma \times B(H \rightarrow \text{inv}) / \sigma_{SM}$ obtained from the combination of the VBF and $Z(\ell\ell)H$ searches. The green and yellow bands indicate the 68% and 95% confidence intervals on the expected limit respectively [1].

above, overlaps between the VBF and monojet searches were explicitly removed by vetoing events in the monojet search passing the VBF selection. The resolved category of the monojet search was also removed from the combination to avoid large overlap with the $Z(b\bar{b})H$ search. This removal did not change the expected limit, as the resolved category is the least sensitive to invisibly decaying Higgs bosons. The remaining overlaps between the monojet search and the ZH searches are small as discussed in Section 5.1.3.

After resolving the issue of overlaps, it was necessary to study which uncertainties were correlated. A summary of the correlated uncertainties, and the analyses they affect is given in Table 5.4. Of particular note are the decisions taken in correlating the jet and \cancel{E}_T uncertainties. For the jet uncertainties, as in the combination with the VBF prompt data analysis, the uncertainties on the jet energy in the $Z(b\bar{b})H$ analysis are not correlated with the other analyses due to the very different method of determining the jet energy. In the remaining three analyses, the JES and JER uncertainties vary as a function of a jet's p_T and η , so it is important to study the jet kinematic distributions when deciding which of the uncertainties should be correlated. As described in Section 5.1.3, the two categories of the monojet search used in this combination require very high p_T jets which are mostly in the central region of the detector. By contrast the high p_T jets in the VBF parked data analysis are mostly in the forward region of the detector due to the large

Table 5.4.: Uncertainties correlated between the VBF parked data, $Z(\ell\ell)H$, $Z(b\bar{b})H$ and monojet searches and the analyses they affect.

Nuisance	Analyses which it affects
JES	VBF, $Z(\ell\ell)H$
PDFs	VBF, $Z(b\bar{b})$, $Z(\ell\ell)H$, monojet
QCD scale	VBF, $Z(b\bar{b})$, $Z(\ell\ell)H$, monojet
Luminosity	VBF, $Z(b\bar{b})H$, $Z(\ell\ell)H$, monojet
JER	VBF, $Z(\ell\ell)H$
UES	VBF, $Z(b\bar{b})H$, $Z(\ell\ell)H$
Muon identification efficiency	VBF, $Z(\ell\ell)H$, monojet
Electron identification efficiency	VBF, $Z(\ell\ell)H$
Diboson cross-section	VBF, monojet

$\Delta\eta_{jj}$ requirement. The $Z(\ell\ell)H$ analysis uses low p_T jets with $p_T > 30$ GeV similar to those used to calculate $\min\Delta\phi(j, \cancel{E}_T^{\text{no-}\mu})$ in the VBF analysis, but very different from the high p_T central jets in the monojet analysis. The decision was therefore taken to correlate the VBF and $Z(\ell\ell)H$ analyses JES and JER uncertainties and to leave those from the monojet analysis uncorrelated. A study of the impact of [this](#) choices was carried out, and it was found that all combinations of correlations resulted in the same expected limit.

In the case of the \cancel{E}_T uncertainties, the two ZH searches and the VBF search use the same \cancel{E}_T corrections, whereas the monojet search applies a different set of corrections [108]. The monojet analysis UES uncertainty was therefore not correlated with that from the other analyses.

With these uncertainty correlations the four searches were combined for a Higgs boson mass of 125 GeV assuming SM production-cross-sections for each channel. The 95% CL observed (expected) limit on $\mathcal{B}(H \rightarrow \text{inv})$ for a 125 GeV Higgs boson was found to be 0.36 (0.30). The log-likelihood obtained as a function of $\mathcal{B}(H \rightarrow \text{inv})$ is shown in Figure 5.4. The favoured observed value can be seen to be greater than zero, however this is not significant.

As well as the full combination of all analysis categories, sub-combinations were also performed of all the categories targeting a particular production mode. The results of these sub-combinations and the full combination is shown in Figure 5.5, where the VBF-tagged limit comes from the VBF parked data analysis, the VH-tagged limit from

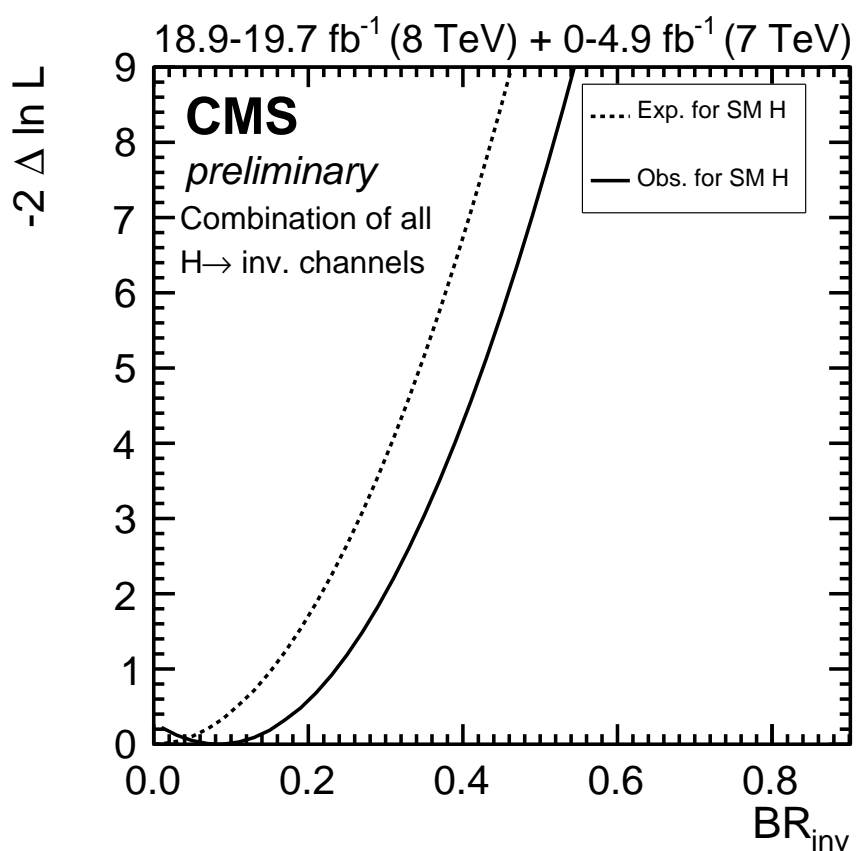


Figure 5.4.: Log-likelihood versus $\mathcal{B}(H \rightarrow \text{inv})$. The solid curve represents the observation in data and the dashed curves represent the median expected result for no invisible decays of the Higgs boson [3].

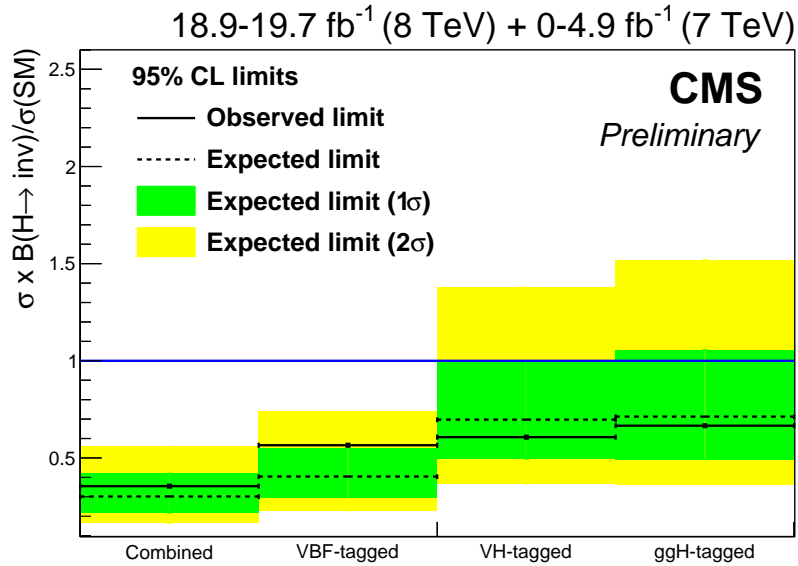


Figure 5.5.: Expected and observed 95% CL upper limits on production cross-section times $\mathcal{B}(H \rightarrow \text{inv})$ normalised to the SM production cross-section obtained from the combination of all channels targeting each Higgs boson production mode. The green and yellow bands indicate the 68% and 95% confidence intervals on the expected limit respectively [3].

the resolved category of the monojet analysis and the two ZH searches, and the ggH tagged limit comes from the monojet category of the monojet analysis. It can be seen that whilst the VBF channel is the most sensitive, the limits, are improved significantly by the addition of the analyses targeting the two other production modes.

Chapter 6.

Dark matter interpretations of Run 1 searches for invisibly decaying Higgs bosons

As well as using the analyses presented to place limits on Higgs boson decays to invisible final states, it is also possible to interpret them as limits on models incorporating DM. The particular models that are studied fall into two classes, EFTs and simplified models, which are described in detail in Section 1.2.2. These studies were not carried out as part of the CMS collaboration, so it was necessary to develop and validate an independent framework for simulating the events resulting from these models.

6.1. Simulation techniques and validation

The CMS GEANT based detector simulation is very computing intensive, so an alternative detector simulation with the DELPHES fast reconstruction package was used. Whilst DELPHES has been extensively validated by its authors against the CMS reconstruction [40], two of the variables used in the invisible Higgs boson decay searches described in this thesis are not implemented in the standard version of DELPHES. Specifically, a calculation of the \cancel{E}_T ignoring objects with $|\eta| > 3$ was added, to replicate the behaviour of the CMS L1 trigger, this quantity is referred to as L1 \cancel{E}_T . The total transverse energy calculated using all particles in the event with no minimum threshold on their energy, which is required for the calculation of \mathcal{S} , was also added.

Another difference from the CMS analysis is that the studies described in this chapter use MADGRAPH to simulate the hard-scattering process, whilst the CMS analysis uses POWHEG. Both the internal CMS simulation and that described in this chapter use PYTHIA for parton-showering and hadronisation. Yields and kinematic distributions of events after selection criteria are applied are obtained from these simulations using an analysis framework developed and validated by the MasterCode collaboration [109].

The validation of these simulations and the analysis framework was carried out in two steps, both using a centre of mass energy of 8 TeV. First, POWHEG and PYTHIA were used to simulate a VBF produced 125 GeV Higgs boson decaying to invisible final states, as in the internal CMS simulation. This sample of events was then processed using the DELPHES based reconstruction and MasterCode analysis framework. The resulting event yields were compared to those obtained from a POWHEG and PYTHIA produced sample processed using the full CMS reconstruction and analysis framework. The event yields were found to agree within 10%.

The second step was to compare the 125 GeV VBF produced invisibly decaying Higgs boson sample generated with POWHEG to one generated with MADGRAPH with both samples being processed using DELPHES. This comparison was carried out starting from the following requirements:

$$\begin{aligned} \eta_{j1} \cdot \eta_{j2} &< 0, \text{jet 1 and jet 2 } p_T > 35 \text{ GeV}, \mathcal{S} > 3, \\ \Delta\eta_{jj} &> 3.6, M_{jj} > 700 \text{ GeV}, \text{L1 } \cancel{E}_T > 40 \text{ GeV}. \end{aligned} \quad (6.1)$$

Cuts were then added to this selection one at a time until the applied selection was the same as the parked data analysis signal region selection, which is described in Equation 4.13. The resulting event yields can be seen in Table 6.1. It is important to note that the MADGRAPH samples include both VBF and VH production of the Higgs boson, while the POWHEG samples only include VBF production. This difference explains the MADGRAPH yield being larger than that from POWHEG at the starting point of the comparison. As the selection is tightened the disagreement between POWHEG and MADGRAPH can be seen to reduce until the difference in yield is below 5% for the full selection, where very few VH events are still present. Only event yields after the full selection are used in the results presented in Section 6.2, so the level of agreement is considered acceptable.

The Run 1 signal and background estimates made public in Ref. [2] are quoted with their statistical and systematic errors. However, no information on the correlation between

Table 6.1.: Event yields obtained, for several sets of event selection requirements, from two samples where the hard-scatter was simulated using MADGRAPH (second column) and POWHEG (third column), both of which were processed using the DELPHES fast detector reconstruction package. For each line the selection stated in the first column is added to the selection present for the line before. The starting point for the selection is described in Equation 6.1.

Selection added	MADGRAPH	POWHEG
Start point	2653	2311
jet 1 $p_T > 50$ GeV, jet 2 $p_T > 45$ GeV	2056	1834
$\cancel{E}_T^{\text{no-}\mu} > 90$ GeV	2000	1793
$M_{jj} > 1200$ GeV	704	689
$\mathcal{S} > 4$	539	519
$\min\Delta\phi(j, \cancel{E}_T^{\text{no-}\mu}) > 2.3$	244	248

the signal and background systematic errors is given. In order to estimate the effect of these correlations on the limits obtained, the observed and expected limits for the parked data analysis, described in Chapter 4.4, were calculated assuming no correlation between the signal and background uncertainties. The observed (expected) 95% CL limit on $\mathcal{B}(H \rightarrow \text{inv})$ for a 125 GeV Higgs boson was found to be 0.58 (0.42), which agrees well with the 0.57 (0.40) obtained using the full CMS uncertainty model. Correlations between the signal and background uncertainties were therefore considered negligible.

Having validated the simulation and uncertainty models at Run 1’s 8 TeV centre of mass energy, projections of the expected performance of the analysis at the increased 13 TeV Run 2 centre of mass energy were made. The validated MADGRAPH hard-scattering plus DELPHES detector reconstruction simulation framework was used to generate events from the signal models described in Section 1.2.2 at a centre of mass energy of 13 TeV. The distribution of \cancel{E}_T for a representative sample of these models is shown in Figure 6.1. It can be seen that whilst all of these models result in large values of \cancel{E}_T compared to the selection present in the VBF Higgs to invisible searches, the \cancel{E}_T is typically less than 500 GeV. The assumption that must be made in the case of the EFT models, that the momentum transferred through the mediator is less than the mediator’s mass, is therefore valid for mediators with masses above 500 GeV.

In order to carry out estimations of the sensitivity of VBF Higgs to invisible searches using the Run 2 LHC data, it is also necessary to estimate how the expected yield from background processes changes when the centre of mass energy is increased. The yields expected from each background process at 8 TeV, listed in Table 4.16, were therefore

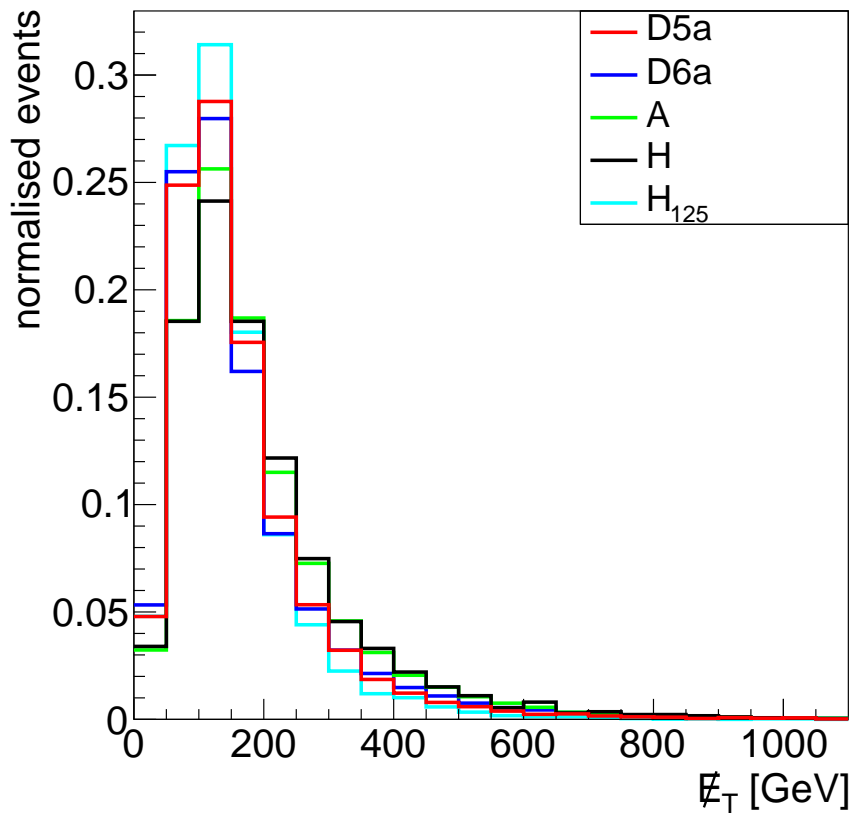


Figure 6.1.: The \cancel{E}_T distribution for two EFT signal models (D5a and D6a), and spin-0 simplified models, described in Section 1.2.2, with representative model parameter values. For the 125 GeV Higgs boson model, the dark matter mass, m_χ is assumed to be 56.2 GeV, whereas for the other models m_χ is assumed to be 100 GeV. For the scalar and pseudoscalar models the mass of the mediator is assumed to be 316.2 GeV. It is important to note that the 125 GeV Higgs boson model simulation includes VH production of the Higgs boson as well as VBF [4].

scaled by the cross-section ratio between 13 and 8 TeV. These cross-section ratios were calculated using **FEWZ** 3.1 for W and Z boson production, **TOP++** v2.0 for top quark pair production and **MADGRAPH** for diboson production. Samples of W and Z bosons produced in association with jets were also produced at centre of mass energies of 8 and 13 TeV, using the same simulation framework used for the signal processes. The efficiency for these events passing the full Run 1 parked data VBF Higgs to invisible search selection was then calculated. The expected yields from W and Z boson plus jets backgrounds, which make up 94% of the expected background events, were corrected using the ratio of the selection efficiencies obtained at 8 and 13 TeV. The resulting total expected yield from background processes was 741 events.

In addition to scaling the expected event yields, the uncertainties on the yields must also be calculated. When extrapolating from 8 to 13 TeV all statistical uncertainties are scaled by the square root of the ratio between the expected yields at 8 TeV and 13 TeV. The statistical uncertainties are then assumed to scale with the square root of the integrated luminosity collected at 13 TeV.

For 19.2 fb^{-1} of integrated luminosity collected, the Run 2 fractional systematic uncertainties are assumed to be the same as those seen in the Run 1 parked data analysis. Two prescriptions are then used to estimate how the systematic uncertainties change with the integrated luminosity. The first prescription is to keep the systematic uncertainties constant as the integrated luminosity changes. The second, more realistic, prescription is to assume that the fractional systematic uncertainty scales as $1/\sqrt{\mathcal{L}}$, as many systematic uncertainties result from measurements which use statistically limited data samples. This second prescription also implies that for integrated luminosities below 19.2 fb^{-1} the fractional systematic uncertainty will be larger than that seen in the Run 1 parked data VBF Higgs to invisible search.

6.2. Results

First, the sensitivity of the CMS search for invisibly decaying 125 GeV Higgs bosons was projected to 13 TeV for several integrated luminosities. The results of these projections are shown in Figure 6.2a for both systematic uncertainty scaling prescriptions. It can be seen that assuming the systematic uncertainties improve with square root of the integrated luminosity, CMS has the potential to exclude values of $\mathcal{B}(H \rightarrow \text{inv})$ as small as $\sim 5\%$. However, this will require control of systematic uncertainties at the 1%

level. If the systematic uncertainties do not improve, the sensitivity of the analysis becomes systematically limited when $\sim 100 \text{ fb}^{-1}$ of integrated luminosity have been collected, at a limit on $\mathcal{B}(H \rightarrow \text{inv})$ of approximately 20%. Given that the assumption that the systematic uncertainties show no improvement with increasing luminosity is very conservative, the rest of the results in this chapter assume that the systematic uncertainties scale as the square root of the integrated luminosity.

The next projection made was for the limit that can be obtained on the coupling, g_χ , of DM to the 125 GeV Higgs boson. For on-shell Higgs bosons this projection was made using Equation 1.34, whereas for off-shell Higgs bosons, the assumption of equal couplings to visible particles and DM was made and the DM production rate was calculated as described in Section 1.2.2. The results of this projection are shown in Figure 6.2b, for integrated luminosities of 20, 300, and 3000 fb^{-1} , which are those expected to be collected by CMS by the end of 2016, Run 2 and the high luminosity upgrade of the LHC respectively. It can be seen that whilst the limits on g_χ are considerably weaker for off-shell production, values of the coupling of order 1 can still be excluded with 3000 fb^{-1} .

Next, projections were made of the limits on the couplings of spin 0 mediators with non-125 GeV masses to DM. As described in Section 1.2.2, for DM production via an on-shell mediator, the rate of production is proportional to g_χ^2 , whereas for production via off-shell mediators it is proportional to $g_v^2 g_\chi^2 = g_\chi^4$. This difference leads to a discontinuity in the projected limits at the on-shell to off-shell boundary. The projected limits obtained on scalar and pseudoscalar mediators are shown in Figures 6.3a and 6.3b respectively as a function of mediator and DM mass for both the on and off-shell production regions. Very large luminosities are required to exclude values of the coupling of order π or below due to the production rates for these models being very low. However, for large couplings, DM and mediator masses up to 1 TeV can be excluded.

Finally, limits are set on the EFT class of models. Limits on the D5, D6 and D7 operators are shown in Figures 6.4a, 6.4b and 6.4c respectively. Several of the EFTs produce very similar limits, so a subset has been chosen for clarity. It is important to note that the values of Λ that are probed are much higher than the approximately 500 GeV average momentum transfer expected through the mediator, as shown in Figure 6.1, justifying the EFT assumptions made, for couplings of order 1 or below.

As the power of Λ by which the coupling to DM is suppressed increases with the dimensionality of the operator, it would be expected that the D5 models would have the

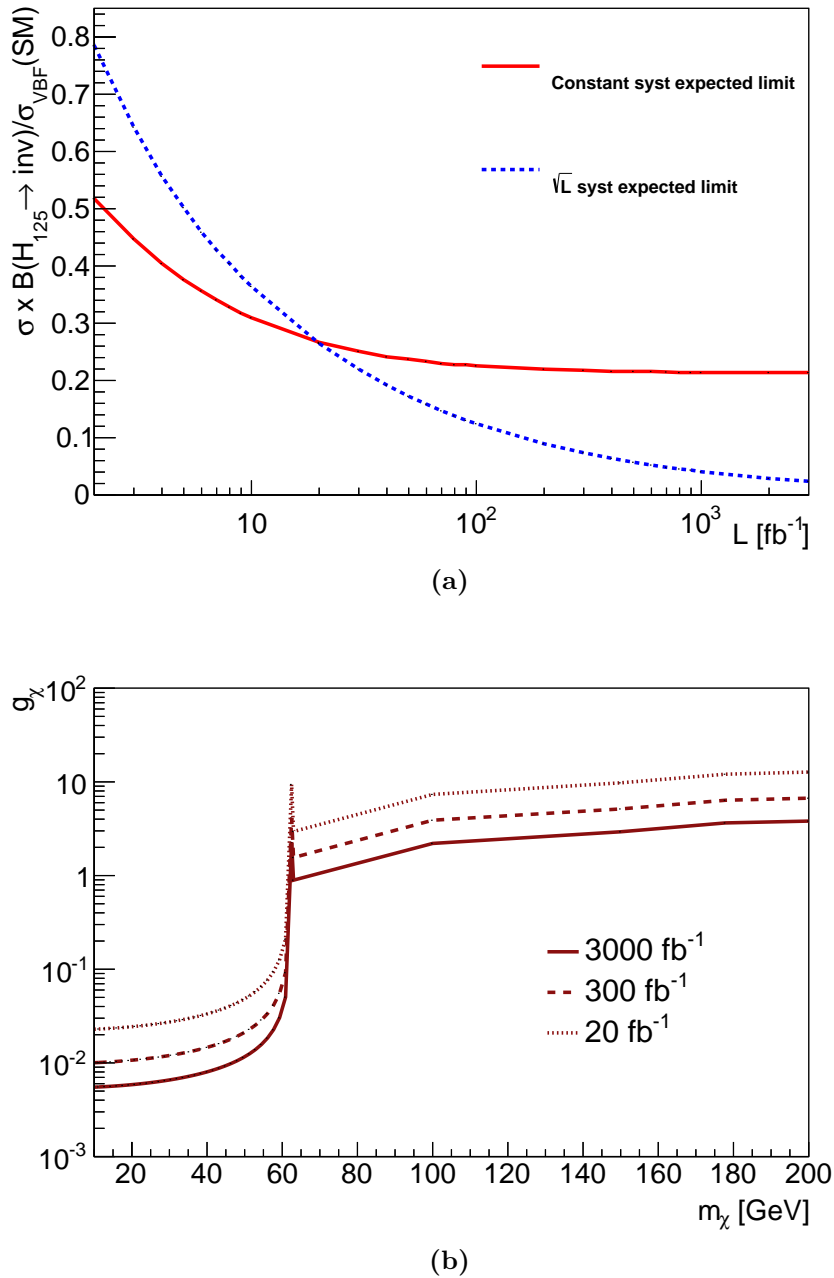


Figure 6.2: (a) Expected limits on $B(H \rightarrow \text{inv})$ for a 125 GeV Higgs boson, as a function of integrated luminosity, projections were made both assuming constant systematic uncertainties (red) and assuming the systematic uncertainties improve with the square root of the integrated luminosity (blue). (b) Expected limits on the coupling, g_χ , of DM to the 125 GeV Higgs boson as a function of DM mass, m_χ for several integrated luminosities [4].

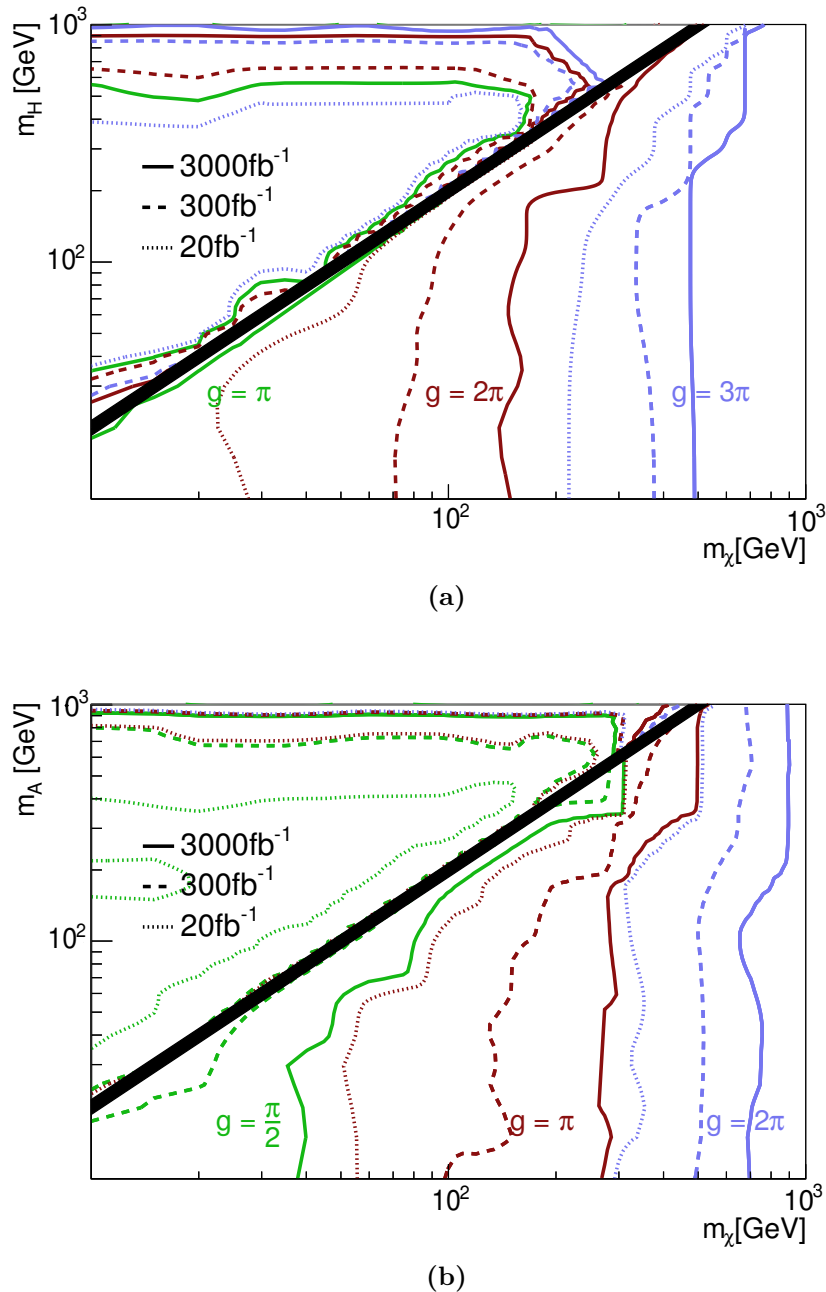


Figure 6.3.: Expected exclusions on the coupling of DM to scalar (a) and pseudoscalar (b) mediators as a function of mediator mass, m_H/m_A , and DM mass, m_χ . Note that some contours are not shown because the corresponding value of the coupling is not excluded at that integrated luminosity [4].

most sensitivity, with the D6 and D7 models being less sensitive. Whilst the D5a model does provide the best sensitivity, with values of Λ up to 5 TeV being excluded with the full LHC dataset, it can be seen from Figure 6.4 that there are several deviations from this pattern. The D5c and D5d operators exclude significantly lower values of Λ than D5a and D5b, due to the primary DM production mechanism being via a single Z boson (as can be seen from Equations 1.23 and 1.24) resulting in a lack of forward jets. This production via a Z boson also explains the decrease in the limit on Λ seen above $m_\chi = m_Z/2$.

Furthermore, the D6 and D7 operators show similar exclusions on Λ , despite the dimensionality being greater for the D7 models. This is again due to the lack of forward jets in the D6 operators which, like the D5c and D5d operators, allow DM production through a single Z boson, while the D7 models don't.

6.3. Conclusions

In conclusion the direct limit on $\mathcal{B}(H \rightarrow \text{inv})$ for the 125 GeV Higgs boson can be expected to reach 5% after the full LHC dataset, providing systematic uncertainties improve with the square root of the integrated luminosity collected. Furthermore, searches for invisible Higgs boson decays in the VBF production channel in Run 2 will allow limits to be set on a wide range of models. The EFT models studied will allow new physics to be probed up to the 5 TeV scale in the case of the most sensitive operators. Simplified models with spin 0 mediators, large couplings, and mediator and DM masses up to the TeV scale are also expected to be excluded by the end of LHC running.

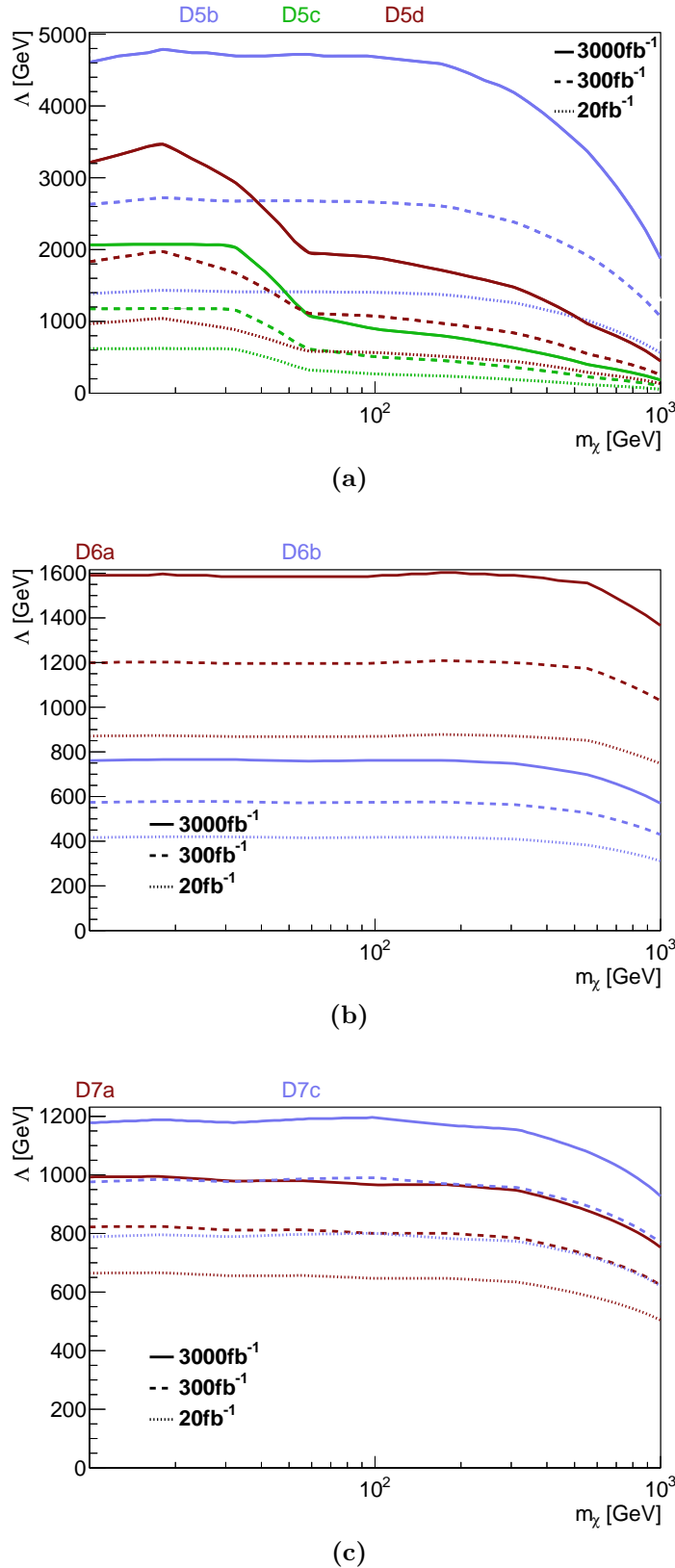


Figure 6.4.: Expected 95% CL lower limits on the EFT scale, Λ , for D5 (a), D6 (b) and D7 (c) type EFT operators for several values of the integrated luminosity. The D5b, D7b and D7d operators have very similar exclusions to the D5b, D7a and D7c operators respectively, so are not shown for clarity [4].

Chapter 7.

Conclusions

Several searches for invisibly decaying Higgs bosons using data from proton-proton collisions at the LHC, collected by the CMS detector, and their interpretations have been shown. The searches include the first invisibly decaying Higgs boson search carried out in the VBF channel, which used promptly reconstructed data from CMS, and placed an observed (expected) limit on $\mathcal{B}(H \rightarrow \text{inv})$ of 0.65 (0.49) at 95% CL [1].

The searches also include an updated search for VBF produced invisibly decaying Higgs bosons carried out using data collected using the so-called parked triggers. These parked triggers had looser thresholds than those used for the first search in this channel, increasing the sensitivity of the analysis. Taking advantage of this increased sensitivity required measurements of the trigger efficiency which accounted for correlations between the variables used, and also a full re-optimisation of the analysis selection. This re-optimisation included the addition of new variables to discriminate against QCD backgrounds. The observed (expected) limit on $\mathcal{B}(H \rightarrow \text{inv})$ obtained from this analysis was 0.57 (0.40) at 95% CL [2].

Combinations of these two searches with searches performed in other Higgs boson production channels were also presented. The prompt data search was combined with two searches in the ZH production channel where the Z boson decays either to leptons or b-quarks. The observed (expected) limit on $\mathcal{B}(H \rightarrow \text{inv})$ obtained from this combination was 0.58 (0.44) at 95% CL.

The search using data collected with the parked triggers was combined with the same two searches in the ZH production channel and a further search targeting ggH production and VH production where the vector boson decays hadronically. The observed (expected) limit on $\mathcal{B}(H \rightarrow \text{inv})$ obtained from this combination was 0.36 (0.30) at 95% CL [3].

This was the first combination of invisible Higgs boson decay searches featuring analyses targeting the three highest cross-section Higgs boson production channels.

Interpretations of invisibly decaying Higgs boson searches as limits on several models models of beyond the SM physics, which include dark matter, were also shown. Projections of the parameter space that the search for invisibly decaying Higgs bosons in the VBF channel will be able to exclude at a centre of mass energy of 13 TeV were shown for several values of integrated luminosity. For EFT models new physics scales up to 5 TeV were found to be accessible with the full LHC dataset. For simplified spin 0 mediator models mediator and dark matter masses of up to 1 TeV were found to be accessible for dark matter couplings of order 1.

Finally, projections of the sensitivity of the VBF channel invisibly decaying Higgs boson search in Run 2 were made for several values of integrated luminosity. It was found that providing systematic uncertainties can be controlled to the 1% level, limits on $\mathcal{B}(H \rightarrow \text{inv})$ of 5% should be possible with the full LHC dataset.

Appendix A.

Parked data trigger efficiencies

This appendix contains the trigger efficiency curves with overlaid error function fits and their errors as described in Section 4.5. Due to the event selection applied in the parked data analysis only the highest bin in M_{jj} is used.

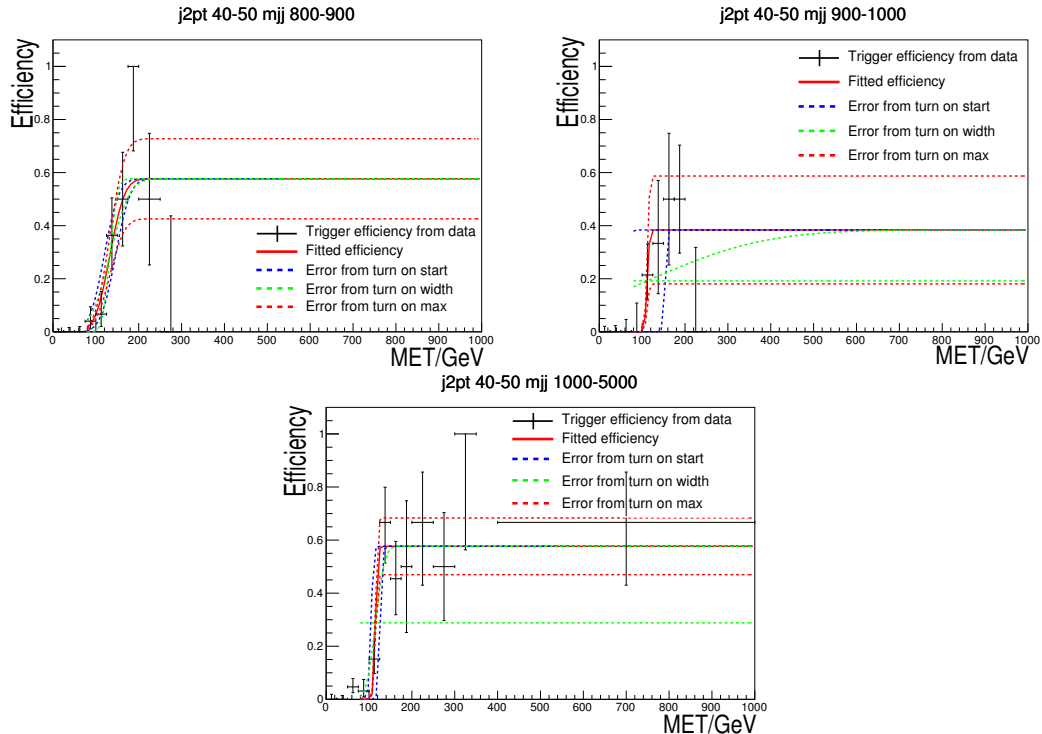


Figure A.1.: The measured efficiency of the trigger used in run A as a function of MET in bins of dijet mass (m_{jj}) and sub-leading jet p_T (j2pt). The bin that each plot corresponds to is displayed at the top of the plot.

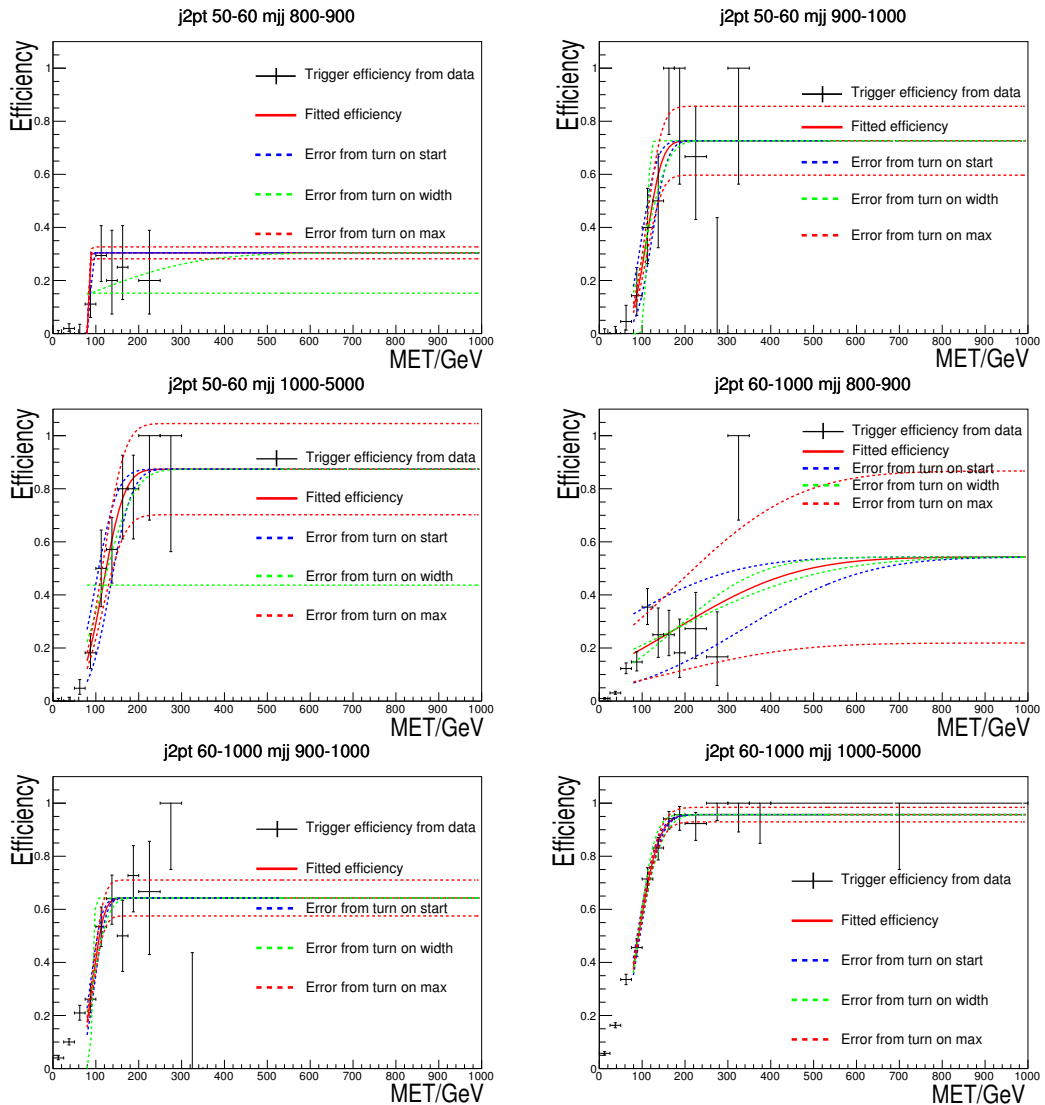


Figure A.2.: The measured efficiency of the trigger used in run A as a function of MET in bins of dijet mass (mjj) and sub-leading jet p_T (j2pt). The bin that each plot corresponds to is displayed at the top of the plot.

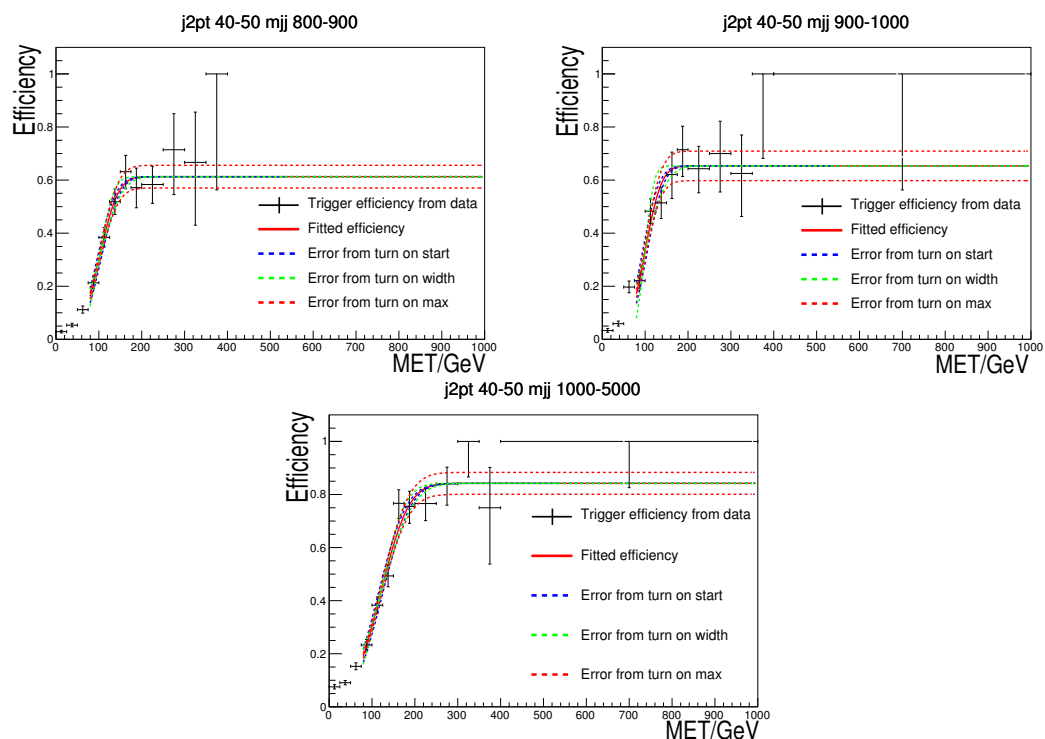


Figure A.3.: The measured efficiency of the trigger used in runs B and C as a function of MET in bins of dijet mass (mjj) and sub-leading jet p_T (j2pt). The bin that each plot corresponds to is displayed at the top of the plot.

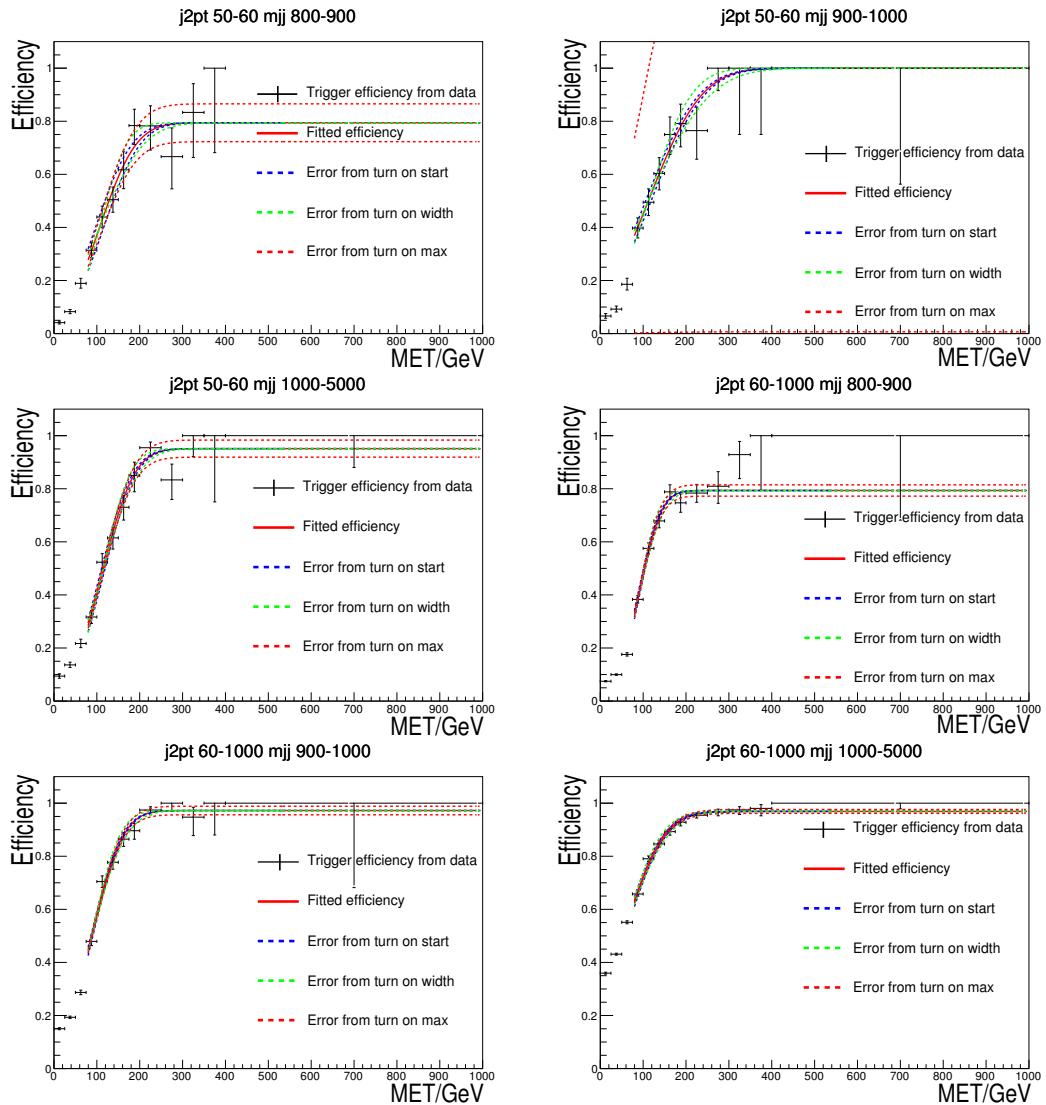


Figure A.4.: The measured efficiency of the trigger used in runs B and C as a function of MET in bins of dijet mass (mjj) and sub-leading jet p_T (j2pt). The bin that each plot corresponds to is displayed at the top of the plot.

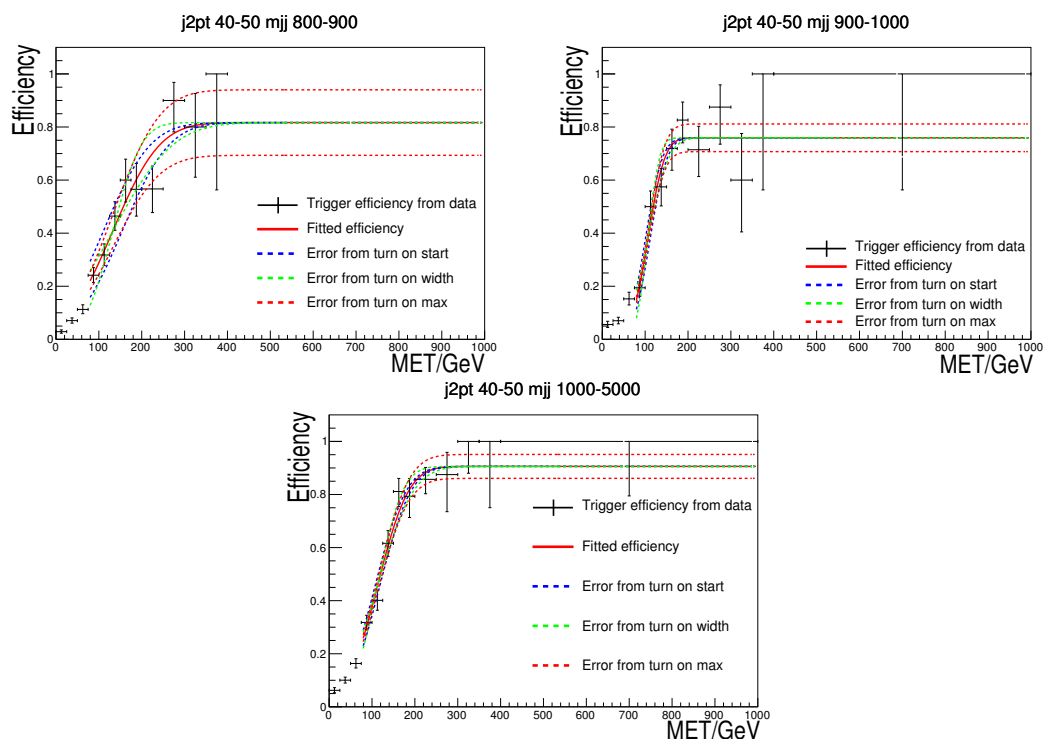


Figure A.5.: The measured efficiency of the trigger used in run D as a function of MET in bins of dijet mass (m_{jj}) and sub-leading jet p_T ($j2pt$). The bin that each plot corresponds to is displayed at the top of the plot.

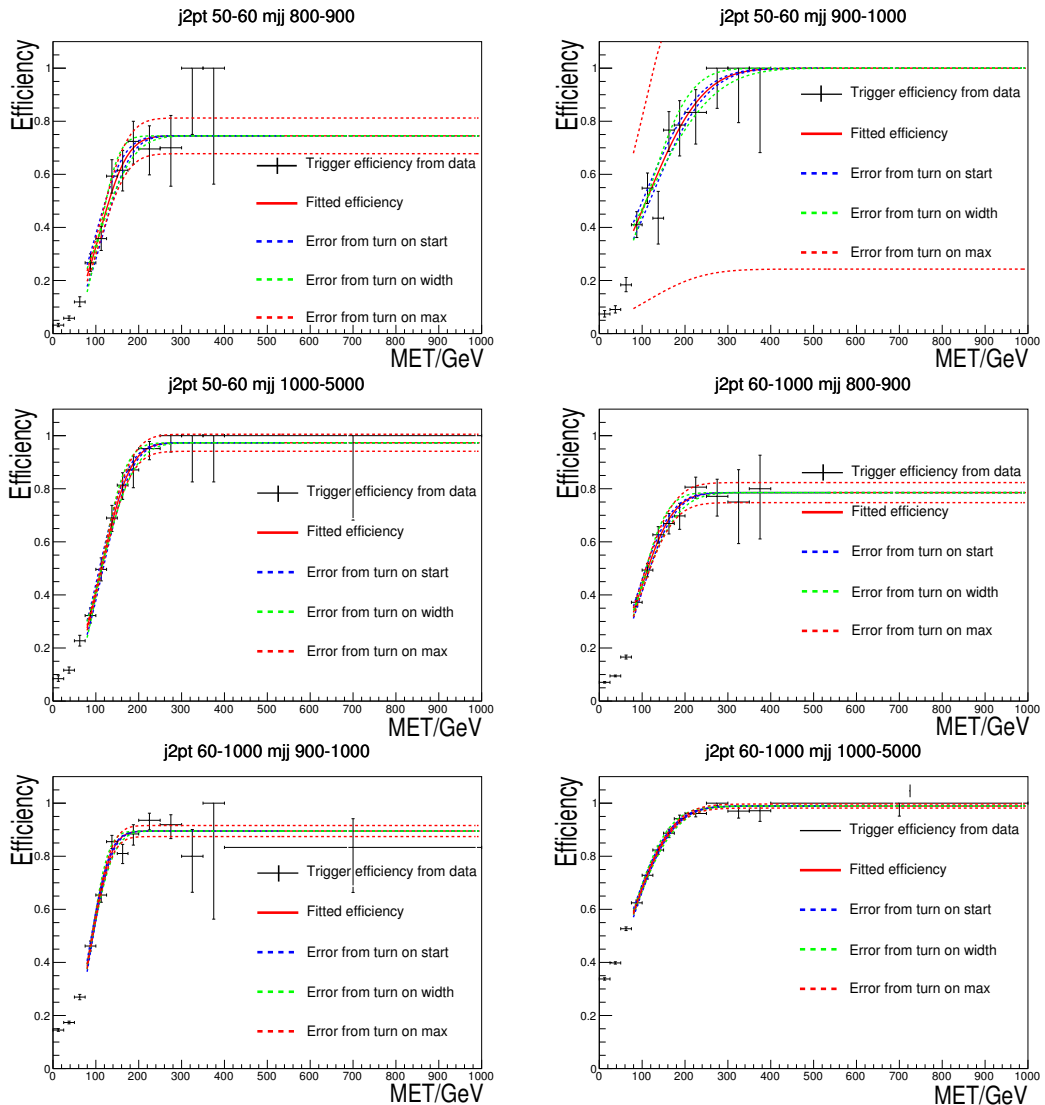


Figure A.6.: The measured efficiency of the trigger used in run D as a function of MET in bins of dijet mass (m_{jj}) and sub-leading jet p_T ($j_{2\text{pt}}$). The bin that each plot corresponds to is displayed at the top of the plot.

Bibliography

- [1] CMS Collaboration, “Search for invisible decays of Higgs bosons in the vector boson fusion and associated ZH production modes”, *Eur. Phys. J.* **C74** (2014) 2980, doi:10.1140/epjc/s10052-014-2980-6, arXiv:1404.1344.
- [2] CMS Collaboration, “Search for invisible decays of Higgs bosons in the vector boson fusion production mode”, Technical Report CMS-PAS-HIG-14-038, CERN, Geneva, (2015).
- [3] CMS Collaboration, “A combination of searches for the invisible decays of the Higgs boson using the CMS detector”, Technical Report CMS-PAS-HIG-15-012, CERN, Geneva, (2015).
- [4] J. Brooke, M. R. Buckley, P. Dunne et al., “Vector Boson Fusion Searches for Dark Matter at the LHC”, arXiv:1603.07739.
- [5] R. Aggleton, C. Asawatangtrakuldee, J. Brooke, O. Buchmueller, D. Colling, G. Davies, P. Dunne, S. Kumar, Q. Li, A. Magnan, K. Mazumdar, A. Nikitenko, J. Pela, P. Srimanobhas, D. Wang, “Search for an Invisible Higgs Boson”, *CMS Analysis Note: AN-12-403* (2012).
- [6] S. L. Glashow, “Partial Symmetries of Weak Interactions”, *Nucl. Phys.* **22** (1961) 579, doi:10.1016/0029-5582(61)90469-2.
- [7] S. Weinberg, “A Model OF Leptons”, *Phys. Rev. Lett.* **19** (1967) 1264–1266.
- [8] A. Salam, “Weak and electromagnetic interactions”, in *Elementary particle physics: relativistic groups and analyticity*, N. Svartholm, ed., p. 367. Almqvist & Wiksell, Stockholm, 1968. Proceedings of the eighth Nobel symposium.
- [9] Y. N. Murray Gell-Mann, “The eightfold way a review, with a collection of reprints,” ..

- [10] D. Hanneke, S. Fogwell, and G. Gabrielse, “New Measurement of the Electron Magnetic Moment and the Fine Structure Constant”, *Phys. Rev. Lett.* **100** (Mar, 2008) 120801, doi:10.1103/PhysRevLett.100.120801.
- [11] E. Noether, “Invariant Variation Problems”, *Gott. Nachr.* **1918** (1918) 235–257, doi:10.1080/00411457108231446, arXiv:physics/0503066. [Transp. Theory Statist. Phys.1,186(1971)].
- [12] E. Noether, “Invariant variation problems”, *Transport Theory and Statistical Physics* **1** (1971), no. 3, 186–207, doi:10.1080/00411457108231446.
- [13] C. N. Yang and R. L. Mills, “Conservation of Isotopic Spin and Isotopic Gauge Invariance”, *Phys. Rev.* **96** (Oct, 1954) 191–195, doi:10.1103/PhysRev.96.191.
- [14] Particle Data Group Collaboration, “Review of Particle Physics”, *Chin. Phys. C* **38** (2014) 090001, doi:10.1088/1674-1137/38/9/090001.
- [15] F. Englert and R. Brout, “Broken symmetry and the mass of gauge vector mesons”, *Phys. Rev. Lett.* **13** (1964) 321, doi:10.1103/PhysRevLett.13.321.
- [16] P. W. Higgs, “Broken symmetries, massless particles and gauge fields”, *Phys. Lett.* **12** (1964) 132, doi:10.1016/0031-9163(64)91136-9.
- [17] P. W. Higgs, “Broken symmetries and the masses of gauge bosons”, *Phys. Rev. Lett.* **13** (1964) 508, doi:10.1103/PhysRevLett.13.508.
- [18] G. S. Guralnik, C. R. Hagen, and T. W. B. Kibble, “Global conservation laws and massless particles”, *Phys. Rev. Lett.* **13** (1964) 585, doi:10.1103/PhysRevLett.13.585.
- [19] P. W. Higgs, “Spontaneous symmetry breakdown without massless bosons”, *Phys. Rev.* **145** (1966) 1156, doi:10.1103/PhysRev.145.1156.
- [20] T. W. B. Kibble, “Symmetry breaking in non-Abelian gauge theories”, *Phys. Rev.* **155** (1967) 1554, doi:10.1103/PhysRev.155.1554.
- [21] D. Griffiths, “Introduction to Elementary Particles”. Physics textbook. Wiley, 2008.
- [22] ATLAS Collaboration, “Observation of a new particle in the search for the Standard Model Higgs boson with the {ATLAS} detector at the {LHC}”, *Physics Letters B* **716** (2012), no. 1, 1 – 29, doi:<http://dx.doi.org/10.1016/j.physletb.2012.08.020>.

- [23] CMS Collaboration, “Observation of a new boson at a mass of 125 GeV with the {CMS} experiment at the {LHC}”, *Physics Letters B* **716** (2012), no. 1, 30 – 61, doi:<http://dx.doi.org/10.1016/j.physletb.2012.08.021>.
- [24] Super-Kamiokande Collaboration, “Measurements of the Solar Neutrino Flux from Super-Kamiokande’s First 300 Days”, *Phys. Rev. Lett.* **81** (Aug, 1998) 1158–1162, doi:[10.1103/PhysRevLett.81.1158](https://doi.org/10.1103/PhysRevLett.81.1158).
- [25] F. Zwicky, “Die Rotverschiebung von extragalaktischen Nebeln”, *Helv. Phys. Acta* **6** (1933) 110–127.
- [26] D. Clowe, M. Brada, A. H. Gonzalez et al., “A Direct Empirical Proof of the Existence of Dark Matter”, *The Astrophysical Journal Letters* **648** (2006), no. 2, L109.
- [27] Planck Collaboration, “Planck 2013 results. I. Overview of products and scientific results”, *Astronomy and Astrophysics* **571** (2014) A1, doi:[10.1051/0004-6361/201321529](https://doi.org/10.1051/0004-6361/201321529).
- [28] K. Freese, “Review of Observational Evidence for Dark Matter in the Universe and in upcoming searches for Dark Stars”, *EAS Publ. Ser.* **36** (2009) 113–126, doi:[10.1051/eas/0936016](https://doi.org/10.1051/eas/0936016), arXiv:0812.4005.
- [29] LHC Higgs Cross Section Working Group, S. Dittmaier, et al., “Handbook of LHC Higgs Cross Sections: 3. Higgs Properties: Report of the LHC Higgs Cross Section Working Group”, Technical Report [arXiv:1307.1347](https://arxiv.org/abs/1307.1347). CERN-2013-004, Geneva, (2013). Comments: 404 pages, 139 figures, to be submitted to CERN Report. Working Group web page:
<https://twiki.cern.ch/twiki/bin/view/LHCPhysics/CrossSections>.
- [30] CMS Collaboration, “The CMS experiment at the CERN LHC”, *JINST* **3** (2008) S08004, doi:[10.1088/1748-0221/3/08/S08004](https://doi.org/10.1088/1748-0221/3/08/S08004).
- [31] D. J. Gross and F. Wilczek, “Ultraviolet Behavior of Non-Abelian Gauge Theories”, *Phys. Rev. Lett.* **30** (Jun, 1973) 1343–1346, doi:[10.1103/PhysRevLett.30.1343](https://doi.org/10.1103/PhysRevLett.30.1343).
- [32] H. D. Politzer, “Reliable Perturbative Results for Strong Interactions?”, *Phys. Rev. Lett.* **30** (Jun, 1973) 1346–1349, doi:[10.1103/PhysRevLett.30.1346](https://doi.org/10.1103/PhysRevLett.30.1346).

- [33] CMS Collaboration, “Constraints on the Higgs boson width from off-shell production and decay to Z-boson pairs”, *Physics Letters B* **736** (2014) 64 – 85, doi:<http://dx.doi.org/10.1016/j.physletb.2014.06.077>.
- [34] ATLAS Collaboration, “The ATLAS Experiment at the CERN Large Hadron Collider”, *JINST* **3** (2008) S08003, doi:[10.1088/1748-0221/3/08/S08003](https://doi.org/10.1088/1748-0221/3/08/S08003).
- [35] “Measurements of the Higgs boson production and decay rates and constraints on its couplings from a combined ATLAS and CMS analysis of the LHC pp collision data at $\sqrt{s} = 7$ and 8 TeV”, Technical Report CMS-PAS-HIG-15-002, CERN, Geneva, (2015).
- [36] R. C. Cotta, J. L. Hewett, M.-P. Le et al., “Bounds on dark matter interactions with electroweak gauge bosons”, *Phys. Rev. D* **88** (Dec, 2013) 116009, doi:[10.1103/PhysRevD.88.116009](https://doi.org/10.1103/PhysRevD.88.116009).
- [37] M. R. Buckley, D. Feld, and D. Gonçalves, “Scalar simplified models for dark matter”, *Phys. Rev. D* **91** (Jan, 2015) 015017, doi:[10.1103/PhysRevD.91.015017](https://doi.org/10.1103/PhysRevD.91.015017).
- [38] G. D’Ambrosio, G. Giudice, G. Isidori et al., “Minimal flavour violation: an effective field theory approach”, *Nuclear Physics B* **645** (2002), no. 12, 155 – 187, doi:[http://dx.doi.org/10.1016/S0550-3213\(02\)00836-2](http://dx.doi.org/10.1016/S0550-3213(02)00836-2).
- [39] S. Agostinelli, J. Allison, K. Amako et al., “Geant4a simulation toolkit”, *Nuclear Instruments and Methods in Physics Research Section A: Accelerators, Spectrometers, Detectors and Associated Equipment* **506** (2003), no. 3, 250 – 303, doi:[http://dx.doi.org/10.1016/S0168-9002\(03\)01368-8](http://dx.doi.org/10.1016/S0168-9002(03)01368-8).
- [40] J. Favereau, C. Delaere, P. Demin et al., “DELPHES 3: a modular framework for fast simulation of a generic collider experiment”, *Journal of High Energy Physics* **2014** (2014), no. 2, 1–26, doi:[10.1007/JHEP02\(2014\)057](https://doi.org/10.1007/JHEP02(2014)057).
- [41] T. Sjöstrand, S. Mrenna, and P. Skands, “A brief introduction to {PYTHIA} 8.1”, *Computer Physics Communications* **178** (2008), no. 11, 852 – 867, doi:<http://dx.doi.org/10.1016/j.cpc.2008.01.036>.
- [42] J. Alwall, R. Frederix, S. Frixione et al., “The automated computation of tree-level and next-to-leading order differential cross sections, and their matching to parton shower simulations”, *Journal of High Energy Physics* **2014** (2014), no. 7, 1–157, doi:[10.1007/JHEP07\(2014\)079](https://doi.org/10.1007/JHEP07(2014)079).

- [43] P. Nason, “A New method for combining NLO QCD with shower Monte Carlo algorithms”, *JHEP* **11** (2004) 040, doi:10.1088/1126-6708/2004/11/040, arXiv:hep-ph/0409146.
- [44] S. Frixione, P. Nason, and C. Oleari, “Matching NLO QCD computations with Parton Shower simulations: the POWHEG method”, *JHEP* **11** (2007) 070, doi:10.1088/1126-6708/2007/11/070, arXiv:0709.2092.
- [45] S. Alioli, P. Nason, C. Oleari et al., “A general framework for implementing NLO calculations in shower Monte Carlo programs: the POWHEG BOX”, *JHEP* **06** (2010) 043, doi:10.1007/JHEP06(2010)043, arXiv:1002.2581.
- [46] J. Campbell, R. K. Ellis, and D. Rainwater, “Next-to-leading order QCD predictions for $W + 2$ jet and $Z + 2$ jet production at the CERN LHC”, *Phys. Rev. D* **68** (Nov, 2003) 094021, doi:10.1103/PhysRevD.68.094021.
- [47] J. Baglio et al., “Release Note - VBFNLO 2.7.0”, arXiv:1404.3940.
- [48] K. Arnold et al., “VBFNLO: A Parton Level Monte Carlo for Processes with Electroweak Bosons – Manual for Version 2.5.0”, arXiv:1107.4038.
- [49] K. Arnold, M. Bhr, G. Bozzi et al., ‘**Vbfmlo**: A parton level Monte Carlo for processes with electroweak bosons”, *Computer Physics Communications* **180** (2009), no. 9, 1661 – 1670, doi:<http://dx.doi.org/10.1016/j.cpc.2009.03.006>.
- [50] M. Czakon and A. Mitov, “Top++: A program for the calculation of the top-pair cross-section at hadron colliders”, *Computer Physics Communications* **185** (2014), no. 11, 2930 – 2938, doi:<http://dx.doi.org/10.1016/j.cpc.2014.06.021>.
- [51] Y. Li and F. Petriello, “Combining QCD and electroweak corrections to dilepton production in the framework of the FEWZ simulation code”, *Phys. Rev. D* **86** (Nov, 2012) 094034, doi:10.1103/PhysRevD.86.094034.
- [52] F. Krauss, “Phenomenology at collider experiments”, http://www.ippp.dur.ac.uk/~krauss/Lectures/MonteCarlos/Pheno_5_08.pdf (Accessed March, 2016).
- [53] “Procedure for the LHC Higgs boson search combination in summer 2011”, Technical Report ATL-PHYS-PUB-2011-011, CMS NOTE 2011/005, CERN, Geneva, (Aug, 2011).

- [54] G. Cowan, K. Cranmer, E. Gross et al., “Asymptotic formulae for likelihood-based tests of new physics”, *Eur. Phys. J.* **C71** (2011) 1554,
doi:10.1140/epjc/s10052-011-1554-0, *10.1140/epjc/s10052-013-2501-z*,
arXiv:1007.1727. [Erratum: *Eur. Phys. J.C73,2501(2013)*].
- [55] L. Evans and P. Bryant, “LHC Machine”, *JINST* **3** (2008), no. 08, S08001,
doi:10.1088/1748-0221/3/08/S08001.
- [56] LEP Injector Study Group, “LEP design report, volume I: The LEP injector chain;
LEP design report, volume II: The LEP Main Ring”. CERN, Geneva, 1983.
- [57] ALICE Collaboration, “The ALICE experiment at the CERN LHC”, *JINST* **3** (2008) S08002, *doi:10.1088/1748-0221/3/08/S08002*.
- [58] LHCb Collaboration, “The LHCb Detector at the LHC”, *JINST* **3** (2008) S08005, *doi:10.1088/1748-0221/3/08/S08005*.
- [59] ATLAS collaboration, “ATLAS detector photos”,
http://atlas.ch/atlas_photos/lhc/lhc_03.html (Accessed March, 2016).
- [60] M. Benedikt, P. Collier, V. Mertens et al., “LHC Design Report”. CERN, Geneva,
2004.
- [61] CMS Collaboration, “CMS Luminosity - Public Results”.,
- [62] W. J. Stirling, “Private communication”.,
- [63] T. Sakuma and T. McCauley, “Detector and Event Visualization with SketchUp at
the CMS Experiment”, *J. Phys.: Conf. Ser.* **513** 022032,
doi:10.1088/1742-6596/513/2/022032.
- [64] CMS Collaboration, “Interactive Slice of the CMS detector”, *CMS Document*
4172-v2.
- [65] Tricomi, Alessia, “Performances of the ATLAS and CMS silicon tracker”, *Eur
Phys J C* **33** (2004) s1023–s1025, *doi:10.1140/epjcd/s2004-03-1801-1*.
- [66] CMS Collaboration, “Description and performance of track and primary-vertex
reconstruction with the CMS tracker”, *J. Instrum.* **9** (May, 2014) P10009. 80 p.
Comments: Replaced with published version. Added journal reference and DOI.
- [67] CMS Collaboration, “History of ECAL response with laser data”.,

- [68] USCMS, ECAL/HCAL Collaboration, “The CMS barrel calorimeter response to particle beams from 2-GeV/c to 350-GeV/c”, *Eur. Phys. J.* **C60** (2009) 359–373, doi:10.1140/epjc/s10052-009-0959-5, 10.1140/epjc/s10052-009-1024-0. [Erratum: Eur. Phys. J.C61,353(2009)].
- [69] CMS Collaboration, “CMS Physics: Technical Design Report Volume 1: Detector Performance and Software”. Technical Design Report CMS. CERN, Geneva, 2006. There is an error on cover due to a technical problem for some items.
- [70] CMS Collaboration, “Data Parking and Data Scouting at the CMS Experiment”, .
- [71] CMS Collaboration, “Description and performance of track and primary-vertex reconstruction with the CMS tracker”, *Journal of Instrumentation* **9** (2014), no. 10, P10009.
- [72] K. Rose, “Deterministic Annealing for Clustering, Compression, Classification, Regression, and related Optimization Problems”, *Proceedings of the IEEE* **86** (1998) 2210.
- [73] R. Fruhwirth, W. Waltenberger, and P. Vanlaer, “Adaptive vertex fitting”, *J. Phys.* **G34** (2007) N343, doi:10.1088/0954-3899/34/12/N01.
- [74] CMS Collaboration, “Particle-Flow Event Reconstruction in CMS and Performance for Jets, Taus, and MET”, *CMS Physics Analysis Summary CMS-PAS-PFT-09-001* (2009).
- [75] CMS Collaboration, “Commissioning of the Particle-flow Event Reconstruction with the first LHC collisions recorded in the CMS detector”, *CMS Physics Analysis Summary CMS-PAS-PFT-10-001* (2010).
- [76] CMS Collaboration, “Commissioning of the Particle-Flow reconstruction in Minimum-Bias and Jet Events from pp Collisions at 7 TeV”, *CMS Physics Analysis Summary CMS-PAS-PFT-10-002* (2010).
- [77] S. Baffioni, C. Charlot, F. Ferri et al., “Electron reconstruction in CMS”, *Eur. Phys. J.* **C49** (2007) 1099–1116, doi:10.1140/epjc/s10052-006-0175-5.
- [78] CMS Collaboration, “Performance of electron reconstruction and selection with the CMS detector in proton-proton collisions at s=8TeV”, *Journal of Instrumentation* **10** (2015), no. 06, P06005.

- [79] W. Adam, R. Frühwirth, A. Strandlie et al., “Reconstruction of Electrons with the Gaussian-Sum Filter in the CMS Tracker at the LHC”, *CMS Note CMS-NOTE-2005-001* (2005).
- [80] L. Sani, “Private communication”,.
- [81] CMS Collaboration, “Performance of CMS muon reconstruction in pp collision events at $\sqrt{s} = 7$ TeV”, *JINST* **7** (2012) P10002, doi:10.1088/1748-0221/7/10/P10002, arXiv:1206.4071.
- [82] G. P. Salam, “Towards Jetography”, *Eur. Phys. J. C* **67** (2010) 637–686, doi:10.1140/epjc/s10052-010-1314-6, arXiv:0906.1833.
- [83] M. Cacciari, G. P. Salam, and G. Soyez, “The anti- k_t jet clustering algorithm”, *Journal of High Energy Physics* **2008** (2008), no. 04, 063.
- [84] M. Cacciari, G. P. Salam, and G. Soyez, “FastJet User Manual”, *Eur. Phys. J. C* **72** (2012) 1896, doi:10.1140/epjc/s10052-012-1896-2, arXiv:1111.6097.
- [85] N. Saoulidou and E. Tziaferi, “Performance of the Particle-Flow jet identification criteria using proton-proton collisions at 8 TeV”, *CMS Analysis Note: AN-14-227* (2014).
- [86] CMS Collaboration, “Pileup Jet Identification”, *CMS Physics Analysis Summary CMS-PAS-JME-13-005* (2013).
- [87] A. Hocker, J. Stelzer, F. Tegenfeldt et al., “TMVA - Toolkit for Multivariate Data Analysis”, *PoS ACAT* (2007) 040, arXiv:physics/0703039.
- [88] CMS Collaboration, “Determination of jet energy calibration and transverse momentum resolution in CMS”, *JINST* **6** (2011) 11002, doi:10.1088/1748-0221/6/11/P11002, arXiv:1107.4277.
- [89] CMS Collaboration, “Performance of Missing Transverse Momentum Reconstruction Algorithms in Proton-Proton Collisions at $\sqrt{s} = 8$ TeV with the CMS Detector”, *CMS Physics Analysis Summary CMS-PAS-JME-12-002* (2013).
- [90] Particle Data Group Collaboration, “Review of Particle Physics”, *Chin. Phys. C* **38** (2014) 090001, doi:10.1088/1674-1137/38/9/090001.

- [91] CMS Collaboration, “Performance of tau-lepton reconstruction and identification in CMS”, *JINST* **7** (2012) P01001, doi:10.1088/1748-0221/7/01/P01001, arXiv:1109.6034.
- [92] CMS Collaboration, “CMS Luminosity Based on Pixel Cluster Counting – Summer 2013 Update”, CMS Physics Analysis Summary CMS-PAS-LUM-13-001, (2013).
- [93] CMS Collaboration, “Summaries of CMS cross section measurements”,.
- [94] CMS Collaboration, “Top pair cross section in dileptons”,.
- [95] CMS Collaboration, “Measurement of the single-top t-channel cross section in pp collisions at centre-of-mass energy of 8 TeV”,.
- [96] CMS Collaboration, “Measurement of WW production rate”,.
- [97] CMS Collaboration, “Measurement of WZ production rate”,.
- [98] CMS Collaboration, “Measurement of the ZZ production cross section and anomalous trilinear gauge couplings in lll'l' decays at $\text{sqrt}(s) = 8 \text{ TeV}$ at the LHC”,.
- [99] CMS Collaboration, “Performance of τ -lepton reconstruction and identification in CMS”, *J. Instrum.* **7** (Sep, 2011) P01001. 33 p.
- [100] LHC Higgs Cross Section Working Group, S. Dittmaier, et al., “Handbook of LHC Higgs Cross Sections: 1. Inclusive Observables”, CERN Report CERN-2011-002, (2011).
- [101] LHC Higgs Cross Section Working Group, S. Dittmaier, et al., “Handbook of LHC Higgs Cross Sections: 2. Differential Distributions”, CERN Report CERN-2012-002, (2012).
- [102] J. Linnemann, “Measures of Significance in HEP and Astrophysics”, in *Statistical Problems in Particle Physics, Astrophysics, and Cosmology*, L. Lyons, R. Mount, and R. Reitmeyer, eds., p. 35. 2003. arXiv:physics/0312059.
- [103] CMS Collaboration, “Identification of b-quark jets with the CMS experiment”, *JINST* **8** (2013) P04013, doi:10.1088/1748-0221/8/04/P04013, arXiv:1211.4462.

- [104] C. Asawatangtrakuldee, J. Brooke, D. Colling, G. Davies, P. Dunne, A. Magnan, A. Nikitenko, J. Pela, “Search for a Higgs boson decaying to invisible final states”, *CMS Analysis Note: AN-14-243* (2012).
- [105] CMS Collaboration, “Measurement of the and {ZZ} production cross sections in pp collisions at”, *Physics Letters B* **721** (2013), no. 45, 190 – 211, doi:<http://dx.doi.org/10.1016/j.physletb.2013.03.027>.
- [106] CMS Collaboration, “Search for invisible Higgs produced in association with a Z boson”, Technical Report CMS-PAS-HIG-13-018, CERN, Geneva, (2013).
- [107] CMS Collaboration, “Search for the Higgs boson decaying to invisible particles produced in association with Z bosons decaying to bottom quarks”, Technical Report CMS-PAS-HIG-13-028, CERN, Geneva, (1900).
- [108] CMS Collaboration, “Search for New Physics in the V/jet + MET final state”, Technical Report CMS-PAS-EXO-12-055, CERN, Geneva, (2015).
- [109] K. J. de Vries et al., “The pMSSM10 after LHC Run 1”, *Eur. Phys. J.* **C75** (2015), no. 9, 422, doi:[10.1140/epjc/s10052-015-3599-y](https://doi.org/10.1140/epjc/s10052-015-3599-y), arXiv:[1504.03260](https://arxiv.org/abs/1504.03260).

List of Acronyms

VBF vector boson fusion

ggH gluon fusion

VH vector boson associated production

ZH Z boson associated production

DM dark matter

CL confidence level

ISR initial state radiation

EFT effective field theory

PSB Proton Synchrotron Booster

PS Proton Synchrotron

SPS Super Proton Synchrotron

PU pile-up

SM standard model

BSM beyond the SM

QFT quantum field theory

ECAL electromagnetic calorimeter

HCAL hadron calorimeter

EB ECAL barrel

EE ECAL endcaps

HB hadron barrel

HE hadron endcaps

HF hadron forward

HO hadron outer

L1 Level-1

HLT high-level trigger

CSC cathode strip chamber

DT drift tube

RPC resistive plate chamber

WLCG Worldwide LHC Computing Grid

PV Primary vertex

CTF combinatorial track finder

DA “deterministic annealing”

PF Particle flow

GSF Gaussian sum filter

BDT boosted decision tree

MC Monte Carlo

HPS hadron plus strips

JES jet energy scale

EM electromagnetic

CJV central jet veto

MVA multi-variate analysis

JER jet energy resolution

UES unclustered energy scale

CSV combined secondary vertex

NLO next-to-leading order

NNLO next-to-next-to-leading order

PDF parton distribution function

QCD Quantum Chromodynamics